# Investigations on Thin-Wall Machining of Curved Geometries

**THESIS**

Submitted in partial fulfilment of the requirements for the degree of

**DOCTOR OF PHILOSOPHY**

by

**PAWAR SHRIKANT SHANKARRAO**

Under the Supervision of

**Prof. TUFAN CHANDRA BERA**

**Prof. KULDIP SINGH SANGWAN**

Department of Mechanical Engineering

**BIRLA INSTITUTE OF TECHNOLOGY & SCIENCE**
**PILANI-333031 (RAJASTHAN) INDIA**

**2024**

**BIRLA INSTITUTE OF TECHNOLOGY AND SCIENCE, PILANI**

# CERTIFICATE

This is to certify that the thesis titled **"Investigations on Thin-Wall Machining of Curved Geometries"** submitted by **Pawar Shrikant Shankarrao** ID No **2016PH410091P** for award of Ph.D. of the Institute embodies original work done by him under our supervision.


(Supervisor)

**Prof. Tufan Chandra Bera**

Associate Professor,

Department of Mechanical Engineering,

BITS Pilani, Pilani Campus,

Rajasthan-333031, India

Date:

(Co-Supervisor)

**Prof. Kuldip Singh Sangwan**

Senior Professor,

Department of Mechanical Engineering,

BITS Pilani, Pilani Campus,

Rajasthan-333031, India

Date:

# Acknowledgement

It is my pleasure to convey my gratitude and acknowledge all those who have made it possible for me to complete this thesis. First of all, I am extremely thankful and express my deep sense of gratefulness to my research supervisor **Prof. Tufan Chandra Bera** his timely and constructive suggestions, which helped me to tackle the queries during this dissertation work. I feel indebted to him for not only teaching me each and every aspect of the art of doing research but also other important aspects of life. Without his trust and constant support, the successful achievement of this work would have remained a dream.

I would like to convey my gratitude to my research co-supervisor, **Prof. Kuldip Singh Sangwan** for his supervision, motivation and guidance during every step of this research work. Also, for giving me an opportunity with complete freedom to made use of the facilities in the BITS Workshop for the purpose of research as well as learning and practicing. He helped me unconditionally in all as aspects and I had the privilege of learning many things from him.

I am grateful to **Prof. V. Ramgopal Rao**, Vice-Chancellor, BITS Pilani, and **Prof. Sudhir Kumar Barai**, Director, BITS Pilani, Pilani Campus for giving me the opportunity to pursue my research work at the institute. I owe my sincere thanks to **Prof. Shamik Chakraborty**, Associate Dean, Academic-Graduate Studies & Research Division (AGSRD) for his motivation, constant support and encouragement. I would also like to thank **Prof. Srikanta Routroy**, Head of the Department of Mechanical Engineering for his moral support and kind assistance. I am highly indebted to my Doctoral Advisory Committee (DAC members **Prof. Girish Kant** and **Prof. Prateek Kala** for their valuable suggestions and for sparing their valuable time for departmental evaluation of this thesis. I express sincere thanks to **Prof. Arun Kumar Jalan**, DRC convener, Department of Mechanical Engineering.

I enjoyed the company of fellow research scholars of Mechanical Engineering Department, who were always ready to help whenever required. I express my thanks to my colleague of Mechanical Department **Dr. H. Manikandan** for his unstinting guidance, valuable suggestions and kind help at various stages of my work. I would like to thank and appreciate my dearest friend **Mr. Ajay Pingale, Mr. Prakash Taur and Mr. Deshbhushan Patil** for their support. I also thank BITS workshop staff**, Mr. Ashok Kumar Lagari, Mr. Rakesh Kumar, Mr. Ramesh Das, Mr. Vinod Naruka, Mr. Bhim Singh** and **Mr. Mahender Kumar Saini** for helping me in fabricating specimen of my research work. I sincerely thanks those persons whom I miss to acknowledge and who have directly or indirectly helped me to accomplish this task.

I would also like to pay high regard to my family, there are no words to acknowledge them for their constant support and encouragement. I owe my deepest gratitude to my parents **Mr. Shankar Krishnanath Pawar** & **Mrs. Jayashree Shankarrao Pawar** for giving me freedom, support and love which made me reach this level. I would like to extend my gratitude to my sister **Mrs. Payal Hrushikesh Dhomase**

& brother-in-law **Mr. Hrushikesh Mohanrao Dhomase** for their constant encouragement. I am thankful to my in-laws **Mr. Aabasaheb Nanasaheb Deshmukh** & **Mrs. Meena Aabasaheb Deshmukh** and **Mr. Abhishek Aabasaheb Deshmukh** for their support. Last but not the least I would like to thank my beloved wife **Pooja** for her constant support and encouragement during my research journey.

Besides this, several people have knowingly and unknowingly helped me in the successful completion of this project. I thank all of them for their assistance.

**Shrikant Pawar**

# Abstract

Peripheral milling is a widely used machining operation in automobile, aerospace, marine and die-mold making industries due to its versatility. It is capable to manufacture precisely a variety of complex components including jet engine blades, wing sections, compressor impellors, die-molds, etc. One of the common problems encountered during milling of these components is cutting force induced tool deflection resulting into dimensional as well as geometric error in the finished part. This issue is addressed by many researchers for straight geometries by properly calculating cutting forces, tool deflection and concerned surface error in the machined components. In many situations, workpiece geometry is not straight rather curved one having finite value of curvature. In the presence of workpiece curvature, mechanics of milling gets changed completely along with various process geometry variables.

The machining situation becomes more complicated when workpiece is thin-walled curved geometry. In case of thin-wall milling, the workpiece behaves like a cantilever plate having free-free-free-clamp (FFFC) boundary conditions. The magnitudes of workpiece deflection need to be calculated along the peripheral length from start to end of cut. In addition, during thin-wall milling, there is a continuous reduction in workpiece rigidity due to gradual material removal. Therefore, the calculation of cutting forces and deflection induced surface error become more difficult and cumbersome. It becomes more challenging and complex when workpiece is thin-walled curved in the presence of workpiece curvature. Keeping these aspects in mind, a focus is given firstly on estimation of tool and workpiece deflection induced surface error and its error compensation and secondly making the milling process energy efficient.

In order to estimate deflection induced surface error, the process geometry and cutting force models are prerequisite for computation of nodal deflections tool and workpiece. For easy understanding of surface error generation, workpiece is considered as straight having zero curvature initially. Next, the focus has been moved to milling of constant curved and variable curved geometries. Modelling of process geometry, cutting force and tool deflection has been done using MATLAB commercial software. For calculation workpiece deflection, the finite element method (FEM) is applied in ANSYS commercial software. Finally, the effect of workpiece curvature on cutting forces and

concerned surface errors is explored in case of variable curved geometries. In the present thesis, the results obtained from computational modelling work are compared with their experimental counterparts.

Tool and workpiece deflection induced surface error is manifested on machined components leading to dimensional as well as geometric inaccuracy of the parts. For a given cutting conditions (speed, feed rate, axial and radial depth of cut) the surface errors generated on machined component do not remain constant and change along the axial direction of the cut. It has been also observed that change in cutting conditions, the axial variation of surface error does not remain consistent and varies significantly. A methodology is presented in the research work for characterizing the axial surface error profiles and correlating it with cutting conditions. By identifying and recognizing the engagement pattern and correlating those to cutting conditions, a generic classification scheme consisting of six distinct cutting types is introduced in the present work. Later on, the geometric errors are also calculated based on the generic surface error classification scheme using particle swarm optimization (PSO) technique. Due to change in workpiece curvature continuously along the tool path, the axial variation of surface error is more challenging during machining of curved geometries. The thesis also examines the variation of surface error profiles along tool path in machining of curved geometries.

Another important aspect of the present thesis is estimation of energy consumption in milling and a detailed analysis in order to make the machining energy efficient. Demand-driven energy generation is a major cause of climate change and carbon dioxide emissions. Therefore, reduction in energy consumption is crucial factor in sustainable manufacturing. Additionally, as a result of rising energy prices and demand around the globe, conserving energy is crucial for cost containment and sustainable economic growth. Thesis also attempts to investigate an energy consumption in machining and develop an energy efficient machining system for reduction of energy consumption and making manufacturing system more sustainable.

The present work concentrates on developing an energy consumption model in milling of variable curved geometries where cutting forces differ along tool contact path in the presence of workpiece curvature. A hybrid energy consumption model consisting of empirical and analytical approaches is developed in MATLAB having modules for idle, auxiliary and cutting power. The proposed model is also validated by conducting machining experiments. The model is generic and versatile in nature and is useful for milling of

straight, circular and curved surfaces. In addition, the influence of workpiece curvature on power consumption has been investigated to realize the variation of power consumption along the tool contact path. Further, an energy efficient machining strategy developed for milling of variable curved components where more uniform cutting force and power profiles are accomplished due to constant chip load along the peripheral length of curved geometry. The proposed strategy is compared with conventional cutting in order to confirm the acceptability of the present algorithm. The proposed algorithm is formulated based on constant chip load by regulating entry angle of milling cutter according to workpiece curvature along the peripheral length. Thus, the cutting power fluctuation occurred due to variation of workpiece curvature is reduced by regulating tool-workpiece engagement.

The dimensional and geometric deviation of machined components is caused by the change in axial profile of surface error when machining curved geometries. A hybrid error compensation strategy has been developed in the thesis work to reduce variation of surface error in axial as well as peripheral direction. A hybrid error compensation strategy is proposed based on the regulation of tool engagement along cutter contact path and mirror image method. The step-by-step process for error generation and its compensation along the tool path is discussed in the thesis work. A detailed analysis surface error after implementing error compensation approach has been done for assessment of the performance of the proposed scheme.

Keywords: Peripheral milling, Curved geometry, Energy consumption, Energy efficient milling, Error compensation

# Table of Contents


| Caption | | Page No. |
|---|---|---|
| *Acknowledgement* | | i |
| *Abstract* | | iii |
| *Table of Contents* | | vii |
| *List of Figures* | | xiii |
| *List of Tables* | | xix |
| *List of Symbols and Abbreviations* | | xxi |
| **Chapter 1. Introduction** | | **1-10** |
| 1.1 | Introduction | 1 |
| 1.2 | Research Motivation | 3 |
| 1.3 | Research Objectives | 6 |
| 1.4 | Research Methodology | 6 |
| 1.5 | Organization of Thesis | 8 |
| **Chapter 2. Literature Review** | | **11-35** |
| 2.1 | Introduction | 11 |
| 2.2 | Cutting Force Models | 11 |
| 2.3 | Tool and Workpiece Deflection Models | 15 |
| 2.4 | Surface Error Characterization in Machining | 18 |
| 2.5 | Error Compensation in Machining | 18 |
| 2.6 | Energy Consumption in Machining | 24 |
| 2.7 | Energy Efficient Machining System | 28 |
| 2.8 | Summary of Previous Research Work | 29 |
| 2.9 | Research Limitations and Gaps | 32 |
| 2.10 | Need for Present Research | 34 |
| 2.11 | Concluding Remarks | 35 |
| **Chapter 3. Surface Error Generation in Milling** | | **37-72** |
| 3.1 | Introduction | 37 |
| 3.2 | Milling Process Geometry | 37 |

| | | |
|---|---|---|
| 3.2.1 | Process geometry for straight workpiece | 38 |
| 3.2.2 | Process geometry for circular workpiece | 39 |
| 3.2.3 | Process geometry for curved workpiece | 41 |
| 3.3 | Cutting Force Model | 44 |
| 3.3.1 | Modelling of cutting forces | 44 |
| 3.3.2 | Identification of cutting force coefficients | 49 |
| 3.4 | Estimation of Tool Deflection | 49 |
| 3.5 | Estimation of Workpiece Deflection | 51 |
| 3.6 | Surface Error Generation Mechanism in Milling | 53 |
| 3.7 | Surface Error Variation in Milling of Curved Geometries | 54 |
| 3.8 | Generation of Geometric Error in Machined Surface | 54 |
| 3.9 | Machining Experiments | 58 |
| 3.9.1 | Job design for experiment | 60 |
| 3.9.2 | Experimental setup | 62 |
| 3.9.3 | Machining conditions | 63 |
| 3.10 | Results and Discussions | 65 |
| 3.10.1 | Determination of cutting force coefficients | 66 |
| 3.10.2 | Model validation | 68 |
| 3.11 | Concluding Remarks | 71 |
| **Chapter 4.** | **Characterization of Surface Errors in Thin-Wall Milling** | **73-110** |
| 4.1 | Introduction | 73 |
| 4.2 | Characterization of Tool Deflection Induced Errors | 73 |
| 4.2.1 | Single flute engagement | 75 |
| 4.2.2 | Multi flute engagement | 77 |
| 4.3 | Characterization of Workpiece Deflection Induced Errors | 82 |
| 4.3.1 | Surface error shapes in single flute cutting | 82 |
| 4.3.2 | Surface error shapes in multiple flutes cutting | 85 |
| 4.4 | Surface error variation in milling of curved geometries | 88 |
| 4.5 | Machining Experiments | 89 |

4.5.1 Experimental setup 89
4.5.2 Machining conditions 89
4.6 Results and discussions 91
4.6.1 Comparison of predicted and measured forces profiles in milling of straight geometries 91
4.6.2 Comparison of dimensional error profiles for various types of cutting in milling of thick-walled straight geometries 92
4.6.3 Comparison of geometric error for various types of cutting in milling of thick-walled straight geometries 96
4.6.4 Comparison of predicted and measured surface error variation in milling of thick-walled curved geometries 98
4.6.5 Comparison of dimensional error profiles for various types of cutting in milling of thin-walled straight geometries 102
4.6.6 Comparison of geometric error for various types of cutting in milling of thin-walled straight geometries 106
4.6.7 Comparison of predicted and measured surface error variation in milling of thin-walled curved geometries 107
4.7 Concluding Remarks 110

**Chapter 5. Energy Consumption in Milling 111-152**

5.1 Introduction 111
5.2 Energy Consumption Model 111
5.2.1 The idle power consumption 113
5.2.2 The cutting power consumption 114
5.2.3 The auxiliary power consumption 115
5.2.4 Total power consumption 116
5.3 Energy Efficient Milling 117
5.3.1 Constant engagement method for variable curved geometry 117
5.3.2 Computation of tool engagement 117
5.3.3 Regulating constant tool engagement 120
5.3.4 Proposed algorithm 121
5.3.5 Criteria for selecting the desired value of constant engagement 126

5.3.6 Computation of specific cutting energy 128
5.4 Experimental Details 129
5.4.1 Experimental setup 129
5.4.2 Machining conditions 131
5.4.3 Energy consumption model calibration 132
5.5 Results and Discussions 135
5.5.1 Validation of energy consumption model 135
5.5.2 Comparison of forces for straight, concave and convex circular geometry 139
5.5.3 Influence of workpiece curvature on cutting force and feed forces 140
5.5.4 Influence of workpiece curvature on power consumption 142
5.5.5 Validation of constant engagement algorithm 143
5.5.6 Milling strategies for variable curved geometry 145
5.5.7 Realization of energy efficiencies in machining 150
5.6 Concluding Remarks 152

**Chapter 6. Error compensation in milling of curved geometries** **153-170**

6.1 Introduction 153
6.2 Hybrid Error Compensation Methodology 153
6.2.1 Constant engagement method 155
6.2.2 Mirror image method 156
6.2.3 Tool path modification using hybrid method 159
6.3 Machining Experiments 161
6.4 Results and Discussion 163
6.4.1 Comparison of results with and without compensation scheme for thick- walled geometry 163
6.4.2 Comparison of results with and without compensation scheme for thin-walled geometry 167
6.5 Concluding Remarks 170

**Chapter 7. Conclusions** **171-174**

7.1 Summary 171

7.2 Major Conclusions 172
7.3 Scope of Future Work 174
**References** 175
**List of Publications** A1
**Biographies** B1-B2

# List of Figures


| Figure No. | Caption | Page No. |
|---|---|---|
| Figure 1.1 | Cutting forces in milling | 1 |
| Figure 1.2 | Tool and workpiece deflection induced surface error in peripheral milling | 3 |
| Figure 1.3 | Flow Chart for Research Methodology | 7 |
| Figure 3.1 | Process geometry of straight workpiece | 38 |
| Figure 3.2 | Process geometry for circular workpiece | 40 |
| Figure 3.3 | Milling for variable curved geometry | 42 |
| Figure 3.4 | Cutting Force Components Acting on Axial Disk Element | 45 |
| Figure 3.5 | Milling forces for variable curved geometry | 46 |
| Figure 3.6 | Cutting force distribution in machining of straight geometry | 47 |
| Figure 3.7 | Cutting force distribution in machining of curved geometry | 48 |
| Figure 3.8 | Tool deflection model | 50 |
| Figure 3.9 | Flow chart for estimating workpiece deflections | 52 |
| Figure 3.10 | FEA model of thin-walled part | 53 |
| Figure 3.11 | Tool-workpiece contact surface in peripheral milling | 54 |
| Figure 3.12 | Flatness error representation | 56 |
| Figure 3.13 | Flowchart of PSO algorithm | 59 |
| Figure 3.14 | Straight workpiece | 61 |
| Figure 3.15 | The concave and convex elliptical workpiece | 61 |
| Figure 3.16 | Thin-wall workpieces | 61 |
| Figure 3.17 | Schematic representation of experimental setup | 63 |
| Figure 3.18 | The experimental setup | 64 |
| Figure 3.19 | Plot for cutting constants vs. average chip thickness | 68 |
| Figure 3.20 | Variation of cutting forces for straight geometry at a single feed station and curved geometry along curved length | 69 |
| Figure 3.21 | Predicted and measured surface error | 69 |

| | | |
|---|---|---|
| Figure 3.22 | Predicted and measured flatness error | 70 |
| Figure 3.23 | Variation of surface error along curve length in machining of concave elliptical curved geometry | 71 |
| Figure 4.1 | Expanded Engagement Section | 74 |
| Figure 4.2 | Classification scheme for surface error shapes | 75 |
| Figure 4.3 | Type I cutting | 76 |
| Figure 4.4 | Type II cutting | 77 |
| Figure 4.5 | Type III cutting | 78 |
| Figure 4.6 | Type IV cutting | 79 |
| Figure 4.7 | Type V cutting | 80 |
| Figure 4.8 | Type VI cutting | 80 |
| Figure 4.9 | Type I cutting | 83 |
| Figure 4.10 | Type II cutting | 84 |
| Figure 4.11 | Type III cutting | 85 |
| Figure 4.12 | Type IV cutting | 86 |
| Figure 4.13 | Type V cutting | 87 |
| Figure 4.14 | Type VI cutting | 88 |
| Figure 4.15 | Force profiles for various cutting types | 92 |
| Figure 4.16 | Surface error profiles for various cutting types | 93 |
| Figure 4.17 | Variation of surface errors on machined component | 96 |
| Figure 4.18 | Evaluation of experimental and computational flatness error | 97 |
| Figure 4.19 | The details of elliptical workpiece geometry | 99 |
| Figure 4.20 | Variation of engagement angle for curved geometry | 99 |
| Figure 4.21 | Surface error variation in milling of concave elliptical geometries | 100 |
| Figure 4.22 | Surface error variation in milling of concave elliptical geometries | 100 |
| Figure 4.23 | Surface error variation in milling of convex elliptical geometries | 101 |
| Figure 4.24 | Surface error variation in milling of convex elliptical geometries | 101 |
| Figure 4.25 | Surface error profiles for various cutting types | 102 |

| | | |
|---|---|---|
| Figure 4.26 | Variation of surface error on machined component | 105 |
| Figure 4.27 | Evaluation of experimental and computational flatness error | 107 |
| Figure 4.28 | Surface error variation in milling of concave elliptical geometries | 108 |
| Figure 4.29 | Surface error variation in milling of concave elliptical geometries | 108 |
| Figure 4.30 | Surface error variation in milling of convex elliptical geometries | 109 |
| Figure 4.31 | Surface error variation in milling of convex elliptical geometries | 109 |
| Figure 5.1 | Methodology for estimation of power consumption in milling of curved geometry | 112 |
| Figure 5.2 | A typical power profile of a milling process | 113 |
| Figure 5.3 | Tool engagement for circular geometries | 118 |
| Figure 5.4 | Tool engagement for concave circular geometries | 119 |
| Figure 5.5 | Tool engagement for milling of variable curved geometry | 120 |
| Figure 5.6 | Tool engagement at current, preceding and succeeding positions along the peripheral length | 122 |
| Figure 5.7 | Shifting of tool entry points | 124 |
| Figure 5.8 | Methodology for constant engagement algorithm | 127 |
| Figure 5.9 | Regulating cutter engagement by tool path modification | 128 |
| Figure 5.10 | The experimental setup | 130 |
| Figure 5.11 | Variation of idle power at different spindle rotational speeds | 133 |
| Figure 5.12 | Co-relationship between auxiliary and cutting power | 134 |
| Figure 5.13 | The details of elliptical workpiece geometry | 136 |
| Figure 5.14 | Force variation with respect to curve parameter for concave and convex geometries | 137 |
| Figure 5.15 | Comparison of experimental and computational power variations for concave and convex elliptical geometry | 138 |
| Figure 5.16 | Comparison of estimated forces for concave, straight and convex geometry | 139 |
| Figure 5.17 | Comparison of experimental and computational total power for concave, straight and convex geometry | 140 |

| | | |
|---|---|---|
| Figure 5.18 | Variation of cutting forces and feed forces with respect to curvature for concave and convex elliptical geometries | 141 |
| Figure 5.19 | Comparison of cutting and feed forces for concave and convex elliptical geometry | 141 |
| Figure 5.20 | Variation of cutting power consumption with respect to curvature for concave ellipse and convex ellipse geometries | 142 |
| Figure 5.21 | Workpiece geometry along with curvature variation | 143 |
| Figure 5.22 | Variation of cutting forces in X and Y direction in conventional cutting and constant engagement method | 144 |
| Figure 5.23 | Variation of resultant forces and power consumption in conventional cutting and constant engagement method | 145 |
| Figure 5.24 | Typical representation of modified semi-finished workpiece geometry for various strategies | 147 |
| Figure 5.25 | Comparison of tool engagement and uncut chip thickness for various strategies | 148 |
| Figure 5.26 | Comparison of cutting force variations for various strategies | 149 |
| Figure 5.27 | Comparison of power profile variation for various strategies | 150 |
| Figure 5.28 | Comparison of MRR variation for various machining strategies | 151 |
| Figure 5.29 | Comparison of energy and specific energy consumption for various machining strategies | 151 |
| Figure 6.1 | Surface error compensation in straight geometry | 156 |
| Figure 6.2 | Surface error compensation in machining of curved geometries | 157 |
| Figure 6.3 | Compensation methodology | 158 |
| Figure 6.4 | Tool deflection induced error compensation | 160 |
| Figure 6.5 | Workpiece deflection induced error compensation | 161 |
| Figure 6.6 | Illustration of four selected sections of elliptical geometry | 163 |
| Figure 6.7 | Predicted and measured surface errors before and after compensation at four sections of the concave thick-walled geometry | 164 |
| Figure 6.8 | Predicted and measured surface errors before and after compensation at four sections of the convex thick-walled | 166 |

geometry

Figure 6.9 Predicted and measured surface errors before and after compensation at four sections of the concave thin-walled geometry 168

Figure 6.10 Predicted and measured surface errors before and after compensation at four sections of the convex thin-walled geometry 169

# List of Tables


| Table No. | Caption | Page No. |
|---|---|---|
| Table 3.1 | Chemical composition of Aluminum 6351-T6 | 62 |
| Table 3.2 | Mechanical properties of aluminum 6351-T6 | 62 |
| Table 3.3 | Geometry and dimensional details of the workpiece | 62 |
| Table 3.4 | Cutting conditions for determination of cutting constants | 64 |
| Table 3.5 | Machining conditions for machining of straight and curved components | 65 |
| Table 3.6 | Values of Specific Cutting Constants | 67 |
| Table 4.1 | Angles criteria for various cutting types | 81 |
| Table 4.2 | Analytical equations for various kink points | 82 |
| Table 4.3 | Machining conditions for machining of straight component | 90 |
| Table 4.4 | Machining Conditions for machining of elliptical component | 90 |
| Table 4.5 | Determination of angular parameters along with kink positions | 94 |
| Table 4.6 | Flatness values for various cutting types | 98 |
| Table 4.7 | Determination of angular parameters along with kink position | 103 |
| Table 4.8 | Flatness values for various cutting types | 107 |
| Table 5.1 | Technical specifications of the machine tool, spindle and feed motors | 130 |
| Table 5.2 | Cutting conditions for auxiliary power | 131 |
| Table 5.3 | Machining conditions for elliptical component | 131 |
| Table 5.4 | Experimental conditions used in experiments | 132 |
| Table 5.5 | Data for measured idle power | 133 |
| Table 5.6 | Measured total power ($P_{total}$) and predicted cutting power ($\bar{P}_{cutting}$) | 134 |
| Table 5.7 | Comparison of the predicted power with measured power at different positions along tool path for concave and convex elliptical geometries | 139 |

| | | |
|---|---|---|
| Table 5.8 | Machining strategies | 146 |
| Table 6.1 | Machining conditions for elliptical component | 162 |
| Table 6.2 | Variation of range of surface error at various sections | 165 |
| Table 6.3 | Variation of surface error along peripheral direction of workpiece at section-4 | 165 |
| Table 6.4 | Variation of range of surface error at various sections | 167 |
| Table 6.5 | Variation of surface error along peripheral direction of workpiece at section-4 | 167 |
| Table 6.6 | Variation of range of surface error at various sections | 168 |
| Table 6.7 | Variation of surface error along peripheral direction of workpiece at section-4 | 169 |
| Table 6.8 | Variation of range of surface error at various sections | 170 |
| Table 6.9 | Variation of surface error along peripheral direction of workpiece at section-4 | 170 |

# List of Symbols and Abbreviations

| | |
|---|---|
| RDOC | Radial depth of cut |
| ADOC | Axial depth of cut |
| MRR | Material removal rate |
| $\theta_{en}$ | Entry angle |
| $a_e$ | Radial depth of cut |
| $r$ | Radius of milling cutter |
| $\theta_{ex}$ | Exit angle |
| $\theta_{engg}$ | Engagement angle |
| $\beta$ | Instantaneous tooth positioning angle |
| $\varphi$ | Cutter rotation angle |
| $\phi_p$ | Tooth spacing angle |
| $i$ | Index for cutting flute |
| $\alpha_{helix}$ | Helix angle |
| $z$ | Thickness of disc element |
| $N_f$ | Number of flutes |
| $t_c$ | Inner diameter of hollow cylinder |
| $\beta$ | Outer radius of hollow cylinder |
| $f_t$ | feed per tooth |
| $f_{cc}$ | feed per tooth along cutter contact path |
| $R$ | workpiece radius after cut |
| $u$ | curve parameter |
| $X_t(u), Y_t(u)$ | Parametric curve of locus of tool center |
| $X_{wb}(u), Y_{wb}(u)$ | Parametric curve of before cut workpiece trajectory |
| $X_{wa}(u), Y_{wa}(u)$ | Parametric curve of after cut workpiece trajectory |
| $X'(u), Y'(u)$ | Derivative of parametric w.r. parameter |
| $(X_t(u_a), Y_t(u_a))$ | Tool center position at point P along the locus of tool center |
| $(X_t(u_b), Y_t(u_b))$ | Tool center position at point Q along the locus of tool center |
| $(X_{wb}(u_c), Y_{wb}(u_c))$ | Position of tooth entry point R corresponding to point P |
| $(X_{wb}(u_d), Y_{wb}(u_d))$ | Position of tooth entry point S corresponding to point Q |
| $K$ | Curvature |

| | |
|---|---|
| $R_k$ | Local radius of curvature of geometry at $k^{th}$ feed position |
| $Ni$ | Number of axial elements |
| $j$ | Index of axial disk element |
| $dF_t$ | Elemental tangential force acting on $i^{th}$ flute |
| $dF_r$ | Elemental radial force acting on $i^{th}$ flute |
| $K_t, K_r$ | Cutting constants |
| $dF_f$ | Feed force acting on tooth $i$ at angular rotation $\varphi$ |
| $dF_n$ | Normal force acting on tooth $i$ at angular rotation $\varphi$ |
| $F_x$ | Force in X direction |
| $F_y$ | Force in Y direction |
| $\tau$ | Instantaneous tangent angle |
| $\Delta$ | Deflection in normal direction |
| $E$ | Young modulus |
| $I$ | Area moment of inertia |
| $L$ | gauge length of end mill |
| $D_e$ | equivalent tool diameter |
| $D$ | tool diameter |
| $x_j$ | Distance of $j^{th}$ element from fixed end |
| $a_m$ | Point of application for elemental load at nodal station m |
| $(x_u, y_u, z_u)$ | Coordinates of data point |
| $f$ | Objective or fitness function |
| $X^u$ | Current position of particle |
| $V^u$ | Current velocity of particle |
| $P_{best}$ | Individual best fitness value |
| $G_{best}$ | Global best fitness value |
| $t$ | Iteration number |
| $T$ | Maximum number of iterations |
| $w$ | Inertia weight |
| $c_1, c_2$ | Acceleration coefficients |
| $r_1, r_2$ | Random variables |
| $\alpha_{sweep}$ | Sweep angle |
| $h_b, h_l, h_m, h_n$ | Kink point positions |

| | |
|---|---|
| $a_p$ | Axial depth of cut |
| $P_{idle}$ | Idle power |
| $P_{cutting}$ | Cutting power |
| $P_{auxiliary}$ | Auxiliary power |
| $P_{total}$ | Total power |
| $n$ | Spindle RPM |
| $dP_{rotational}$ | Elemental power consumed due to rotational motion |
| $dP_{feed}$ | Elemental power consumed due to feed motion |
| $V$ | Cutting speed |
| $\bar{P}_{cutting}$ | Average cutting power |
| $u_1$ | Minimum value of curve parameter |
| $u_2$ | Maximum value of curve parameter |
| $R_k$ | Local radius of curvature of geometry at $k^{th}$ feed position |
| $i$ | Count for machining pass |
| $C_i(k)$ | Centre of local radius of curvature of geometry $(R_k)$ |
| $B_i(k)$ | Cutter entry point at $k^{th}$ feed station along $i^{th}$ tool path |
| $T_i(k)$ | Cutter center point |
| $A_i(k)$ | Cutter exit point |
| $B_i^*(k)$ | Modified cutter entry point |
| $\theta_{engg}^*$ | Desired engagement angle in radian |
| $\bar{V}_N$ | Normal vector at the tool center point |
| $\bar{V}_T$ | Tangent vector |
| SEC | Specific energy consumption |
| $E_{cutting}$ | Cutting energy |
| $V_{material}$ | Volume of material to be removed |
| $f$ | Feed rate |

# Chapter 1

# Introduction

## 1.1 Introduction

Peripheral milling is a common and widely used machining process in various manufacturing industries due to its versatility and competency to generate complex shapes with higher material removal rate. It is extensively used for manufacturing of power generation equipment, components of die/mold assembly, aeronautical parts, various components of military and shipbuilding industries etc. During peripheral milling, an end milling cutter is used to remove unwanted material from raw stock to obtain desired shape, size and surface finish. In peripheral milling, cutting force is exerted on tool-workpiece interface to remove unwanted material in the form of chips as shown in Fig.1.1. This cutting force can be resolved into three components namely axial, radial and tangential components. The axial component acts along the axis of milling cutter whereas radial and tangential components act along the radial and tangential direction of the milling cutter respectively. Out of these three components, only radial and tangential components are responsible for feed force and normal force during machining operation. The normal force component acting on the tool and workpiece contact surface leads to static and dynamic deflections of cutting tool and workpiece which result into significant amount of surface error on machined component.

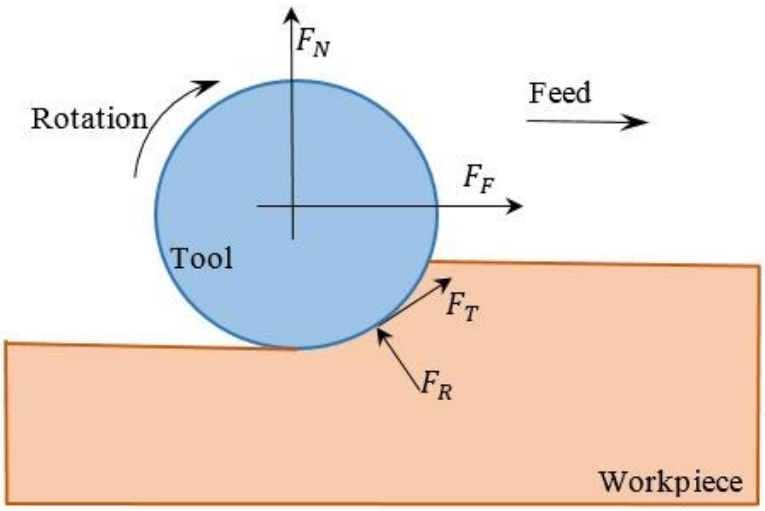


Fig.1.1 Cutting forces in peripheral milling

There are many situations, where large tool overhang is essential especially during higher axial depth of cut or during avoidance of tool-workpiece collision between upward projecting section of a component and tool adaptor. Under these circumstances, the tool deflection contributes remarkably to imprint surface errors on finished workpiece as shown in Fig. 1.2(a). This is referred to as thick-wall machining where workpiece deflection is not taken into account. The machining situation becomes more complicated when workpiece becomes thin-walled i.e. the thickness of workpiece is smaller as compared to height of the part. A part is termed as thin-walled workpiece when the aspect ratio (height to thickness ratio) is greater than four [1]. Machining of such type of thin-walled components is commonly known as thin-wall machining. In thin-wall machining, low stiffness of workpiece leads to workpiece deflection and contribute to surface error on finished workpiece significantly. The schematic representation of thin-wall machining is shown in Fig. 1.2(b). In the presence of workpiece deflection, nominal cutting conditions such as radial depth of cut and axial depth of cut get modified which leads to change in overall process geometry of peripheral milling. Due to complex engagement of tool with workpiece, the part deflection is not uniform in axial and peripheral directions over the length of workpiece. Surface error generated during the thin-wall machining differs from surface error generated during the thick-wall machining in a number of ways, and this difference is the one of the focus of the current thesis.

Global climate change and depletion of fossil fuel are matter of concerns to the world along with the increase in air pollution and carbon emissions. Manufacturing enterprises are one of the leading consumers of electricity which is majorly produced by burning fossil fuels. It not only generates huge carbon footprints but also changes global climate. The IEA (International Energy Agency) has announced that the generation of energy is the largest man-made source of air pollutants and the major energy demand is associated with the manufacturing sector [2]. According to their study, manufacturing industries account for one third of global energy consumption and 36% of the net global carbon emissions. Energy efficiency has become an integral part of the metal manufacturing industries as a means to improve competitiveness ,and economic and environmental performances [3]. Machine tools are dominant end users of electrical energy in manufacturing, and responsible for high carbon emissions [4]. Machine tools have a major

potential for energy efficiency gains and carbon emission reduction as a reduction of 1% in the energy consumption by machining activities will lead to the saving of approximately 200 petajoules/year (~ 55 kWh/year) [ 3].

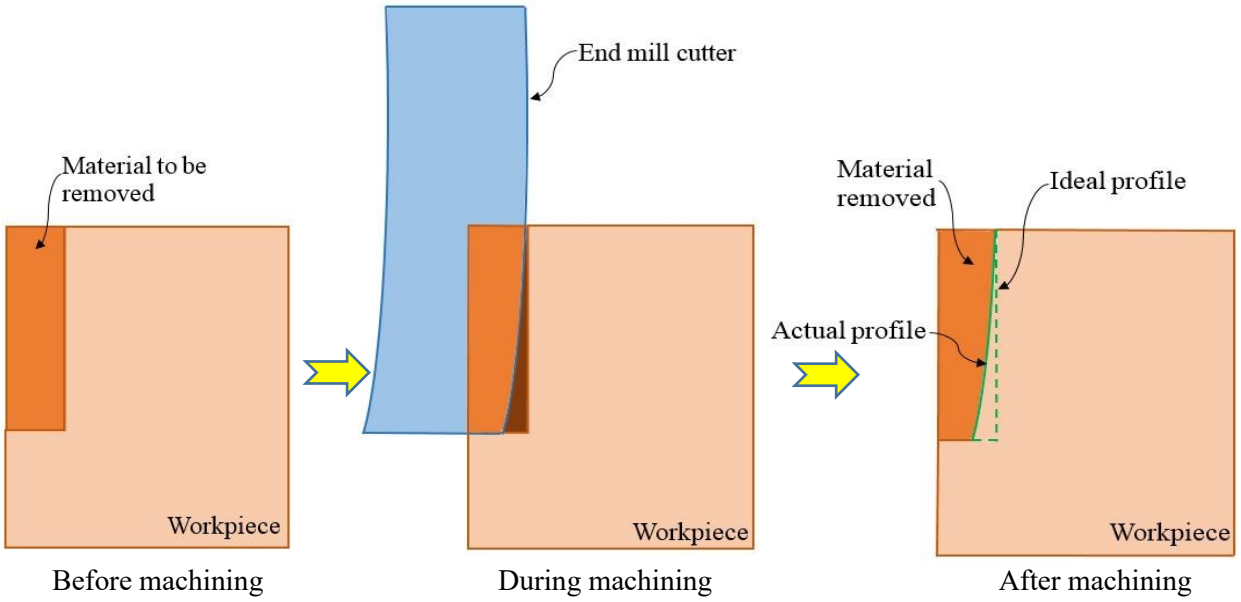


(a) Tool deflection in peripheral milling

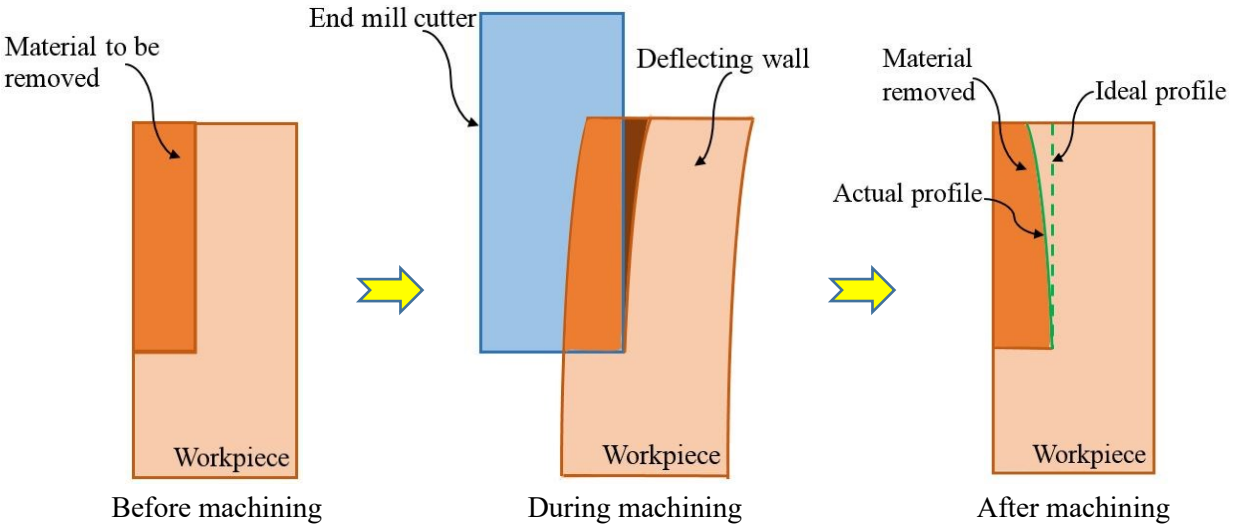


(b) Workpiece deflection in peripheral milling

Fig.1.2 Tool and workpiece deflection induced surface error in peripheral milling

## 1.2 Research Motivation

In a milling operation, inaccuracy in machined parts is caused due to the presence of various errors such as cutting force induced tool and workpiece deflection errors, machine tool error, thermal error, servo error, measuring system error, tool wear error *etc*.

Among these errors, dimensional and geometric errors caused due to the static deflection of tool have significant impact on the overall error generated on the machined parts. The cutting tool deflection induced surface errors produce a complex shape along the axial length of cut based on the cutting strategy, tool geometry and cutting parameters. The various complex shapes of surface error profiles are manifested on the machined component due to the variation of cutting forces in the chip engagement section and surface generating forces during material removal. As the cutting force depends on cutting strategy, tool-workpiece geometry and cutting parameters, the magnitudes and profile of the deflection induced errors are also affected by these machining conditions. Therefore, the prediction of tool deflection magnitudes is important to investigate the nature and shape profile of surface errors along the axial length accompanied by critical positioning of kinks (key points) throughout the machined surface. The distribution of surface errors points and their complicated arrangements in the machined surface provide a scope of in-depth study of surface characteristics in order to investigate dimensional and geometric errors of the machined surface. Therefore, a comprehensive surface error classification scheme is required to identify all the possible types of surface error profiles based on generic cutting conditions with the help of various dedicated analytical equations.

The situation becomes more complex when geometry of thin-walled workpiece comes into the picture. In case of straight geometry, magnitude of curvature is zero. It is the simplest geometry among all different geometries of workpiece. In case of straight geometry, machining process is relatively simpler and easier for modelling and analyzing cutting forces and surface errors. But in case of circular geometries, the curvature of workpiece is constant and non-zero. Depending upon curvature, a circular workpiece can be concave or convex in nature. The process geometry of peripheral milling is completely different for machining of concave and convex workpieces. Therefore, deflection induced surface error are expected to be different for concave and convex workpieces. In case of circular geometry, tool and workpiece engagement remains constant along the cutter contact path. So analysis of machining process is little simpler. The situation becomes more complex when workpiece geometry is variable where curvature varies along the workpiece profile. Due to complex engagement of tool and workpiece, process geometry of milling changes continuously along the tool path in presence of curvature of workpiece. This leads

to change in cutting forces, combined deflection values and corresponding surface errors. This surface error not only hampers dimensional accuracy but geometrical accuracy of part also. Eventually, it adversely affects the functional requirement as well as performance of the parts. Therefore, it is necessary to study comprehensively the machining of thin-walled variable curved geometries along with accurate estimation of cutting forces and corresponding surface errors.

To get an in-depth knowledge of energy use in a machining process, the key initiative is to realize and characterize energy distribution in the process. The accurate estimation of energy consumption for peripheral milling is a big challenge to the research community due to varying chip load and continuous alteration of cutting forces along the helical teeth of a cutter based on depths of cut selected during the process. The machining situation becomes more complicated in the presence of workpiece curvature as magnitude of feed per tooth changes continuously along tool contact path. As the cutting process is fast and complex, it is very difficult to understand tool-workpiece interaction and concerned energy consumption in the presence of complex cutter engagement. As the industry is moving towards cloud manufacturing and industry 4.0, the simulation, modelling and computational studies of energy consumption in milling are getting importance for accurate estimation of energy consumed during material removal process. This will also be helpful for planning of machining processes effectively so that manufacturers can develop energy-efficient and sustainable machining systems.

The study of surface error in milling of curved geometries is incomplete until it is compensated to achieve desired accuracy in the machined components. Traditionally, process design approach is followed to reduce cutting forces by restricting process parameters such as speed, feed rate and depth of cut. The reduction in cutting forces results into reduction in tool and workpiece deflections and the concerned surface errors on machined components. Hence, dimensional accuracy of a part can be improved upto certain extent. The major problem of this approach is increase in machining time as well as improper utilization of machine tool capability. This approach also hampers machining productivity and increases machining cost. Therefore, it is essential to develop an error compensation scheme to improve accuracy of curved geometries without sacrificing the machining productivity and utilizing machine tool capability to its full extent.

## 1.3 Research Objectives

Main objective of the present research work is to establish and verify an energy efficient machining strategy and off-line tool path compensation technique that takes tool and workpiece deflections into account in machining of curved geometries. In order to accomplish this, the research objectives of the present work can be stated as follows:

i. Estimation of tool and workpiece deflection induced surface errors in peripheral milling of curved geometries.
ii. Development of a surface error classification scheme for peripheral milling of curved geometries.
iii. Development of an energy consumption model and energy efficient machining strategy for milling of curved geometries.
iv. Development of an error compensation scheme for milling of curved components to enhance part accuracy.

## 1.4 Research Methodology

The following research methodology will be followed to accomplish the aforementioned research objectives.

First step of research methodology is to develop surface error model. Surface error estimation necessitates models that account for process geometry variables, cutting forces, tool and workpiece deflections, and the surface error generation mechanism. First, the process geometry of peripheral milling has been developed by taking care of geometry of workpiece. During modelling of process geometry of milling, several process geometry variables such as uncut chip thickness, feed per tooth, entry and exit angles, and engagement angle are determined. To develop the cutting force model, the basic required input is process geometry of milling. The predicted cutting forces obtained from the mechanistic cutting force model are used as inputs for deflection model of tool and workpiece. After that, surface errors are calculated by error generation mechanism based on estimated tool-workpiece deflection values. The estimated values of surface errors computed using the aforementioned models have been verified by performing machining experiments.

Second step of research methodology is to develop surface error classification scheme for peripheral milling. The correlations of surface error variations with RDOC

(Radial depth of cut) and ADOC (Axial depth of cut) are established by analyzing the effect of changes in RDOC and ADOC on engagement angle and sweep angle together with tooth spacing angle. Based on this relationship, surface error profiles have been classified into six types of cutting combining single flute and multi flute engagement. Further, the significance of proposed classification is highlighted in milling of curved geometries where curvature of workpiece effects the tool-workpiece engagement, which changes surface error profiles.

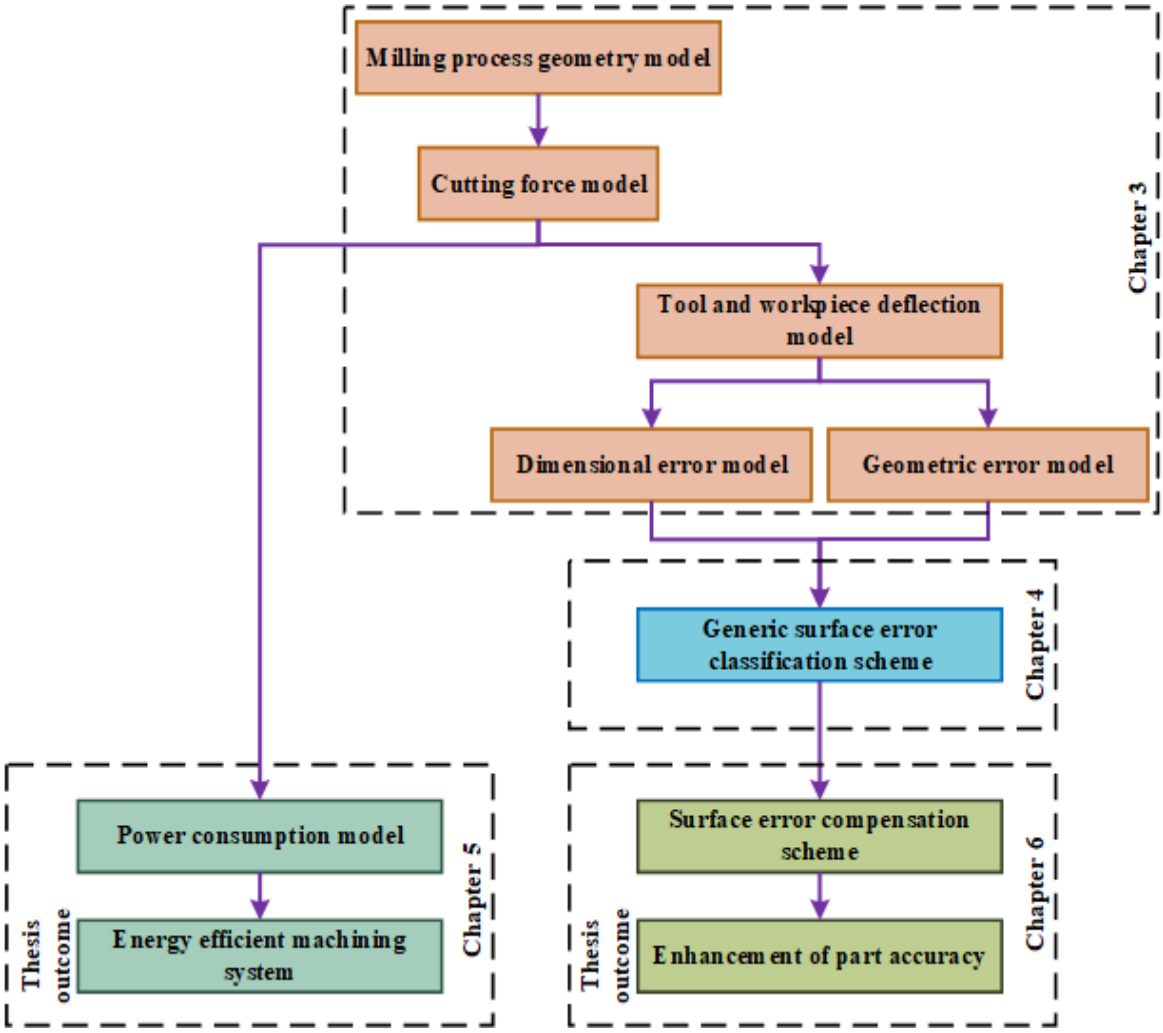


Fig.1.3 Flow Chart for Research Methodology

Third step of research methodology is to investigate the modelling of power consumption and energy efficient machining system in peripheral milling of curved workpieces. First, a hybrid energy consumption model has been developed involving process mechanics, cutting forces and energy consumption by incorporating various modules of idle, auxiliary and cutting power. In addition to it, the influence of workpiece

curvature on power consumption is investigated to realize the variation of power consumption along the tool contact path. Furthermore, a machining strategy has been built based on constant engagement cutter path modification for milling of a variable curved geometry for developing energy efficient machining. All these models have been validated by the experimental work.

Final step of methodology is to establish an error compensation methodology to reduce surface error caused due to tool-workpiece deflection. In the present work, an offline tool path modification approach based on estimated surface error has been adopted and implemented in milling of curved geometries. On the basis of compensated points, computational work has been done to modify tool paths and generate compensated tool paths. The off-line tool path computation has been performed to estimate tool-workpiece deflection-induced surface error and error compensation. Both concave and convex curved surfaces have been used to examine the efficacy of error compensation methodology. The adopted methodology for compensation is validated using machining experiments. The Fig.1.3 shows a flow chart for research methodology.

## 1.5 Organization of the Thesis

There are seven chapters in the thesis. The first chapter provides an overview of thin-wall milling, the research backdrop, research motivation, research objectives, as well as a summary of the thesis. The organization of the remaining chapters in the thesis is as follows:

Chapter 2 discusses key contributions and past research attempts in milling of straight, circular and curved components. In the framework of the current research, this chapter contains a thorough literature survey on modelling of cutting forces, tool and workpiece deflections, surface errors, and energy consumption in milling. Furthermore, brief discussion of the earlier proposed energy efficient machining strategies and error compensation mechanisms have been included. Finally, based on the earlier work, research gaps are highlighted, and the need for the current research is presented.

In chapter 3, a model of milling process geometry variables and cutting forces has been developed for concave and convex curved geometries. The nature of the curvature of the workpiece have been incorporated into the modelling of cutting forces for both

geometries. For given cutting conditions, mechanistic model estimates cutting forces that, as previously noted, are used to determine tool and workpiece deflections. Using surface generation mechanism, the predicted deflections are transformed into estimated surface errors. The cutting force model along with surface error generation mechanism are employed for estimating surface errors and corresponding error profiles manifested on the machined surface. Later on, geometric errors are also computed for milling of straight geometry based on nodal deflections of tool-workpiece. The variation of surface error with workpiece curvature in milling of curved geometries is also studied. Machining experiments are performed to conform the validity of the proposed models. Also, by carrying out a number of machining tests, a discussion has been made in this chapter regarding cutting force constants and technique to find the constants values.

In chapter 4, a methodology is presented to classify surface error profiles based on three parameters namely engagement angle, sweep angle and tooth spacing angle for peripheral milling considering only tool deflection. This surface error classification scheme is extended for thin-wall machining. The chapter also investigates some of the key challenges that arise during machining of thin-walled components such as thinning and end effects. Machining experiments are performed to validate the proposed scheme by comparing predicted results with measured results. Further, the significance of proposed classification is highlighted in milling of curved geometries where curvature of workpiece effects the tool-workpiece engagement and the corresponding surface error profiles.

Chapter 5 covers the analysis of energy consumption and energy efficient machining systems. Unlike straight geometries and circular geometries, the cutting forces and respective cutting powers vary continuously along the entire tool path in case of machining of variable curved workpiece due to workpiece curvature. The estimation of energy consumption has been performed for curved geometries. In the proposed energy consumption model, the idle and auxiliary powers are also included along with cutting power to obtain total energy consumption. The influence of workpiece curvature on cutting power consumption during milling of variable curved geometry is also investigated. The continuous fluctuation in force profile during machining of variable curved components creates a barrier to stable machining and cutting power consumption. Therefore, an energy efficient machining strategy for milling of variable curved components is presented where more uniform cutting force and power profiles are accomplished due to constant chip load

along the peripheral length of the curved geometry.

Chapter 6 presents a methodology of off-line surface error compensation for milling of curved geometries with an objective of improving part quality. Both concave and convex surfaces have been used to examine the efficacy of error compensation methodology. The adopted methodology for compensation is validated using machining experiments.

Chapter 7 highlights the main conclusions from the present study along with the summary of major contributions and suggested areas for future research.

# Chapter 2
# Literature Review

## 2.1 Introduction

Modelling of milling process is crucial in order to analyze the entire process for realizing the outputs of the process and identifying challenges in the process or inaccuracies in the part. The computation and analysis of tool-workpiece deflection induced surface errors and energy consumption are prerequisites for improving part accuracy and developing of energy efficient machining system. The modeling of milling process includes modelling of cutting forces, cutting power, tool and workpiece deflection, and generation of surface error on the machined components. In this chapter, an overview of prior modelling work on the milling process have been discussed within the context of the present research. Along with process modelling, a various energy efficient machining strategies and error compensation techniques utilized on the shop floor have also been briefly reviewed.

## 2.2 Cutting Force Models

Cutting force models are the most essential component for milling process modelling. Various approaches are followed to develop cutting force models for machining operations. Three popular approaches for developing force models are referred as: **analytical approach**, **empirical approach**, and **mechanistic approach**. **Analytical approach** establishes relationships between the cutting force components and cutting parameters such as cutter geometry, friction, cutting conditions, and mechanical behaviour of workpiece materials. Zhang et al. [5] investigated on analytical force model in peripheral milling of curved surfaces considering the effect of workpiece curvature on cutting forces. It was demonstrated that during the peripheral milling of circular profiles, the fluctuation of forces differs noticeably from that of straight geometries. Budak [6] developed an analytical model for high-performance milling by examining the process and optimum cutting conditions. Tsai [7] investigated the geometrical analysis of the three-dimensional force model for end milling. It explains the relative relationships between chip flow angle, shear plane area, cutting velocity, rake angle, and undeformed chip thickness. By considering the effect of material strengthening and edge radius, Rao and Shunmugam [8] presented

analytical force model, and cutting force coefficients which are calculated using oblique cutting method.

By taking into account the varying sliding friction coefficient and cutter run out, Zhou et al. [9] studied a theoretical model for prediction of cutting forces based on oblique cutting model and material physical properties. The results of the experiments indicated that the model are reliable to produce expected outcomes. Using the proposed model, it has been investigated how the cutting forces in micro end-milling are affected by material strengthening, edge radius, rake angle, and cutting speed. Luo [10] established analytical force model in milling of curved geometries. On the basis of an oblique cutting model, a new calibration method for the cutting force coefficients developed, and vector method proposed for modeling of process geometry such as equivalent feed rate, entry angle and exit angle considering variable radial depth of cut. Further, the effect of workpiece curvature and variable depth of cut on cutting forces are investigated. For prediction of forces in end milling, Moufki et al. [11] presented a new approach based on thermomechanical model of oblique cutting considering friction at tool-chip interface and thermomechanical behavior of workpiece material. The cutting edge effect has also been incorporated in order to take into account particular condition when the uncut chip thickness falls within the cutting edge radius range. By taking into account the effect of helix angle on cutting forces generated during milling, Masmali and Mathew [12] developed an analytical force model based on variable flow stress machining theory. For prediction of forces with regular end mill and variable helix end mill in peripheral milling, Lin et al. [13] proposed analytical model based on oblique cutting principle considering the effect of helix angle and pitch angle. In oblique cutting model, cutting geometric angles, cutting velocities, cutting energy, differential cutting forces are determined and later, resulting cutting forces are obtained considering the effect of feed velocity. Although these models are simple to use, it is necessary to be familiar with the shear angle, mean friction angle, and chip flow angle beforehand. These parameters must be obtained experimentally, which restricts the application and precision of these models.

**Empirical approaches** deal with experimental force models where large number of machining experiments need to be performed to establish empirical relationships among various parameters. Arsecularatne et al. [14] formulated power function equations to establish relationship between cutting forces and cutting conditions. Based on the mathematical equation, it is concluded that cutting speed has a relatively minimal effect on

the force components because of the small exponents. Abou-El-Hossein et al. [15] suggested first order and second order models using the response surface methodology (RSM) to estimate cutting forces generated during milling operation. The influence of cutting parameters such as feed, cutting speed, axial depth and radial depth on cutting force is also studied. It is concluded that the cutting force is primarily affected by the feed rate, with the axial depth, radial depth of cut, and cutting speed following closely behind. Ding et.al. [16] proposed an empirical model for milling forces and an analysis of variance (ANOVA) revealing that a linear model reflects best the variation in milling forces. Furthermore, they studied the effects of feed rate, cutting speed, and depth of cut on the milling forces and found that the two significant factors impacting the milling forces are the feed and the axial depth of cut.

Zhang et al. [17] used the nonlinear regression fitting approach to build an empirical model of milling force which encompasses both cutting parameters and tool geometric parameters. The effect of the geometric characteristics of a solid carbide end mill on milling force is investigated, and a corresponding mathematical relationship is determined for milling aviation aluminium alloy with a cemented carbide tool. It is observed that, several geometrical parameters, besides relief angle, clearly affect milling force. Bolar et al. [18] applied a response surface method (RSM) to establish a quadratic regression model for milling force by taking into account feed, tool diameter, radial depth and axial depth as influential factors. Furthermore, they investigated the effect of process parameters on milling forces and surface roughness. Li et al. [19] considered cutting parameters such as feed per tooth, axial depth, radial depth and cutting speed as the influencing factors and conducted a set of milling experiments. They developed a RSM based cubic polynomial regression estimation model for milling force based on the experimental data collected. The experiments are conducted to validate the proposed model. In experimental force models, the empirical correlations between the cutting forces and cutting parameters are unique to a particular tool-workpiece combination. In many other circumstances, it might not be useful. Also, development of these correlations needs a lot of cutting data, and the selected parameters make the expressions complicated and impractical in many situations. Mechanistic force models are frequently employed to address challenges observed in analytical and experimental force models.

**Mechanistic force models** are semi-analytical techniques that can precisely forecast cutting forces based on the mechanics of the cutting process. However, they are not fully

analytical and their modelling capability heavily relies on experimental cutting data. The relationship between cutting forces and chip geometry is established through a characteristic coefficient (a specific cutting constant). These constants depend on material of workpiece and geometry of tool and determined through machining experiments. Using the assumption that the tool and workpiece are a rigid system, Kline et al. [20] constructed a comprehensive framework for the estimation of cutting forces in milling operation. In order to machine low rigidity parts, Ratchev et al. [21] devised a flexible force model that took into account variations in the immersion angles of the engaged teeth. A force model was proposed by Wan and Zhang [22] that takes into account the variation in instantaneous uncut chip thickness (IUCT) caused by changes in the tool-workpiece deflection and the immersion boundaries of the tool and workpiece contact surface. Wan et al. [23] developed cutting force model by proposing a quick and effective calibration procedure for cutting force coefficients and cutter. Wei et al. [24] proposed an approach for prediction of cutting forces in pocket milling by considering the variation in cutter engagement, feed direction, and equivalent federate. Wan et al. [25] established a cutting force model taking chip removal, flank wear, and bottom cutting effects into account.

Perez et al. [26] presented a model to predict cutting forces based on specific cutting force coefficients that are calculated as a function of chip thickness. Baohai et al. [27] deduced a force model for circular end milling process. The effect of curvature of tool path on entry, exit angles and chip thickness are analyzed. Aydın [28] developed a force model by proposing a new methodology for determining the milling coefficients by taking into account the effects of tool geometry and cutting parameters. The milling coefficients are calibrated by evaluating the force distribution as the function of cutting and edge force components on each element. Hao et al. [29] established force model for peripheral milling of curved geometry by suggesting a calculation formula of simplifying instantaneous undeformed chip thickness considering tool runout. By taking into account actual engagement angle and actual undeformed chip thickness, Han et al. [30] proposed a method for prediction of forces in corner milling. The actual engagement angle calculated based on engagement relationship between tool and corner considering cutter radius, corner radius and tool trajectory. The actual undeformed chip thickness is obtained using proposed iteration algorithm that uses the trochoid trajectories of adjacent teeth.

By taking into account the tool path, tool runout, actual movement of the tool and workpiece geometry, Zhang et al. [31] developed a new method to calculate instantaneous

undeformed chip thickness, entry angle and exit angle. Furthermore, a method for finding cutter runout parameters and calibrating of force coefficients proposed which enables to predict forces in peripheral milling of curved geometry. Zhang et al. [32] presented a quick and effective calibration method for determination of cutter run out parameters and force coefficients simultaneously. Lumped-mechanism model used to express cutting force coefficients as a function of instantaneous uncut chip thickness. Moges et al. [33] established novel mechanistic force model for micro milling operation by incorporating process geometry parameters such as minimum chip thickness, change in effective rake and clearance angle, edge radius of milling cutter and elastic recovery of workpiece. Based on existing mechanistic force model, Wimmer [34] devised a modified model for finishing operation with small chip thickness by integrating cuter runout parameters. Furthermore, effectiveness of model is investigated by comparing it with model that neglects the effect of cutter runout. In the present research work, cutting forces are modelled using mechanistic approach due to close representation of actual forces.

## 2.3 Tool and Workpiece Deflection Models

Since, the surface error is caused due to tool and/or workpiece deflection, review has been made on these models.

### 2.3.1 Tool deflection models

There is a substantial amount of work that deals with cutting force induced tool deflection and concerned inaccuracy to the machined part. Kline et al. [35] proposed a cutting force induced deflection model and concerned dimensional inaccuracy. It is demonstrated that the variables like instantaneous cutting force, force center, cutter overhang, and clamping stiffness of the cutter affect the deflection error on the machined surface. The major limitation of their work is the surface generating force and surface generation points which are not well defined. Budak and Altintas [36] proposed a model dealing with surface generation in end milling with partial separation of cutter and workpiece due to static deflection in order to keep the form error within the specified limit. It has been found that appropriate selection of cutting conditions can substantially increase the material removal rate without compromising the dimensional accuracy of machined components. A virtual machining system is developed by Yun et al. [37] for analysis of kink shape of machined surface based on cutting forces and tracing of movement of cutter. It is

shown that the surface inaccuracy is only affected by a certain portion of the cutting forces normal to the machined surface. A simulation system for estimation of shape error is proposed by Wang et al. [38] considering bending and twisting of end milling cutter. A time simulation method is proposed by Ryu et al. [39] for rapid estimation of surface form error from tool deflection curve and its superposition without surface generation. This technique is effective for process planning and real-time surface shape error predictions in CAD/CAM systems. Dépincé and Hascoët [40] proposed a tool-workpiece contact point methodology to forecast the machined surface resulting from the cutter deformation error in the flat-end milling for constant and non-constant radial depths of cut. By assuming the cutting tool to be a cantilever beam of equivalent diameter, their analysis demonstrated that estimated results match experimental data well. In order to investigate the surface error in the flat end milling process, Aydin et al. [41] introduced a simulation approach anticipating the milling force distribution and deflection of cutter considering bending moments. Soori et al. [42] developed a virtual machining system to monitor and reduce tool deflection error in order to increase part manufacturing productivity and accuracy. To provide a useful methodology for part manufacturing with desired tolerances, the tool deflection error along tool path is monitored. Nghiep et al. [43] studied on mechanism of tool deflection error in order to reduce deflection error by using optimum cutting conditions and suitable lubrication mode. It is observed that productivity may be raised by increasing feed and the axial depth the without significantly sacrificing accuracy. The most of the aforementioned research attempts described about the tool deflection and respective surface errors. There is certain amount of work which deals with workpiece deflection and concerned form errors also.

### 2.3.2 Workpiece deflection models

Finite Element Method (FEM) is a popular and commonly used approach for commutating workpiece deflection and associated forms error. Ratchev et al. [44] introduced simulation environment to estimate deflection of low rigidity components by incorporating cutting force model, workpiece defection model and material removal algorithm. Wan and Zhang [45] proposed a numerical methodology for the prediction of surface errors in thin-walled workpiece peripheral milling using finite element techniques. The technique involves repeated modifications of the radial and axial depths of cut as well as a reduction in the stiffness of the workpiece due to material removal without remeshing. In order to forecast the form errors of workpieces, three-dimensional irregular volume

elements are produced. The small deformation equations are used by Aijun and Zhanqiang [46] to predict the elastic deformation of thin-walled plates during the milling process. In order to further improve machine precision, several cutting parameters are used in each machining layer. It was concluded that that different cutting parameters should be adopted at each machining layer to obtain better part accuracy and machining efficiency during the milling of thin-walled plates. Gang et al.[47] devised three-dimensional finite element models of a helical end mill cutter and thin-walled workpiece with cantilever to analyze the deformations of the thin-walled parts in milling process. A fast methodology is developed by Izamshah et al. [48] for estimation of wall deflection during milling of thin-wall components. The methodology integrates the finite element method with statistical analysis to establish relationship of surface error with cutting parameters and components features. Wu et al. [49] introduced a novel method for estimating deformations in milling of thin-walled plates using finite difference method (FDM).

A three dimensional fully coupled thermal-stress finite element-based mathematical model presented by Bolar and Joshi [50] to represent the intricate physical relationship between the workpiece and the helical milling cutter during the thin-wall milling. By performing milling experiments, the simulation results are validated, and it is found that the model is capable of accurately estimating the cutting forces, workpiece deflection, stress distribution, chip morphology, and surface temperature of the workpiece. Li et al. [51] devised a method for estimation of surface error caused due to workpiece deflections in five-axis milling of thin-walled components. In this model, the time variable stiffness of the component is estimated using an effective structural stiffness modification approach that only requires the finite element model of the initial workpiece and avoids re-mesh the part at each cutter position. Zhang et al. [52] investigated a new mode of workpiece deflections induced due to axial force in milling operation. The deflection function of the rectangular cantilever plate is used to build a prediction approach for the surface error caused by the new deflection mode. The experimental results are verified with the prediction results by changing cutting depth and spindle speed. Based on the elastic deformation theory of thin-walled components, Yue et al. [53] proposed a cutting force prediction model by varying chip thickness and method for predicting surface error based on the coupling relationship between cutting force and workpiece deformation during the milling. Agarwal and Desai [54] carried out comparison of workpiece deflection induced surface error created during thin-wall milling of straight and circular components. It is observed that straight components

deflect more than circular components even though concave components experience higher cutting forces. Cutting force induced surface errors do not have identical form along axial direction. The magnitude and shape of error profiles vary considerably with change in cutting conditions. Therefore, surface error characterization is essential for different cutting parameters and machining strategies.

## 2.4 Surface Error Characterization in Machining

A limited amount of study has been done on the identification of kink types and classification of surface errors in milling operations. In order to investigate surface generating force and kink formation mechanism, Chiang and Wang [56] derived analytical expressions for determining form error profile and positioning kink points on the machined surface. Based on the kink formation criteria, kink charts scaled in normalized axial and radial depths of cut are devised to identify the types of kinked surface generated at any given depths of cut. The study proved that that the form of surface error is not unique, and it changes from down-milling to up-milling. Desai and Rao [57] proposed a method for characterizing various surface error profiles caused by cutter deflections in peripheral milling operations. Six different types of surface error profiles are presented based on the surface generation mechanism and its interaction with the magnitude of tool-workpiece engagement in the axial and radial directions. Morelli et al. [58,59] established a classification scheme for various surface error shapes in both up and down milling. With the help of mathematical equations, the axial positions of key points (kinks) are determined for predicting surface error shape for any cutting parameters.

## 2.5 Error Compensation in Machining

The estimation and generation of surface errors during milling operations has been the subject of extensive investigation. In order to achieve the desirable dimensional and geometric tolerance, one of the most important aspects is the accuracy of the surface profile, which is also directly related to the functional performance of a component. The deflection of the tool and the workpiece during milling, which results into a deviation of the cutting depth, is the primary cause of the inaccuracy of components such as the surface dimensional error. Inaccuracy can result from several types of error factors including tool fracture, tool vibration, cutting force induced tool deflection, thermal deformation, and cutting force induced workpiece deflection. Among these sources of errors, tool and workpiece deflection

might be considered a significant source of error. As a result, controlling the tool-workpiece deflection induced surface error is very important and has drawn a lot of attention from researchers. There have been several approaches put out in the past to address this issue, and they may be categorized into four main groups: process design approach, real time compensation approach, online error compensation approach, and off-line error compensation approach.

### 2.5.1 Process design approach

The primary goal of process design approach is to control the cutting force during the milling operation. Different cutting parameters, such as feed rate, spindle speed, and depth of cut, among others, are optimized in such a manner that cutting force is constrained to a particular level, resulting into less surface error on machined components. Budak and Altintus [36] suggested a strategy for estimation and planning of feed rates along tool path to maintain static form error of plates within desired tolerance. In 3-axis milling of molds and dies with sculptured surfaces, Yazar et al. [60] investigated feed rate optimization based on estimations of cutting force. To cut down on machining cost and time, a technique has been developed to define the optimal rough milling and optimize the machining parameters. For pocket milling, Law et al. [61] adopted a process design technique to compensate tool deflection induced surface errors that vary over the whole length of the cut. Due to variations in radial depth of cut, tool deflection in straight and circular segments during pocket milling is not constant. Therefore, to reduce force and the related tool deflection induced error, the radial depth of cut is gradually changed during corner cuts. Force based feed rate scheduling approach introduced by Erdim et al. [62] to maintain cutting forces at predetermined level. It is demonstrated that a relationship between feed rate and cutting force may be formed to choose the ideal feed rate values for milling of free form surfaces. Smith et al. [63] suggested a new machining method that makes the machining insensitive to the thinness of finished components with the help of sacrificial structures. These structures provide stiffness to the component during machining; nevertheless, they do not become part of the final component. However, they are not a part of the completed component. Sacrifice structures support the part during machining. Wang et al. [64] developed an algorithm that optimizes the order in which blocks are removed during cutting operations in a way that the maximal deflection of the workpiece during the finishing operation is minimized. The efficiency of the proposed strategy in minimizing the geometric error of thin-wall workpiece are investigated by

performing machining experiments.

Despite the fact that the process design technique is frequently used on shop floors, its major problem is that it restricts the potential of the machining process. An operator cannot use a machine tool to its fullest capacity leads to longer machining time and lower machining productivity.

### 2.5.2 Real time compensation approach

In this approach, cutting forces and deflection induced errors are detected and controlled in real time by tilting the tool-workpiece or by regulating tool movement using a specially developed NC controller and sensor feedback closed loop setup. The research works addressing the real time compensation approach are covered in this section. To maintain the constant cutting force, Rober et al. [65] presented a robust controller employing the Quantitative Feedback Theory (QFT)-based delta transformation approach for time varying milling operation. With the requirements of time-domain specifications, such as intended overshoot and settling time, the milling force could be effectively regulated even when there are parametric uncertainties present. Yang and Choi [66] proposed a tool deflection compensation system that uses online feed rate control to regulate cutting forces and increase machining accuracy. This approach encounters a time-delay issue since the machine tool cannot respond quickly enough to carry out modifications in real-time. In order to solve this issue, Diez et al. [67] used a piezoelectric actuator to adjust the relative location of the tool and workpiece throughout the cutting process. By measuring the distance between a diamond tool edge and the workpiece surface using evanescent light, Yoshioka et al. [68] introduced a direct monitoring approach that may be utilized to compensate for machining errors. For the milling the rectangular pockets of a sizable thin-walled component, an improved forecasting compensatory control (FCC) method is presented and verified by Wang et al. [69] based on a precise deformation estimation model and Kalman filtering. The enhanced FCC system offers a reliable approach to ensure the remaining wall thickness. A real-time machining error compensation technique is presented by Liu et al. [70] for cutting forces generated elastic deformation. For the evaluation of feature rigidity and real time cutting force monitoring, the dynamic feature-based model was then established and implemented on a CNC platform using function blocks. For online detection and compensation of tool deflection during milling, Denkena and Boujnah [71] demonstrated a feeling machine outfitted with strain gauges. Based on accurate online

measurement of cutting forces and tool stiffness, either an adaptive feed rate control or an adaptive tool path modification is used to perform the compensation in real time.

In many circumstances, the real time compensation approach produces positive results, but it necessitates the hardware modification of both the controller and the machine tool, which has technical and financial constraints.

### 2.5.3 Online error compensation approach

In this approach, machining errors are detected through online measurement of machined surface and it can be corrected by the tool path modification to enhance machining accuracy. It is first proposed by Lo and Hsiao [72], who used a coordinate measuring machine (CMM) to quantify the surface error on machined component and compensate it by modifying tool path. Cho et al. [73] introduced on machine measurement (OMM) technique to gather the inspection data of machined surface using a touch-trigger probe installed on the spindle and then compensated surface error in three-axis milling. It avoids the additional re-setup errors and time while using CMM for measurement. Chen et al. [74] first separated systematic errors from the machining errors collected from the OMM system and subsequently corrected them using toolpath modification. Bi and Huang [75] developed a new adaptive compensation machining approach to reduce deflection error by analyzing the variation between actual machined surface and cutter envelope surface, where the machined surface is generated using coordinate information collected from the OMM method. The OMM inspection and a machine learning method are recently applied by Ge et al. [76] to build an integrated error compensation model for thin web sections.

In this approach, various surface errors are generated while utilizing the updated tool path. Therefore, it is necessary to go through an iterative process of OMM and experimentation until the machining tolerance is fulfilled, which is extremely time consuming and costly.

### 2.5.4 Offline error compensation approach

Offline error compensation approach is most frequently used and cost-effective compensation strategy out of all the above mentioned approaches due to its flexibility. After accurately modelling of cutting forces, tool and workpiece deflections are accurately estimated by applying the simulated cutting forces to the cantilever beam model of the tool

and the finite element model of the workpiece. This is accomplished by utilizing the mirror image compensation approach, which shifts the tool position backward by the predicted deflection error. This enables error compensation without the need for additional machining experiments.

An off-line error compensation model was presented by Raksiri and Parnichkun [77] to compensate for geometrical and cutting force-induced errors in 3-axis milling machine. A back-propagation neural network was used to estimate both the geometric and force-induced errors, and a camera was utilized to assess the outcomes of the machining errors. Ratchev et al. [78] presented a multi-level strategy for compensating surface errors that are caused by forces during the machining of thin-walled components. The deflection of the component at various locations along the tool path is taken into consideration by the prediction algorithm. When the cutting force and deflection reach a local equilibrium, the machining conditions are changed at each step. Tool deflection effects are taken into consideration for end milling by Depince and Hascoet [79]. According to a proposed technique. the tool deflection error can be compensated by altering the nominal tool path and without affecting production performance. Rao and Rao [80] adopted tool path modification approach to correct tool deflection errors in the machining of variable curved components, where workpiece curvature varies continuously throughout the whole path. According to the results reported, surface errors caused by cutter deflections may be decreased for curved geometries by 65-78%. In order to control cutting engagement at the required level during finishing operation, Uddin et al. [81] adopted a tool path modification strategy by regulating cutting force at the required level to reduce tool deflection and dimensional form error by adjusting the cutting engagement angle throughout the tool path trajectory.

In multilayer machining of a thin-walled component, Chen et al. [82] developed a dynamical model to forecast deflection using FEA, while iterative computation was used to account for the coupling relationship between cutting force and deflection. Each layer of the component is corrected for machining error to provide a lower and more consistent error. The multi-layer machining process has a very long overall cutting time, which considerably reduces productivity. By developing the estimation model for the tool deflection and geometrical inaccuracy, Habibi et al. [83] suggested a compensation method to modify the original tool path. The precision of machined features may be increased by around 8–10

times by employing updated NC code to mill spline contours. Based on analytical model established for the prediction of cutting force in the free-form milling process, Zeroudi and Fontaine [84] proposed an approach for calculating tool deflection from cutter location data obtained using CAM software and generating compensated tool path for it. Ma et al. [85] proposed a novel method to compensate cutting force induced tool deflection error during five axis CNC milling of sculptured parts. An analysis and optimization technique is used to modify tool paths while taking tool deflection into consideration in order to reduce the form error. In order to minimize the machining deformation, Gao et al. [86] developed the cutting force model and determined appropriate cutting parameters that directly affect the machining deformation during machining of thin-walled circular workpieces. Further, the deflection was corrected using a technique known as mirror compensation, which altered the cutter position point on both sides of the workpiece.

Du et al. [87] presented simple and accurate analytical cutting force model on the basis of Fourier series and proposed precise and suitable milling force induced error compensation technique employing analytical cutting force model and effective ANSYS parametric design language (APDL) deflection computation for low rigidity and complex parts. Zuo et al. [88] introduced a strategy of optimizing tool path to compensate deflection error in milling of thin-walled workpieces. Inverse reconstruction model based on discrete point cloud (DPC) representation and error estimated model was employed to design the approach, which accounts for the deflection of discrete workpiece points caused due to milling force-induced error, geometric errors, and other errors. Yue et al. [89] developed cutting force model based on modified model of chip thickness and then compensated tool deflection induced profile error by altering tool path using an offline error compensation strategy in corner milling. With the reconstruction of the concave and convex curves based on the secant compensation approach, Hou et al. [90] established a unique geometric modelling framework for machining of the thin-walled blade that may address the issue of machining error compensation. Huang et al. [91] effectively forecasted and compensated wall thickness error induced by static deflection in peripheral milling of thin plate components. A novel finite element model is initially created by combining the techniques of substructure analysis, specific mesh generation, and static stiffness alterations in order to increase the accuracy of calculating the component deformation.

## 2.6 Energy Consumption in Machining

There are significant amount of earlier research work dealing with various approaches of modelling of energy consumption in machining. These modelling approaches are broadly classified into four different groups; namely machine motion state-based model (**MSM**), specific energy-based model (**SEM**), exponential function-based model (**EFM**), and cutting force-based model (**CFM**). The machine motion state-based model (**MSM**) approach considers various machine states such as machine start-up, standby, idle, air cut, spindle acceleration/deceleration, tool change, etc. to predict power consumption. As power consumption is different at various machine states, the MSM approach calculates total power consumption as a summation of individual power consumption at various machine states. Dietmair and Verl [92] developed a generic model where the machining operation is divided into different operational states. The model is based on functionality for estimating energy consumption for machines and production systems considering each operational state. A similar type of model is developed by Avram and Xirouchakis [93] in which total energy is forecasted as a summation of energy requirements for the actuation drives by taking into account the steady and transient state regimes. Mori et al. [94] decomposed total energy consumption into energy required for tool-workpiece positioning, spindle acceleration and deceleration, tool changing, and workpiece cutting. He et al. [95] established mathematical relationship between energy consuming parts and NC codes and calculated total energy consumption by estimating energy consumed by each part such as spindle, axis feed, coolant pump, etc. Balogun and Mativenga [96] investigated the modelling of total energy demand by classifying machine tool states into three groups: basic, ready, and cutting states. Moradnazhad and Unver [97] suggested an energy consumption model for turn-mill machining centers by splitting the total power into various modules such as power due to main spindle, sub spindle, milling spindle, etc. Altintaş et al. [98] introduced modelling of total energy consumption by dividing it into three categories: basic, auxiliary, and material removal energy.

Edem and Mativenga [99] improved prediction model of energy requirements by incorporating a weight factor for feed drive. In their work, it is concluded that toolpath with longer linear path segments should be selected to reduce energy demand in machining. An energy consumption model for overall machining process is proposed by Gu et al. [100] by decomposing the full machining process into a series of activities and activity transitions for accurate estimation of energy demand. Recently, an improved energy consumption

model is developed by Yu et al. [101] for CNC milling of stainless steel along with prediction of surface roughness of part. The MSM models proposed by various researchers are able to predict energy consumption with decent accuracy for various machining operations. But, there are a large number of machine states in any machining process which need to be considered during modelling of energy consumption. Therefore, the implementation of MSM approach is not very convenient for every machining situation. Apart from it, these models are dependent on an assumption that power consumption for a machining component will remain same in every state. Since, machining conditions may not be same in every state, the power consumption for machining may differ in each state.

The **SEM** approach estimates power consumption using the concept of specific cutting energy which is described as an amount of energy desired for a unit volume of removed material. As material removal rate (MRR) is product of axial, radial immersions and feed rate, the SEM approach calculates cutting power by multiplying specific cutting energy to material removal rate. Gutowski et al. [102] presented an energy consumption model in this category for the first time. The total power consumption is computed as a summation of constant idle power and variable cutting power which is directly proportional to MRR. This model provides a strong thermodynamic exergy framework but the major limitations are that idle power does not remain constant with spindle speed and the model lacks the experimental verifications. In case of turning operation, Li and Kara [103] developed a power consumption model based on experimental data and concluded that specific energy consumption is inversely proportional to MRR. For a milling process, Li et al. introduced an improved energy consumption model that depends on MRR and spindle RPM. Aramcharoen and Mativenga [104] investigated the influence of tool wear in machining and concluded that dull tool requires higher specific cutting energy. Zhou et al. [105] developed specific energy consumption model by establishing relationship among spindle RPM, cutting conditions, MRR with specific energy consumption based on experimental results. A hybrid approach is suggested by Nguyen [106] for reducing specific cutting energy and improving MRR for a stipulated surface roughness on the basis upon cutting parameters. Yuan et al. [107] investigated the energy efficiency for milling based on specific cutting energy. The SEM models proposed by various researchers are considered as powerful tools for energy analysis through establishing mathematical relationships among energy consumption and various cutting parameters. However, in actual machining situation, the SEM models are very difficult to obtain based on large numbers of process

variables. In addition to it, the value of specific cutting energy is not fixed, rather it is affected by workpiece properties and machining environment.

The **EFM** approach predicts power consumption by using empirical formula based on experimental work. It uses various tools such as design of experiments and curve fitting to establish empirical relationship among these cutting parameters and power consumption. Based on a second order regression model, Yoon et al. [108] proposed a model using feed, depth of cut, and spindle speed. Later on, linear relationship between material removal power and tool flank wear was established using surface response methodology. Sealy et al. [109] developed a power regression model for estimation of resultant cutting specific energy including various cutting parameters. From this study, it is observed that tool wear had more effect on resultant cutting specific energy accompanied by feed rate and spindle RPM. For milling process, Xie et al. [110] developed a mapping technique for calculating loading loss coefficients in main driving system. Cutting power is calculated as exponential function of depth of cut, cutting width, feed rate and spindle RPM. Lv et al. [111] followed similar methodology to obtain cutting power for turning process and improved the accuracy of energy consumption model considering non-cutting motions such as spindle rotation, standby, cutting fluid spray, and feeding operations. They also investigated the effect of cutting and non-cutting related specific energy consumption and found that cutting related SEC diminishes rapidly than non-cutting related SEC with increase in MRR. Zhang et al. [112] developed a multistage approach to model power consumption. First, the total power consumption is broken down into three stages: basic energy consumption, sum of power consumption of feeding process & spindle rotation process, and the sum of power consumption of material removal and further load loss. After that, total power consumption is predicted in all these stages by using sliding filter method, multiple linear regression model, and gene expression algorithm respectively. Wang et al. [113] developed an empirical model based on power consumption characteristic curves. In addition, an algorithm to find cutting parameters was developed for low power consumption and short machining time. A statistical regression model has been developed by Wang et al. [114] based on undeformed chip parameters for studying the effect of process geometry on energy consumption in milling. Zhao et al. [115] developed a specific energy consumption model by considering standby power, cutting power, and spindle no-load power. Further, the effect of cutting parameters on surface quality and specific energy consumption were studied by using grey correlation analysis method. Tlhabadira et al. [116] proposed a model for

optimization of energy consumption using response surface methodology and observed that the energy consumption increases as the cutting speed and depth of cut increases, but decreases with the increase of feed rate. The major advantages of EFM approach are that it is simple, easy to apply and requires less theoretical background. But, these models treat the machine tools as a black box and rely on experimental data which require a large number of machining experiments to develop empirical relationships thereby making this approach expensive and time consuming.

The **CFM** approach estimates cutting power consumption using cutting force as a product of cutting constants and chip load. The values of cutting constants determined by conducting a separate set of machining experiments. Later on, cutting power is estimated as a product of cutting force and spindle speed for machining operation. Liu et al. [117] developed a hybrid power consumption model for slot milling for improving energy efficiency in production scheduling. For a turning process, Xie et al. [118] proposed a model for estimating the specific energy consumption (SEC) considering effect of machine tools, process variables, and workpiece material. Cutting force is calculated from an empirical model from mechanical engineering manual. Shi et al. [119,120] developed an efficient energy model by taken into account the effect of tool wear. A polynomial approximation technique was used to model the dynamic condition of the tool. In addition, they also proposed an enhanced power consumption model on the basis upon earlier model established by Liu et al. [117] for slot milling. They considered a statistical relationship among idle power and spindle RPM in place of constant idle power. Yang et al. [121] focused on an analytical cutting energy model for estimating total cutting power based on the power required to form chip and frictional power. For drilling process, Wang et al. [122,123] offered an energy consumption model dealing with idle power, cutting power and auxiliary power for drilling. They also investigated the power consumption model in milling by taking into account the auxiliary load loss. An optimization technique is used by Rao [124] to cut down power consumption in case of micro-ball end milling for predefined surface roughness and vibration. Zhang et al. [125] proposed an energy consumption model by taking into account the tool wear and tool run-out in a micro milling process. A hybrid optimization technique is used for identifying the optimal cutting parameters to reduce the energy consumption.

The CFM approach estimates cutting power consumption based on cutting force and cutting velocity. This approach provides the real nature of cutting force profile and reflects

the actual power profile during a machining operation. But, the major problem in CFM approach is estimation of idle and auxiliary powers.

## 2.7 Energy Efficient Machining System

Energy efficient machining system deals with whole production system along with behavioral characteristics and reduction of energy at system level. It embodies process planning, process monitoring & controlling, energy modeling and system integration for accomplishment of the required part quality and minimum energy consumption [126,127]. For reduction of energy consumption during machining, there are two commonly available approaches strike in our mind. The first one is the development of energy efficient machine tools which will consume lesser amount energy for performing the same task. The second approach is the development of energy efficient machining process by selecting optimized machining conditions, cutting parameters, cutting tool material etc.

There are a few attempts made on developing energy efficient green machine tool using advanced functionalities and energy saving strategies [128,129]. Towards exploring green machine tools, Mori et al. [94] conducted a study on reduction of machine tool power consumption by integrating the spindle acceleration or deceleration with the feed drive system. Abele et al.[130] focused on design and development of energy efficient spindle unit of turning center for improving energy efficiency. An investigation is done by Chen et al. [131] on design of green machine tool by case-based reasoning using an index system that incorporates the eco-design and function performances & energy saving technology. Fujishima et al. [132] identified all considerable energy reduction items for turn-mill centers along switching power to standby mode and curtailing cycle time in order to reduce energy usages for machine tools. An attempt has been made by Denkena et al. [133] to identify the various factors which influence the energy demand for primary and auxiliary units of machine tools. It is also suggested that some energy intensive components of the existing machine tools like cooling systems, cutting fluid supplies and hydraulic units must be replaced by the energy efficient components for saving overall machine tool energy consumption.

The consideration of optimal electrical drive system consisting of the required axes feed drives, spindle drive and supporting drives, development of control device and programs are the key factors for improving energy efficiency. The ISO standard guidelines

are suggested to be followed for designing and developing energy efficient machines in this context. The detailed methodologies and guidelines for developing of machine tool components such as spindles, hydraulic systems and chip conveyor are incorporated in this standard [94]. The replacements of all these energy intensive machine tools in a short span of time is a challenging task for machine tool manufacturers due to high investment of the modern production facilities. Therefore, in many situations, the first approach for developing green machine tool may not be feasible to implement in real scenario due to cost, time and other relevant factors. Hence, the second approach which deals with machining process is preferred to implement towards developing an energy efficient machining system.

Energy-efficient machining is an urgent initiative for sustainable manufacturing, which deserves foremost attentions from any organization for staying competitive in the global market. In many cases, the optimum machining conditions based upon minimum energy usage are selected to diminish energy required for machining operation. Ma et al. [134] proposed an energy optimization model for maximizing machining efficiency and minimizing the energy usage in CNC milling. Online optimization of cutting parameters is studied by Shin et al. [135] to develop energy efficient milling system according to real time need of process planning and machine control. An improved ant colony optimization technique is applied for machining of prismatic parts through STEP-NC by Wang et al. [136] for studying energy efficient sustainable production system. Moreira et al. [137] concentrated on multi-objective optimization technique for developing energy efficient machining system using an improved multi swarm fruit fly optimization algorithm (iMFOA). A simulation-based energy efficient milling process is investigated by Wirtz et al. [138] considering process time, stability and power consumption. Jacso and Szalay [139,140] suggested an algorithm using constant engagement offsetting strategy for milling in order to reduce chip load without considering undercut and overcut situation. These research work mostly deals with developing an energy efficient machining system by selecting optimum cutting parameters for accomplishment of minimum power consumption.

## 2.8 Summary of Previous Research Work

Modelling the milling process is an essential tool from the perspective of design, production, and process planning. Cutting forces, cutting power, and tool or workpiece

deflection-induced dimensional and geometric errors may be accurately estimated for machining processes using milling process models. Modelling of milling forces, modelling of tool or workpiece deflections, and modelling of dimensional and geometric error generation are crucial for precise calculation of dimensional and geometric errors on machined components.

It is clear from the literature mentioned in the previous section that there have been several attempts to predict the cutting forces, cutting powers and tool-workpiece deflections in milling. Cutting forces can be estimated using any one of the three models—the analytical model, the experimental model, or the mechanistic model—that were previously addressed. From the standpoint of metal cutting, each of these models has advantages and disadvantages of its own. However, none of them is comprehensive. The mechanistic modelling technique created by Kline et al. [20] is the most preferred and commonly employed in various machining conditions from sophistication and accuracy perspective.

The mechanistic method does not just use analytical reasoning or experimentation. Both methods are included in it. In a mechanistic method, the geometry of tool-workpiece interactions is used to analytically compute the instantaneous chip thickness, and cutting force constants are obtained through experimental results at various chip thickness values. Later, empirical relations are developed between geometrical parameters derived from the milling process geometry. There has been a significant amount of study on the mechanistic cutting force model for milling of straight geometry. Baohai [27], Han [30] extended this research work and applied to circular geometry. Wei [24], Hao [29] and Zhang [31] extended this study and implemented it to curved geometries, where process geometry fluctuates over the whole tool path. Since cutting force is one of the key input factors for deflection models, a precise cutting force model is crucial for accurate computation of tool or workpiece deflection.

Analytical tool deflection models investigate the empirical correlations between various tool geometry factors, such as tool overhang and tool stiffness. These models are highly effective at precisely estimating tool deflection under continuously fluctuating cutting forces. A cantilever beam model with a point force operating on the force center was suggested by Kline et al. [35] to forecast tool deflections. A modified cantilever beam model developed by Budak et al. [36] takes into account force values that are not uniformly distributed and operate on cutter-workpiece engagement zones. The model directly

estimates tool deflections using nodal force values obtained from the cutting force model. This model is frequently used to forecast tool deflection since it is more realistic to actual milling conditions.

Ratchev et al. [44], Wan and Zhang [45], Wu et al. [49], Agarwal and Desai [54] and others adopted the finite element method to develop workpiece deflection models. Forces estimated from the cutting force model are applied in the tool-workpiece engagement zone to calculate workpiece deflection. A surface error generation model is used to transform deflection values into surface errors after they have been calculated.

In addition to deflection models, error compensation techniques such process design approach, real time compensation approach, online error compensation approach, and offline error compensation approach have been covered in prior sections. The process design methodology is widely utilized in machining applications. The biggest disadvantage of this strategy is that it significantly lowers machining productivity. The real time compensation approach is not recommended due to difficulty in integrating additional measurement sensors and hardware into the manufacturing environment, which restricts the practical applications. The online error compensation approach requires additional time for measurement and experimentation which results in a loss of productivity. In these circumstances, offline error compensation approach is one of the effective ways to make precision components without losing productivity.

In works regarding to modelling of energy consumption, the specific energy-based approach (SEM), the cutting force-based method (CFM), and the exponential function-based method (EFM) have been discussed in earlier sections. Lv et al. [141] used all these methods to evaluate the prediction accuracy of cutting power in turning operations. It is observed that The CFM forecasts the cutting power most precisely when compared to EFM and SEM, and experimentally established coefficients enhance the prediction accuracy of the approaches. In addition, MRR is the sole variable taken into account in SEM. However, the same MRR may be obtained from many distinct processing parameters. Cutting studies have shown that energy consumption is not necessarily the same at the same MRR, as many other impacting factors need to be taken into account. Additionally, EFM only take into account the correlation between cutting power and total power and the coefficients in their model are solely determined by mathematical regression therefore lacking theoretical background.

Energy consumption can be reduced by one of the two approaches that were previously discussed. The first one is the development of energy efficient machine tools and replacement of existing ones available in manufacturing workshops. The replacements of all energy intensive machine tools in a short span of time are a difficult task for machine tool manufacturers due to high investment of the modern production facilities. Therefore, in many situations, this approach may not be feasible to implement in real scenario. The second approach is the development of energy efficient machining process considering energy consumption such as optimizing machining conditions, cutting parameters, cutting tool material etc. Hence, the second approach is preferred to implement towards developing an energy efficient machining system.

Based on literature review discussed above, research gaps have been identified and the need for the present research is addressed in next section.

## 2.9 Research Limitations and Gaps

The aforementioned research work mostly deals with estimation of deflection induced form error which causes dimensional inaccuracy to the machined components. The comprehensive knowledge about surface generating force and kink formation mechanism is lagging for predicting deviated surface due to tool deflection with multi-flute engagement and respective cutting force variations.

The previous research attempts majorly discuss about dimensional form errors and classification schemes for various machining conditions and cutting strategies. It is very difficult to get a comprehensive knowledge base about the maximum and minimum range of forms errors for any common type of cutting strategy and machining conditions. In addition, accomplishment of in-depth knowledge about geometric errors for a machined surface is equally important from a part design requirement and product performance perspectives. Therefore, a generic surface error classification scheme is essential for in-depth understanding of dimensional and geometric error for part manufacturing along with various types of cutting for a given machining conditions and cutting strategies. The current work aims to identify and develop a generic surface error classification scheme using various computational models keeping the earlier research limitations in mind.

A few researchers have participated in the research works on energy consumption during milling operation. But, no single model available in earlier work can highlight energy

consumption modelling issue due to complicacy and level of difficulty. Combining analytical models with empirical ones and intervention of human experience give a cutting edge to the hybrid energy consumption model. The aim is to establish a single model for explaining machine tool behaviour as well as to provide a generic predictive tool framework for machining operation. It will be helpful to fulfill the basic requirements of machining operation for each particular case. In the thesis, an attempt is made to develop a hybrid model combining analytical and empirical one approaches to analyze energy consumption.

During machining of a variable curved geometry, total energy consumption needs to be calculated as a summation of instantaneous energy during the operation periods. Therefore, a hybrid approach is adopted for investigation of energy consumption in milling of variable curved surfaces. The earlier research work concentrated on the modelling of energy consumption in milling of straight and circular geometries where feed rate is constant along the tool path. Therefore, the constant power profile is observed during cutting. However, in case of machining of variable curved workpiece, the magnitude and direction of curvature vary continuously along the entire cutter contact path. Therefore, process geometry of milling changes continuously along the entire tool path in the presence of workpiece curvature. It results into variation in instantaneous cutting forces and respective instantaneous cutting power along the entire tool path. Hence, it necessitates how energy consumption can be estimated in case of milling of curved workpieces along the entire tool path.

In case of milling of straight geometry, the selected cutting parameters like spindle speed, feed rate, depths of cut remain unaltered along periphery of workpiece. Therefore, the approach of selecting optimum cutting parameters contributes significantly for reducing machining energy consumption due to non-variation of process parameters for milling of straight geometry. But, for milling of curved geometry, all these process parameters do not remain constant throughout the machining process even if the optimum cutting parameters are chosen at the beginning of cutting operation. In case of milling of complex and variable geometry, the effective feed rate, depths of cut and respective uncut chip thickness change owing to workpiece curvature and other process related issues like tool/workpiece deflection, deformation of machine tool components etc. It results into alteration in chip load and concerned cutting forces leading to variation in cutting energy consumption. Therefore, a proper machining strategy needs to be designed in process planning stage

during milling of variable curved geometry which results in much larger energy savings in machining.

By employing the mirror compensation technique, which shifts the tool position in reverse by the amount of the predicted deflection error, Depince and Hascoet [79], Habibi et al. [83] and Zeroudi and Fontaine [84] compensated the tool deflection induced surface error while Ratchev et al. [78], Chen et al. [82] and Du et al. [87] reduced the workpiece deflection induced surface error in peripheral milling. Later, Gao et al. [86] and Yue et al. [89] proposed compensation techniques for milling of circular sections. Rao and Rao [80] and Hou et al. [90] compensated surface error in milling of curved geometries. However, the methods mentioned above only compensate surface error by moving the tool position, which is unable to completely reduce deflection errors that fluctuate along the axial direction during the peripheral milling operation. Due to the unaltered surface error in axial direction following the use of the compensation technique, the enhancement in geometric features is negligible. In order to improve dimensional as well as geometric accuracy while maximizing machine performance and maintaining productivity, a strong need for developing a compensating approach is also felt.

## 2.10 Need for Present Research

The aforementioned research limitations and gaps makes milling of curved geometries rather unpredictable and presents an opportunity for a thorough investigation of surface errors and energy consumption. By calculating and analyzing the surface errors and energy consumption during the machining of curved components, the current research study aims to close these gaps. The objectives of the current study have been defined in accordance with the identified research gaps.

i. Estimation of tool and workpiece deflection induced surface errors in peripheral milling of curved geometries.
ii. Development of a surface error classification scheme for peripheral milling of curved geometries.
iii. Development of an energy consumption model and energy efficient machining strategy for milling of variable curved components.
iv. Development of an error compensation scheme for milling of variable curved components to enhance part accuracy.

## 2.11 Concluding Remarks

A thorough literature survey on modelling of cutting forces, tool and workpiece deflection, surface errors, and energy consumption during milling operation has been conducted in this chapter. Research limitations and other challenges related to peripheral milling of curved geometries are properly addressed and research needs are recognised based on the prior work. Later, the necessity for the current research study is also mentioned in the present chapter along with research objectives.

# Chapter 3

# Surface Error Generation in Thin-Wall Milling

## 3.1 Introduction

Cutting force during milling operations has a significant impact on the metal cutting process, impacting machine vibration, tool and workpiece deflection, and ultimately part quality. Therefore, accurate estimation of cutting forces becomes crucial for process characterization, process optimization, and most importantly, for improving machining performance.

First of all, a milling process geometry model is presented in this chapter, to compute process geometry variables, i.e., feed per tooth, entry and exit angles, engagement angle, etc. for machining of straight, circular and curved geometries. On the basis of the process geometry model, the cutting force model is developed to predict the cutting forces. These forces are taken as inputs to estimate the static deflection of cutting tool and workpiece. Using surface generation mechanism, the predicted deflections are further transformed into estimated surface errors and corresponding error profiles manifested on the machined surface. Later on, geometric errors are also computed using particle swarm optimization (PSO) technique in order to find out flatness error of the machined surface. Machining experiments are performed to conform the validity of the proposed models. The following subsection describes about the milling process geometry in order to comprehend the physics of thin-wall machining process.

## 3.2 Milling Process Geometry

In a milling operation, the final shape of the workpiece is influenced by the geometry of tool-workpiece, and their relative motion and interactions. In case of milling, the rotation of the tool about its axis and the feed motion of the tool with respect to the machine table are identified as the two major components of the relative motion. Process geometry variables including feed per tooth along cutter contact path, cutter engagement angle, and instantaneous uncut chip thickness must be determined in order to generate the final shape of the machined component.

The modelling of process geometry of peripheral milling for straight surfaces has been a subject of research for a very long time [142]. Recent work has also been published on determining these process geometry variables in case of milling of circular and curved geometry [30,31]. During machining of curved surfaces, these variables does not remain constant and vary with workpiece curvature continuously. The following section discusses about mathematical expressions for process geometry variables for straight, circular and curved geometries briefly.

### 3.2.1 Process geometry for straight workpiece

Fig.3.1 shows a schematic representation of peripheral milling of straight surface describing various process geometry variables. The process geometry in this case is relatively straightforward. The various process geometry variables such as entry and exit angles, engagement angle, uncut chip thickness remain constant throughout the tool path. The entry angle ($\theta_{en}$) at which a cutting edge of milling cutter starts to cut the workpiece can be expressed as:

$$\theta_{en} = \pi - \cos^{-1}\left[1 - \frac{a_e}{r}\right] \tag{3.1}$$

where $a_e$ is radial depth of cut in mm and $r$ is radius of milling cutter in mm.

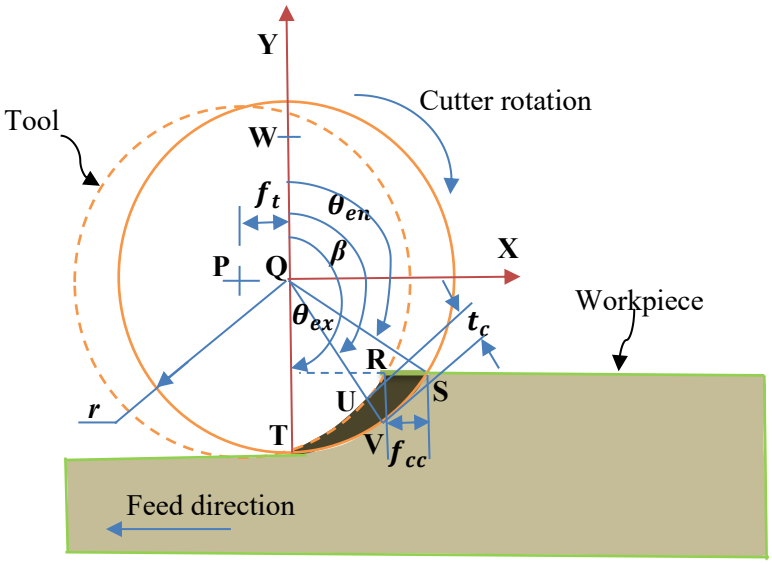


Fig. 3.1 Process geometry for straight geometry

The cutting-edge sweeps through tool-workpiece contact zone by producing varying uncut chip thickness and exits the cut by making a definite angle with workpiece which is

known as exit angle ($\theta_{ex}$). From the Fig.3.1, it can be seen that exit angle is $180^0$ as milling process is the type of down milling. The engagement angle can be calculated based on entry and exit angle of the helical cutting teeth and it is the difference between entry and exit of cut.

Instantaneous tooth positioning angle ($\beta$) is introduced to calculate angular position of cutting edge at any instant in tool-workpiece contact zone. It is expressed as follows:

$$\beta(z) = \varphi - (i-1).\phi_p - \left(\frac{\tan \alpha_{helix}}{r}\right).z \tag{3.2}$$

where $\varphi$ is cutter rotation angle in degree, $\phi_p$ is tooth spacing angle of milling cutter expressed as $\phi_p = 2\pi/N_f$ with $N_f$ indicating number of flutes, $\alpha_{helix}$ is helix angle and $z$ is thickness of disc element. Another process geometry variable is uncut chip thickness and it's mathematical formulation established by Martellotti [142]. It is expressed as:

$$t_c\big(\beta(z)\big) = f_{cc}.\sin(\beta(z)) \tag{3.3}$$

where $f_{cc}$ is feed per tooth along cutter contact path. In case of straight geometry, both feed per tooth ($f_t$) and feed per tooth along cutter contact path ($f_{cc}$) are same. But they are not same for milling of circular geometry which has been discussed in the following subsection.

### 3.2.2 Process geometry for circular workpiece

In case of circular geometry, the radius of curvature is present and it is nonzero. Therefore, process geometry is different in case of milling of circular surfaces in comparison to straight surfaces. Process geometry model for circular surfaces is developed by Zhang et al.[30], Rao and Rao [143] by introducing an additional parameter i.e. workpiece radius in the process geometry model for straight surfaces.

In this study, the geometry of the workpiece after the cut is used as a reference. For calculation of entry and exit angles for circular geometry, the datum or reference line is considered at the outward normal direction of the machined surface. From Fig.3.2, it can be seen that entry and exit angles are measured with respect to the outward normal direction of the machined surface. The entry angle for milling of circular part can be determined using cosine law as given below:

$$\theta_{en} = \pi - \cos^{-1}\left[\frac{(R+r)^2 + r^2 - (R+a_e)^2}{2r.(R+r)}\right] \tag{3.4}$$

where $R$ is the workpiece radius after cut, $r$ is the tool radius and $a_e$ is radial depth of cut. The above mathematical expression (Eq. (3.4)) for entry angle calculation is applicable to convex geometry only. For concave geometry, the mathematical formulation for entry angle is different and it is written as:

$$\theta_{en} = \cos^{-1}\left[\frac{(R-r)^2 + r^2 - (R-a_e)^2}{2r.(R-r)}\right] \tag{3.5}$$

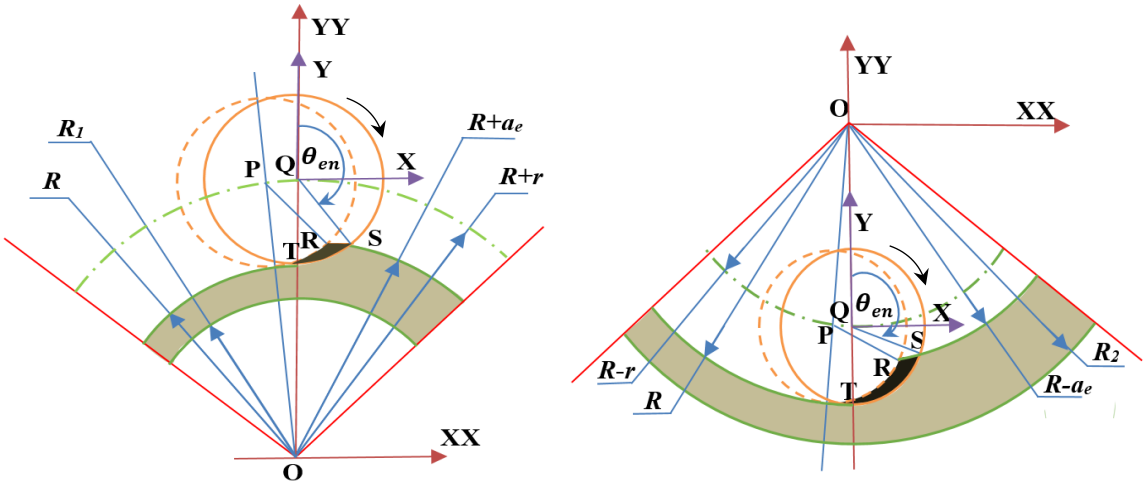


(a) Convex geometry (b) Concave geometry

Fig. 3.2 Process geometry for circular geometry

The feed per tooth which is another important process geometry parameter is also different for convex and concave geometries [144]. For convex geometry, the feed per tooth along cutter contact path ($f_{cc}$) is expressed as:

$$f_{cc} = f_t.\left[\frac{(R+a_e)}{(R+r)}\right] \tag{3.6}$$

In similar manner, the feed per tooth along cutter contact path ($f_{cc}$) for concave geometry is written as:

$$f_{cc} = f_t.\left[\frac{(R-a_e)}{(R-r)}\right] \tag{3.7}$$

The milling process geometry for curved workpiece which is completely different from circular workpiece is described in the following subsection.

### 3.2.3 Process Geometry for curved workpiece

For variable curved geometry, the magnitude of workpiece curvature varies from point to point along tool contact path. Therefore, the process geometry of milling changes continuously along the circumferential length of a component due to workpiece curvature as shown in Fig.3.3. This makes the milling of curved workpieces challenging during process geometry modelling. Each and every process geometry variable needs to be identified properly at each feed station along the cutter contact path. In order to make the model more generic, the parametric representation of curved workpiece and locus of tool center is taken into account.

In Fig.3.3, there are three parametric curves $(X_{wb}(u), Y_{wb}(u))$, $(X(u), Y(u))$ and $(X_t(u), Y_t(u))$ representing before cut, after cut workpiece geometries and locus of tool center respectively. Considering the contour of after cut workpiece geometry (machined surface) as reference, the contour of before cut workpiece geometry and locus of tool center is expressed mathematically as:

$$X_{wb}(u) = X(u) \pm a_e . \frac{Y'(u)}{\sqrt{\left(X'(u)\right)^2 + \left(Y'(u)\right)^2}} \tag{3.8a}$$

$$Y_{wb}(u) = Y(u) \mp a_e . \frac{X'(u)}{\sqrt{\left(X'(u)\right)^2 + \left(Y'(u)\right)^2}} \tag{3.8b}$$

$$X_t(u) = X(u) \pm r . \frac{Y'(u)}{\sqrt{\left(X'(u)\right)^2 + \left(Y'(u)\right)^2}} \tag{3.9a}$$

$$Y_t(u) = Y(u) \mp r . \frac{X'(u)}{\sqrt{\left(X'(u)\right)^2 + \left(Y'(u)\right)^2}} \tag{3.9b}$$

Where $a_e$ is radial depth of cut, $r$ is cutter radius and $X'(u)$ and $Y'(u)$ are differentiation of parametric curve with respect to curve parameter. From Fig. 3.3, it is also seen that the points P $(X_t(u_a), Y_t(u_a))$ and Q $(X_t(u_b), Y_t(u_b))$ are succeeding tool center positions

along the locus of tool center at a distance of nominal feed per tooth ($f_t$). The points R $(X_{wb}(u_c), Y_{wb}(u_c))$ and S $(X_{wb}(u_d), Y_{wb}(u_d))$ are tooth entry points corresponding to point P and point Q, respectively. The point $(O)$ is center of radius of curvature of workpiece for the exit point of cutter $(T)$ lying on machined surface. Using the known parameter $u_a$ of point P, parameter $u_b$ of Q can be obtained by

$$f_t^2 = \left(X_t(u_a) - X_t(u_b)\right)^2 + \left(Y_t(u_a) - Y_t(u_b)\right)^2 \tag{3.10}$$

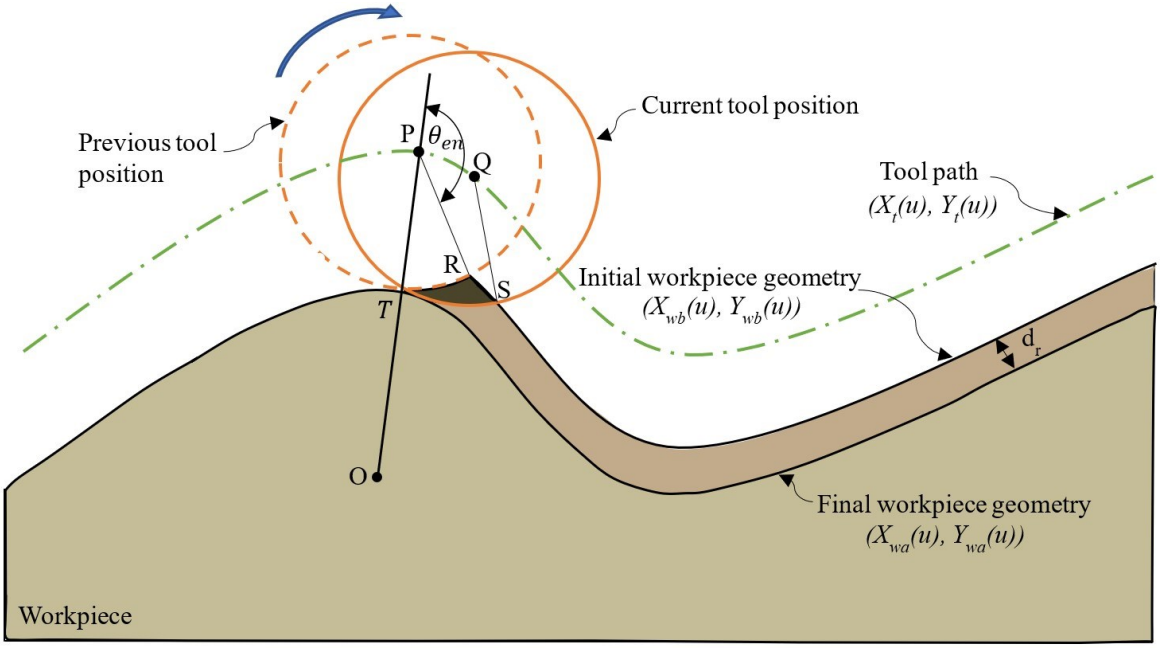


Fig. 3.3 Milling of variable curved geometry

The coordinates of the cutter entry point $(R)$ corresponding to the tool center position $(P)$ is calculated by following equations:

$$X_{wb}(u_c) = X_{wa}(u_c) - a_e.\frac{Y'_{wa}(u_c)}{\sqrt{\left(X'_{wa}(u_c)\right)^2 + \left(Y'_{wa}(u_c)\right)^2}} \tag{3.11a}$$

$$Y_{wb}(u_c) = Y_{wa}(u_c) + a_e.\frac{X'_{wa}(u_c)}{\sqrt{\left(X'_{wa}(u_c)\right)^2 + \left(Y'_{wa}(u_c)\right)^2}} \tag{3.11b}$$

$$\left(X_t(u_a) - X_{wb}(u_c)\right)^2 + \left(Y_t(u_a) - Y_{wb}(u_c)\right)^2 = r^2 \tag{3.12}$$

The coordinates of the cutter entry point S corresponding to tool center position Q is obtained in similar manner. The distance RS that denotes the feed per tooth along tool contact is determined as:

$$f_{cc} = \sqrt{\left(X_{wb}(u_c) - X_{wb}(u_d)\right)^2 + \left(Y_{wb}(u_c) - Y_{wb}(u_d)\right)^2} \tag{3.13}$$

The curvature and radius of curvature for the curve $(X_{wa}(u), Y_{wa}(u))$ at point $T$ can be obtained by Eq. (3.14) & (3.15).

$$K(u_a) = \frac{X'(u_a).Y''(u_a) - Y'(u_a).X''(u_a)}{(X'(u_a)^2 + Y'(u_a)^2)^{3/2}} \tag{3.14}$$

$$R(u_a) = \frac{1}{K(u_a)} \tag{3.15}$$

where $K$ is curvature and $R$ is radius of curvature. During developing of process geometry model for milling of curved surface, it is required to determine the varying uncut chip thickness for calculation of chip load. For determination of chip load in milling, the uncut chip thickness is computed using the Eq. (3.16) based on the mathematical relationship derived as:

$$t_c\big(\beta(z)\big) = f_{cc}\, sin(\beta(z)) \tag{3.16}$$

where $t_c(\beta(z))$ is instantaneous uncut chip thickness realized by $i^{th}$ flute of $j^{th}$ disk element. The parameter $\beta(z)$ represents the angular position of helical tooth at any instant in the immersion zone known as instantaneous tooth positioning angle. The value of $\beta(z)$ can be obtained from Eq. (3.17) with respect to outward normal to workpiece as follows:

$$\beta(z) = \varphi - (i-1).\phi_p - \left(\frac{tan(\alpha_{helix})}{r}\right).z \tag{3.17}$$

where $\varphi$ is cutter rotation angle, $\phi_p$ is pitch angle, $\alpha_{helix}$ is helix angle of milling cutter and $r$ is radius of milling cutter. In order to obtain chip load for a given axial depth of cut, the instantaneous uncut chip thickness is calculated after every incremental rotation of cutter. The following formula can be used to compute the engagement angle corresponding to the cutter center point P:

$$\theta_{engg} = \cos^{-1}\left[\frac{r^2 + (R+r)^2 - (OR)^2}{2r(R+r)}\right] \tag{3.18}$$

The maximum undeformed chip thickness when the tool is at Q can be expressed as equation given below.

$$t_{max} = r - QR \tag{3.19}$$

where $QR = \sqrt{(X_t(u_b) - X_{wb}(u_c))^2 + (Y_t(u_b) - Y_{wb}(u_c))^2}$ and $r$ is radius of milling cutter.

## 3.3 Cutting Force Model

To accurately estimate milling forces, a cutting force model must be developed using the process geometry model that was described earlier. A force model has been developed in the present work based on the mechanistic model proposed by Kline et al. [20].

### 3.3.1 Modelling of cutting forces

First, a cutting force model based on the mechanistic method is studied for straight geometry. In contrast to curved geometry, the development of a mechanistic cutting force model is rather straightforward for straight geometry. In this force model, milling cutter is discretized into a finite number of thin disk elements along the axis of the cutter. At each incremental rotation of the cutter, it is assumed that cutting forces are acting on every axial disc element and helical tooth. After each incremental rotation of the cutter, the engagement state of each axial disc element is subsequently assessed. For determination of chip load in milling, the uncut chip thickness is computed using the Eq. 3.20 based on the mathematical relationship derived as:

$$t_c\big(\beta(z)\big) = f_{cc}\sin\left(\beta(z)\right. \tag{3.20}$$

where $t_c\big(\beta(z)\big)$ is instantaneous uncut chip thickness realized by $i^{th}$ flute of $j^{th}$ disk element. The parameter $\beta(z)$ represents the angular position of helical tooth at any instant in the immersion zone known as instantaneous tooth positioning angle. The value of $\beta(z)$ can be obtained from Eq. (3.21) with respect to outward normal to workpiece as follows:

$$\beta(z) = \varphi - (i-1).\emptyset_p - \frac{\tan(\alpha_{helix})}{r}.z \tag{3.21}$$

where $\varphi$ is cutter rotation angle, $\phi_p$ is pitch angle, $\alpha_{helix}$ is helix angle of milling cutter and $r$ is radius of milling cutter. In order to obtain chip load for a given axial depth of cut, engagement state of every disc element is assessed and the instantaneous uncut chip thickness is calculated after every incremental rotation of cutter. According to the mechanistic force model, the cutting force and chip load are directly proportional. Elemental tangential force and radial force can be expressed as [144]:

$$dF_t(i,j) = K_t.t_c\big(\beta(z)\big).z_{i,j} \tag{3.22a}$$

$$dF_r(i,j) = K_r.t_c\big(\beta(z)\big).z_{i,j} \tag{3.22b}$$

where $dF_t$ is tangential force acting on $i^{th}$ flute, $K_t$ is tangential cutting constants and $K_r$ is radial cutting constant. These constants are obtained empirically for a cutter-workpiece material pair as discussed in next section. After determining these constants, Equations (3.22a) and (3.22b) can be used to calculate the elemental tangential and radial forces acting on disk elements. These components are resolved to compute local feed forces and normal forces which are expressed as follows:

$$dF_f(\varphi) = -dF_t\cos\beta(z) - dF_r sin\beta(z) \tag{3.23a}$$

$$dF_n(\varphi) = dF_t\sin\beta(z) - dF_r cos\beta(z) \tag{3.23b}$$

Fig. 3.4 depicts a typical illustration of all these force components. A schematic representation of milling of curved geometries along with various force components acting on the cutter is shown in Fig. 3.5.

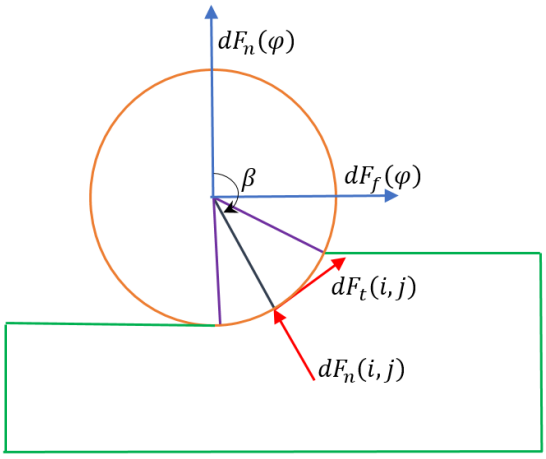


Fig. 3.4 Cutting force components acting on axial disk element

Total cutting forces acting on cutter in feed and normal direction is calculated by summing all forces acting on each disc elements as given below

$$F_f(\varphi) = \sum_{i=1}^{N_f} \sum_{j=1}^{Ni} dF_{i,j,f}(\varphi) \tag{3.24a}$$

$$F_n(\varphi) = \sum_{i=1}^{N_f} \sum_{j=1}^{Ni} dF_{i,j,n}(\varphi) \tag{3.24b}$$

where $F_f(\varphi)$ and $F_n(\varphi)$ are total feed and normal force at cutter rotation angle $(\varphi)$ respectively. $i$ and $j$ stand for the cutting flute and the disc element respectively. $Ni$ and $N_f$ stand for the number of axial elements and flutes, respectively.

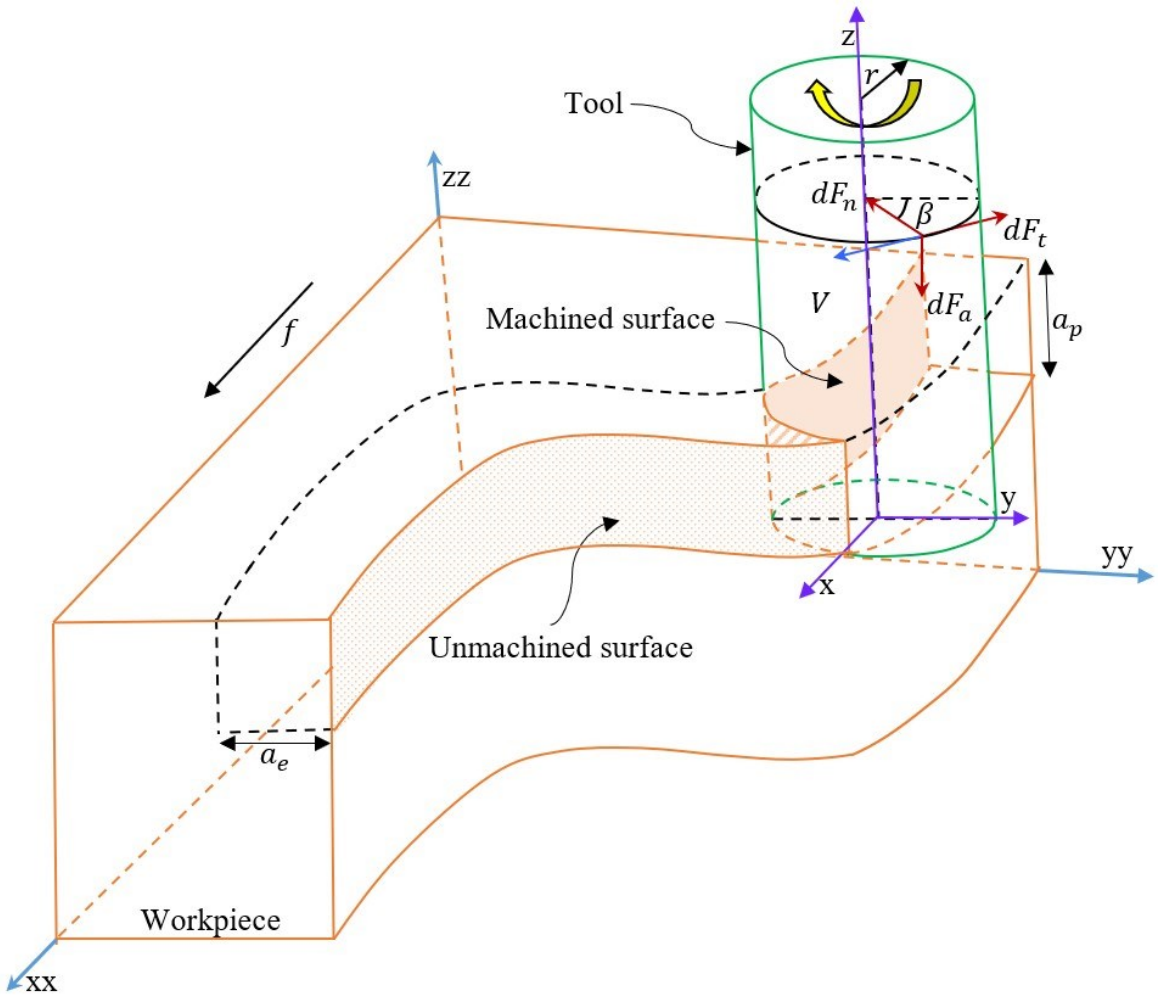


Fig. 3.5 Milling forces for variable curved geometry

In the case of straight geometry, the feed per tooth along the cutter contact path is equal to the nominal feed per tooth when calculating the instantaneous uncut chip thickness. In case of circular geometry, the feed per tooth along the cutter contact path changes and is dependent on the workpiece radius. As discussed in previous section, circular geometry differs even from straight geometry in terms of engagement angle and entry angle. As a result, cutting forces for circular geometries are different. In contrast to straight geometries, chip load acting on disc element varies for circular geometries due to changes in instantaneous uncut chip thickness. The same procedure as above is used to determine the elemental cutting forces for circular geometries.

In case of curved geometry, due to the short time period, there are small changes in the process geometry and cutting forces from one flute to the next. As a result, the cutting forces generated by cutter over a brief period of time can be treated as steady state cutting. Thus, the entire cutting operation can be divided into a sequence of steady state cutting processes with interval of a feed per tooth along the tool path. The cutting force varies from one feed station to another as a result of the varied process geometry at feed station compared to the previous one.

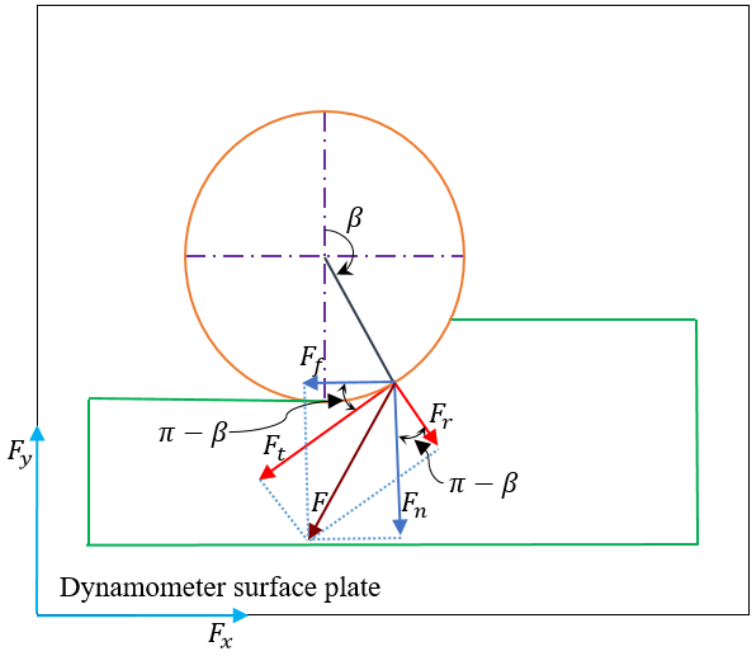


Fig. 3.6 Cutting force distribution in machining of straight geometry

During peripheral milling of straight geometry, the cutting forces acting on tool/workpiece coincide with measured forces using dynamometer as shown in Fig. 3.6.

Therefore, mathematical relationship between predicted feed force and normal force and measured forces for straight geometry can be established as:

$$dF_x = dF_f = -dF_t \cos(\beta) - dF_r \sin(\beta) \quad (3.25a)$$

$$dF_y = dF_n = dF_t \sin(\beta) - dF_r \cos(\beta) \quad (3.25b)$$

However, when machining of curved geometries, as seen in Fig. 3.7, the measured force is dependent on the cutter position with respect to the geometry of the workpiece. As shown in Fig. 3.7, the estimated cutting forces create an angle ($\tau$) with the forces measured by the dynamometer. The mathematical relationship between estimated feed and normal cutting forces, and forces measured by the dynamometer can be established using following expressions.

$$dF_x = -dF_n \sin(\tau) + dF_f \cos(\tau) \quad (3.26a)$$

$$dF_y = dF_n \cos(\tau) + dF_f \sin(\tau) \quad (3.26b)$$

where $\theta$ is instantaneous cutter positioning angle and $\tau$ is instantaneous tangent angle of tool path at feed station.

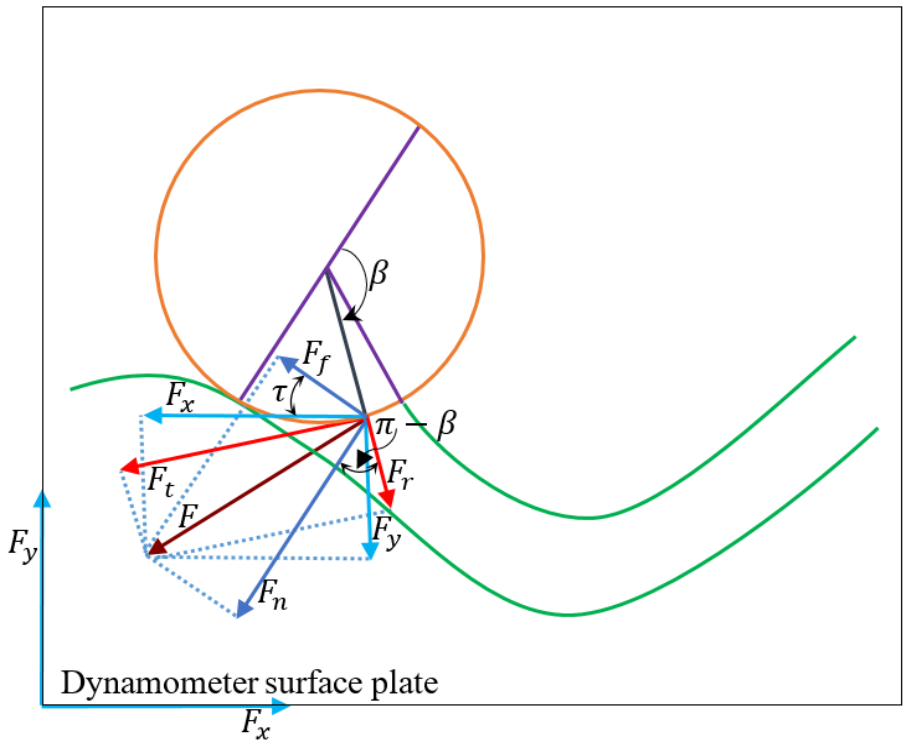


Fig. 3.7 Cutting force distribution in machining of curved geometry

### 3.3.2 Identification of cutting force coefficients

Cutting force coefficients, the determination of which forms the basis of the cutting force model, play a significant role in the accurate and reliable prediction of cutting force. The accurate identification and calculation of cutting constants has a significant impact on cutting force modelling. The cutting constants $K_t$ and $K_r$ for the tangential force and radial force components have already been mentioned. Other names for these constants include cutting force coefficients and cutting pressure constants. The cutting force constant are affected by the material of the cutter and the workpiece and also geometry of the tool. These factors make it difficult to calculate the cutting force constant in many situations. In order to identify and calculate the cutting constant, a reliable approach is essential. A direct calibration method is employed in the present work to find out the same. To determine the cutting force coefficients over range of cutting parameters, a number of machining tests are carried out. In order to consider effect of chip thickness on shear angle, friction angle and shear stress, the mechanistic constants are commonly described by researchers as a non-linear function of uncut chip thickness in the more generic form shown below:

$$K_t = K_T(t_c)^a \tag{3.27a}$$

$$K_r = K_R(t_c)^b \tag{3.27b}$$

where $K_T$ and $K_R$ are specific constants for tangential and radial force components, respectively and $a$ and $b$ are the exponential constants.

## 3.4 Estimation of Tool Deflection

The cutting forces obtained from cutting force model discussed in the previous subsection are used to compute tool deflection components. The surface errors which are manifested on the machined component are calculated based on the computed tool deflections with the help of surface error generation model. As shown in Fig. 3.8, the end mill cutter is considered as a cantilever beam fixed with one end in tool holder and other end remains free. It is discretized into a finite of thin disk-like element along the axis of the cutter. The cutting forces are transferred directly due to the discretization similarity between the force and tool deflection models. When estimating nodal tool deflections, the model

uses the concept of equivalent diameter $(D_e)$ to take cutting flutes into account. The deflection value of cutting tool is calculated by using instantaneous value of cutting force and instantaneous tool overhang with respect to fixed end of the tool. The deflection of each axial disc element $(j)$ in the normal direction caused by the cutting force acting on $m^{th}$ element is estimated using the cantilever beam formulation given below.

$$\Delta(j,m) = \frac{F_m . x_j^2 . (3a_m - x_j)}{6EI} \quad \text{for } 0 < x_j < a_m \tag{3.28a}$$

$$\Delta(j,m) = \frac{F_m . a_m^2 . (3x_j - a_m)}{6EI} \quad \text{for } a_m < x_j < L \tag{3.28b}$$

The superposition of deflections caused by forces acting on all elements can be used to compute the total static deflection in the normal direction at a particular element $(j)$. It is given as:

$$\Delta(j) = \sum_{j=1}^{Ni} \Delta(j,m) \tag{3.29}$$

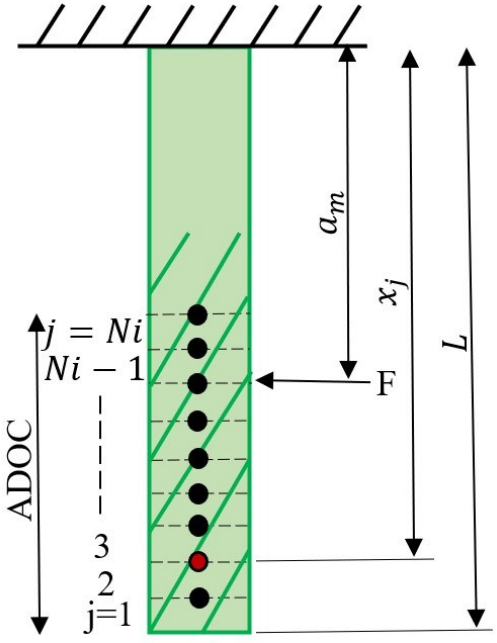


Fig. 3.8 Tool deflection model

## 3.5 Estimation of Workpiece Deflection

Cutting forces which are obtained from mechanistic cutting force model discussed in previous subsection are used as input to FEA model to compute workpiece deflection of thin-walled workpiece. The effect of thinning due to reduced workpiece thickness as machining continues is an important issue in modeling the deflection of thin-walled workpieces. It causes a decrease in workpiece stiffness along the peripheral length of cut. Also, workpiece geometry varies when a tool is moved from one feed station to another. Every feed station along the tool path requires a change in workpiece geometry. Such requirements of workpiece deflection prediction are addressed using FEA model. In present work, the ANSYS Parametric Design Language (APDL) environment is used to model geometry of workpiece for prediction of static deflection of workpiece.

Mechanistic cutting force model gives force values on axial disc element and total cutting force at given rotation angle which can be use as inputs to workpiece deflection model. At each feed station, this total cutting force is applied at node corresponding to geometric center of tool-workpiece engagement section. After calculating workpiece deflection at current feed station, workpiece geometry is modified in order to calculate deflections at the succeeding feed station. The flow chart in Fig. 3.9 provides a detailed overview of the methods used to estimate workpiece deflection.

The workpiece is clamped on one end and the other ends are left free while modelling workpiece deflections. Therefore, it is considered as a Clamped-Free-Free-Free (C-F-F-F) structure. For FE analysis of the workpiece, the "hexahedra brick" element is used with three degrees of freedom in translation per node. The bottom face of the workpiece has fixed nodes everywhere. Each element employed in the FE analysis of the workpiece is considered to have isotropic material characteristics. The equations (3.25a) and (3.25b) are used to compute the cutting force acting on the workpiece in X and Y directions, which is used to estimate its deflections. Tool workpiece contact surface at any instant is shown as “abcd” in Fig. 3.10. A flute is always entered engagement zone through “a” along entry edge “ab” and exit through “c” along exit edge “cd”. The application of a point force operating on the geometric center of tool-workpiece engagement section is represented schematically in Fig. 3.10. The incremental rotation value of the cutter is set the same in every situation in order to synchronize the workpiece deflection model with cutting force model.

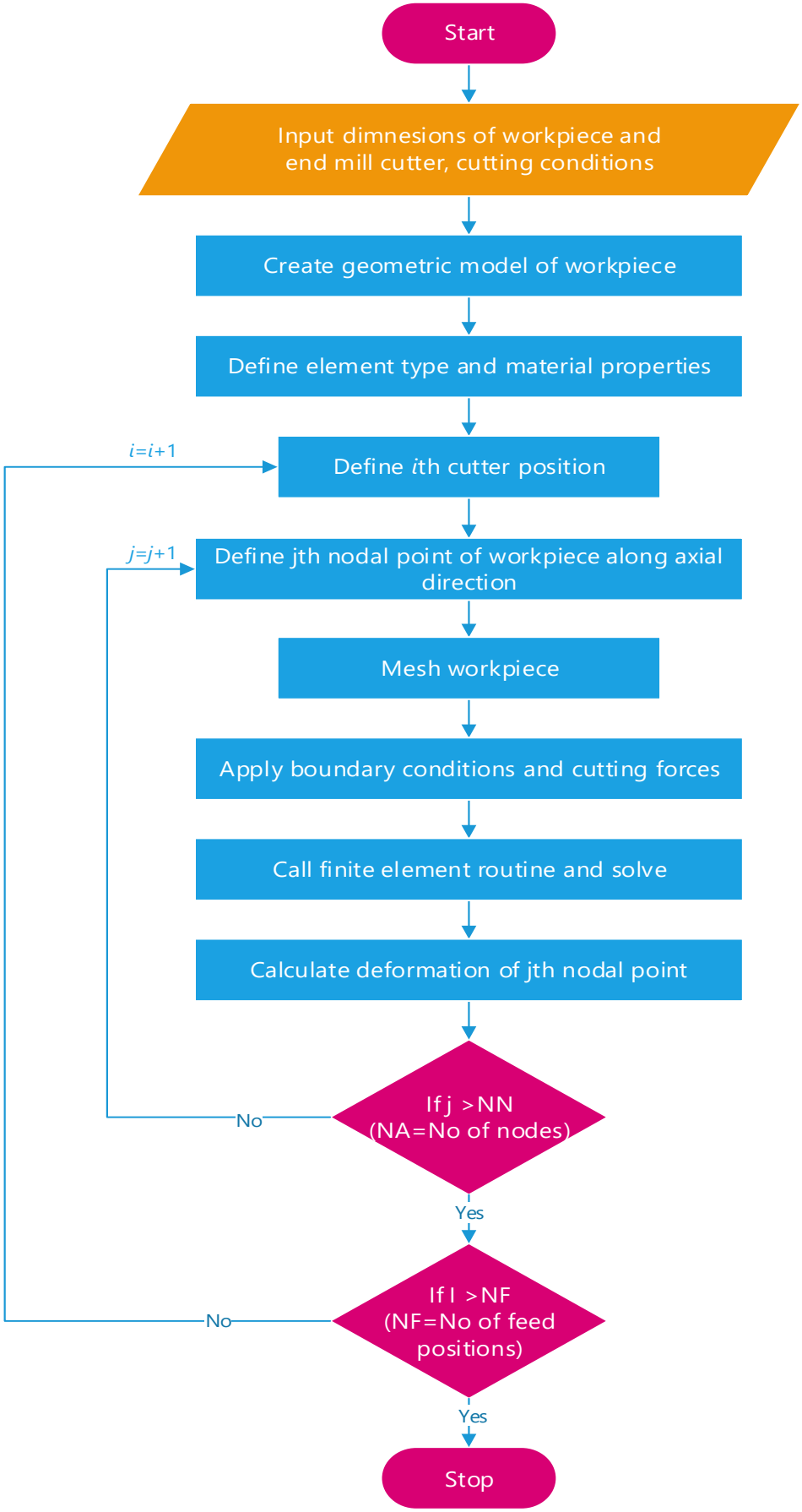


Fig. 3.9 Flow chart for estimating workpiece deflections

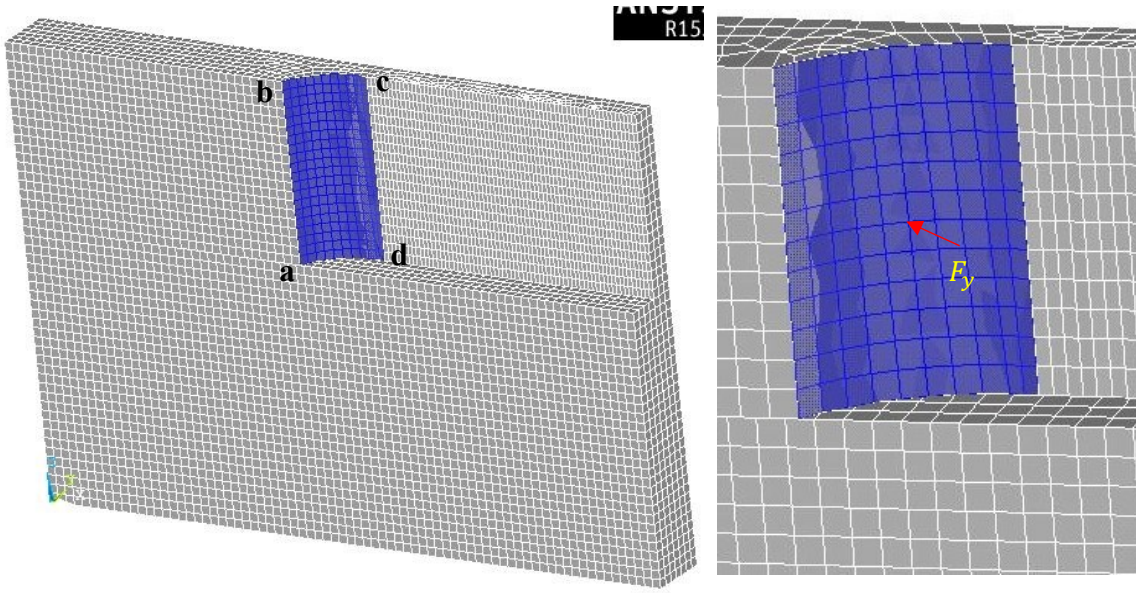


(a) Meshed part (b) Application of point force

Fig. 3.10 FEA model of thin-walled part

## 3.6 Surface Error Generation Mechanism

In end milling process, cutting forces acting on entire tool-workpiece contact surface at any instant does not contribute to surface generation of workpiece. As shown in Fig. 3.11, only exit edge (cd) of tool-workpiece contact surface contributes to generate the machined surface. The machined surface is generated only at the moment when cutting point of helical teeth enters into exit edge and continues up to exit point of the exit edge of the contact surface. In down milling, surface generation point begins to generate the line when cutting point lying on bottom disk element of tool completes rotation angle $\theta = \pi$. As the cutter rotates by an angle $\theta = \theta_1$ with respect to the starting point of exit edge, the surface generation point climbs to axial height $h = h_1$ correspondingly. The surface generation process finishes when the height position of the surface generation point equals the axial depth of cut and cutter rotates by $\theta = \alpha_{sweep}$. For the estimation of surface error, the deflections at surface generation (SG) points located on the exit edge are computed and stored in the database.

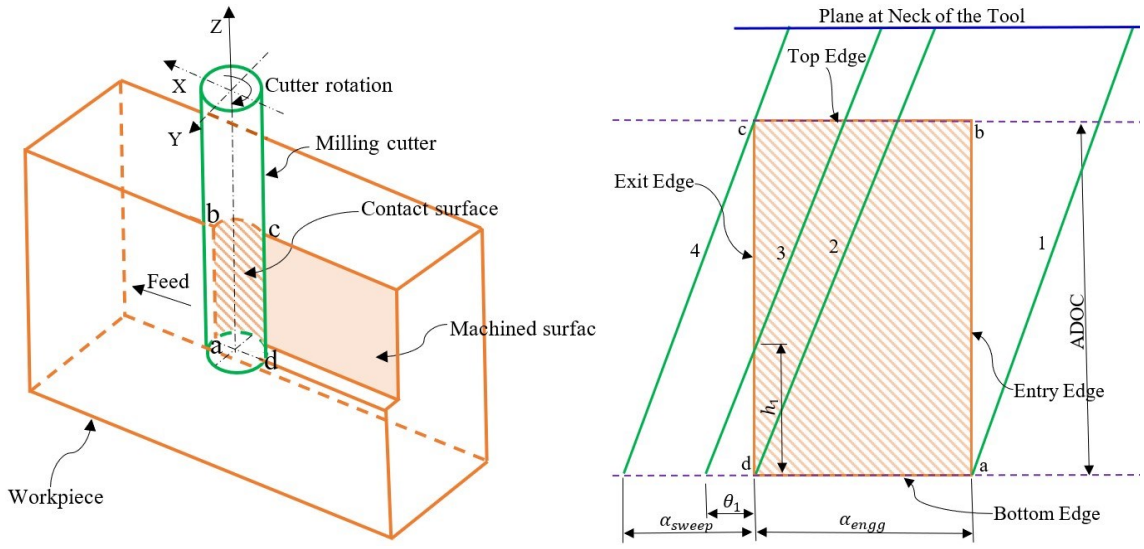


(a) Peripheral milling process (b) Expanded view of tool-workpiece contact surface

Fig. 3.11 Tool-workpiece contact surface in peripheral milling

## 3.7 Surface Error Variation in Milling of Curved Geometries

During machining of straight geometry, surface error profile remains constant along entire tool path at given ADOC and RDOC. But in case of curved geometry, tool-workpiece engagement varies continuously along whole tool path due to curvature of workpiece. In the previous section, it has been shown that the change in tool-workpiece engagement affect cutting forces, which in turn changes the surface error profile. Thus, during machining of curved geometry, surface error profile varies along whole tool path even though ADOC and RDOC kept constant.

## 3.8 Generation of Geometric Error in Machined Surface

It is already mentioned that the geometric error in a machined component is equally important like dimensional error. It plays a significant role in design requirement and performance of a product. Therefore, an attention is given in prediction and analysis of geometric error of a component produced in peripheral milling based on nodal tool deflections. As the magnitudes of nodal tool deflections are highly non-uniform in nature along the axial length of cut at each feed station, the milled surface becomes very complex consisting of non-uniform surface generating points. Therefore, a particle swarm optimization (PSO) algorithm is used to find out the maximum and minimum values of form errors and respective flatness of the planar surface.

### 3.8.1 Flatness error calculation

The flatness of a planar surface is defined as orthogonal distance between two parallel planes containing a set of data points representing the machined surface [145,146]. The data points required for defining a machined surface are represented as $P_u(x_u, y_u, z_u)$ where ($u = 1,2,\ldots,n$ and $n$ is total number of data points). Then, the smallest feasible region as shown in Fig. 3.12 is determined by identifying two parallel planes that are the least distance apart and encompass all of the data points in order to calculate the minimum zone solution of the flatness error [147,148]. The one of two parallel planes is represented by

$$z = ax + by + c \tag{3.30}$$

where $x, y, z$ are coordinates of data points and $a, b$, and $c$ are coefficients.
Now, distance $d_u$ from the data points $P_u(x_u, y_u, z_u)$ to the parallel plane is given as:

$$d_u = \frac{z_u - ax_u - by_u - c}{\sqrt{(1 + a^2 + b^2)}} \tag{3.31}$$

The shortest distance between these two planes can be calculated by:

$$d_s = max(d_u) - min(d_u)$$

$$d_s = \frac{max(z_u - ax_u - by_u - c) - min(z_u - ax_u - by_u - c)}{\sqrt{(1 + a^2 + b^2)}}$$

$$d_s = \frac{max(z_u - ax_u - by_u) - min(z_u - ax_u - by_u)}{\sqrt{(1 + a^2 + b^2)}} \tag{3.32}$$

where $x, y, z$ are coordinates of data points and $a$ and $b$ are optimization variables.
Now, for the minimum zone flatness error, objective or fitness function can be represented as:

$$f = min\left(\frac{max(z_u - ax_u - by_u) - min(z_u - ax_u - by_u)}{\sqrt{(1 + a^2 + b^2)}}\right) \tag{3.33}$$

The above objective function is a function of $a$ and $b$. This objective function is evaluated in order to find values of $a$ and $b$ such that the objective function is the minimum and this minimum value will be flatness error.

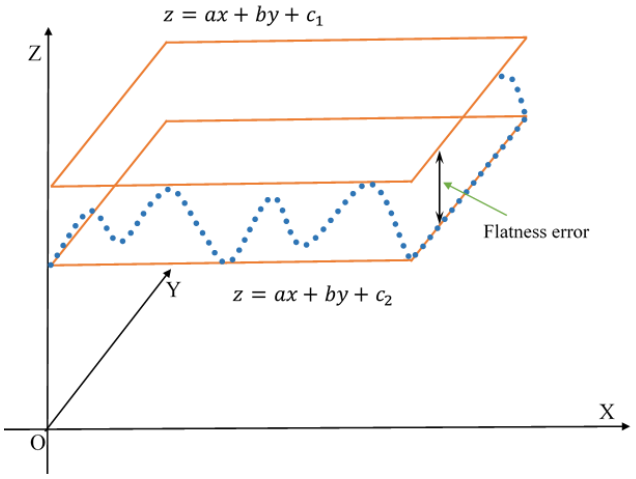


Fig. 3.12 Flatness error representation

### 3.8.2 PSO algorithm

In order to take care optimization problems in engineering, two approaches namely classical and heuristic are very popular. In many cases, heuristic approaches are beneficial over the classical approaches due to dimensionality, continuity and differentiability of objective functions issues. Heuristic approaches are nature-inspired optimization techniques such as Particle swarm optimization (PSO), genetic algorithm (GA), ant colony optimization (ACO), and artificial bee colony (ABC) etc. are utilized for form tolerance evaluation [28-29]. Advantage of PSO over GA is that it can reach an optimal solution more quickly. ACO takes more time, and it is uncertain when it will reach convergence. The implementation of ABC makes it difficult to select the optimum option out of all possible solutions because of its poor convergence rate, rapid fall into local optima, and other drawbacks. High precision, quick convergence and ease of implementation are all benefits of PSO algorithm [30-31]. The PSO algorithm is therefore frequently used to resolve constraint optimum problems. The PSO algorithm developed by Eberhart and Kennedy [32] is a stochastic optimization method based on the swarm.

The PSO method initializes with a set of random particles $(i)$ termed as swarms, which search in space with a velocity in order to find best position. Each particle $(u)$ represented by current position $X^u = [x^u, y^u]$ , current velocity $V^u = [v_x^u, v_y^u]$ , individual best fitness value $(Pbest)$ and global best fitness value $(Gbest)$ . Individual best $(Pbest)$ which is best solution that particle has found so far and global best $(Gbest)$ which is best solution that any particle in population has obtained so far. A mathematically formulated objective or fitness function given by equation (3.33) is used to evaluate the fitness value

for flatness error. Multiple iterations are used to find the best solution. At every iteration, position and velocity of particles are updated using equations (3.34) and (3.35). The termination condition is then verified, and if it is not satisfied, the process is repeated. In the present work, the maximum number of iterations is used as the termination condition.

$$X^u(t+1) = X^u(t) + V^u(t+1) \tag{3.34}$$

$$V^u(t+1) = w(t).V^u(t) + c_1.r_1.\left(Pbest^u - X^u(t)\right) + c_2.r_2.\left(Gbest^u - X^u(t)\right) \tag{3.35}$$

$$w(t) = w_{max} - \frac{t.(w_{max} - w_{min})}{T} \tag{3.36}$$

where $u$ is current particle number, $t$ is the current iteration number and $T$ is maximum number of iterations.

The performance of the PSO algorithm is affected by a few parameters such as swarm size or number of particles, number of iterations, inertia weight, and acceleration coefficients. If there are not enough particles, the algorithm will become stuck in local optimum. On the other hand, large numbers of particles make computations more complex and time-consuming for each iteration. Low number of iterations may result in premature search termination and large number of iterations could unnecessarily increase computing complexity and time[150]. There are two independent random variables $r_1$ and $r_2$ that are utilized to avoid being entrapped on local minimums and to allow a small percentage of particles to diverge in a bigger search space. The value of these variables is distributed at random between [0, 1]. The inertia weight $(w)$ in equation (3.35) regulates how much the previous velocity affects the current velocity and it is determined using equation (3.36) for $t^{th}$ iteration. Low inertia weights concentrate the search on a smaller area while higher inertia weights lead to larger exploration of the search area. PSO typically begins with a high inertia weight that gradually decreases over time. In the present work, the initial value of the inertia weight is fixed at $w_{max} = 0.9$ and linearly decreases to $w_{min} = 0.4$ over whole iteration [151]. While acceleration coefficient $c_1$ draws the particle toward the personal best, acceleration coefficient $c_2$ pulls the particle toward the global best position. Large acceleration coefficient causes particle to move quickly and there is a greater chance of becoming stuck in false optima. On the other hand, large acceleration coefficient induces that the particles travel too slowly resulting increase in the computing load. Therefore, $c_1$ and $c_2$ are taken as a value of 2 in order to balance local convergence and exploration.

The procedure for implementation of PSO algorithm is as follows:

Step 1: Set PSO parameters and randomly initialize particle swarm of a specific size with position and velocity of each particle.

Step 2: Evaluate objective or fitness function of all particles for flatness error using equation (3.33). Store position and objective value in $Pbest$ of each particle and also store the position and objective value with optimum value in all $Pbest$ in $Gbest$.

Step 3: Update position and velocity of particle according to equations (3.34) and (3.35) respectively and weight using equation (3.36).

Step 4: Again, evaluate fitness function for each particle. Compare fitness value with $Pbest$. If current objective value of particle is better than it's $Pbest$ value, then $Pbest$ value is replaced by current objective value.

Step5: Compare best fitness value of all particles with $Gbest$. If current objective value of particle is better than it's $Gbest$ value, then $Gbest$ value is replaced by current objective value.

Step 6: Verify the stop iteration condition. If it is satisfied, search is finished and optimum result is returned and if it is not, repeat step 2-5 until condition is verified. Maximum number of iterations or good fitness or objective value could be used as stop iteration condition.

The summary of the PSO algorithm is given in Fig. 3.13.

## 3.9 Machining Experiments

Computational results and machining experiments have been used to validate various mathematical models mentioned in the previous subsections. To predict surface error in machining of straight and curved geometries, a cutting force model, cutter deflection model, and surface generation process, flatness error model outlined in Section 3 have been applied in the form of computational program in MATLAB. Workpiece deflections are obtained using a FEM model developed using ANSYS APDL. Three sets of milling experiments have been conducted for the determination of cutting constants and validation of the proposed models. The first set of experiments has been performed to determine the values of cutting constants referred in the developed force model. The second set of experiments has been conducted to validate force model, surface error model and flatness error model for machining of straight thick and thin-walled geometries. The third

set of experiments has been performed for validation and assessment of force model and surface error model for machining of curved thick and thin-walled geometries. The following sections describe job design, experimental setup and machining conditions below.

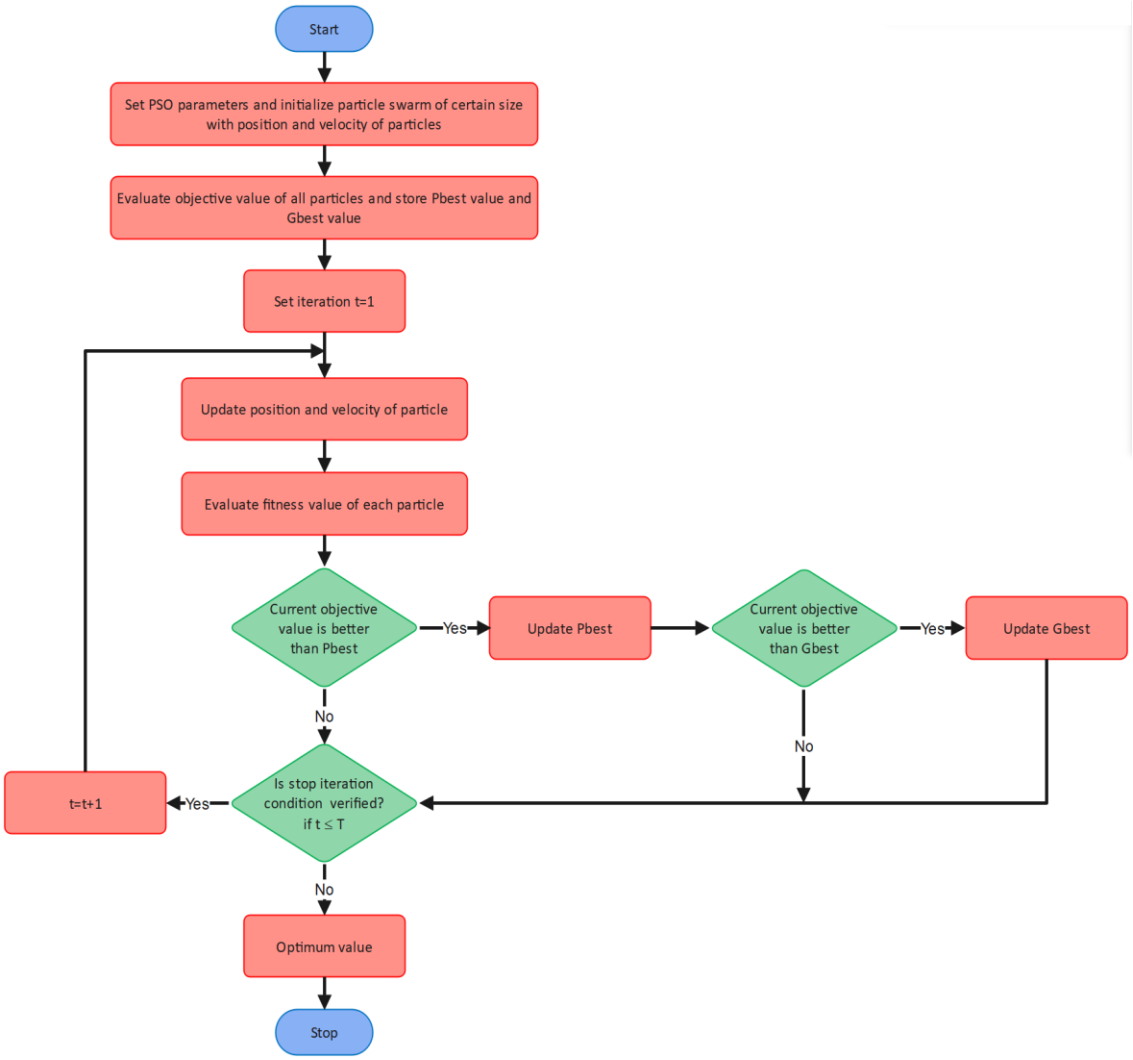


Fig. 3.13 Flowchart of PSO algorithm

### 3.9.1 Job design for experiment

This section deals with design of job for determination of cutting constants and machining experimentation for validation of the proposed models. The machining experiments have been carried out on rectangular and elliptical workpieces of aluminium 6351-T6. The aluminium 6351-T6 alloy is extensively used in the aerospace industry. The elemental composition and mechanical properties of aluminium 6351-T6 are given in Table-3.1 and Table-3.2 respectively. The cutting tool used in the machining experiments is of four fluted HSS end milling cutter with 16 mm diameter and 30º helix angle. All experiments are performed under dry cutting condition.

All pre-machined workpieces of required dimensions is produced from a rectangular block which is cut from a long bar by performing facing, milling and drilling operations. The thickness of the workpiece is selected to be relatively high so that any deflections caused by cutting force and reduction of stiffness will be negligible and may be disregarded. During design of these workpieces, a square base section is made for holding the experimental part to avoid interference of clamping force and additional damage to the part. The square base section is to be clamped to the dynamometer by using two Allen screws for transmitting cutting load to the dynamometer during material removal process. For determination of constants, a simple rectangular workpiece is used. For thick-walled straight geometry, pre-machined workpiece is designed such a way that probe is able to measure whole axial depth and all experiments can be conducted on single workpiece as shown in Fig. 3.14. For thick-walled curved geometry, an elliptical workpiece as shown in Fig. 3.15 is selected to validate force model and surface error model and study effect of curvature on surface error profile. Fig. 3.16 shows physical workpiece used for thin walled straight and curved geometry. All geometric and dimensional details of the workpiece geometries are described in Table-3.3.

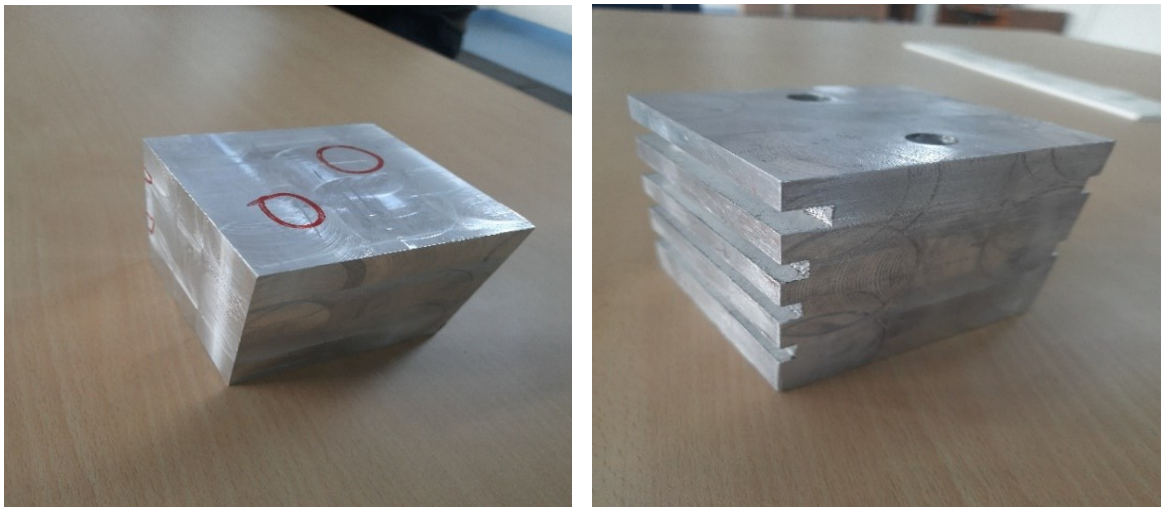

(a) (b)

Fig. 3.14 (a) Raw workpiece; (b) Actual workpiece used for experiments of ADOC variation

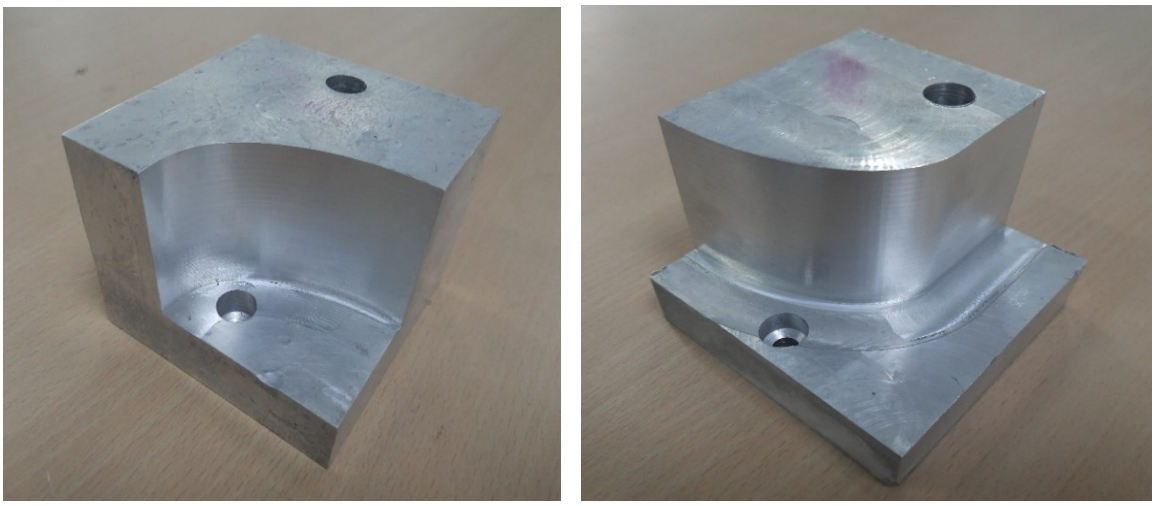

(a) Physical concave elliptical workpiece (b) Physical convex elliptical workpiece

Fig. 3.15 The concave and convex elliptical workpieces.

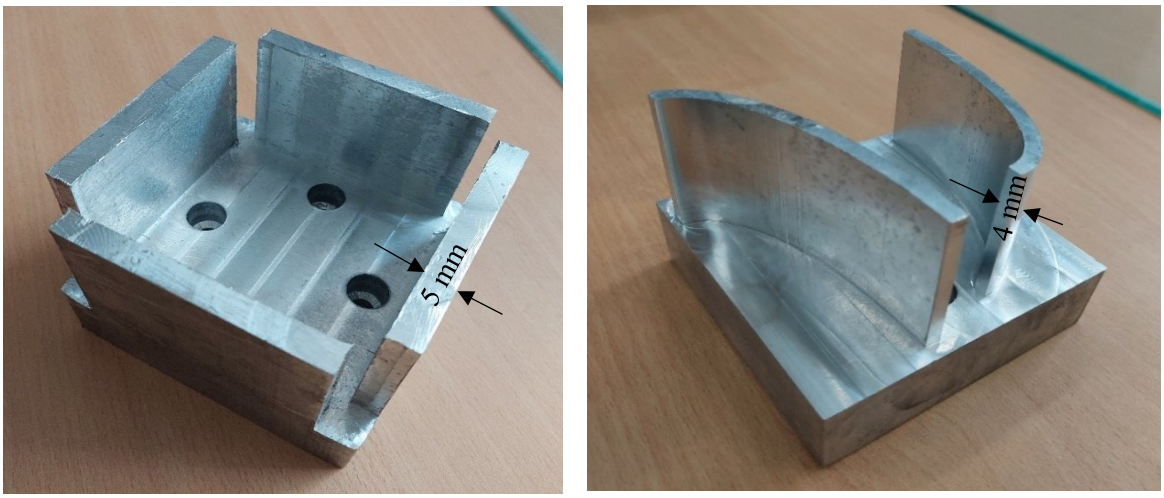


(a) Thin-wall straight workpiece (b) Thin-wall elliptical workpiece

Fig. 3.16 Thin-walled workpieces

Table 3.1 Elemental composition of Aluminum 6351-T6

| Aluminum | Copper | Iron | Magnesium | Manganese | Silicon | Titanium | Zinc |
|---|---|---|---|---|---|---|---|
| 95.9 – 98.5 % | ≤ 0.1% | ≤ 0.5% | 0.4 – 0.8 % | 0.4 – 0.8 % | 0.7 – 1.3 % | ≤ 0.2% | ≤ 0.2% |

Table 3.2 Mechanical properties of aluminum 6351-T6

| | |
|---|---|
| **Density** | 2.71 g/cc |
| **Brinell Hardness** | 95 |
| **Vickers hardness** | 107 |
| **Ultimate tensile strength** | 310 MPa |
| **Yield tensile strength** | 283 MPa |
| **Specific heat capacity** | 0.890 J/g.°C |
| **Thermal conductivity** | 176 W/(m.K) |

Table 3.3 Geometry and dimensional details of the workpiece

| | |
|---|---|
| **Dimensions of rectangular block** | 100 mm × **100** mm × **75 mm** |
| **Major diameter of concave and convex workpieces** | 150 mm |
| **Minor diameter of concave and convex workpieces** | 60 mm |
| **Height of the elliptical workpiece** | 50 mm |
| **Dimension of the square base** | 100 mm × 100 mm |
| **Length of the square base** | 25 mm |

### 3.9.2 Experimental setup

All the machining experiments have been performed on LMW JV-40 three axis vertical machining center (VMC) equipped with a piezo-electric dynamometer (Type-9272 by Kistler) and Renishaw probing system. A universal multi-channel piezo-electric dynamometer has been used for force measurement along with a charge amplifier (Type-5070 by Kistler) and DAQ system as shown in Fig.3.17. The dynamometer is clamped to the VMC machine table with the help of a dedicated flange type circular fixture as shown in Fig. 3.18(a). The force values have been recorded using data acquisition system (DAQ) installed in a desktop computer as shown in Fig. 3.18(b). A dedicated DynoWare software is used to record and store the force data with respect to time.

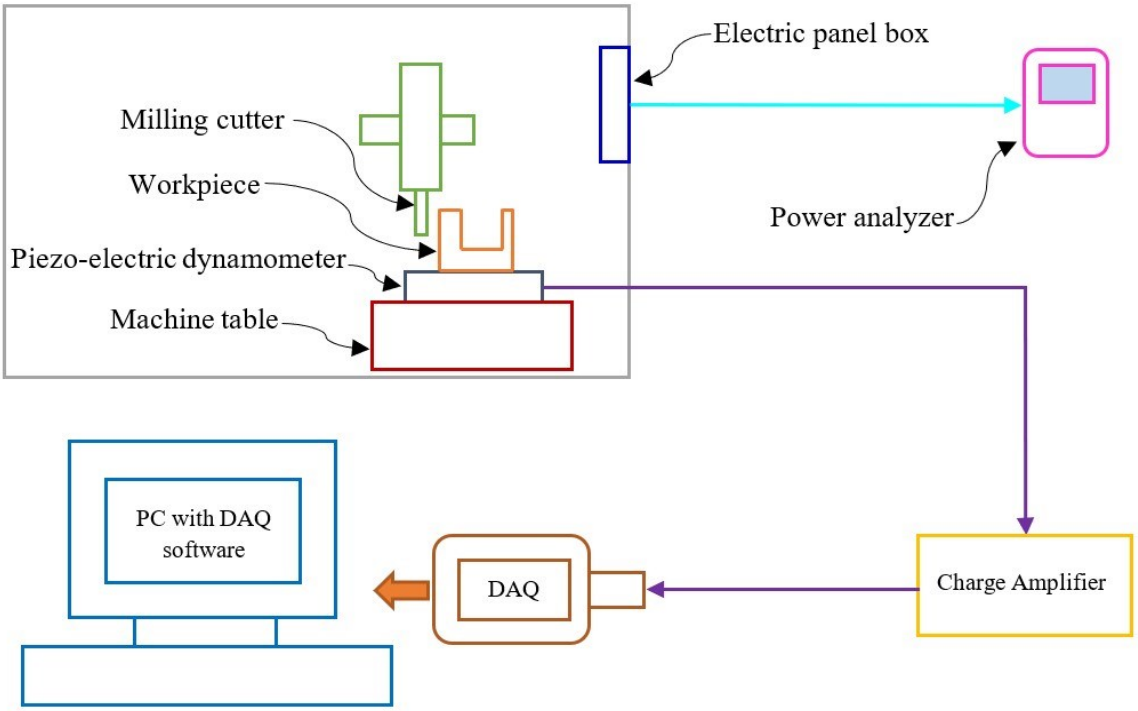


Fig. 3.17 Schematic representation of experimental setup

A spindle mounted Renishaw CNC probing system is used to measure the surface errors on the machined surface as shown in Fig. 3.18(c) and 3.18(d). For measurement of surface error, coordinate values of the touch points are collected from workpiece surface before machining and after machining at 2- and 1- interval along peripheral length and axial length, respectively. Normal distance between two points at same location is computed and this distance is deducted from RDOC to calculate surface error. For entire machined surface, surface error is determined along axial direction and peripheral direction using same methodology.

### 3.9.3 Machining conditions

For carrying out machining experiments, pre-machined workpieces with the necessary dimensions are held on dynamometer on the milling machine. It has previously been stated that the cutting tools are made of HSS and the workpiece is made of AL 6351-T6. The cutting conditions that are applied during experiments to determine cutting constants are given in Table 3.4 in detail. For each machining experiment, milling operation is carried out for 30 seconds while cutting forces are monitored with a piezoelectric dynamometer and recorded with a DAQ system. The captured data is afterwards compiled and analyzed using DynoWare software to determine the average feed force and normal force components.

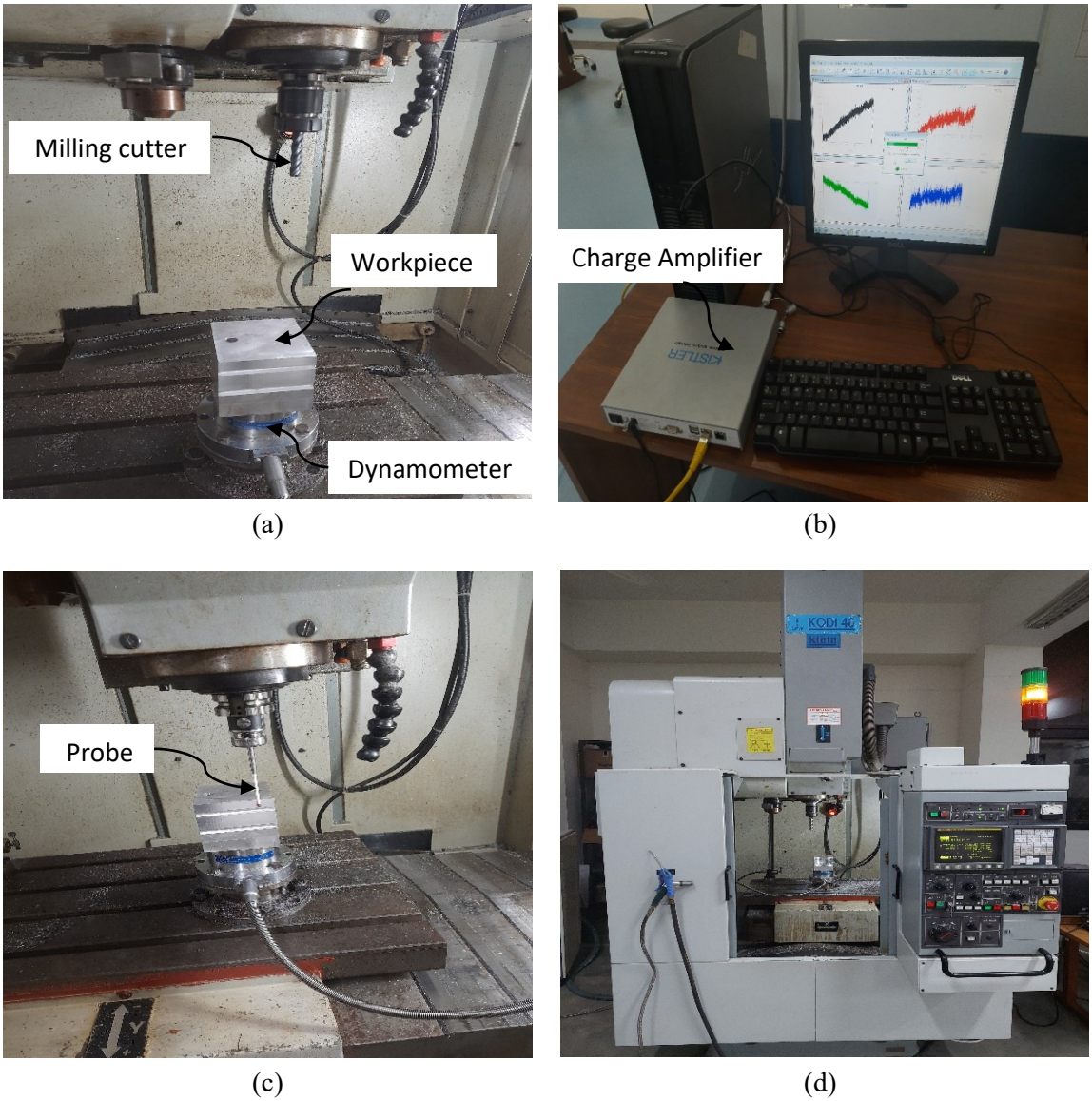


(a) (b)

(c) (d)

Fig. 3.18 The experimental setup: (a) and (b) Installation of force mesurement setup ; (c) and (d) Installation of probing system

Table 3.4 Cutting conditions for determination of cutting constants

| **RDOC [mm]** | **ADOC [mm]** | ***f*** **[mm/min]** |
|---|---|---|
| 3 | 2 | 100,150,200,250,300,350,400 |
| 5 | 2 | 100,150,200,250,300,350,400 |
| 7 | 2 | 100,150,200,250,300,350,400 |

After determining force constants, machining experiments are conducted using end mill cutter having a 77 mm overhang to estimate cutting forces, tool deflection-induced surface error and flatness error during machining of straight and curved thick-walled geometries. Tool deflections will be the main factor in determining the amount of surface error since the tool overhang is maintained at 77 mm, making the tool flexible.

Table 3.5 Machining conditions for straight and curved components

| **Workpiece geometries** | **RDOC (mm)** | **ADOC (mm)** | **Workpiece thickness (mm)** | **Tool overhang (mm)** |
|---|---|---|---|---|
| Straight thick-walled geometry | 2.5 | 10 | 40 | 77 |
| Straight thin-walled geometry | | | 5 | 44 |
| Concave elliptical thick-walled geometry | 2.2 | 11 | 40 | 77 |
| Concave elliptical thin-walled geometry | | | 5 | 44 |
| Spindle speed (RPM): 2000<br>Feed (mm/min): 400<br>Cutter diameter (mm): 16<br>Number of flutes: 4<br>Helix angle ( °): 30<br>Milling type: Down milling | | | | |

Later on, machining experiments are conducted using end mill cutter having a 44 mm overhang and 5 mm workpiece thickness for validation of workpiece deflection-induced surface error model for milling of thin walled straight and thin-walled curved geometries. In comparison to tool overhang and tool diameter, the wall thickness of the workpiece is thinner which makes workpiece flexible. This results workpiece deflection as major contributor in surface error. Machining conditions used for these experiments are described in Table 3.5.

## 3.10 Results and Discussion

In this section, computational results obtained from models discussed earlier are compared and analyzed with results obtained from various machining experiments.

### 3.10.1 Determination of cutting force coefficients

This section examines the behaviour of cutting constants for a given tool-workpiece pair and their dependence on uncut chip thickness. Average cutting forces over a cutter revolution is required for determining cutting force constants. As a result, set of experiments are carried out at different chip thickness values by varying radial depth of cut and feed rates and keeping axial depth of cut constant. In mechanistic cutting force models, it is believed that the average cutting constants will only be computed for a given tool-workpiece combination. The overall force exerted by the cutter during one rotation is computed and divided by the number of teeth on cutter in order to prevent the effects of cutter run out on measurements. Cutting force coefficients are calculated by substituting measured average cutting forces into analytically derived average milling force formulas. The equation for cutting force can be used to express the typical milling force per tooth period as follows:

$$\overline{F_A} = \frac{\int_{\theta_{en}}^{\theta_{ex}} F_A(\varphi) d\varphi}{\emptyset_p} \text{ where A} = \text{x, y} \tag{3.37}$$

The following mathematical formulation can be used to calculate the average chip thickness ($\overline{t_c}$) during one cutter revolution:

$$\overline{t_c} = \frac{\int_{\theta_{en}}^{\theta_{ex}} f_t . sin(\beta) d\beta}{\emptyset_p} \tag{3.38}$$

Table 3.6 lists the cutting parameters along with corresponding average chip thickness, measured average cutting forces, and mechanistic cutting constants.

The values of the cutting constants are plotted as dependent variables versus the uncut chip thickness as an independent variable. The graph in Fig. 3.19 shows the relationship between the cutting constants for force components and the uncut chip thickness. The following mathematical equation has been used to obtain the exponential relationship between $K_t$ and $K_r$ with average chip thickness with 95% confidence bounds in the present study:

$$K_t = 287.1(\overline{t_c})^{-0.48} \tag{3.39}$$

$$K_r = 106.8(\overline{t_c})^{-0.66} \tag{3.40}$$

Table 3.6 Cutting Conditions for Determination of Cutting Constants

| Sr No | Cutting parameters | | | Average chip thickness ($\bar{t_c}$) | Measured average cutting force (N) | | Mechanistic cutting constant | |
|---|---|---|---|---|---|---|---|---|
| | RDOC (mm) | ADOC (mm) | Feed rate (mm/min) | | $\overline{F_x}$ | $\overline{F_y}$ | $K_t$ | $K_r$ |
| 1 | 3 | 2 | 100 | 0.010 | 16.07 | 48.20 | 1716 | 1331 |
| 2 | 3 | 2 | 150 | 0.015 | 22.77 | 57.10 | 1441 | 991.6 |
| 3 | 3 | 2 | 200 | 0.020 | 27.79 | 68.48 | 1302 | 885.5 |
| 4 | 3 | 2 | 250 | 0.026 | 33.72 | 79.76 | 1231 | 811.4 |
| 5 | 3 | 2 | 300 | 0.031 | 40.41 | 93.22 | 1209 | 781.7 |
| 6 | 3 | 2 | 350 | 0.036 | 42.98 | 91.31 | 1047 | 632.9 |
| 7 | 3 | 2 | 400 | 0.041 | 48.05 | 100.2 | 915.4 | 553.2 |
| 8 | 5 | 2 | 100 | 0.013 | 13.19 | 61.75 | 1372 | 914.9 |
| 9 | 5 | 2 | 150 | 0.019 | 18.08 | 79.59 | 1191 | 772.7 |
| 10 | 5 | 2 | 200 | 0.026 | 23.21 | 98.54 | 1113 | 709.6 |
| 11 | 5 | 2 | 250 | 0.032 | 26.86 | 107.1 | 979.5 | 605.6 |
| 12 | 5 | 2 | 300 | 0.039 | 31.70 | 116.2 | 900.1 | 531.3 |
| 13 | 5 | 2 | 350 | 0.045 | 33.12 | 94.47 | 665.7 | 331.9 |
| 14 | 5 | 2 | 400 | 0.052 | 38.90 | 126.1 | 752.2 | 411.9 |
| 15 | 7 | 2 | 100 | 0.015 | 5.02 | 73.88 | 1185. | 764.8 |
| 16 | 7 | 2 | 150 | 0.022 | 8.26 | 87.60 | 953.5 | 581.1 |
| 17 | 7 | 2 | 200 | 0.030 | 14.46 | 92.71 | 788.7 | 417.5 |
| 18 | 7 | 2 | 250 | 0.037 | 16.33 | 125.3 | 837.8 | 471.2 |
| 19 | 7 | 2 | 300 | 0.044 | 19.80 | 133.5 | 752.4 | 406.2 |
| 20 | 7 | 2 | 350 | 0.052 | 25.14 | 139.6 | 688.1 | 344.7 |
| 21 | 7 | 2 | 400 | 0.059 | 24.16 | 171.3 | 719.2 | 395.5 |

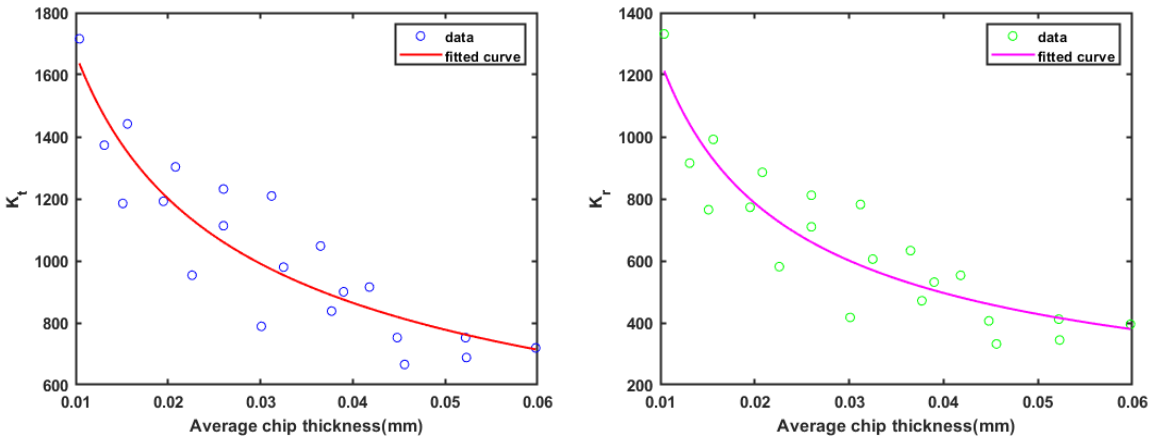


(a) $K_t$ vs. average chip thickness (b) $K_r$ vs. average chip thickness

Fig. 3.19 Plot for cutting constants vs. average chip thickness

## 3.10.2 Model validation

Fig. 3.20 shows comparison of experimental measured forces and estimated forces for machining of straight and curved geometries. It is noticed that the estimated cutting force results are in good agreement with their measured counterpart. Therefore, the cutting force model is acceptable and reliable to compute surface error and flatness error and analyze the surface error profile. Fig. 3.20(a) shows force profile at a single feed station in case of machining of straight geometry and this profile remains same along cutter contact path. Fig. 3.20(b) illustrates average force profile along cutter constant path in machining of concave elliptical geometries. It is observed that, cutting force does not remain constant along cutter contact path. In this case, as the curvature value gradually decreases, the cutting force is gradually increasing along the tool contact path from the beginning to end of cut due to decrement in magnitude of uncut chip thickness.

Fig. 3.21 displays comparison of predicted and measured surface error profiles for machining of straight thick-walled and thin-walled geometries. As illustrated in Fig. 3.21(a), during down milling of straight thick-walled geometries with a short axial depth of cut, the surface error is greatest at the tool tip and almost zero at the top surface due to the higher cutting force when the cutting flute first begins to form the surface and drop to zero due to the diminishing engaged section. Similar surface error profile is observed in case of machining of straight thin-walled geometries as shown in Fig. 3.21(b) but surface generation mechanism is different. Because of the workpiece's higher rigidity, light cutting conditions and less variation in movement of surface generation point with respect to fixed

end compared to height of workpiece, movement of surface generation point towards the free end has little impact. As a result, maximum surface error is generated at the bottom due to the considerably higher cutting force. Due to zero cutting force at the top of the cut, surface error drops to zero.

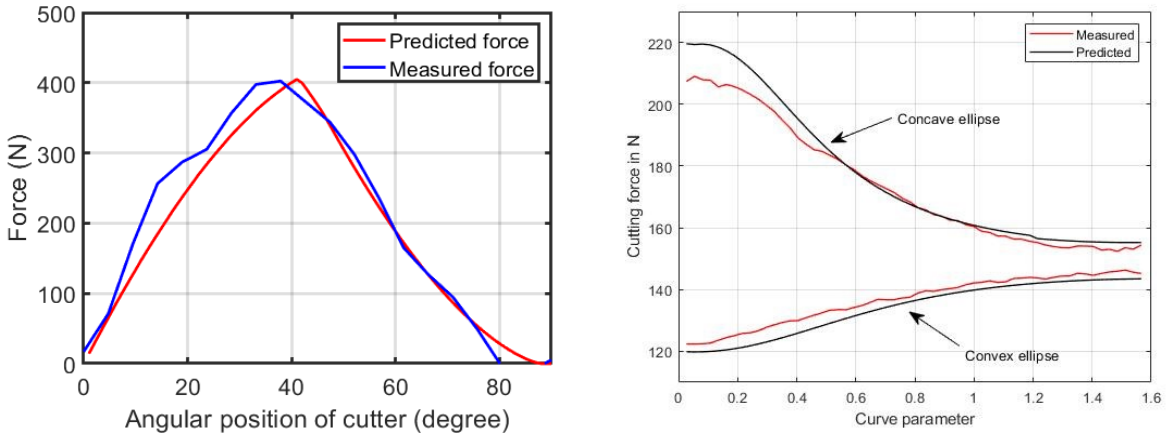


(a) Straight geometry (b) Elliptical curved geometry

Fig. 3.20 Variation of cutting forces for straight geometry at a single feed station and curved geometry along curved length

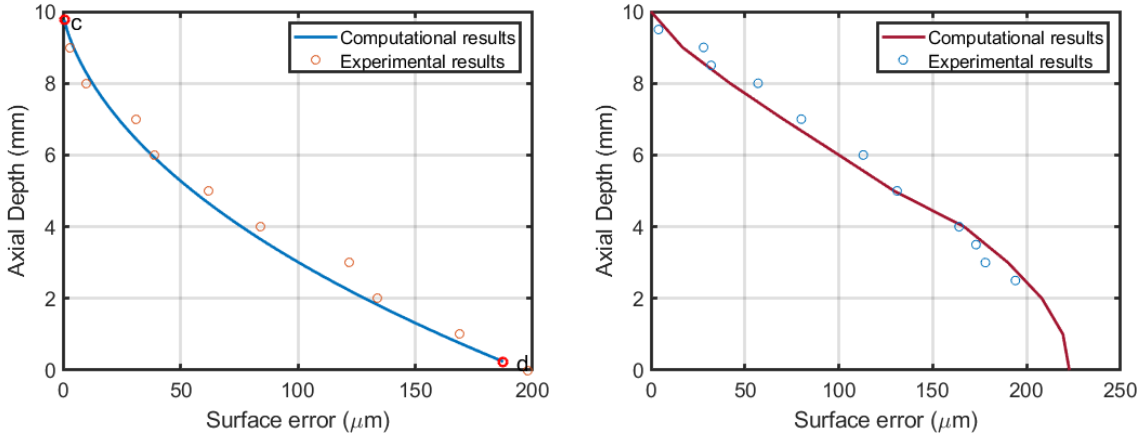


(a) Thick-walled geometry (b) Thin-walled geometry

Fig. 3.21 Predicted and measured surface error for straight geometry

A comparison of the computationally obtained flatness error with the experimental results for straight thick-walled and thin-walled geometries is shown in Fig 3.22. In case of thick-walled geometries, computational and experimental flatness error is 190 $\mu m$ and 215 $\mu m$ respectively. In case of thin-walled geometries, computational and experimental flatness error is 227 $\mu m$ and 248 $\mu m$ respectively. It is clear from results that flatness error predicted from model are in good agreement with the values obtained through experimental measurement.

Fig. 3.23 shows variation of surface errors along curve length for machining of thick walled and thin-walled concave elliptical curved geometry. It can be observed that estimated variation in surface error matches with their experimental counterpart well in terms of both form and magnitude. Results further demonstrate that variation of surface error along axial length does not remain constant along tool path but it varies with workpiece curvature. In machining of both geometry, curvature of workpiece has increasing trend from start to end of cut. In case of thick-walled geometry, the surface error profile remains constant for a certain length of tool path but after some time, it changes as illustrated in Fig. 3.23(a). The surface error profile changes significantly with further increase in the workpiece curvature. As thinning of workpiece is absent in this case, only workpiece curvature is main factor in variation in surface error. But this is not case in machining of thin-walled curved geometry as shown in Fig. 3.23(b). Rigidity of workpiece decreases along curve length due to thinning effect but at same time, it increases due to workpiece curvature. Due to this and increment of cutting forces, surface error decreases gradually from start of cut to middle of cut and then increases gradually and reaches maximum value at end.

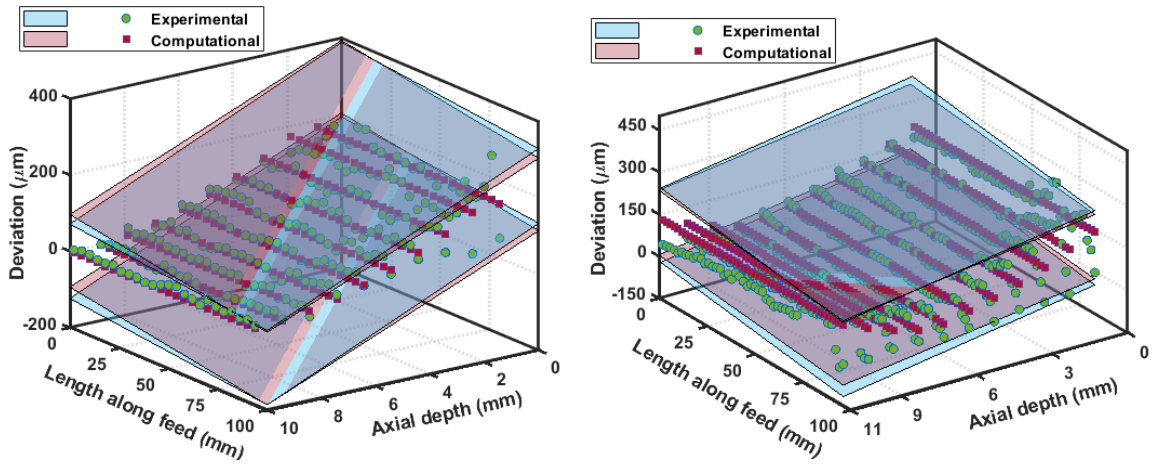


(a) Thick wall (b) Thin wall

Fig. 3.22 Predicted and measured flatness error

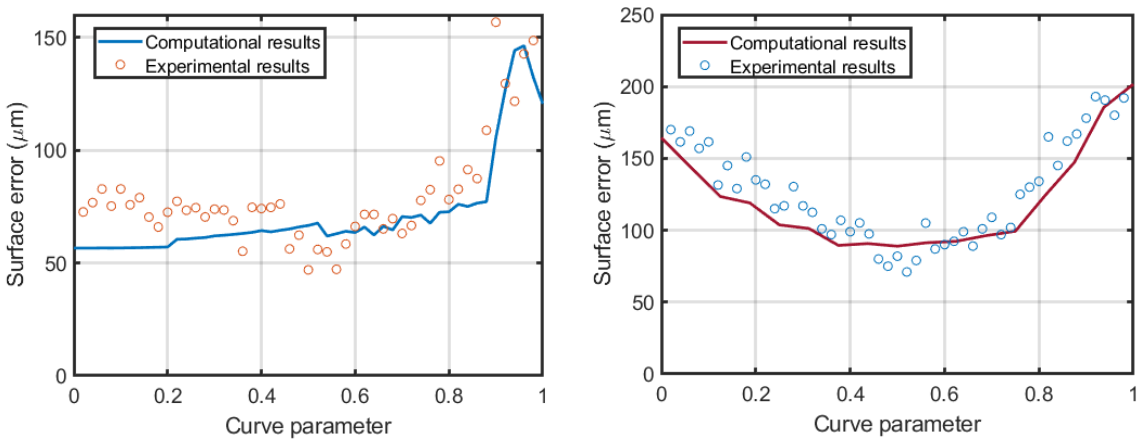


(a) Thick-walled curved geometry (b) Thin-walled curved geometry

Fig. 3.23 Variation of surface error along curve length in machining of concave elliptical curved geometry

## 3.11 Concluding Remarks

The present chapter deals with the modelling of cutting forces, tool and workpiece deflection surface error for milling of straight and curved geometries along with flatness error During development of force model, cutting force coefficients are obtained experimentally for a given tool-workpiece pair. To examine the effectiveness of the suggested model, the estimated forces derived from the force model are compared with their measured values. Further, results of proposed classification scheme and flatness error model are validated by performing machining experiments. Later on, due to presence of workpiece curvature, qualitative and quantitative variations in surface error that occur during the machining of curved geometries are also studied and validated with machining experiments.

# Chapter 4

# Characterization of Surface Error in Thin-Wall Milling

## 4.1 Introduction

In machining of thin-walled components, workpiece deflection induced surface error is also one of the obstacles for manufacturers like tool deflection induced surface error to achieve desired part accuracy. These surface errors do not have identical shape and form along axial direction and their magnitudes vary considerably with change in cutting conditions. In this chapter, a methodology is presented to classify surface error profiles based on three angular parameters namely engagement angle, sweep angle and tooth spacing angle. Machining experiments are performed to validate the proposed scheme by comparing the predicted results with their measured counterparts. The chapter also investigates some of the key challenges that arise during machining of thin-walled components such as thinning and end effects. Furthermore, the significance of proposed classification scheme is highlighted in milling of curved geometries where curvature of workpiece influences the tool-workpiece engagement and corresponding surface error profiles.

## 4.2 Characterization of Tool Deflection Induced Errors

Based on the previous work, it is observed that surface error variation along axial direction is related to cutting force variation with cutter rotation. Therefore, it is necessary to study variation of cutting forces prior to variation of surface errors. Although, the magnitude of cutting force is affected by tool and workpiece material and geometry, cutting conditions, etc. the force profile is mainly affected by RDOC and ADOC [151]. The changes in RDOC and ADOC have an impact on cutter-workpiece engagement in the radial direction ($\alpha_{engg}$) and sweep angle($\alpha_{sweep}$).

Cutter-workpiece engagement section for peripheral milling is shown in Fig.4.1 in the form of rectangle “abcd”. A flute always enters at the point “a” and exits at the point “c”, but the order in which it goes through vertices “d” and “b” is determined by the dimensions of rectangle “abcd”. The change in ADOC and RDOC results into variation in magnitude of engagement and sweep angles due to its effect on dimensions of rectangle

"abcd" as shown in Fig. 4.1. The changes in boundary conditions impact on engagement pattern of flutes and magnitude of chip load at exit of flute.

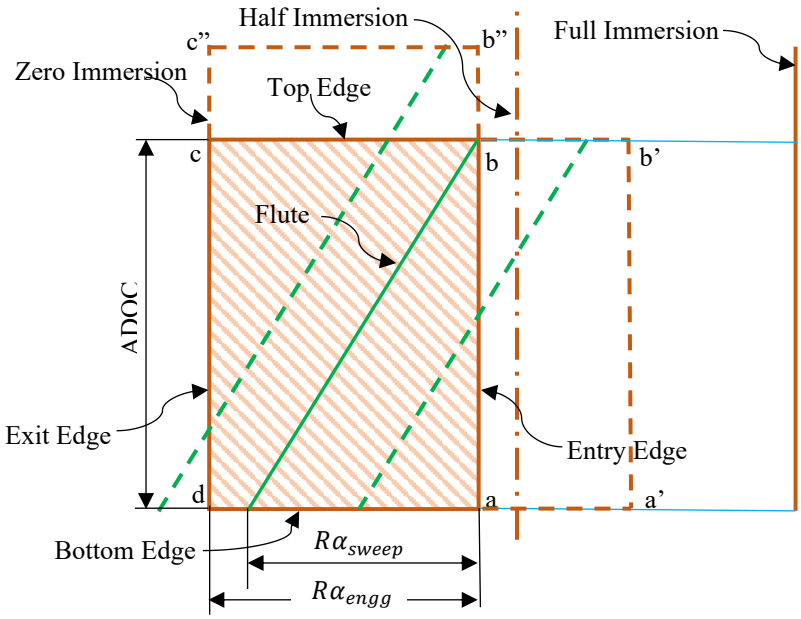


Fig. 4.1 Expanded Engagement Section

This section deals with correlation of variation in surface errors with RDOC and ADOC by analyzing the effect of changes in RDOC and ADOC on $\propto_{engg}$ and $\propto_{sweep}$ together with tooth spacing angle ($\phi_p$). Using the following Eqs. 4.1-4.3, these three angular parameters ($\propto_{engg}$ , $\propto_{sweep}$ and $\phi_p$) can be linked to the nominal cutting parameters defined at beginning of cut.

$$\alpha_{sweep} = \frac{a_p . \tan \alpha_{helix}}{r} \tag{4.1}$$

$$\alpha_{engg} = \theta_{ex} - \theta_{en} = \cos^{-1}\left(\frac{r - a_e}{r}\right) \tag{4.2}$$

$$\phi_p = \frac{2\pi}{N_f} \tag{4.3}$$

Based on the relationship of these three angular parameters, surface error profiles are classified into six groups namely Type I to Type VI cutting combining single flute and multi flute engagement. For a four-fluted end mill with a 30-degree helix angle, the classification scheme is graphically represented in Fig. 4.2 as a function of RDOC and ADOC. In each cutting group, contour area of engagement section changes with ADOC and

RDOC but engagement characteristics remain same. Therefore, shape of surface error profile will be similar for each cutting group. The following subsection discusses all these various types of cutting in brief.

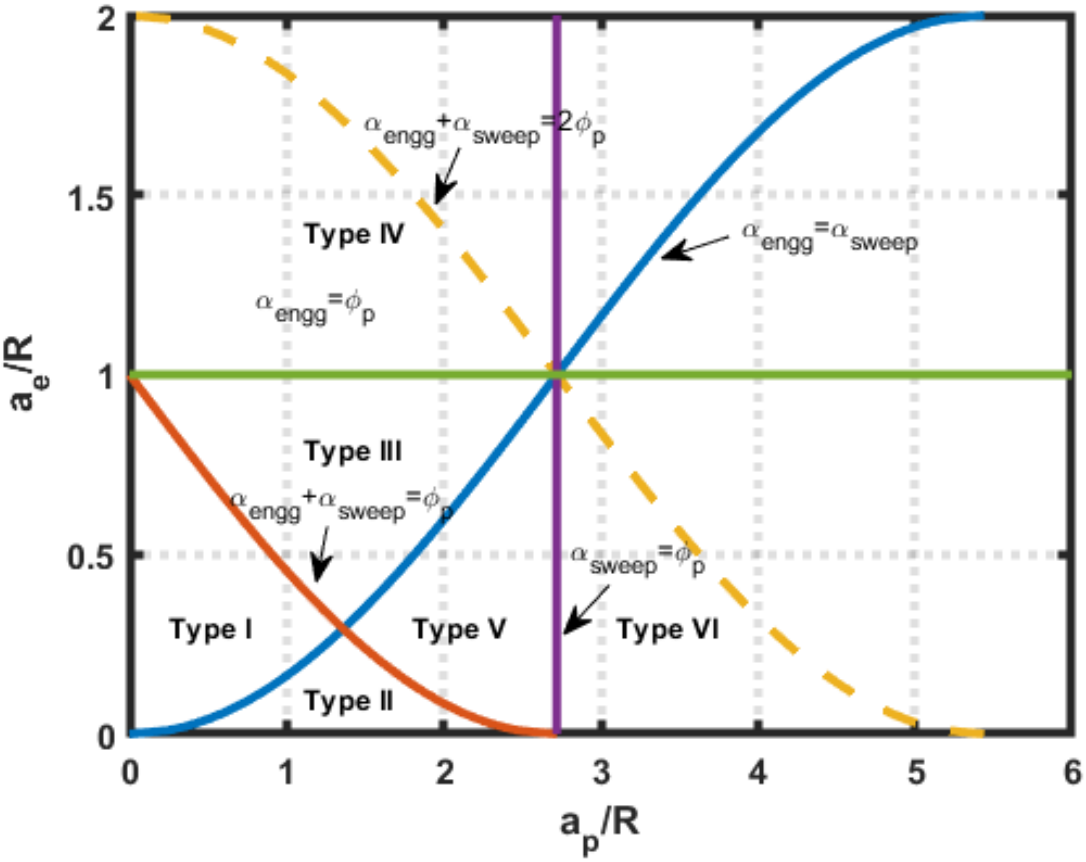


Fig.4.2 Classification scheme for surface error shapes [57]

### 4.2.1 Single flute engagement

The single flute engagement in milling occurs under light cutting conditions where small ADOC and RDOC are used as nominal depths of cut. During cutting, the combination of ADOC and RDOC is selected in such way that the summation of $\propto_{engg}$ and $\propto_{sweep}$ is less than $\phi_p$. Therefore, only a single helical flute engages in the cutting at a time without any overlapping to other flutes.

#### 4.2.1.1 Type I cutting: ( $\alpha_{engg} + \alpha_{sweep} < \phi_p$ and $\propto_{sweep} < \propto_{engg}$)

Fig. 4.3 illustrates the movement of the cutting flute in the cutter-workpiece engagement section, as well as the cutting force and surface error variation for Type I cutting. The surface error only develops while tracing the exit edge, despite the milling

force being present practically at all angular positions. As the current flute exits the cut, the surface generation starts from the bottom. This flute produces the maximum value of surface error at bottom due to its large magnitude of force and low force center. The length of engaged flute reduces and the surface generation point advances upward as the cutter rotates. The gradually decreasing surface error profile is produced due to continuous increasing force center and decreasing force magnitude. The surface generation point exits cut at top with zero force and zero surface error.

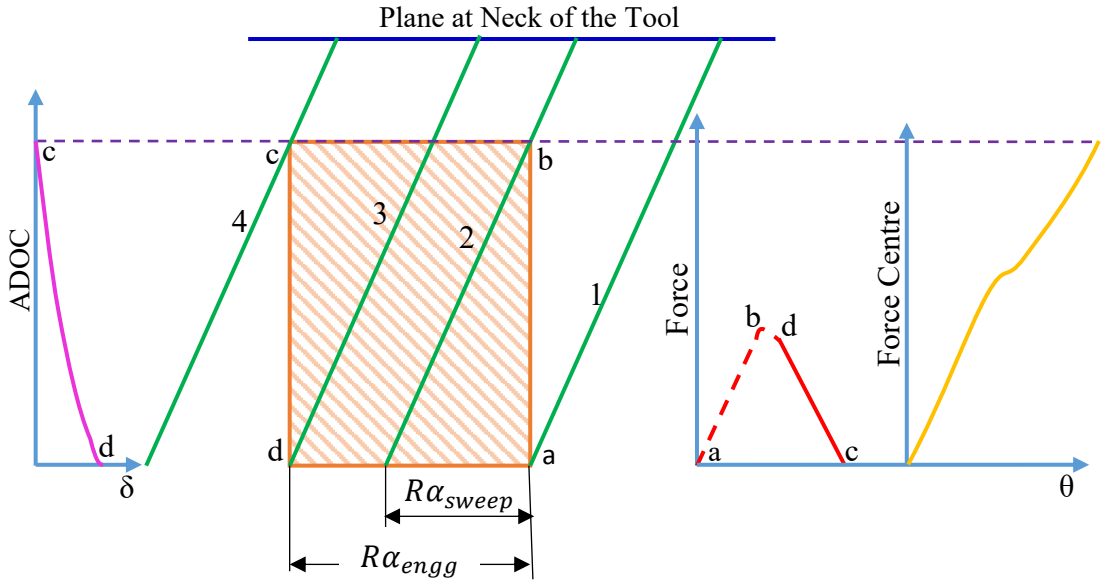


Fig. 4.3 Type I cutting

### 4.2.1.2 Type II cutting: ( $\alpha_{engg} + \alpha_{sweep} < \phi_p$ and $\propto_{sweep} > \propto_{engg}$)

Fig. 4.4 shows the section of tool-workpiece engagement, variation in cutting force and resulting surface error profile for Type II cutting. Unlike the previous case, a flute passes through "d" first instead of "b" as sweeping angle in this case is greater than engagement angle. The engaged flute length and force remain constant after it passes through the point "d". At the start of surface generation, decreasing surface error profile with almost constant slope is generated due to constant cutting force and increasing cutting force center. The length of engaged flute and cutting force remain constant until flute passes through "b". Then, a gradually diminishing surface error profile is generated as a result of the decreasing profile of cutting force and the increasing trend of the force center. It can be observed that the kink on the surface error indicated by the discontinuity in the slope of the

error profile at "b" caused due to the discontinuity in the slope of the force profile at the end of the constant force area.

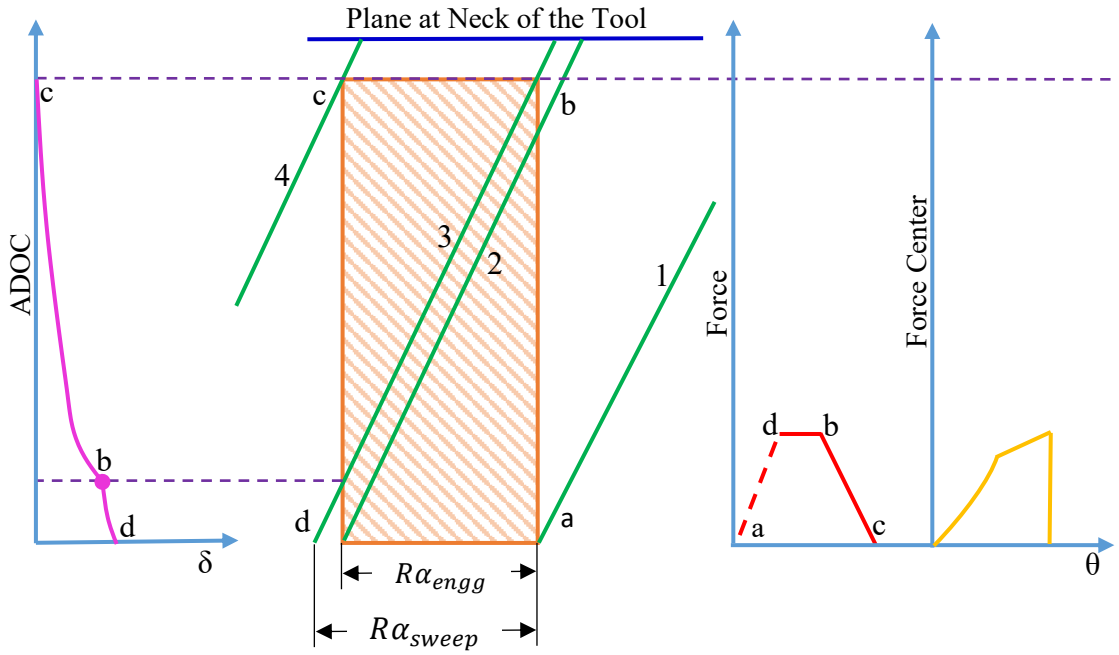


Fig. 4.4 Type II cutting

### 4.2.2 Multi flute engagement

The heavy cutting conditions like high radial depth of cut and large axial depth cut lead to involvement of more than one flutes during cutting. In these situations, the resultant force is calculated by adding the forces acting on the individual flutes. The surface error profile with different kink characteristics is generated when an additional flute is engaged as it causes variations in the force magnitudes and force center.

#### 4.2.2.1 Type III cutting: ( $\alpha_{engg} < \phi_p$ and $\propto_{sweep} < \propto_{engg}$)

Unlike in Type II cutting, the cutting force profile generated during this type of cutting does not have a constant force profile. Therefore, the type of kink generated in Type II cutting is absent in the surface error profile. But, due to variation in number of flute engagement, different type of force pattern generates that is reflected on the machined surface. Fig. 4.5 shows the section of tool-workpiece engagement along with location of flutes, cutting force, force center and surface error variation for Type III cutting. In this type of cutting, the previous flute is already in the cut when the current flute is entered, but it

exits the cut entirely before the current flute is fully engaged. The length of the current flute increases resulting into increase in cutting forces while the previous flute continues to produce machined surfaces until it exits the cut. It leads to increasing surface error profile at top section due to combine effect of increasing cutting force and decreasing force center. This portion of the surface error profile caused by the double-flute engagement, which has a reasonably constant slope like Type II does but generates at top section. Also, it is proven to have a steeper slope than Type II due to the larger force magnitude in the multi-flute engagement. Also, a sharp change in the slope of force profile and the force center leads to formation of kink on surface error profile at "*l*" due to the transition of cutting force into and out of the double-flute engagement. Once the previous flute has been cut through, the current flute starts to generate remaining surface. In this portion of single flute engagement, force profile and surface error profile is similar to Type I cutting with kink free error profile.

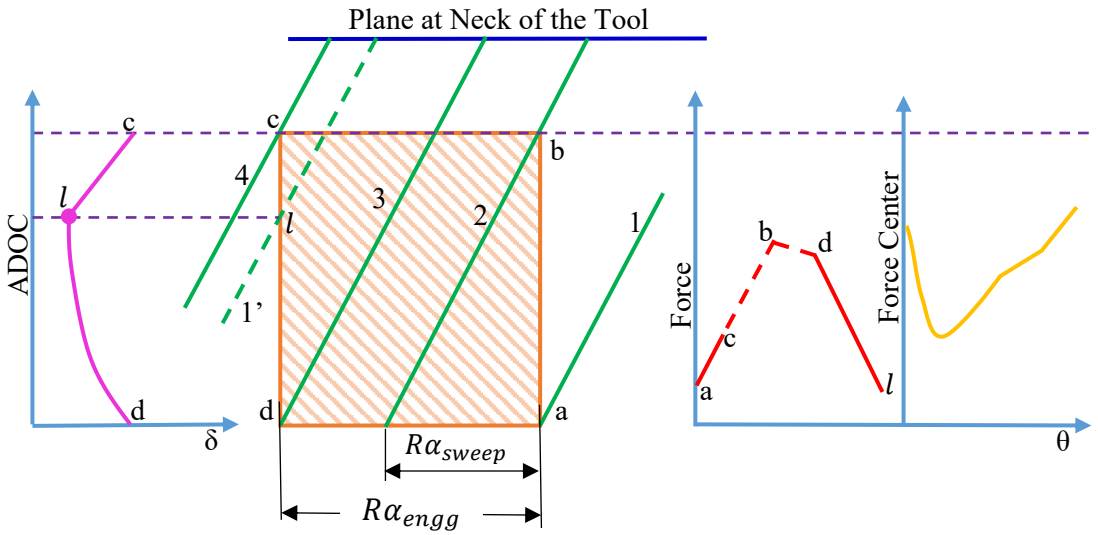


Fig. 4.5 Type III cutting

### 4.2.2.2 Type IV cutting: ( $\alpha_{engg} > \phi_p$ and $\propto_{sweep} < \propto_{engg}$)

The section of tool-workpiece engagement, cutting force, force center and surface error profile for Type IV cutting are shown in Fig. 4.6. In this type, when the current flute starts to cut, there is no flute on the exit edge because the location of the preceding flute is at angular distance $\phi_p$. The surface generation starts as soon as the preceding flute reaches the point "d". Along with the movement of the surface error generation point, the engaged length of the current flute and cutting force also increases resulting increasing surface error

profile. As soon as the current flute reaches the point "b", the engaged flute length becomes constant, but the cutting force increases since the flute did not reach the half immersion line. During this period, the preceding flute exits the cut, producing the highest amount of surface error at the top. Even though two flutes are engaged in the cut, the Type IV cutting is a unique case of multiple flute engagement in which a single flute (previous flute) creates the entire surface error profile.

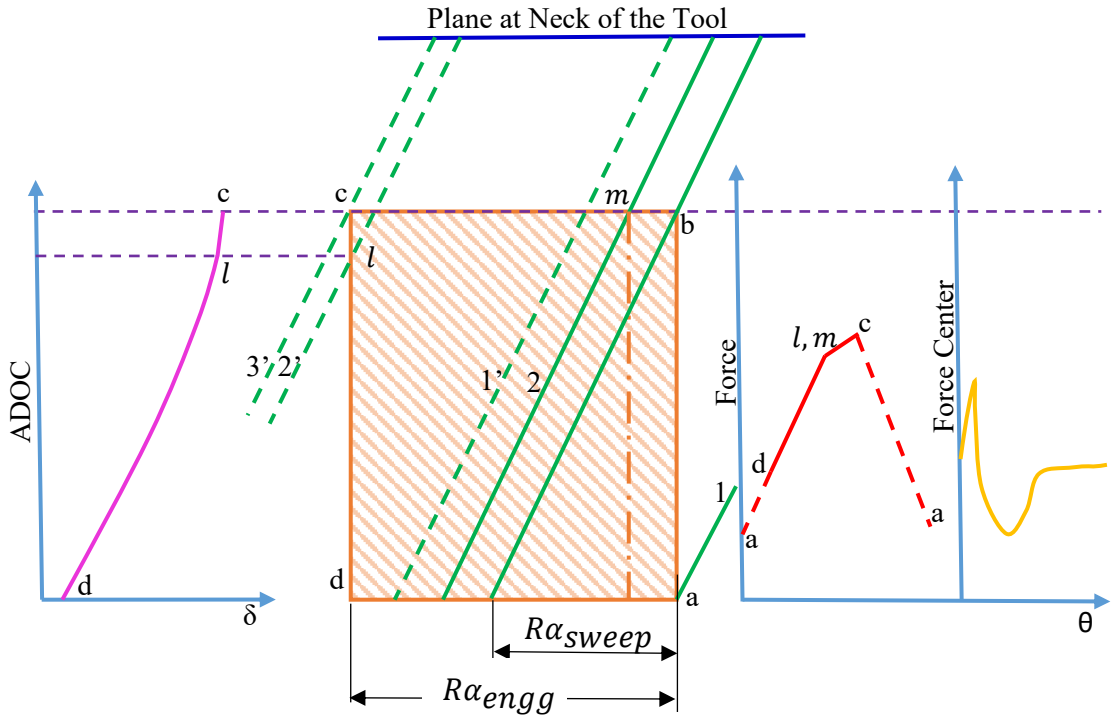


Fig. 4.6 Type IV cutting

### 4.2.2.3 Type V cutting: ( $\alpha_{sweep} < \phi_p$ and $\propto_{sweep} > \propto_{engg}$)

A force profile and surface error generated during Type V cutting will have combined characteristics of Type II and Type III cutting, where the Type II produces a constant force region and Type III experiences a greater force because of multi-flute engagement. The cutter–workpiece engagement, cutting force, force center and surface error variations are shown in Fig.4.7. The surface error profile shows the presence of two kinks (*b,l*). The bottom section of the error profile for down milling are found to have kink generated in Type-II cutting corresponding to constant force region and kink in Type-III cutting is seen at the top section of the error profile which corresponds to the double-flute engagements. The positions of these kinks generated by cutting flutes are located at same positions as those found in Type II and Type III.

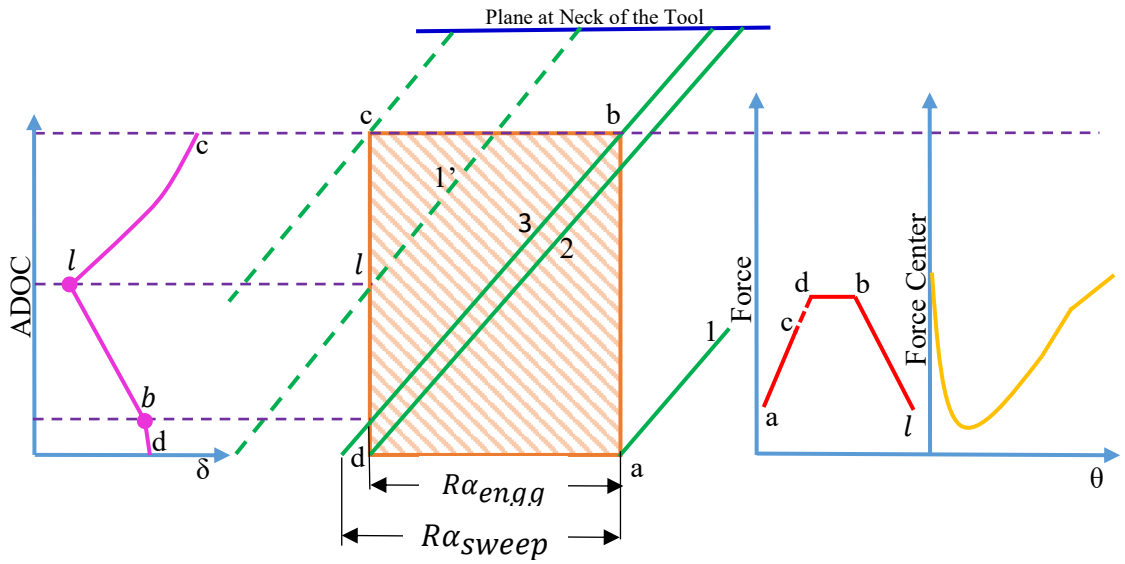


Fig. 4.7 Type V cutting

### 4.2.2.4 Type VI cutting: ( $\alpha_{sweep} > \phi_p$ and $\propto_{sweep} > \propto_{engg}$)

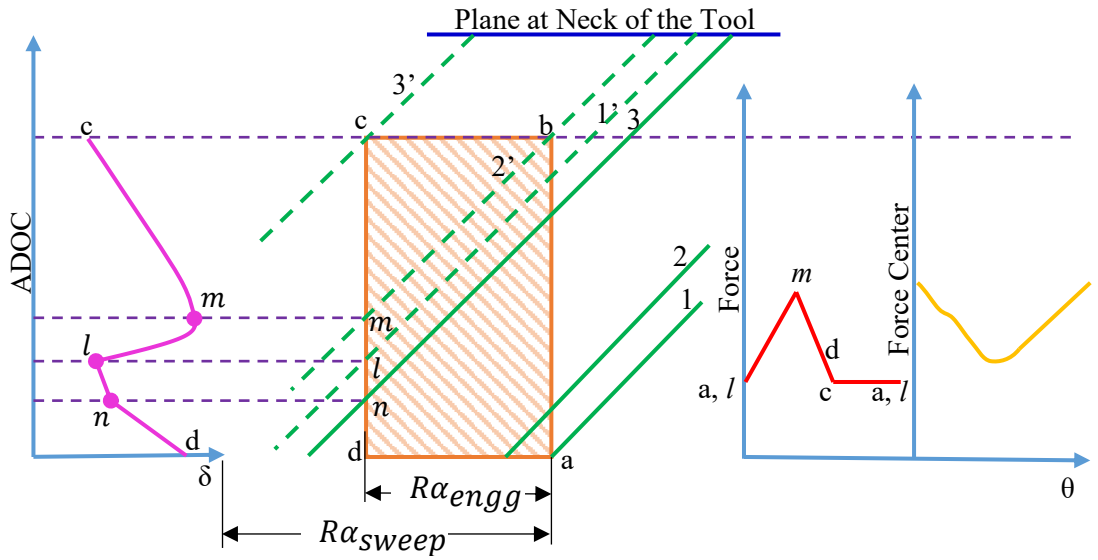


Fig. 4.8 Type VI cutting

As illustrated in Fig. 4.8, the previous flute generates machined surface at the point "*l*" when current flute enters the cut. The engaged flute length and cutting force remains constant for the previous flute but increases for current flute until it reaches to the point "d". As a result, until the previous flute reaches at the point "b" and the surface generation point reaches at the point "m", the effective cutting force operating on the cutter increases and reaches maximum at "m" resulting into increasing surface error profile between "*l*" and "*m*". The kinks are generated at point "*l*" due to beginning of double-flute engagement

similar to Type III cutting and the point "*m*" due to sharp change in the slope of the force profile. Once the previous flute passes the point "b", the engaged flute length and cutting force acting on previous flute decreases but that of the current flute still increases. It leads to decrease in cutting force and results into decreasing surface error profile at top. During this time, the previous flute continues to produce the machined surface at the top while the current flute travels and passes through "d" to start generating surface at the bottom section. During this time, surface error decreases until the previous flute exits the cut and the current flute reaches at the point "*n*". The kink is generated at point "*n*" due to ending of double-flute engagement.

**The kink position:**

The height positions of all kink points mentioned in previous subsections are determined using Eqs. 4.4-4.7. For all surface error types, the relationship among three angular parameters (engagement angle, sweep angle and tooth spacing angle) and corresponding kink points are summarized in Table 4.1 and analytical equations of kink points are given in Table 4.2.

$$h_b = \frac{(\propto_{sweep} - \propto_{engg}).r}{\tan(\propto_{helix})} \tag{4.4}$$

$$h_l = a_p - \frac{[(\propto_{sweep} + \propto_{engg}) - \phi_p].r}{\tan(\propto_{helix})} \tag{4.5}$$

$$h_m = h_l + \frac{(\propto_{sweep} - \phi_p).r}{\tan(\propto_{helix})} \tag{4.6}$$

$$h_n = \frac{\left(\propto_{sweep} - \phi_p\right).r}{\tan(\propto_{helix})} \tag{4.7}$$

Table 4.1 Angles criteria for various cutting types

| Type | Angles criteria | Kink points |
|---|---|---|
| I | $\alpha_{engg} + \alpha_{sweep} < \phi_p$ & $\alpha_{sweep} < \alpha_{engg}$ | Free |
| II | $\alpha_{engg} + \alpha_{sweep} < \phi_p$ & $\alpha_{sweep} > \alpha_{engg}$ | *b* |
| III | $\alpha_{engg} + \alpha_{sweep} > \phi_p$ , $\alpha_{sweep} < \alpha_{engg}$ & $\phi_p > \alpha_{engg}$ | *l* |
| IV | $\alpha_{engg} + \alpha_{sweep} > \phi_p$ , $\alpha_{sweep} < \alpha_{engg}$ & $\phi_p < \alpha_{engg}$ | Free |
| V | $\alpha_{engg} + \alpha_{sweep} > \phi_p$ , $\alpha_{sweep} > \alpha_{engg}$ & $\phi_p > \alpha_{sweep}$ | *l*+*m* |
| VI | $\alpha_{engg} + \alpha_{sweep} > \phi_p$ , $\alpha_{sweep} > \alpha_{engg}$ & $\phi_p < \alpha_{sweep}$ | *l*+*m*+*n* |

Table 4.2 Analytical equations for various kink points

| Type | Kink point *"b"* | Kink point *"l"* | Kink point *"m"* | Kink point *"n"* |
|---|---|---|---|---|
| I | - | - | - | - |
| II | $\frac{(\propto_{sweep}-\propto_{engg}).r}{\tan(\propto_{helix})}$ | - | - | - |
| III | - | $a_p$ $-\frac{[(\propto_{sweep}+\propto_{engg})-\phi_p].r}{\tan(\propto_{helix})}$ | - | - |
| IV | - | - | - | - |
| V | $\frac{(\propto_{sweep}-\propto_{engg}).r}{\tan(\propto_{helix})}$ | $a_p$ $-\frac{[(\propto_{sweep}+\propto_{engg})-\phi_p].r}{\tan(\propto_{helix})}$ | - | - |
| VI | | $a_p$ $-\frac{[(\propto_{sweep}+\propto_{engg})-\phi_p].r}{\tan(\propto_{helix})}$ | $h_l$ $+\frac{(\propto_{sweep}-\phi_p).r}{\tan(\propto_{helix})}$ | $\frac{(\propto_{sweep}-\phi_p).r}{\tan(\propto_{helix})}$ |

## 4.3 Characterization of Workpiece Deflection Induced Errors

Based on relationship among engagement angle, sweeping angle and tooth spacing angle, a classification scheme to identify surface error profiles due to tool deflection is discussed in previous section. In this section, a similar classification scheme is applied to milling of thin-walled components where surface errors mainly caused due to workpiece deflections.

### 4.3.1 Surface error shapes in single flute cutting

This type of cutting occurs under light cutting conditions where small ADOC and RDOC are used. The combination of ADOC and RDOC is selected in such a way that the summation of $\propto_{engg}$ and $\propto_{sweep}$ is less than $\phi_p$. Therefore, only single flute engages in the cutting at a time.

#### 4.3.1.1 Type I cutting: ( $\alpha_{engg} + \alpha_{sweep} < \phi_p$ and $\propto_{sweep} < \propto_{engg}$)

In this case, flute passes ''b'' first instead of "d" as $\propto_{sweep}$ is less than $\propto_{engg}$. As

shown in Fig. 4.9, the cutting force increases as the flute travels from "a" to "b" due to increase in engaged flute length. The flute's engaged length remains constant as it travels from "b" to "d", but the cutting force decreases as the flute moves from higher uncut chip thickness region to lower uncut chip thickness region. Once flute passes "d", the flute begins to leave the cut from the bottom and exits entirely out of the cut from "c". The engaged flute length decreases continuously as the flute travels from "b" to "c" resulting reduction in cutting force. As a result, the highest point is at "b". Fig. 4.9 shows the resultant cutting force profile. The angular distance between the entry point "a" and peak point "b" is $\propto_{sweep}$ and the angular distance between the entry point and point "d" is $\propto_{engg}$. Despite the presence of the milling force at almost all angular positions, the surface error is only generated when flute traces exit edge 'dc'. During this portion of cut, surface generation point moves up i.e., towards top end of plate and leaves cut at "c". During this period, plate deflects with respect to cutting force only. Because of the higher rigidity of workpiece, light cutting conditions and less variation in movement of surface generation point with respect to fixed end compared to height of workpiece, the movement of surface generation point towards the free end has little impact. As a result, the maximum surface error is generated at the bottom due to the considerably higher cutting force. Due to zero cutting force at the top of the cut, surface error drops to zero at the top end of plate. Along axial length, decreasing surface error profile from bottom to top similar to cutting force profile is generated as shown in Fig.4.9.

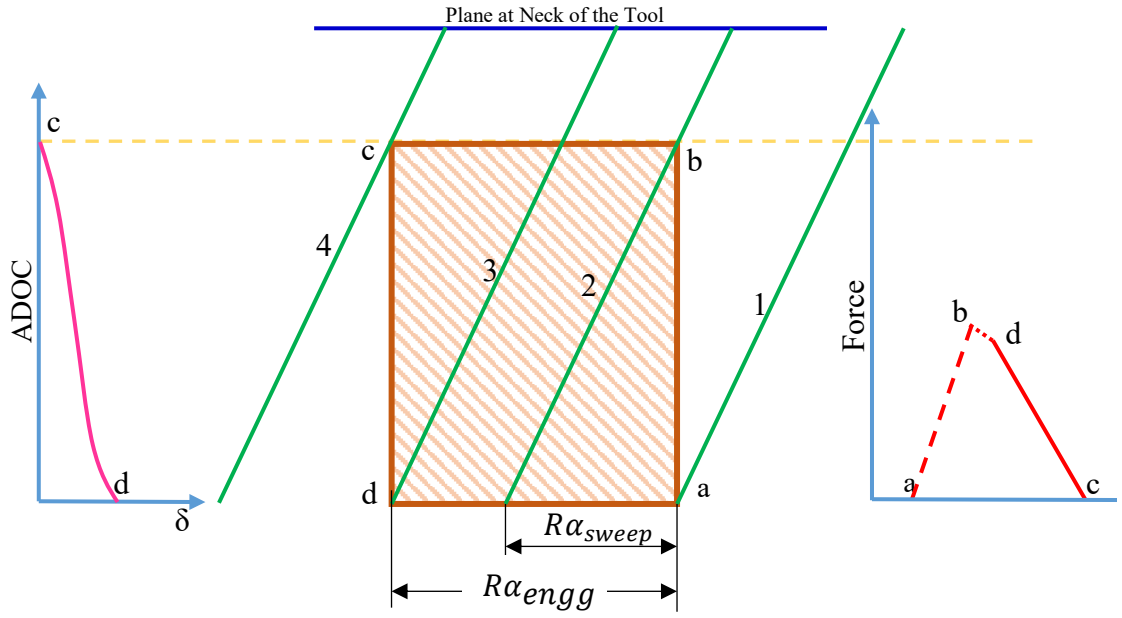


Fig. 4.9 Type I cutting

### 4.3.1.2 Type II cutting: ( $\alpha_{engg} + \alpha_{sweep} < \phi_p$ and $\propto_{sweep} > \propto_{engg}$)

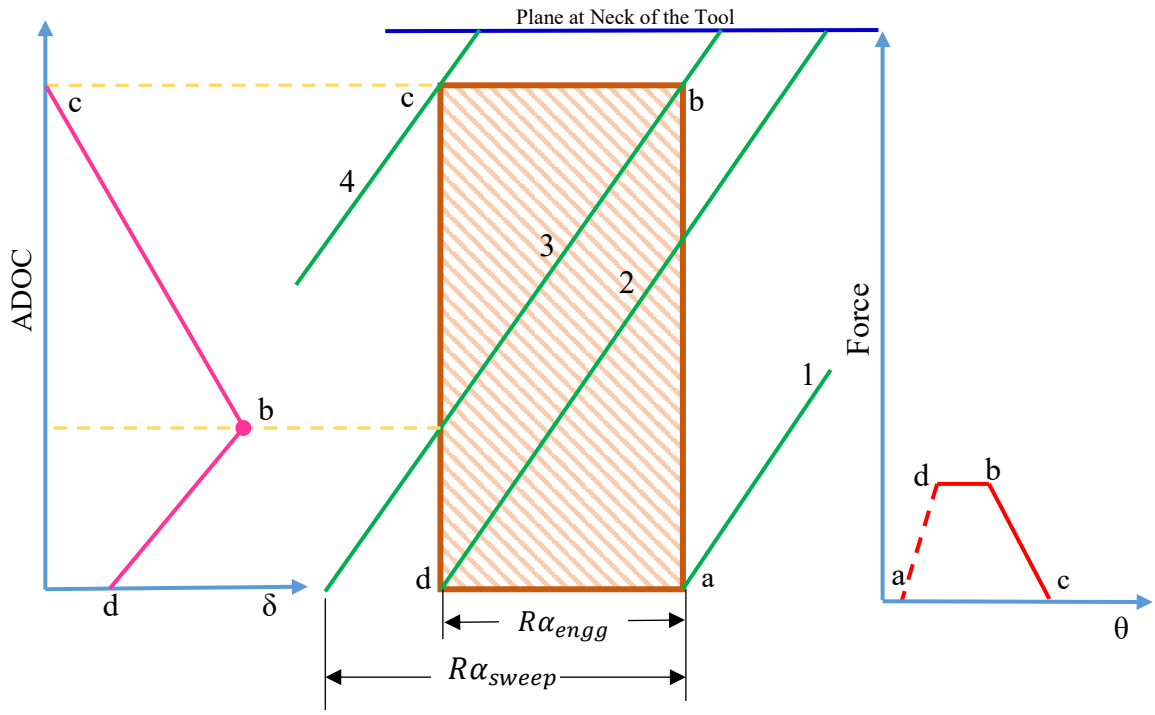


Fig. 4.10 Type II cutting

Since $\propto_{sweep}$ is more than $\propto_{engg}$, flute passes through "d" first before "b". The cutting force increases as the flute travels from "a" to "d" due to the increased engaged length of the flute. The engaged flute length remains unchanged as the flute travels from "d" to "b". Since the chip load is constant, the cutting force is constant during this period. Since the engaged flute length reduces continuously as the flute travels from "b" to "c", the cutting force reduces until the cutter is entirely out of the cut. Therefore, vertex "d" is the highest point. A flat top extends from vertex "d" to "b". The resultant cutting force profile generated during type-II cutting is shown in Fig. 4.10. Line d-b-c in force profile is responsible for generation of surface error. The magnitude of the surface error generated during d-b is only dependent on the position of the surface generation point as cutting force is constant. During this period, the surface error increases due to movement of the surface generation point towards free end of plate. The Eq. 4.4 is used for determining the axial position corresponding to flute at "b". During b-c period, surface error decreases as reduction in cutting force is more dominant than movement of surface generation point towards free end. Surface error profile during this period is similar to Type I cutting. As seen in Fig.4.10, the resulting surface error profile has two components: d-b and b-c. Under

Type II cutting, any combination of ADOC and RDOC results in the same surface error profile, but the length of individual components d-b and b-c would be different.

### 4.3.2 Surface error shapes in multiple flutes cutting

Heavy cutting conditions with large axial and radial cutting depths are often associated with this case. In this case, the sum of the engagement and sweep angles is greater than the tooth spacing angle. Therefore, multiple flutes are engaged in cutting while one or more flutes are responsible for the surface generation process.

#### 4.3.2.1 Type III cutting: ( $\alpha_{engg} < \phi_p$ and $\propto_{sweep} < \propto_{engg}$)

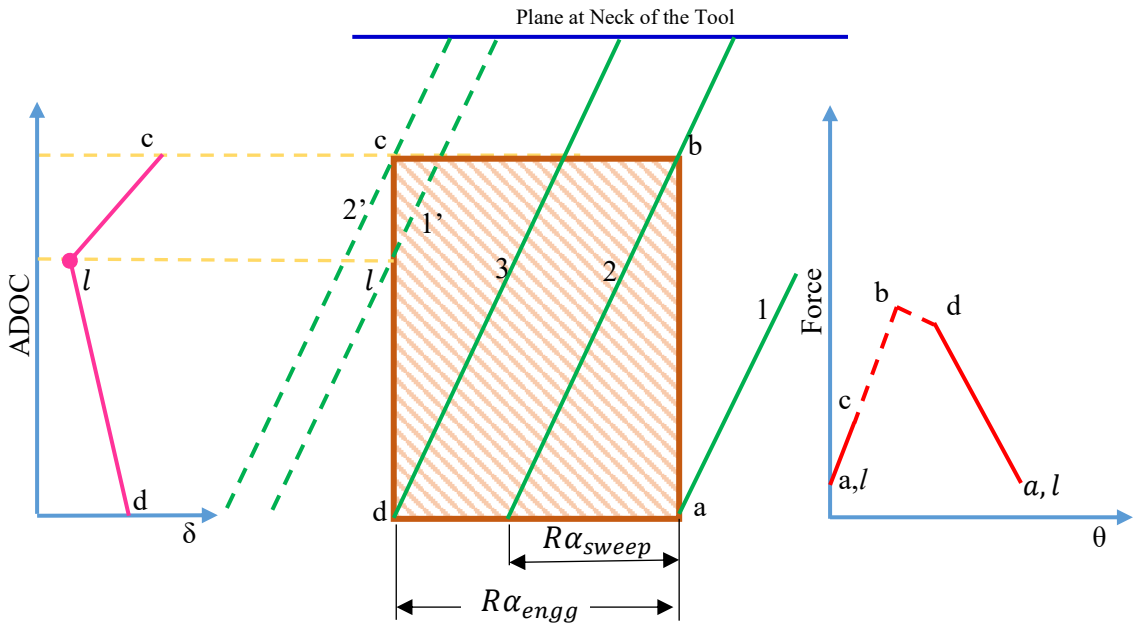


Fig. 4.11 Type III cutting

In this type, cutting conditions are in such a way that the previous flute is already in the cut when the current flute enters, but it exits before the current flute fully engages. The engagement section of cutter and workpiece is shown in Fig. 4.11. When current flute enters into cut at "a", previous flute is at exit edge. Position of surface generation point of previous flute is marked as "*l*" in Fig. 4.11 and it can be found from Eq. 4.5. While the previous flute continues to generate machined surfaces until it exits the cut, the cutting force increases as the engaged length of the current flute increases. During this period, the combined cutting action of the current and previous flutes is responsible for the surface error profile generated by the previous flute. Increase in the cutting forces and the movement of surface generation

point to the free end of plate results in an increase in surface error which is shown as *l*-c. Once previous flute exits the cut, remaining machined surface d-*l* is generated by current flute which has similar pattern to Type I cutting.

#### 4.3.2.2 Type IV cutting: ( $\alpha_{engg} > \phi_p$ and $\propto_{sweep} < \propto_{engg}$)

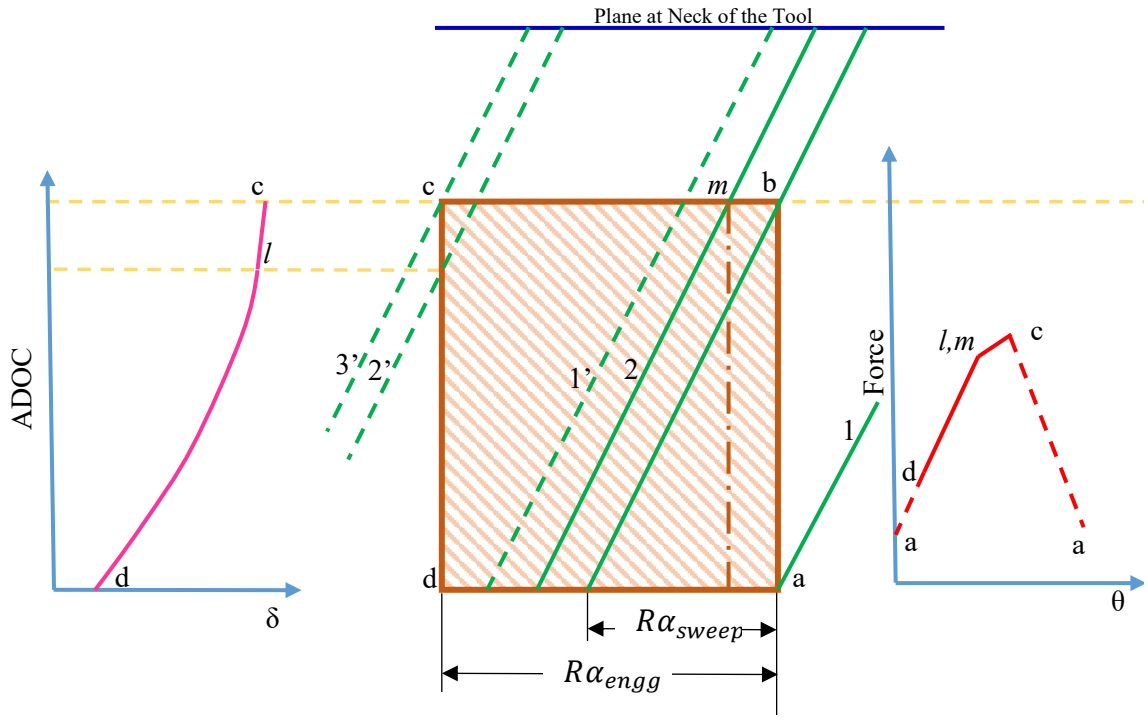


Fig. 4.12 Type IV cutting

In this type, radial depth of cut is higher than radius of end milling cutter resulting into occurrence of combination of up milling and down milling. Therefore, at start of cut, the chip thickness increases till half immersion line then decreases. In this type, when the current flute starts to cut, there is no flute on the exit edge. Surface generation starts as soon as the preceding flute reaches "b". The preceding flute produces the minimum value of surface error at bottom due to lower force and position of surface generation point away from free end. After that, the engaged length of preceding flute starts to decrease but that of current flute increases. Their combined effect is increment in cutting force resulting into increasing surface error profile. As soon as the current flute reaches "d", the engaged flute length becomes constant, but the cutting force increases since the flute did not reach the half immersion line. During this period, the preceding flute exits the cut, producing the highest amount of surface error at the top. As the machined surface is produced, the cutting force increases, results into completely reversing the trend of Type I cutting.

### 4.3.2.3 Type V cutting: ( $\alpha_{sweep} < \phi_p$ and $\propto_{sweep} > \propto_{engg}$)

The combination of $\propto_{sweep}$, $\propto_{engg}$ and $\phi_p$ for this type is selection in such a way that procedure for surface generation process is combination of Type II and Type III cutting. In same way as Type III cutting, the previous flute generates machined surface from "*l*" to "c". Once the current flute passes point "d", it starts generating machined surface. In this type of cutting, current flute reaches point "d" before "b" as sweeping angle is higher than engagement angle. Up to point "d', cutting force increases due to increase in engaged flute length. While the current flute moves from point "d" to "b", chip load remain constant due to constant flute engaged length resulting into constant cutting force which is shown as d-b in Fig.4.13. Therefore, surface error generated during d-b increases as surface generation point moves towards free end with constant force which is shown as d-*m* in Fig. 4.13. Due to reduction in the engaged flute length, chip load and cutting force start reducing once current flute passes through "b". This leads to decrease in surface error between "*l*" and "*m*". The resultant surface error profile is shown in Fig.4.13.

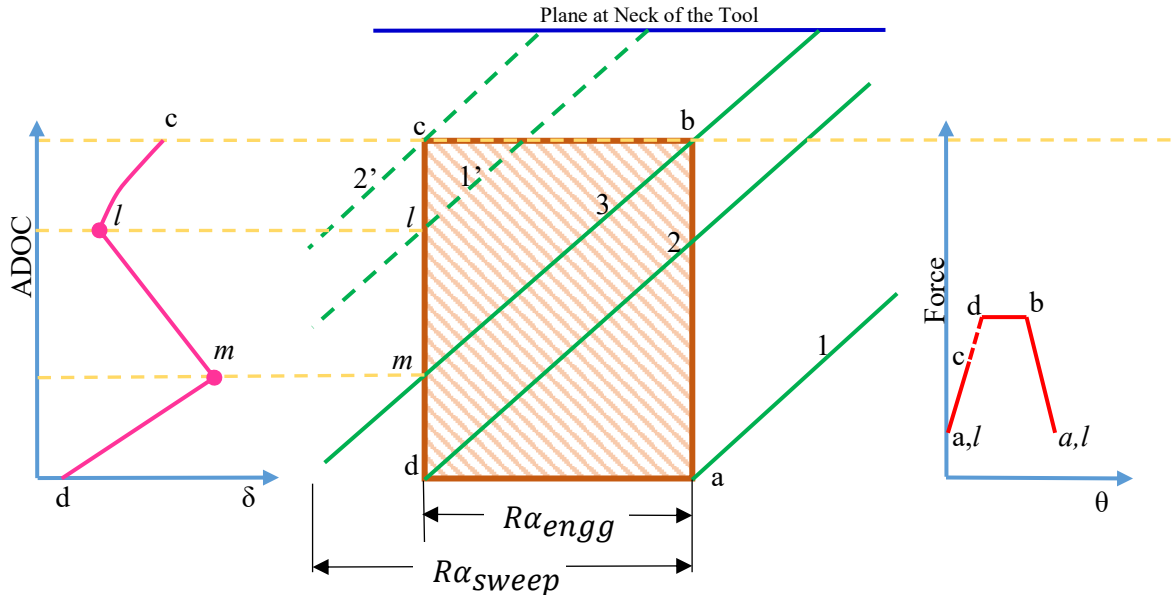


Fig. 4.13 Type V cutting

### 4.3.2.4 Type VI cutting: ( $\alpha_{sweep} > \phi_p$ and $\propto_{sweep} > \propto_{engg}$)

The sweeping angle in this type of cutting is greater than both engagement angle and tooth spacing angle resulting significantly greater engagement than in earlier cases. As shown in Fig.4.14, when the current flute enters in the cut, the previous flute start generating

a machined surface at "*l*" and axial position of surface generation point can be determined in the same way as Type III cutting. Due to higher ADOC, previous flute did not pass through "b" at this time. Therefore, chip load for previous flute remains constant till it reaches "b", but chip load for current flute increases. This leads to increase in effective cutting forces and resulting surface error. In Fig. 4.14, the resultant surface error profile produced by previous flute is shown as *l*-*m*. Once previous flute passes "b", force acting on previous flute decreases but force on current flute continue to increase. When any flute that leaves the cut exits from the high chip thickness area first, the rate of reduction in chip load caused by the previous flute is greater than the rate of increase in chip load caused by the current flute. Therefore, during this period, effective chip load and cutting force decrease, but the surface generation point moves towards free end of plate. Resultant of these lead to increase in surface error which is shown as *m*-c in figure. At this time, the current flute passes "a" and starts to generate surface at the bottom of the cut while the previous flute proceeds to generate machined surface at the top.

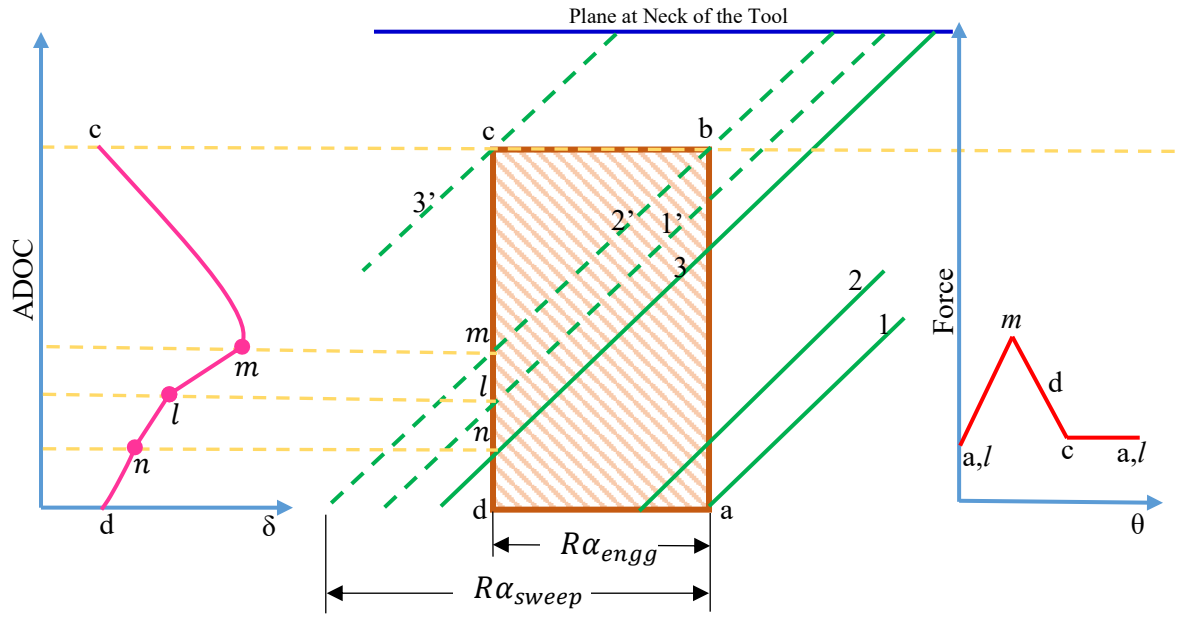


Fig. 4.14 Type VI cutting

## 4.4 Surface Error Variation in Milling of Curved Geometries

During machining of straight geometry, surface error profile remains constant along entire tool path at given ADOC and RDOC. But in case of curved geometry, tool-workpiece engagement varies continuously along entire tool path due to curvature of workpiece. In the previous section, it has been shown that the change in tool-workpiece engagement affect

cutting forces, which in turn changes the surface error profile. Thus, during machining of curved geometry, surface error profile varies along whole tool path even though ADOC and RDOC kept constant.

## 4.5 Machining Experiments

The computational results and machining experiments have been performed to validate the surface error characterization schemes mentioned in the previous sections. Two set of machining experiment are conducted to assess effectiveness of classification scheme for straight geometries and curved geometries respectively. The following subsections describe experimental setup, and machining conditions in details.

### 4.5.1 Experimental setup

The LMW JV-40 three axis vertical machining center (VMC) are used for all the machining tests using a piezo-electric dynamometer (Type-9272 by Kistler) as cutting force measuring system. The details about experimental setup are already covered in details in chapter 3. A comprehensive overview of job design and job preparation is also illustrated in chapter 3.

### 4.5.2 Machining conditions

The first set of machining experiments is conducted using end mill cutter having a 77 mm overhang from collet end to comprehend the effect of axial and radial immersions on cutting forces, tool deflection-induced surface error, workpiece deflection-induced surface error and flatness error. Total six machining experiments are carried out along with various ADOC and RDOC values and other cutting parameters given in Table 4.3. Each set of RDOC and ADOC combination is used for each individual type of cutting explained in the earlier section.

The second set of machining experiments are conducted for validation of surface error model for milling of curved geometries. Machining conditions used for experiments are described in Table 4.4.

Table 4.3 Machining conditions for machining of straight component

| **Cutting Types** | $a_e$**(mm)** | $a_p$**(mm)** |
|---|---|---|
| Type I | 2.5 | 10 |
| Type II | 1 | 13 |
| Type III | 4 | 11 |
| Type IV | 9 | 10 |
| Type V | 2 | 15 |
| Type VI | 1 | 25 |
| Spindle speed: 2000 rpm<br>Feed: 400 (mm/min)<br>Cutter overhang: 77 (mm)<br>Diameter of milling tool: 16 (mm)<br>Flute number of milling tool: 4<br>Cutter helix angle: 30 °<br>Type of milling: Down milling | | |

Table 4.4 Machining conditions for machining of elliptical component

| **Workpiece geometry** | **Elliptical concave, Elliptical convex** |
|---|---|
| Spindle speed | 2000 rpm |
| Nominal feed rate | 400 mm/min |
| Nominal feed per tooth | 0.05 mm/tooth |
| Axial depth of cut | 10,12 mm |
| Radial depth of cut | 2.2,2.4 mm |
| Tool overhang | 77 mm |
| Tool diameter | 16 mm |
| Tool helix angle | 30º |
| Milling type | Down milling with no coolant |

## 4.6 Results and Discussion

The cutting forces, surface errors, and concerned flatness errors for various cutting types obtained during experimental and computational investigations of the milling of thick-walled and thin-walled straight geometries are discussed in this section. The variation of surface errors in machining of curved geometries are investigated and analyzed in order to obtain surface error characterization of the machined surface. To understand the characteristics and varied aspects of surface errors of the machined components, the magnitudes and profile of surface errors along both the axial length and peripheral length of workpiece are studied. The comparison of computational and experimental results is covered in the next subsection.

### 4.6.1 Comparison of predicted and measured forces profiles in milling of straight geometries

Fig. 4.15 shows the variation of resultant cutting force with respect to angular position of cutter for all six types of cutting during milling of straight geometry. The estimated cutting forces are compared with the measured cutting force component. It is noticed that the estimated cutting force results are in good agreement with their measured counterpart. The proposed cutting force model is reliable and capable of predicting cutting forces accurately for any given machining condition for a prescribed tool-workpiece pair. The predicted cutting forces are used further as inputs to the tool deflection model for computing nodal deflection points of the machined surface.

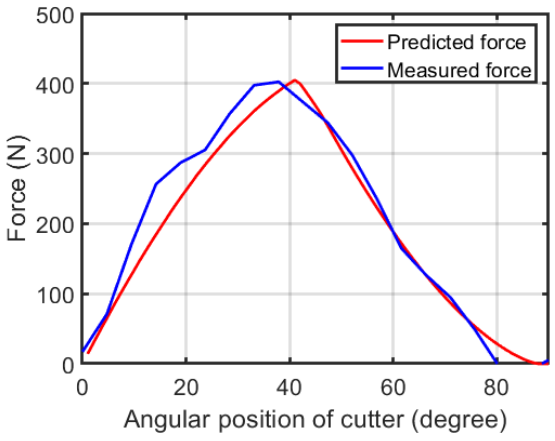


(a) Cutting Type I

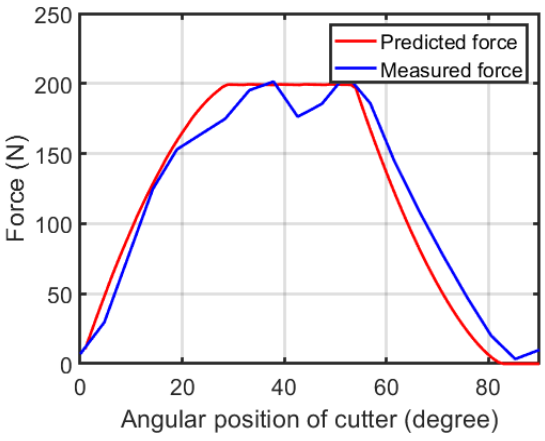


(b) Cutting Type II

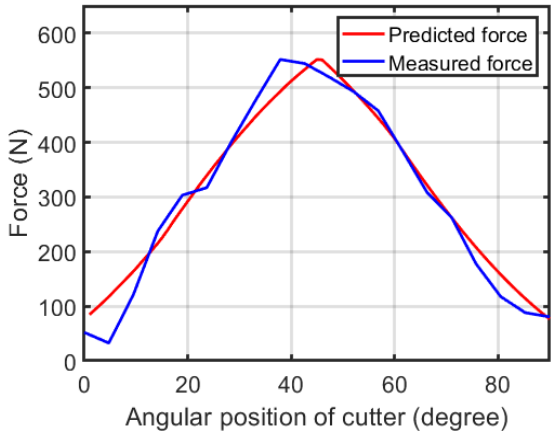


(c) Cutting Type III

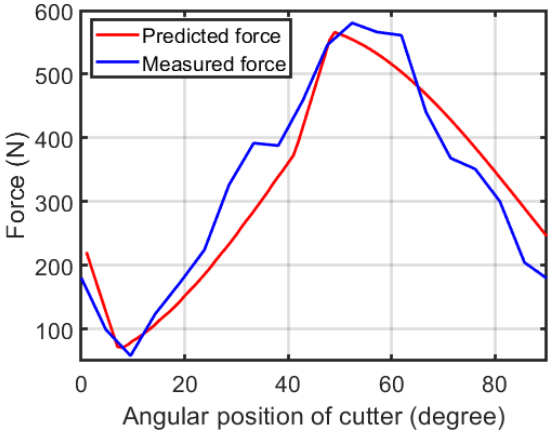


(d) Cutting Type IV

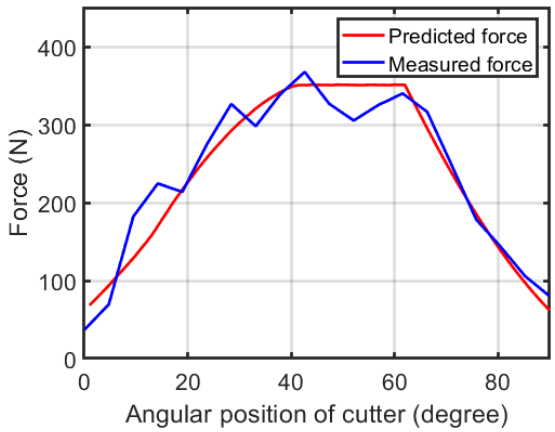


(e) Cutting Type V

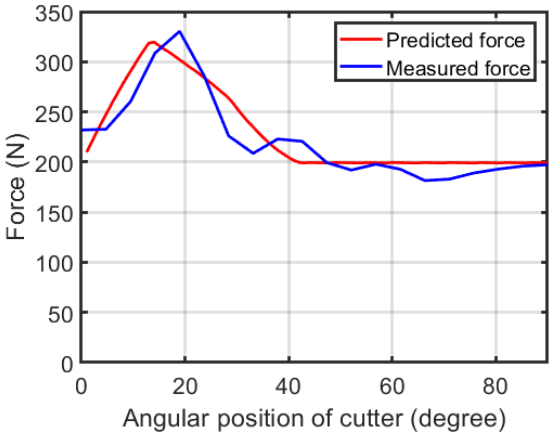


(f) Cutting Type VI

Fig. 4.15 Force profiles for various cutting types

### 4.6.2 Comparison of dimensional error profiles for various types of cutting in milling of thick-walled straight geometries

The dimensional error profiles obtained from the surface error generation model are presented and analyzed for all six types of cutting. Afterward, they are compared with the measured counterpart. Fig. 4.16 depicts the variation of surface errors along the axial length of cut for all six types of cutting at various positions of cutter along the axial length at a given feed station (at 50 mm from free end of the workpiece). To evaluate the effectiveness of the proposed tool deflection and surface error generation models, the results of surface errors obtained from computational studies are compared with their experimental results counterpart. The outcomes of the proposed models reveal that they are qualitatively and quantitatively in good agreement with their measured counterparts. Table 4.5 compares anticipated and measured results for the location of the various 'kinks' (key points) for

every surface error profile where the direction and slope of each error profile changes abruptly.

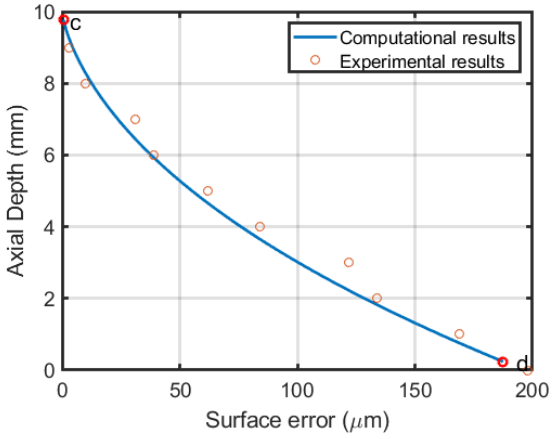


(a) Cutting Type I

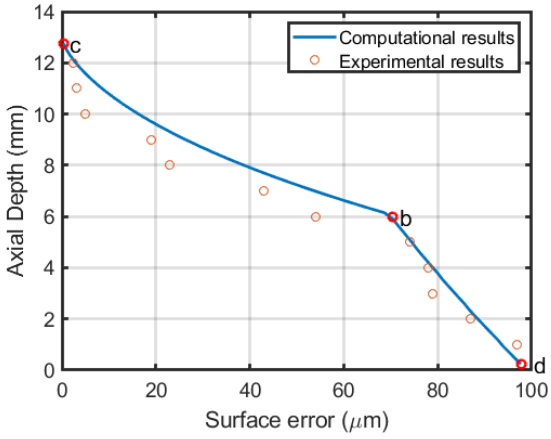


(b) Cutting Type II

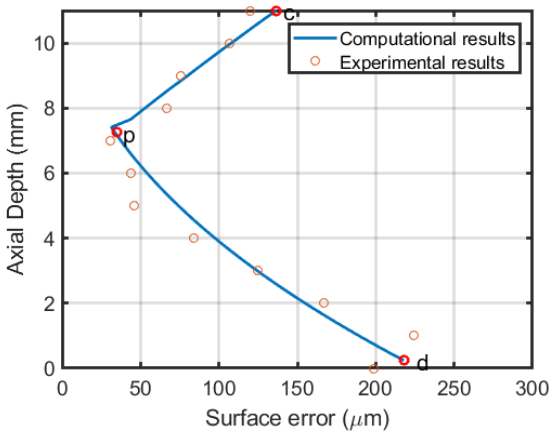


(c) Cutting Type III

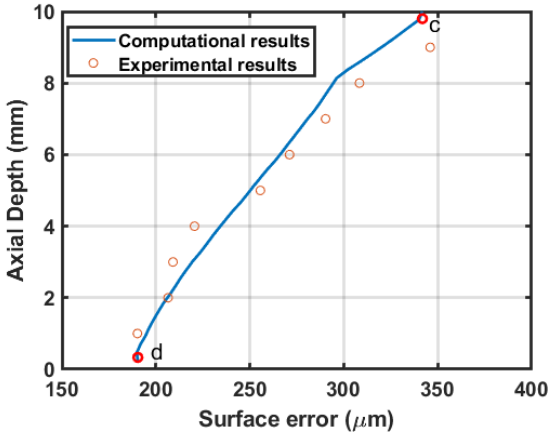


(d) Cutting Type IV

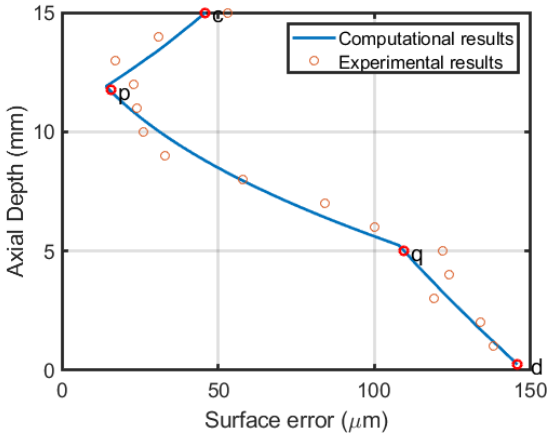


(e) Cutting Type V

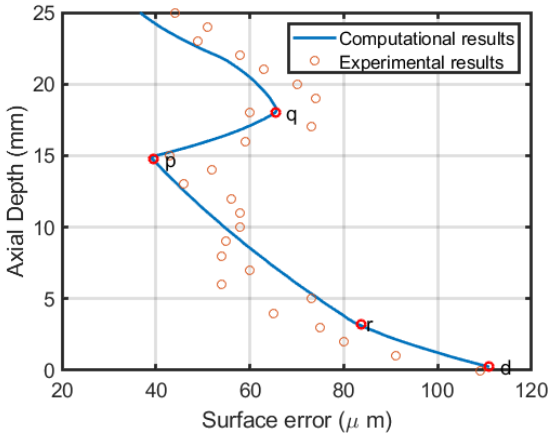


(f) Cutting Type VI

Fig. 4.16 Surface error profiles for various cutting types

Table 4.5 Determination of angular parameters along with kink positions

| Cutting types | Angular parameters ( $^0$) | | Kink position from bottom surface (mm) | | Value of surface error at kink position (µm) | |
|---|---|---|---|---|---|---|
| | Sweep angle | Engagement angle | Estimated | Measured | Estimated | Measured |
| Type I | 41.35 | 46.57 | - | - | - | - |
| Type II | 53.75 | 28.95 | $h_b$=5.97 | $h_b$=6 | 70.39 | 62.54 |
| Type III | 42.45 | 59.24 | $h_l$=7.41 | $h_l$=7 | 31.4 | 29.1 |
| Type IV | 39.54 | 89.38 | - | - | - | - |
| Type V | 62.02 | 41.41 | $h_l$=11.9 | $h_l$=12 | 15.89 | 18.74 |
| | | | $h_b$=4.98 | $h_b$=5 | 109.53 | 102.79 |
| Type VI | 103.37 | 28.95 | $h_l$=14.76 | $h_l$=15 | 39.54 | 43.12 |
| | | | $h_m$=17.99 | $h_m$=18 | 65.47 | 68.21 |
| | | | $h_n$=3.23 | $h_n$=3 | 83.66 | 79.36 |

Fig. 4.17 shows the variation of three-dimensional surface error profiles of the machined components for all six types of cutting. It can be observed that the estimated surface error profiles match well with its measured counterpart in terms of nature and magnitudes. It is also observed that the surface error profiles from the beginning to end of cut along the tool path remains almost constant.

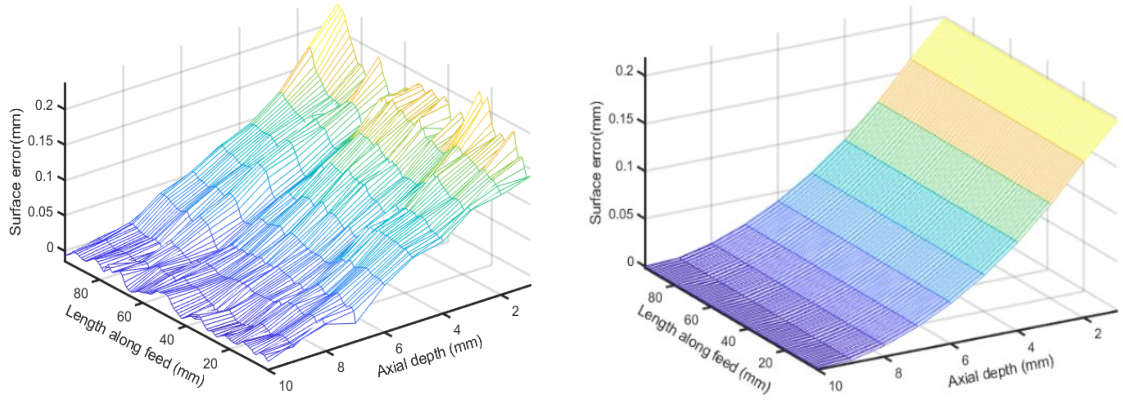


Experimental results Computational results

Cutting Type I

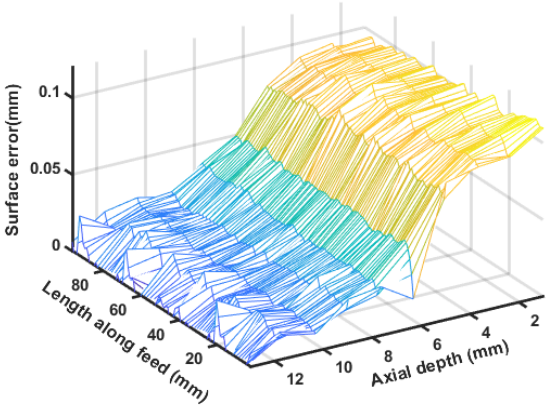


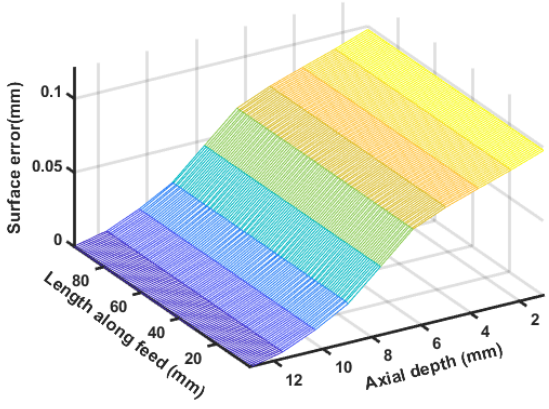


Experimental results Computational results

Cutting Type II

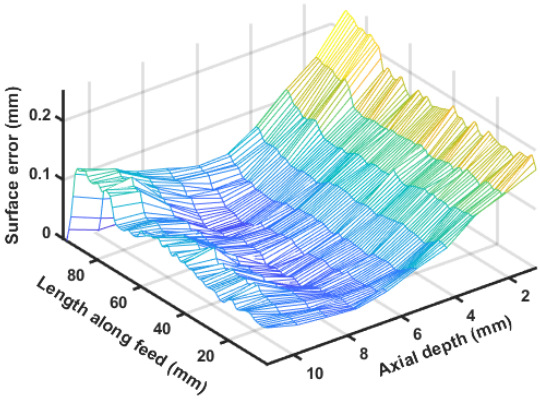


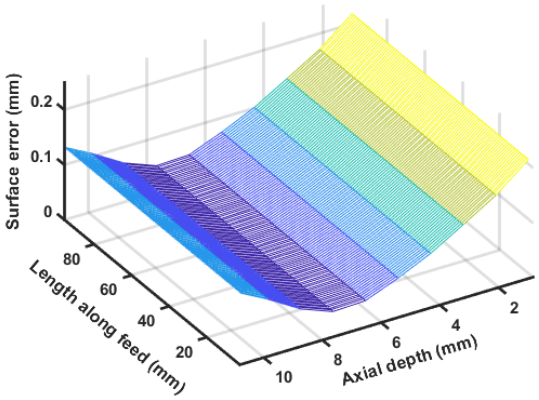


Experimental results Computational results

Cutting Type III

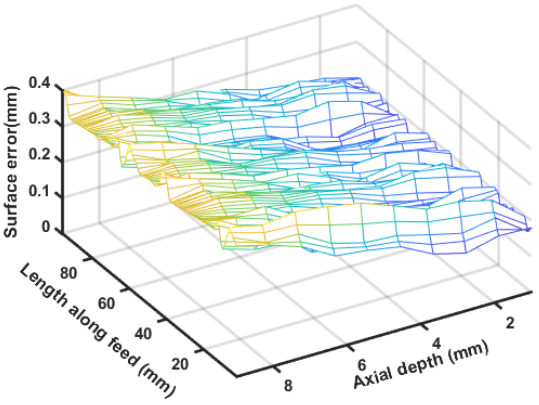


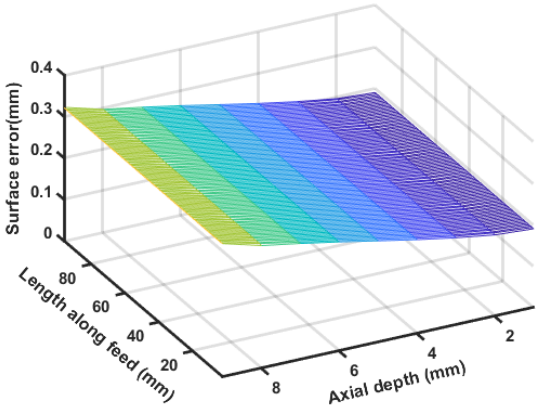


Experimental results Computational results

Cutting Type IV

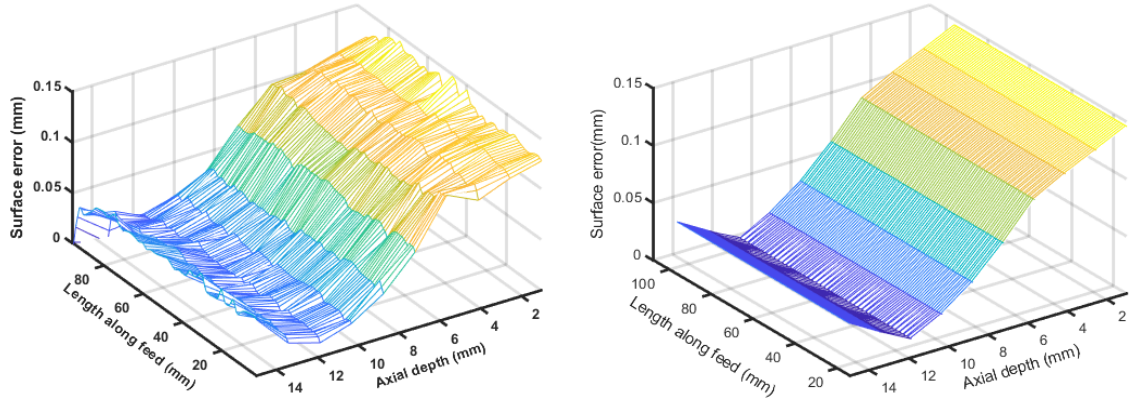


Experimental results Computational results

Cutting Type V

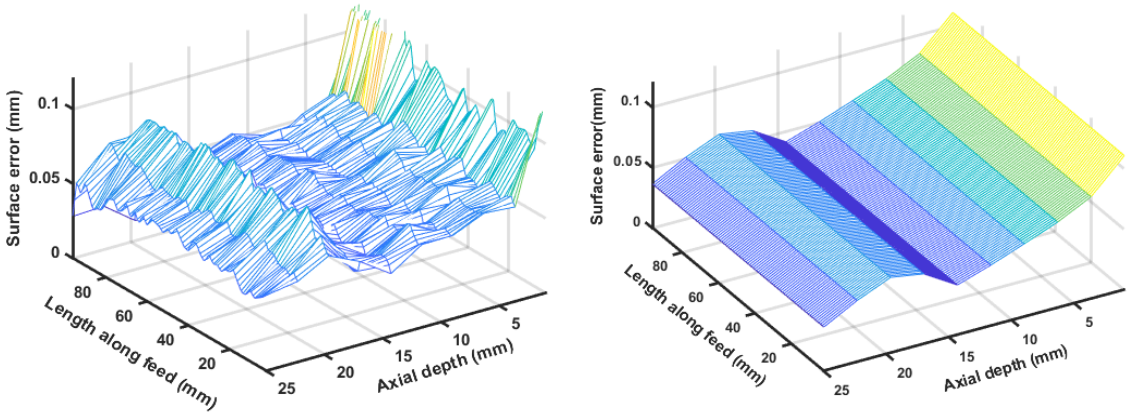


Experimental results Computational results

Cutting Type VI

Fig. 4.17 Variation of surface errors on machined component

### 4.6.3 Comparison of geometric error for various types of cutting in milling of thick-walled straight geometries

As the workpiece for peripheral milling is a straight geometry, flatness error for the machined surface is considered as a part of geometric error of the component. Based on the nodal tool deflection points obtained from the proposed models, flatness error is computed for each surface of each type of cutting. Afterward, the estimated flatness error is compared with its measured counterpart. Fig. 4.18 shows the three-dimensional representation of the evaluation of predicted and measured flatness error for all six types of cutting. It is observed from the Fig. 4.18 that predicted results are in good agreement with their measured counterpart. The magnitudes of flatness errors for all these six types of cutting are provided

in Table 4.6. The results clearly show that, in the most of types, the flatness values calculated using the computational approach correspond well with experimentally obtained values.

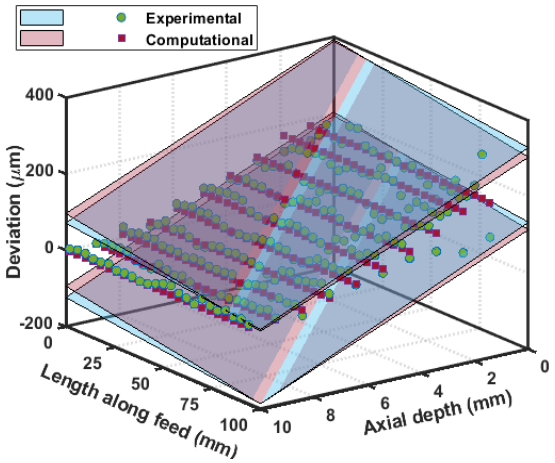


(a) Cutting Type I

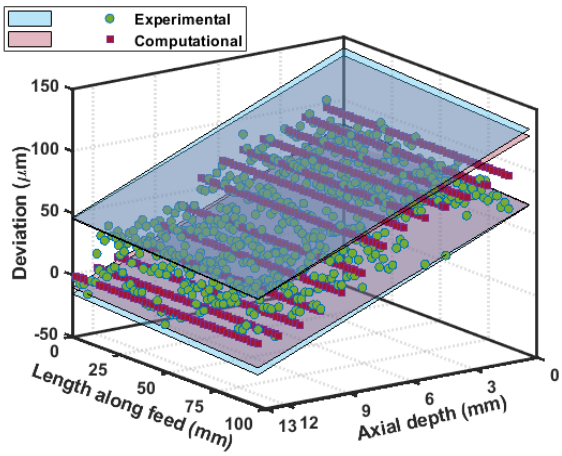


(b) Cutting Type II

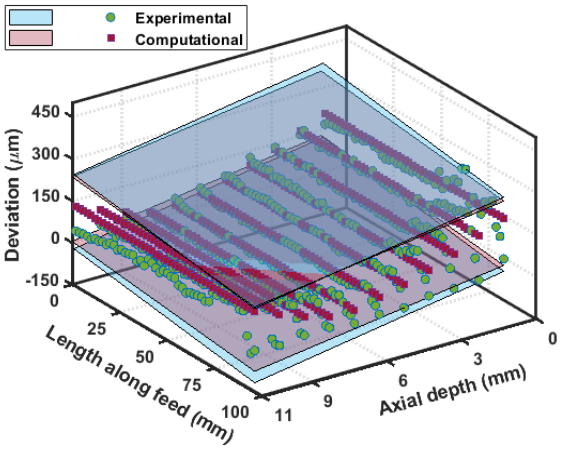


(c) Cutting Type III

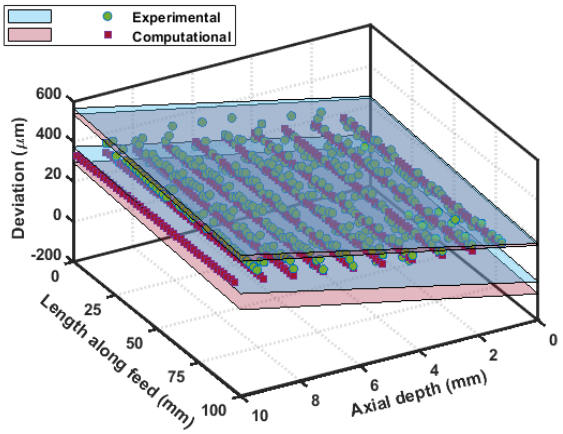


(d) Cutting Type IV

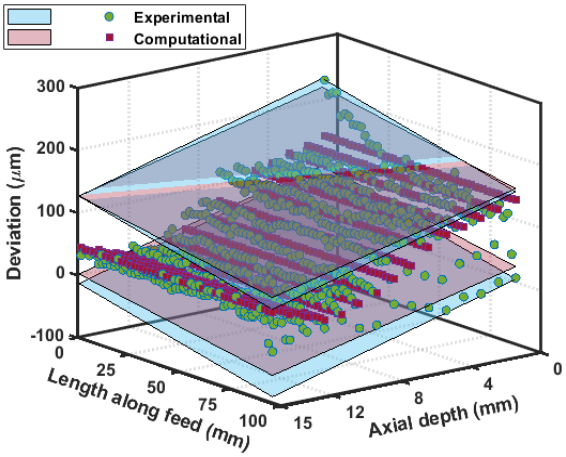


(e) Cutting Type V

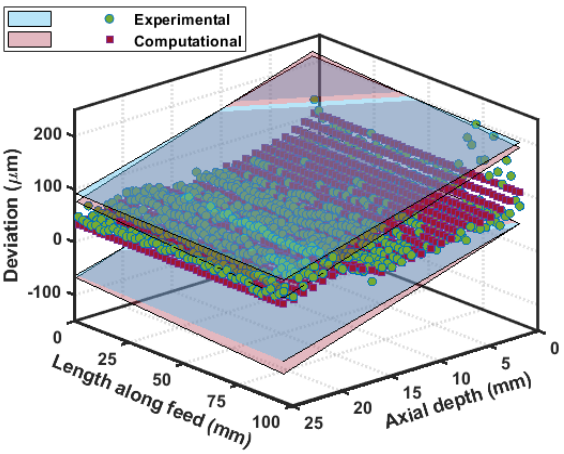


(f) Cutting Type VI

Fig. 4.18 Evaluation of experimental and computational flatness error

Table 4.6 Flatness values for various cutting types.

| Cutting types | Experimental results ($\mu m$) | Computational results ($\mu m$) |
|---|---|---|
| Type I | 215 | 190 |
| Type II | 61 | 57 |
| Type III | 255 | 225 |
| Type IV | 181 | 209 |
| Type V | 137 | 126 |
| Type VI | 141 | 137 |

### 4.6.4 Comparison of predicted and measured surface error variation in milling of thick-walled curved geometries

Here, an elliptic arc is selected as a representative geometry to examine how workpiece curvature affects surface error profile. The parametric form of the elliptical geometry is expressed as:

$$X(t) = a.\sin(u)$$

$$Y(t) = b.\cos(u)$$

where $a$ and $b$ are the radius on the $X$ and $Y$ axes respectively and $u$ is curve parameter which ranges from 0 to 1 for elliptical geometry. The values of $a$ and $b$ are taken as 75 mm and 30 mm respectively during design of workpiece geometry. Fig. 4.19 shows the details of elliptical workpiece geometry along with curvature variation from start to end of the profile. It can be seen that value of workpiece curvature gradually increases along peripheral length in machining of elliptical geometry that is used here.

Two sets of machining experiments are conducted, one set for the convex side and the other set for the concave side, to observe the effect of workpiece curvature on surface error. When a geometry is concave, the tool center and the center of curvature of the workpiece geometry are on the same side of the geometry, whereas, when a geometry is convex, the tool center and center of curvature of the workpiece geometry are on different sides. Variation of engagement angle along peripheral length during machining of concave and convex geometries are shown in Fig.4.20. Results clearly show that engagement angle is not maintained constant along tool path like in case of straight and circular geometry but

there is substantial amount of variation in engagement angle. In case of concave geometry, engagement angle increases with workpiece curvature and decreases with workpiece curvature in case of convex geometry. For given cutting conditions, the value of engagement angle is $45^0$ at the beginning of the cut, rising to $72^0$ at the end, while the value of sweeping angle remains constant at $35^0$ during machining of concave geometry. The engagement angle is $45^0$ at start of cut and decreases to $36^0$ at the end of cut, while the value of sweeping angle remains constant at $50^0$ during machining of convex geometry.

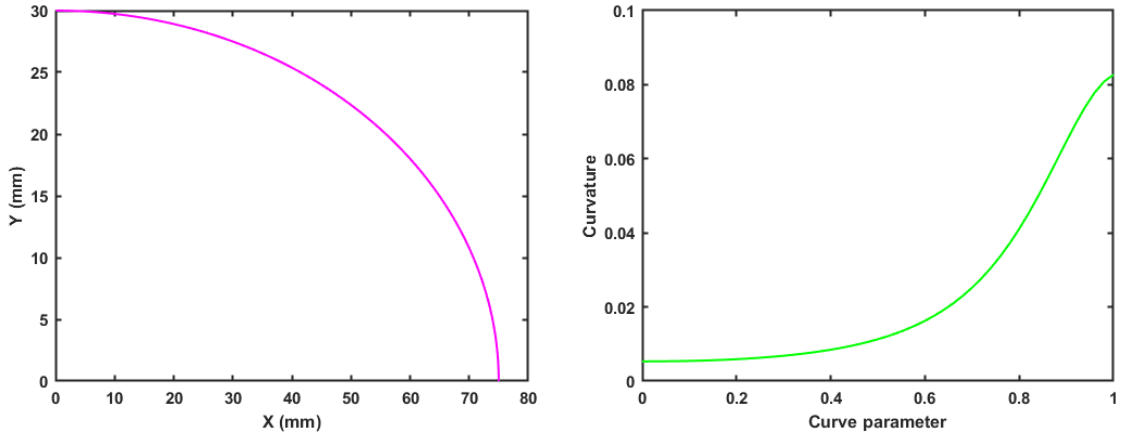


(a) Elliptical geometry in XY plane (b) Curvature variations for ellipse

Fig. 4.19 The details of elliptical workpiece geometry.

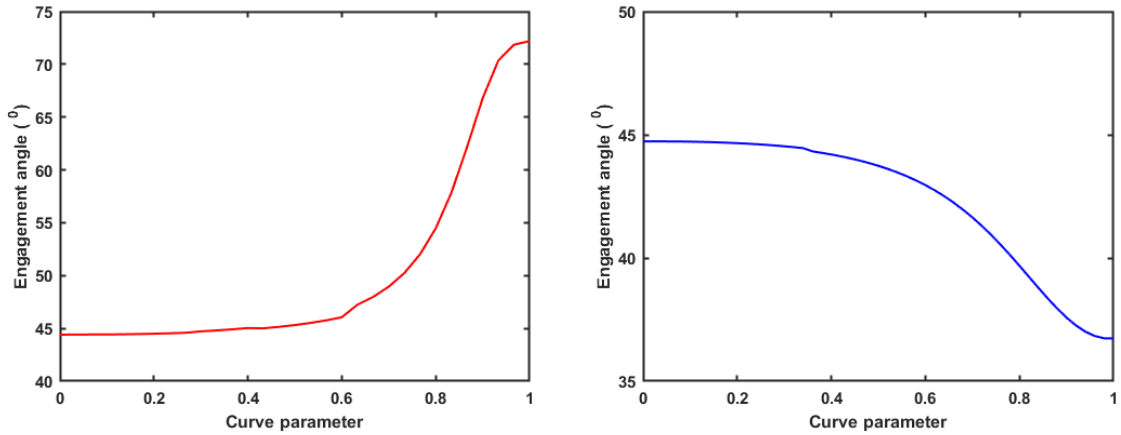


(a) Concave geometry (b) Convex geometry

Fig. 4.20 Variation of engagement angle for curved geometry

Variation of surface error along tool path using computational studies and experimental studies during machining of concave geometries are shown in Fig.4.21. It can be observed that estimated variation in surface error matches with their experimental counterpart well in terms of both form and magnitude. Results further demonstrate that variation of surface error along axial length does not remain constant along tool path but it

varies with workpiece curvature. Fig. 4.22(a) shows that surface error profile at the start of the cut is similar to Type I cutting since value of surface error is practically negligible at the top and highest at the bottom. For a certain length of tool path, the surface error profile remains constant but after some time, it changes. The surface error profile changes significantly with further increase in the workpiece curvature and the location of the minimum surface error begins to move from the top to bottom. From this point on, the surface error profile no longer maintains its original shape and changes into a new shape with a "kink" in the profile. The difference in the engagement pattern of the cutting flutes in the presence of workpiece curvature is the primary cause of this shift in the surface error profile throughout the tool path. Because the flutes are overlapping, the surface error profile is similar to Type III cutting in the high curvature zone. Fig. 4.22(b) shows surface error profile at end of cut in milling of concave elliptical geometries.

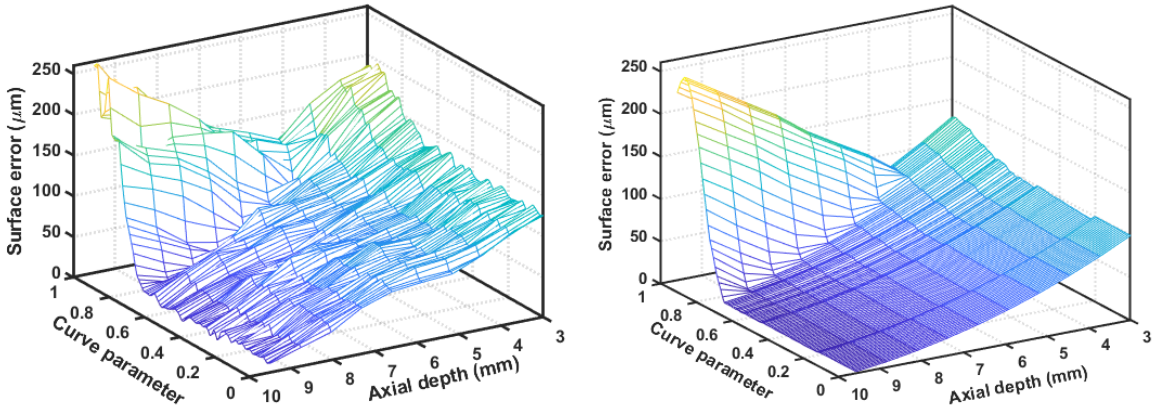


(a) Experimental results (b) Computational results

Fig. 4.21 Surface error variation in milling of concave elliptical thick-walled geometries

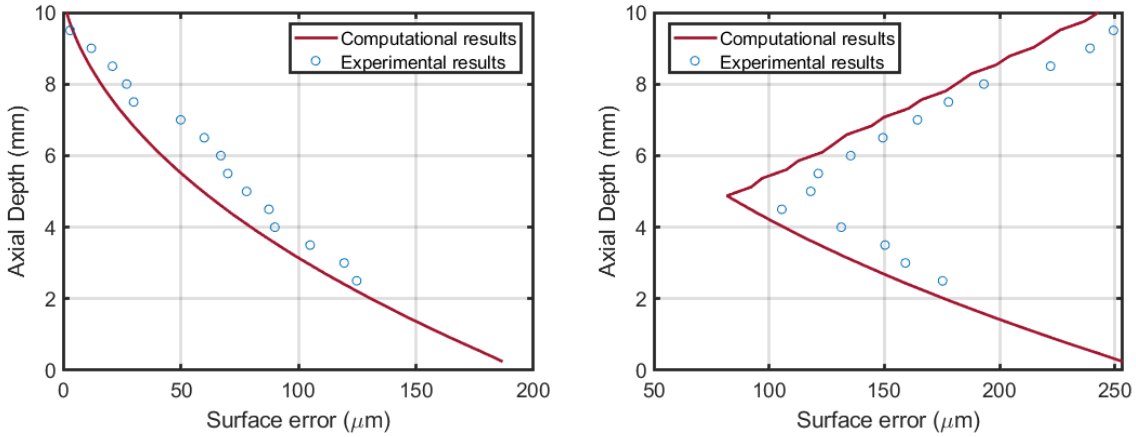


(a) Surface error profile at start of cut (b) Surface error profile at end of cut

Fig. 4.22 Surface error profiles at start and end of cut in milling of concave elliptical thick-walled geometries

Fig. 4.23 shows variation in surface error along tool path during machining of convex geometries. Again, because of the presence of workpiece curvature and a change in engagement angle, the variation in the surface error along axial length does not remain constant along the tool path. At the start of the cut, the surface error profile has a "kink" at the top of the workpiece surface similar to Type V cutting. As the engagement angle decreases, kink in surface error profile goes away. At the end which is high curvature zone, surface error profile generated on machined surface is similar to Type II cutting. Surface error profiles at start and end of cut in milling of convex elliptical geometries is shown in Fig. 4.24.

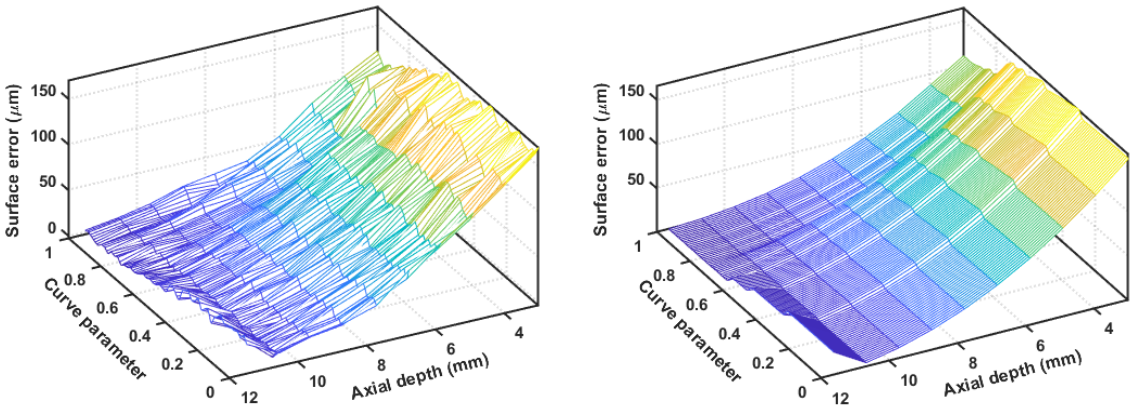


(c) Experimental results (d) Computational results

Fig. 4.23 Surface error variation in milling of convex elliptical thick-walled geometries

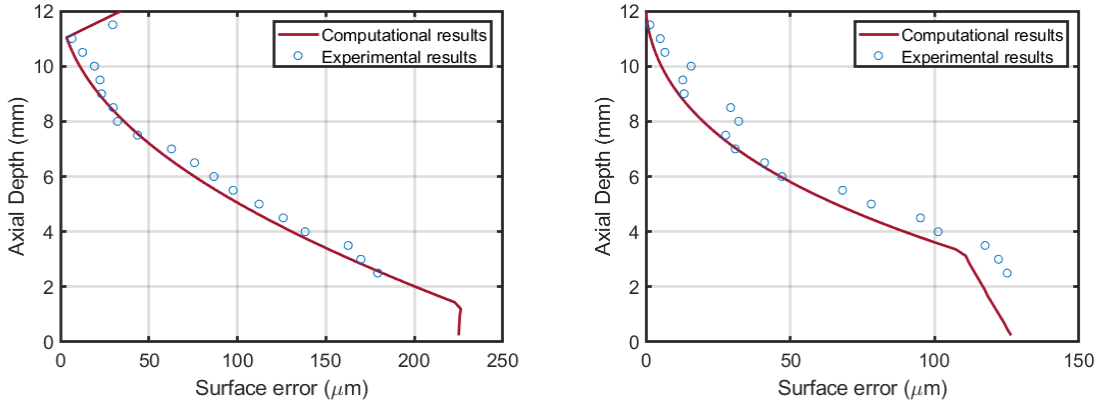


(a) Surface error profile at start of cut (b) Surface error profile at end of cut

Fig. 4.24 Surface error profiles at start and end of cut in milling of convex elliptical thick-walled geometries

### 4.6.5 Comparison of dimensional error profiles for various types of cutting in milling of thin-walled straight geometries

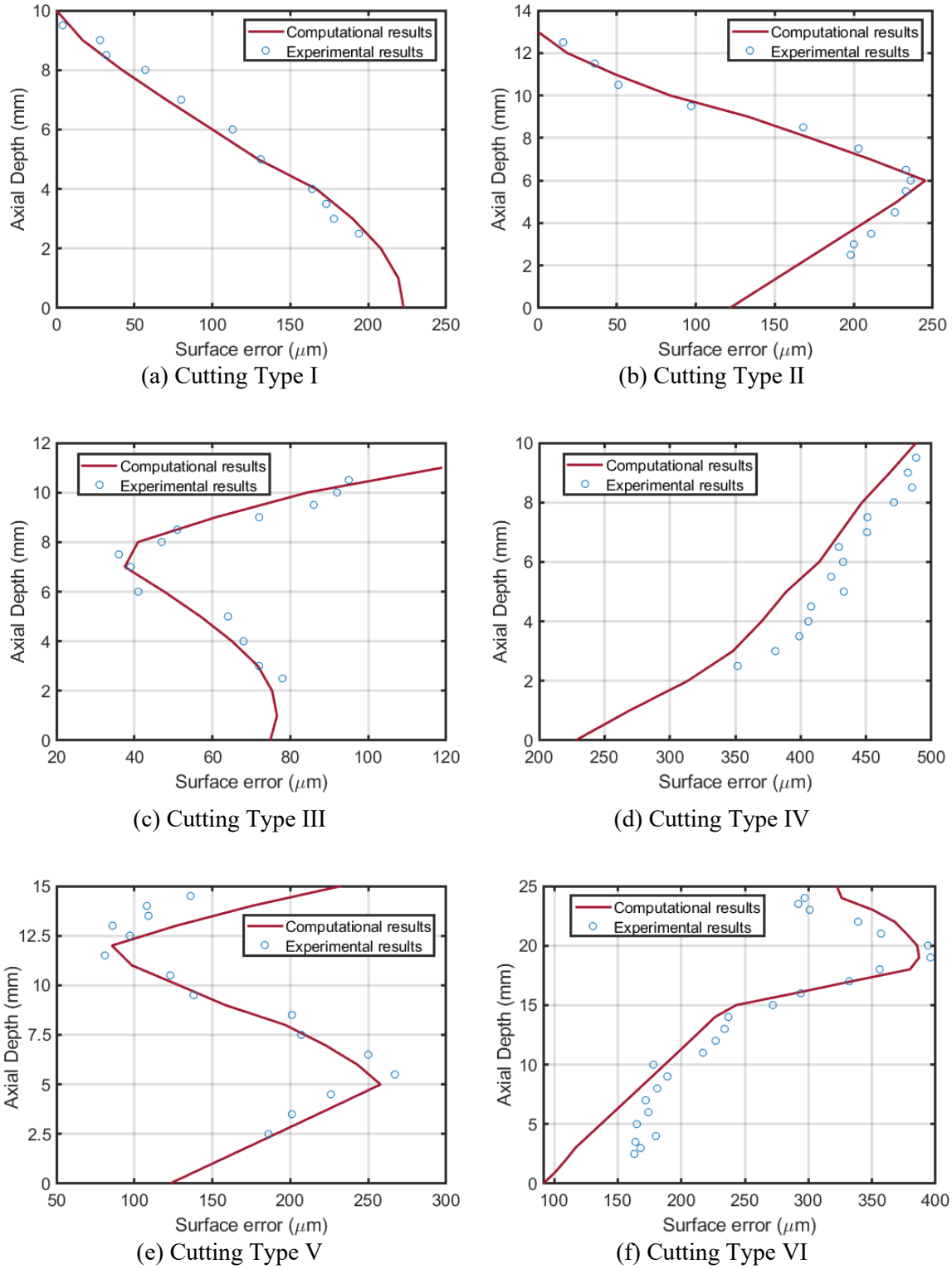


(a) Cutting Type I (b) Cutting Type II

(c) Cutting Type III (d) Cutting Type IV

(e) Cutting Type V (f) Cutting Type VI

Fig. 4.25 Surface error profiles for various cutting types

Fig. 4.25 depicts the variation of surface errors for all 6 types at various positions along the axial length at a given feed station (at 50 mm from free end). To evaluate the

effectiveness of the suggested classification scheme, surface errors obtained from computational and experimental results are compared. The outcome reveals that they are qualitatively and quantitatively in reasonable agreement with their measured counterparts, and the proposed characterization scheme is quite effective in classifying surface error types. Table 4.7 compares anticipated and measured findings for the location of the 'kink' or the point at which the slope of the surface error profile abruptly changes. It is shown that estimated height positions of all kink points are in good agreement with measured results in all experiments.

Table 4.7 Determination of angular parameters along with kink positions

| **Cutting types** | **Angular parameters ( $^0$)** | | **Kink position from bottom surface (mm)** | | | **Value of surface error at kink position (µm)** | |
|---|---|---|---|---|---|---|---|
| | **Sweep angle** | **Engagement angle** | **Computed** | **Estimated** | **Measured** | **Estimated** | **Measured** |
| Type I | 41.35 | 46.57 | - | - | - | - | - |
| Type II | 53.75 | 28.95 | $h_b$=5.97 | $h_b$=6 | $h_b$=6 | 171.2 | 158 |
| Type III | 42.45 | 59.24 | $h_l$=7.41 | $h_l$=7 | $h_l$=7.5 | 132.5 | 145 |
| Type IV | 39.54 | 89.38 | - | - | - | - | - |
| Type V | 62.02 | 41.41 | $h_l$=11.9 | $h_l$=12 | $h_l$=11.5 | 228.1 | 213 |
| | | | $h_b$=4.98 | $h_b$=5 | $h_b$=5.5 | 110.1 | 115 |
| Type VI | 103.37 | 28.95 | $h_l$=14.76 | $h_l$=15 | $h_l$=14.5 | 391.5 | 380 |
| | | | $h_m$=17.99 | $h_m$=18.5 | $h_m$=19 | 231.2 | 240 |
| | | | $h_n$=3.23 | $h_n$=3 | $h_n$=3 | 121.5 | 160 |

Fig. 4.26 shows variation of surface error over whole machined surface estimated using computational studies and machining experiments for all 6 types. It can be observed that the estimated variation in surface error matches its measured counterpart well in terms of both form and magnitude. The outcomes further demonstrate that the surface error exhibits axial variation in addition to a significant difference in the peripheral direction in the machining situations outlined above. This is because there is thinning effect in the workpiece deflection case because the workpiece rigidity reduces as the cut progresses. It is also observed that surface error is higher at free ends and lower at mid-section due to end effect.

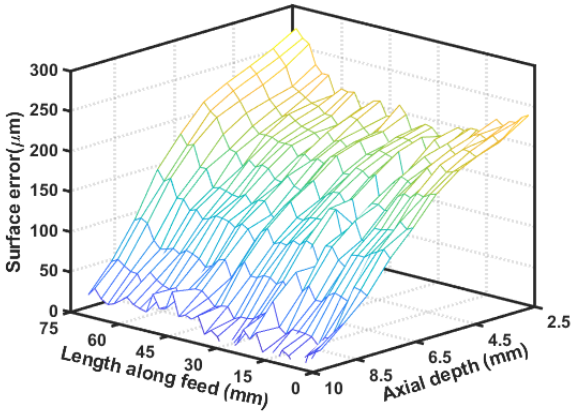


(a) Experimental results

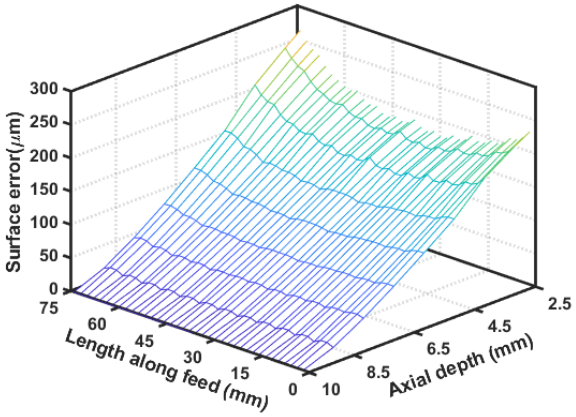


(b) Computational results

Type I cutting

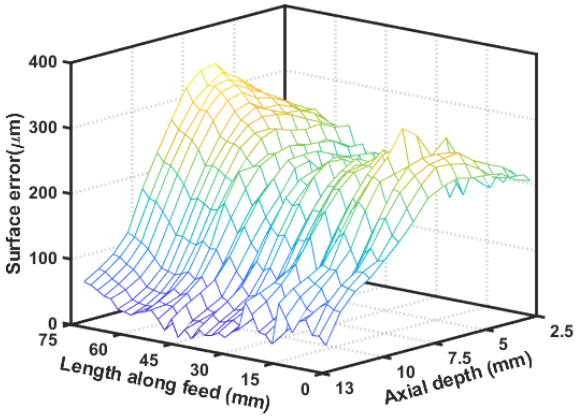


(a) Experimental results

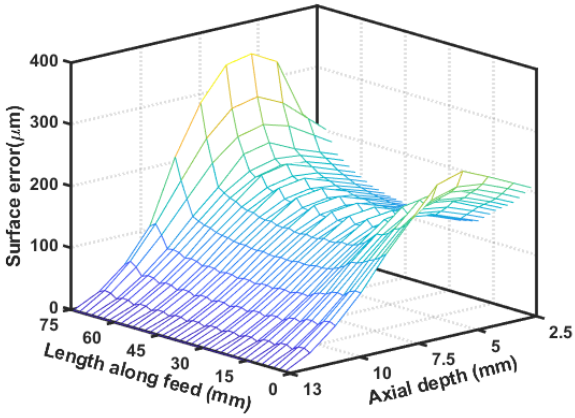


(b) Computational results

Type II cutting

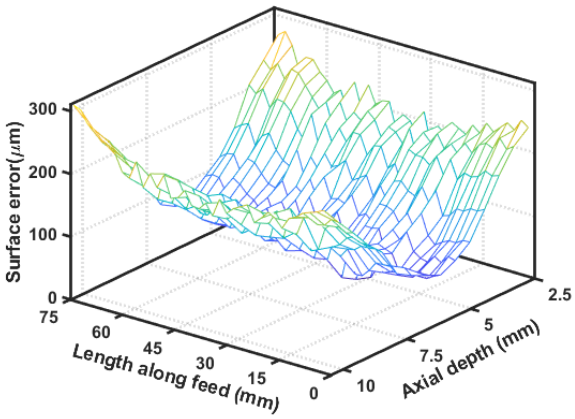


(a) Experimental results

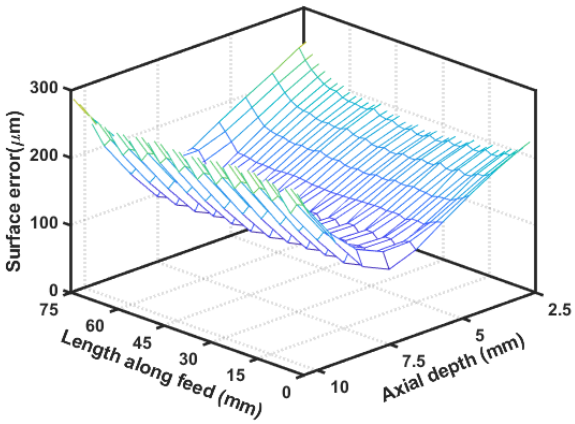


(b) Computational results

Type III cutting

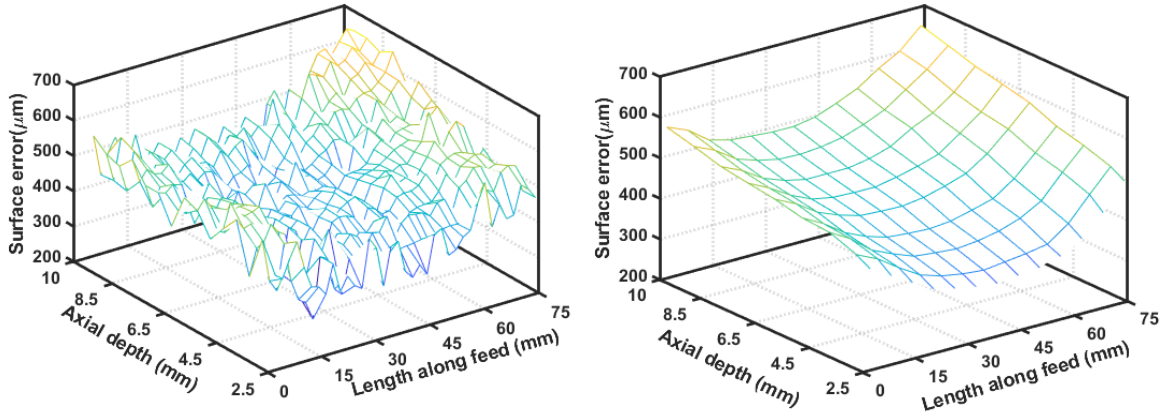


(a) Experimental results (b) Computational results

Type IV cutting

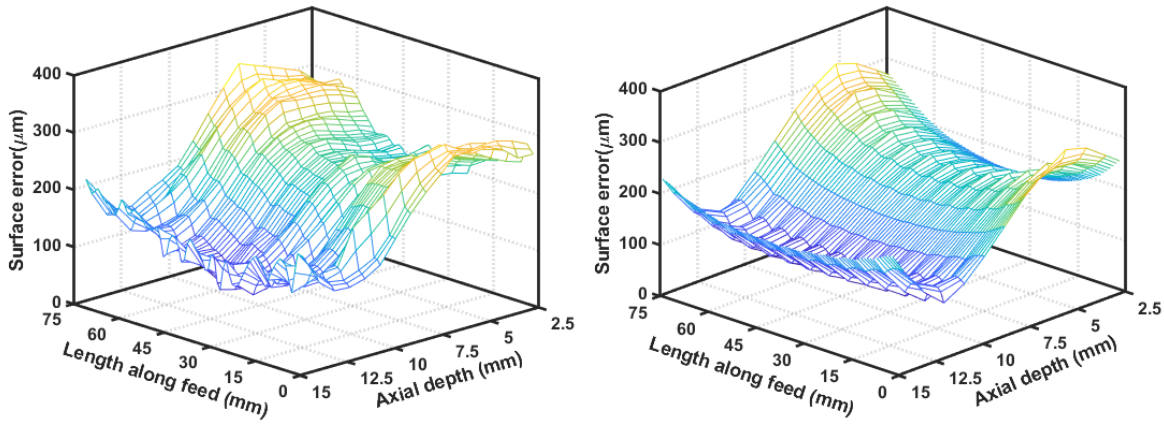


(a) Experimental results (b) Computational results

Type V cutting

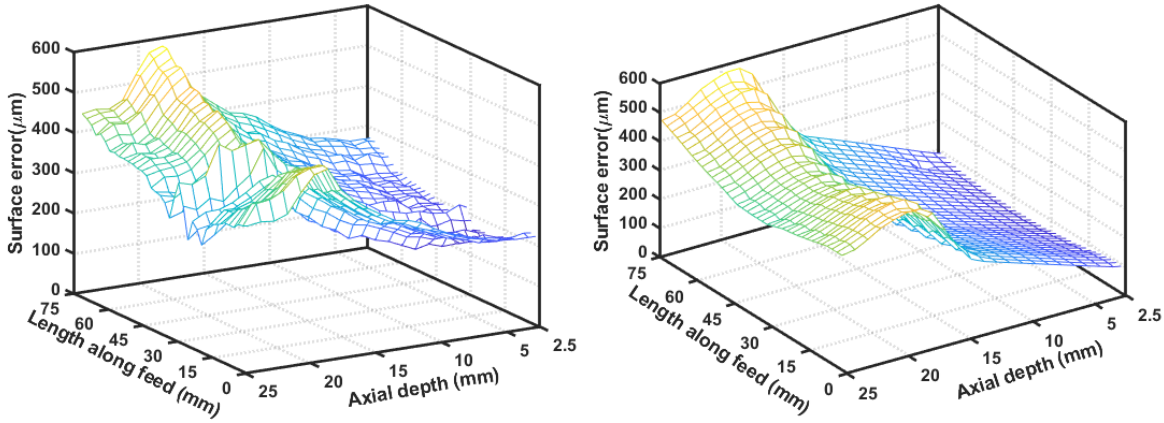


(a) Experimental results (b) Computational results

Type VI cutting

Fig. 4.26 Variation of surface error on machined component

### 4.6.6 Comparison of geometric error for various types of cutting in milling of thin-walled straight geometries

A comparison of the computationally obtained flatness error with the experimental results for all 6 cutting types is shown in Fig. 4.27. It is clear from results that flatness error predicted from model are in geed agreement with the values obtained through experimental measurement. The comparison of flatness error obtained using a computational model and machining experiments for all 6 types is summarized in Table 4.8. The results clearly show that, in the most of types, the flatness values calculated using the computational approach correspond well with experimentally obtained values.

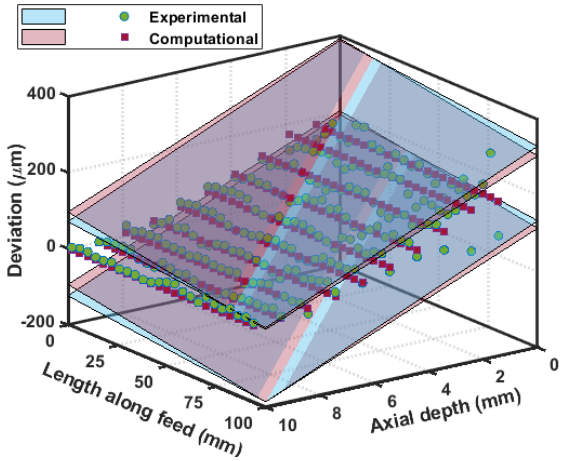


(a) Cutting Type I

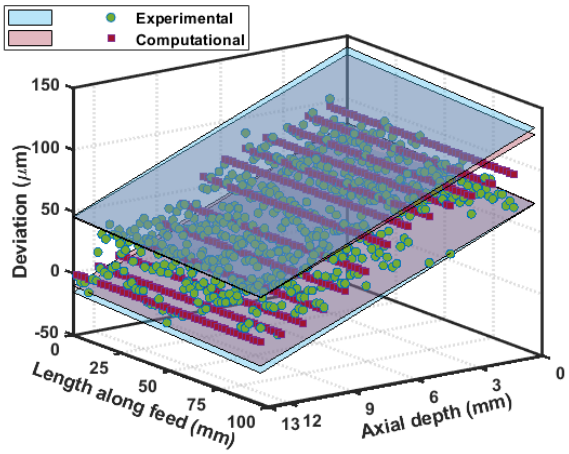


(b) Cutting Type II

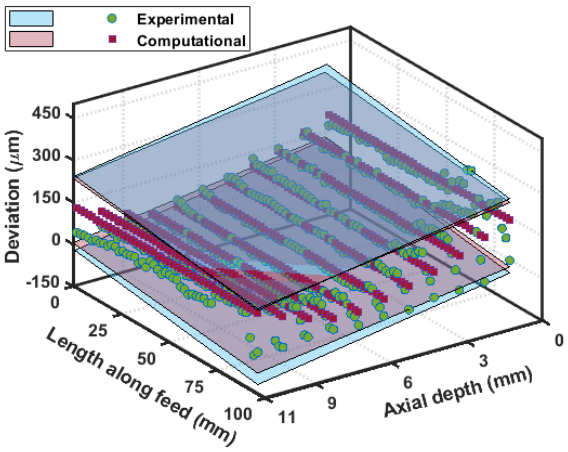


Cutting Type III

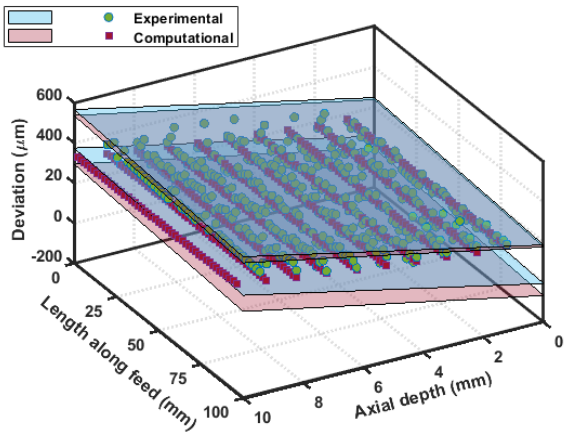


Cutting Type IV

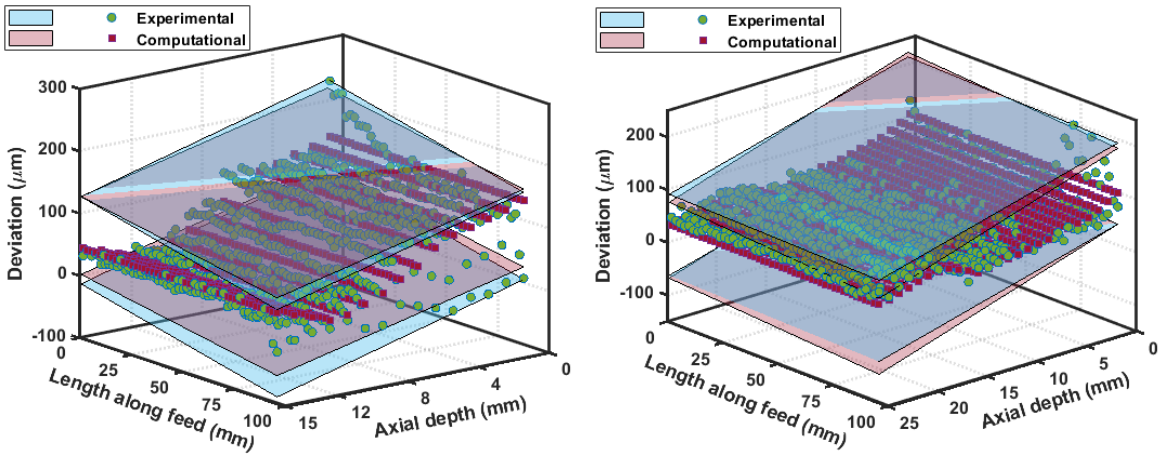


Cutting Type V Cutting Type VI

Fig. 4.27 Evaluation of experimental and computational flatness error

Table 4.8 Flatness values for various cutting types.

| Cutting types | Experimental results ($\mu m$) | Computational results ($\mu m$) |
|---|---|---|
| Type I | 345 | 367 |
| Type II | 261 | 237 |
| Type III | 255 | 225 |
| Type IV | 284 | 260 |
| Type V | 342 | 326 |
| Type VI | 451 | 434 |

### 4.6.7 Comparison of Predicted and Measured Surface error variation in milling of thin-walled curved geometries

Variation of surface error along tool path using computational studies and experimental studies during machining of thin-walled concave geometries are shown in Fig. 4.28. It can be observed that estimated variation in surface error matches with their experimental counterpart well in terms of both form and magnitude. Results further demonstrate that variation of surface error along axial length does not remain constant along tool path but it varies with workpiece curvature similar to thick-walled curved geometry. But in this case, effect of thinning, free ends, variation in effective moment of inertia come into picture. Due to this, variation in magnitude of surface error is different unlike thick-walled curved geometry. At the start of the cut, surface error profile similar to Type I cutting is observed since value of surface error is practically negligible at the top and highest at the

bottom. The surface error profile is similar to Type III cutting in the high curvature zone at the end of cut. At start of cut, effective moment of inertia and cutting force is minimum due to low workpiece curvature. At end of cut, effective moment of inertia and cutting force is maximum due to low workpiece curvature. Combined effect of these, at free ends, magnitude of surface error value at bottom is maximum and almost same unlike thin-walled straight geometry.

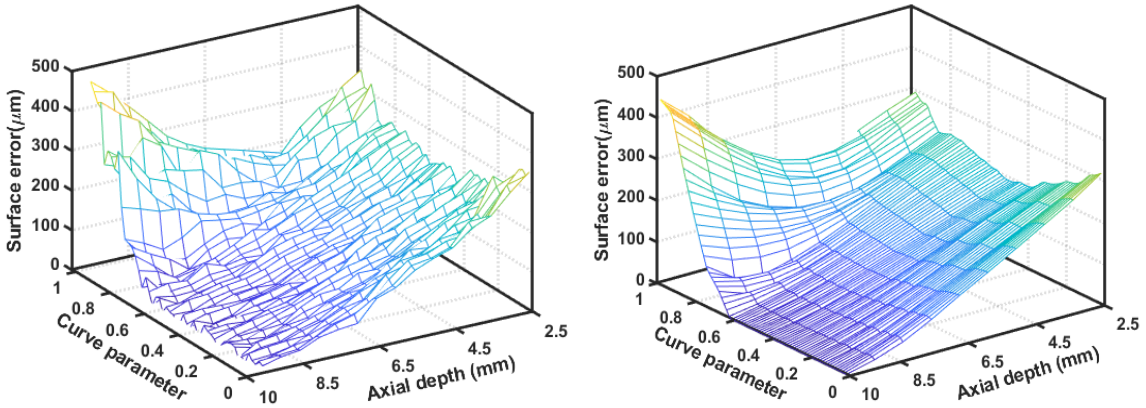


Experimental surface error Computational surface error

Fig. 4.28 Surface error variation in milling of concave elliptical thin-walled geometries

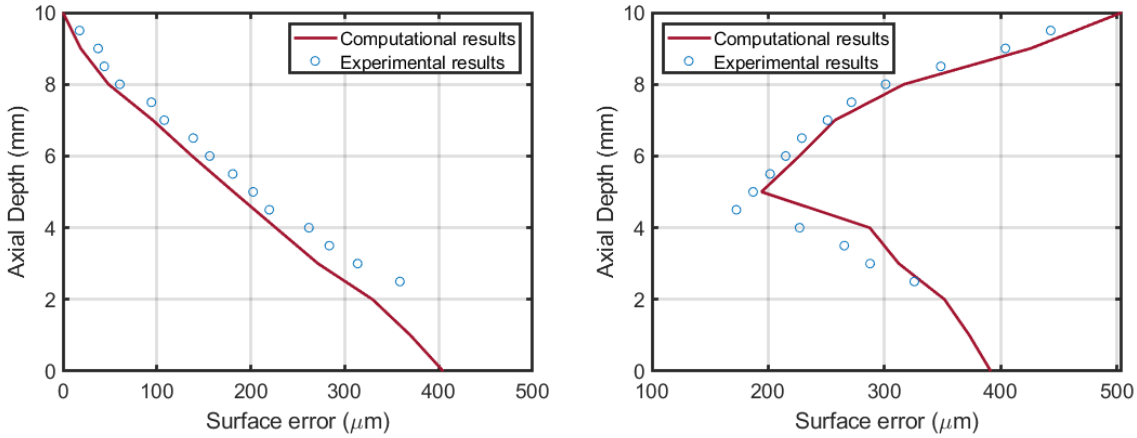


(c) Surface error profile at start of cut (d) Surface error profile at end of cut

Fig. 4.29 Surface error profiles at start and end of cut in milling of concave elliptical thin-walled geometries

Fig. 4.30 shows variation in surface error along tool path during machining of thin-walled convex geometries. Again, because of the presence of workpiece curvature and a change in engagement angle, the variation in the surface error along axial length does not

remain constant along the tool path. At the start of the cut, the surface error profile has a "kink" at the top of the workpiece surface similar to Type V cutting. As the engagement angle decreases, kink in surface error profile goes away. At the end which is high curvature zone, surface error profile generated on machined surface is similar to Type II cutting. At start of cut, effective moment of inertia is minimum and cutting force is maximum due to low workpiece curvature. At end of cut, effective moment of inertia is maximum and cutting force is minimum due to low workpiece curvature. Combined effect of these, maximum value of surface error at bottom is observed at start of cut compared to end of cut unlike thin-walled straight geometry.

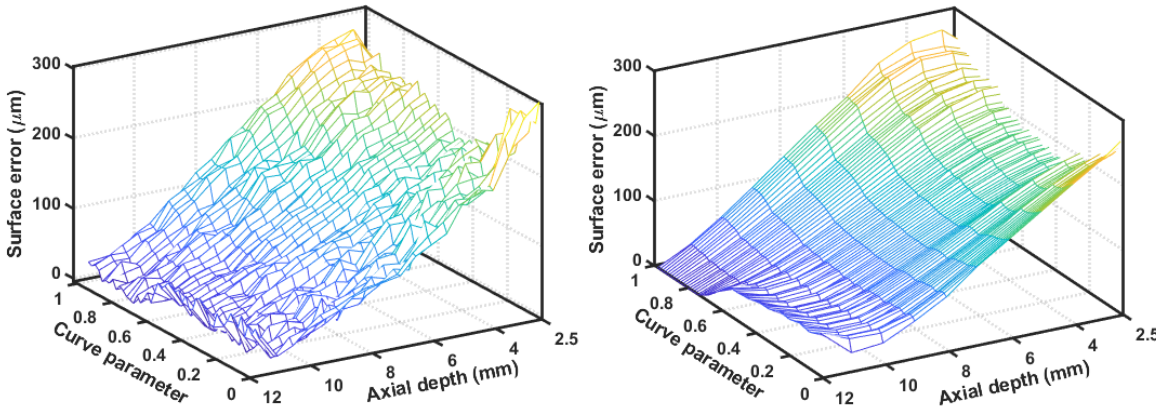


Experimental surface error Computational surface error

Fig. 4.30 Surface error variation in milling of convex elliptical thin-walled geometries

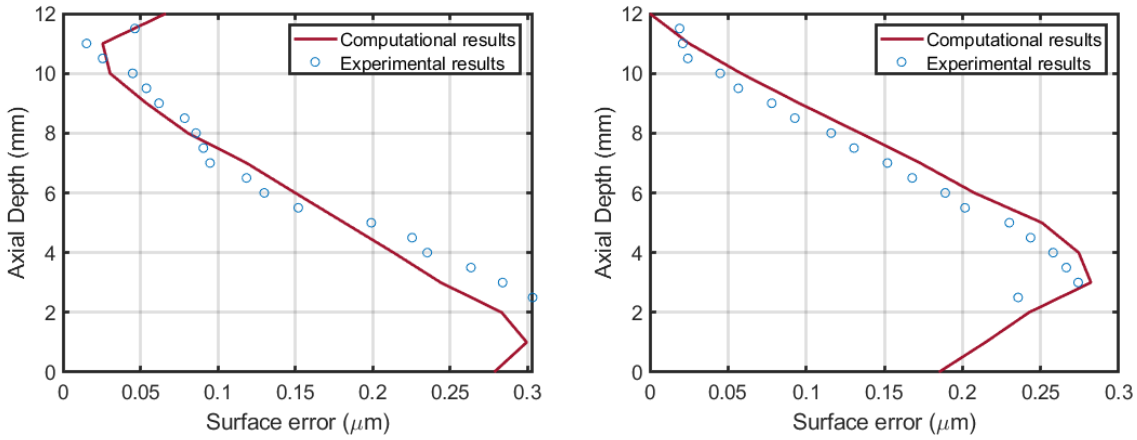


Surface error profile at start of cut Surface error profile at end of cut

Fig. 4.31 Surface error profiles at start and end of cut in milling of convex elliptical thin-walled geometries

## 4.7 Concluding Remarks

In this chapter, a methodology is presented for characterizing axial surface error profiles and correlating them to cutting conditions (ADOC and RDOC). By recognizing cutting patterns in engagement and correlating them to cutting conditions, the scheme divides surface error profiles into six separate categories. In machining of curved geometries, the axial variation of surface error is more challenging due to the constantly changing workpiece curvature along the tool path. Through the correlation of changes in workpiece curvature with cutting engagements, axial variation of surface error in the machining of curved geometries also examined.

# Chapter 5

# Energy Consumption in Milling

## 5.1 Introduction

The accurate estimation of energy consumption and development of energy efficient machining is the focus of industries for reduction of energy consumption and making the manufacturing system more sustainable. The continuous fluctuation in force profile during machining of variable curved components creates a barrier in stable machining and cutting power consumption. The fluctuation in force profile happens due to alteration in chip load in the presence of workpiece curvature. In this chapter, an energy consumption model of milling of variable curved geometries is developed in MATLAB. The proposed model considers process mechanics, cutting forces and energy consumption and have modules for idle, auxiliary and cutting power. Later on, an energy efficient machining strategy for milling of variable curved components is established where more uniform cutting force and power profiles are accomplished due to constant chip load along the peripheral length of curved geometry. The effectiveness of these proposed models is then assessed through machining experiments by comparing estimated outcomes with their measured counterparts.

## 5.2 Energy Consumption Model

In this section, a hybrid model consisting of analytical and empirical approaches is proposed for developing the energy consumption model in milling of variable curved surfaces for exploiting their relative advantages. In order to illustrate the detailed course of actions during the design and development of the power consumption model, a flowchart is given in Fig. 5.1.

Before carrying out any machining operation, the machine tool must be ready for performing metal cutting operations. In order to calculate various components of power consumption, various motion states of a machine tool need to be taken into account. Based on the machine tool motion state, the entire machining operation can be classified into three operational states of standby, idle, and cutting. The power profile for a typical milling process is shown in Fig. 5.2 consisting of cutting and non-cutting operations for a constant

spindle RPM and given cutting conditions. During machining, the total energy consumption of the machine is broadly categorized into the idle power ($P_{idle}$), the cutting power ($P_{cutting}$), and the auxiliary power ($P_{auxiliary}$), which are given below:

$$P_{total} = P_{idle} + P_{cutting} + P_{auxiliary} \tag{5.1}$$

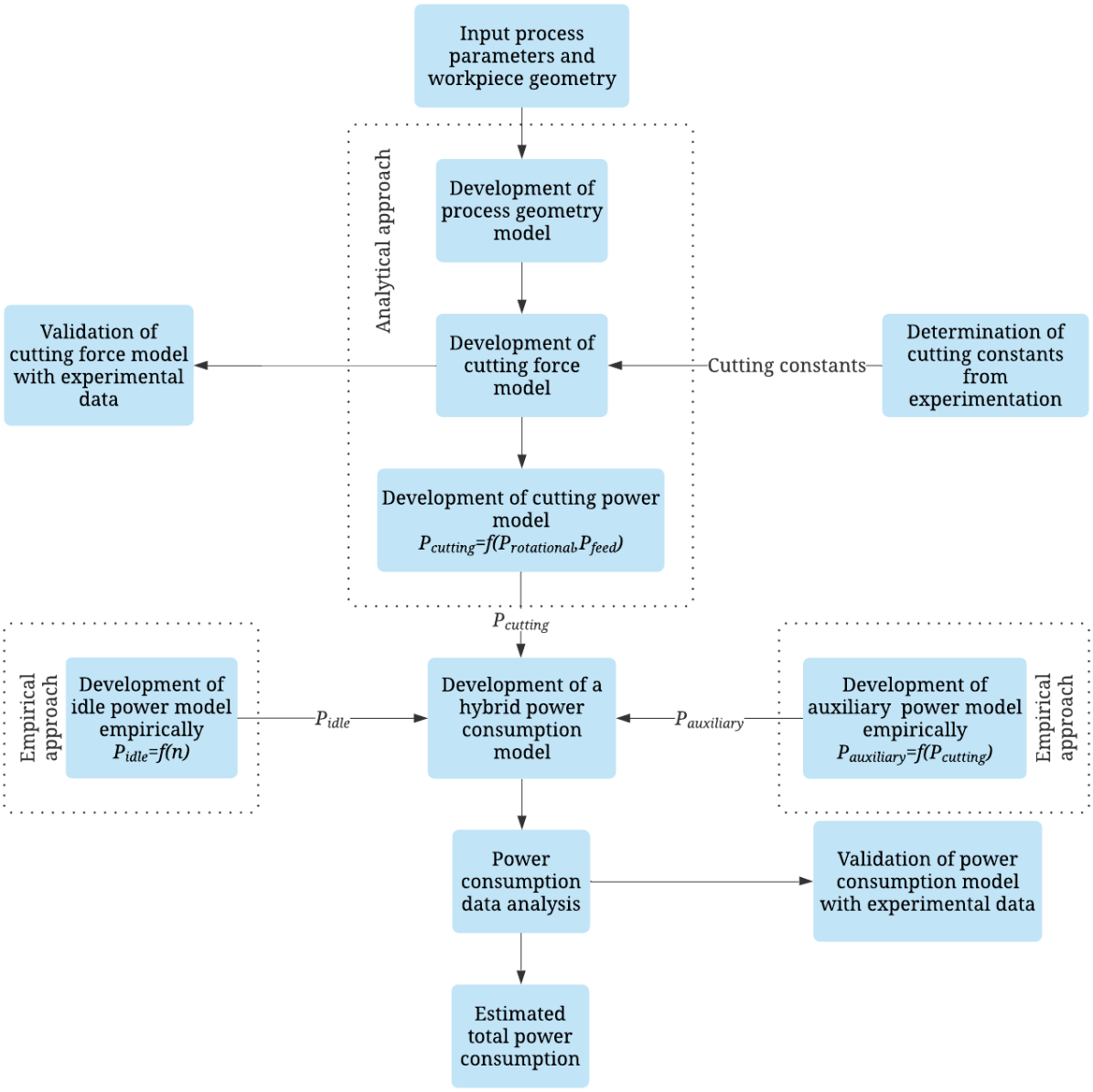


Fig. 5.1 Methodology for estimation of power consumption in milling of curved geometry

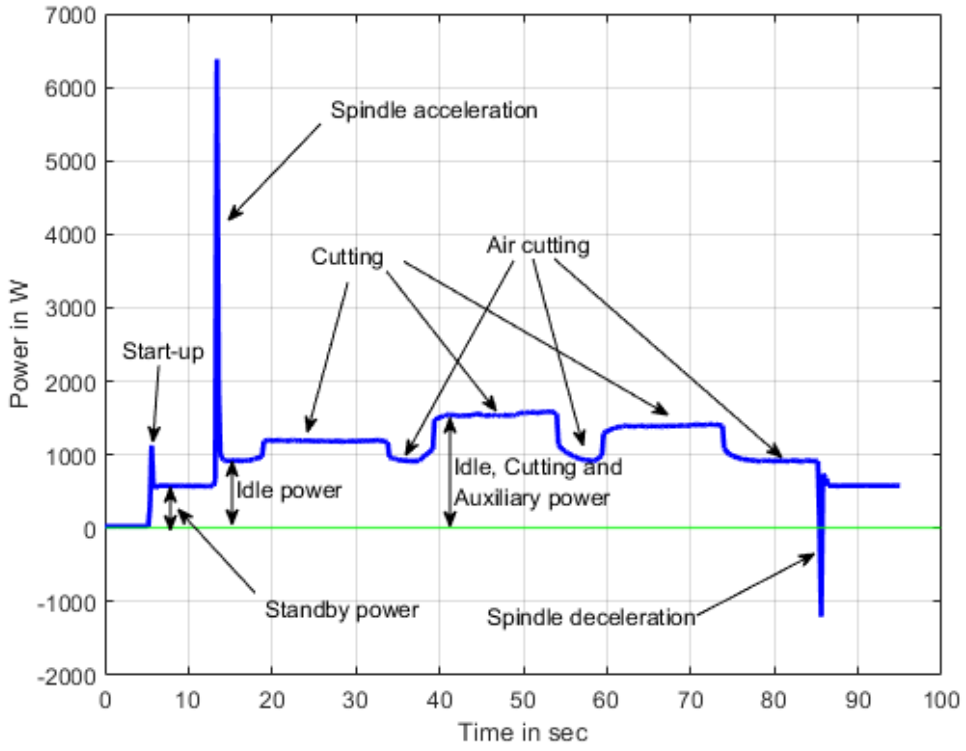


Fig. 5.2 A typical power profile of a milling process

### 5.2.1 The idle power consumption

The idle power includes the power consumed by auxiliary components and machine spindle while the spindle rotates without any feed and cutting motion. On the basis of power profile analysis, the idle power can be calculated as a summation of standby power demand and power required to rotate the spindle [153]. The idle power ($P_{idle}$) can be expressed as a function of spindle RPM (n). The idle power includes the power consumed by auxiliary components and spindle of machine when the spindle rotates without any feed and cutting motion. Based on the power profile analysis, the idle power can be calculated as a sum of standby power demand and power required to rotate the spindle Idle power is mostly affected by spindle rotation due to mass moment of inertia of spindle [93]. It can be expressed as:

$$P_{idle} = f(n) \tag{5.2}$$

### 5.2.2 The cutting power consumption

For cutting power calculation, the tool tip energy is required during metal cutting operation. In case of peripheral milling, generally cutting teeth are helical in nature; process is intermittent and produces chips of varying thickness making the milling operation more complex and difficult to predict tool tip energy. The basic input for modelling of cutting power is instantaneous cutting forces acting along the helical cutting edge. As process geometry in milling is prerequisite for developing cutting force model, identification and determination of process geometry variables are essential which are discussed briefly in the following subsection.

The cutting power at the tool tip is the amount of power required at tip point during the machining process to remove workpiece material. The relative movement between tool and workpiece causes power consumption during a machining process. Rotational motion due to spindle drive and feed motion due to feed drive are two types of relative movements. These two motions are considered separately to calculate power consumption. In rotational motion, radial force and axial force are perpendicular to the cutting speed. Therefore, their contribution in computation of power consumption is zero. But the tangential force component coincides with the direction of cutting speed which contributes to the determination of power consumption. Differential powers consumed at each elemental cutting edge in tangential, radial, and axial directions can be expressed as:

$$dP_{rotational,t} = dF_t.V \tag{5.3a}$$

$$dP_{rotational,r} = 0 \tag{5.3b}$$

$$dP_{rotational,a} = 0 \tag{5.3c}$$

where $V$ is cutting speed which is a function of spindle rpm and diameter of milling cutter. Total power consumed by each elemental helical cutting edge owing to rotational motion can be given by

$$dP_{rotational} = dF_t.V \tag{5.4}$$

During the feed motion of the cutter, the axial force component is also perpendicular to feed direction. Therefore, its contribution to the power consumption is zero. Differential powers are

$$dP_{feed,t} = dF_t.\cos\beta\,.f_{cc}/60000 \tag{5.5a}$$

$$dP_{feed,r} = dF_r.\sin\beta\,.f_{cc}/60000 \tag{5.5b}$$

$$dP_{feed,a} = 0 \tag{5.5c}$$

where $f_{cc}$ is feed rate along cutter contact path in mm/min. The total power consumed by each disk element along the cutting edge owing to feed motion

$$dP_{feed} = dF_t.\cos\beta\,.f_{cc}/60000 + dF_r.\sin\beta\,.f_{cc}/60000 \tag{5.6}$$

According to Eq. (3.23a) and Eq. (5.6), it can be expressed as

$$dP_{feed} = -dF_f.f_{cc}/60000 \tag{5.7}$$

Instantaneous cutting power consumption at any given instant can be given by

$$P_{cutting} = P_{rotational} + P_{feed} = \int dP_{rotational} + \int dP_{feed}$$

$$= V.\int dF_t + f_{cc}/60000\,.\int\left(-dF_f\right) \tag{5.8}$$

This is an instantaneous cutting power at a particular rotation angle. However, since the rotation period is too short for the measurement device to record, the average power instead of the instantaneous power is of interest in this research work. Average cutting power for one complete cutter rotation can be written as:

$$\bar{P}_{cutting} = \frac{1}{2\pi}\int_0^{2\pi} P_{cutting} \tag{5.9}$$

### 5.2.3 The auxiliary power consumption

There are several factors contributing to the total power consumption excluding spindle rotation and metal cutting process. They may come from frictional forces between various moving elements of machine tool, heat generation and thermal effects of machine tool, resistivity of electrical components, etc. Auxiliary power consumption includes the power loss due to the movement of table axis drive, electrical load loss, magnetic power loss, etc. It includes all forms of power loss except idle and cutting power consumption.

Initially, the cutting power and idle power are added together, and later on, it is deducted from the total power consumption in order to compute auxiliary power consumption as given in Eq. (5.10).

$$P_{auxiliary} = P_{total} - \left(P_{cutting} + P_{idle}\right) \tag{5.10}$$

The auxiliary power consumption is also expressed as a function of average cutting power. Based on the research work suggested by Hu et al. [154], auxiliary power consumption is expressed as

$$P_{auxiliary} = C_0.\bar{P}_{cutting} + C_1.\bar{P}_{cutting}{}^2 = f\left(\bar{P}_{cutting}\right) \tag{5.11}$$

where $C_0$ and $C_1$ are the coefficients used in the polynomial equations which need to be determined by conducting a set of machining experiments.

### 5.2.4 Total power consumption

Total power consumption consists of three power components such as idle, cutting and auxiliary power. It is widely accepted that idle power depends on the specific machine tool and the cutting power is influenced by the workpiece material and the cutting conditions. The machine tool power consumption (total power) is measured in-line using power quality analyzer with the help of current and voltage sensors. The idle power consumption is measured experimentally without axis movement and cutting operation. Therefore, the machine tool energy consumption reflects idle power component considering standby power and spindle rotation. During milling operation, the cutting force is measured directly using the force sensor (dynamometer) for obtaining the spindle power, and machine tool power consumption is measured in-line, simultaneously for accomplishing of total power which includes idle, cutting and auxiliary power components. Therefore, sum of idle and auxiliary power components is calculated experimentally by subtracting the cutting power from the machine total power consumption. The auxiliary power is difficult to measure or model directly due to complexity of various time-dependent and independent parameters [122]. Therefore, the auxiliary power is determined from the machine total power consumption by subtracting the idle and cutting power consumption. Eventually, an empirical relationship based on experimental results is established between auxiliary and cutting power consumption. Later on, the values of various coefficients of the mathematical equation are used in the proposed model for computing the auxiliary power component for varying machining conditions.

## 5.3 Energy Efficient Milling

Development of energy consumption model is discussed in previous section. An energy efficient machining strategy needs to develop for milling of variable curved components where more uniform cutting force and power profiles are accomplished due to constant chip load along the peripheral length of curved geometry. The following subsections discusses constant engagement algorithm based on tool path modification approach.

### 5.3.1 Constant engagement method for variable curved geometry

It is already mentioned in the previous chapter that curvature of curved workpiece varies continuously along the curved profile. During milling of such type of workpiece, fluctuations in force profile take place due to alteration in tool engagement and concerned uncut chip thickness in the presence of workpiece curvature. The continuous, non-uniform fluctuations in force profile create an obstacle in stable machining and in cutting power consumption. A machining strategy which deals with constant engagement of tool along the peripheral length of cut helps to maintain consistent uncut chip thickness and concerned chip load. Therefore, the following subsection describes about computation of tool engagement for milling briefly.

### 5.3.2 Computation of tool engagement

The tool engagement angle is a subtended angle between entry and exit angles of milling teeth in tool-workpiece contact zone. In peripheral milling, the shape of force profile is regulated by tool engagement and the swept angles. The tool engagement angle depends on radial depth of cut and cutter radius whereas, the swept angle of tool is governed by axial depth of cut, radius and helix angle of cutter. In case of $2\frac{1}{2}$ axis milling, the cutting process involves contour tool path in XY plane for desired profile of workpiece. Mostly, the axial depth of cut remains constant throughout the machining process which leads to negligible variation in swept angle for a given cutting tool-workpiece pair. Therefore, the controlling of engagement angle is more essential for regulation and reduction of cutting force fluctuation during material removal process. For milling of straight geometry, the calculation of tool engagement angle ($\theta_{engg}$) is straightforward and expressed as:

$$\theta_{engg} = \theta_{ex} - \theta_{en} = \operatorname{acos}\left(1 - \frac{a_e}{r}\right) \tag{5.12}$$

where $\theta_{ex}$ is exit angle, $\theta_{en}$ is entry angle, $a_e$ is radial depth of cut and $r$ is radius of end mill cutter.

During milling of constant curved (circular) component, the magnitudes of tool engagement for convex and concave geometries are different and it is more for concave workpiece as compared to convex ones. As the radius of curvature ($R$) for circular workpiece is constant, the tool engagement angle remains unaltered at each feed station along the cutter path. The schematic representation of tool engagement angles for convex and concave geometries at current, preceding and succeeding feed stations along the cutter path are shown in Figs. 5.3 and 5.4.

In order to calculate the magnitude of engagement angle for convex and concave geometries at an individual feed station for given cutting conditions, the following mathematical equations based on cosine rule are used.

$$\theta_{engg} = acos\left[\frac{(R+r)^2 + r^2 - (R+a_e)^2}{2r.(R+r)}\right] \tag{5.13}$$

$$\theta_{engg} = \pi - acos\left[\frac{(R-r)^2 + r^2 - (R-a_e)^2}{2r.(R-r)}\right] \tag{5.14}$$

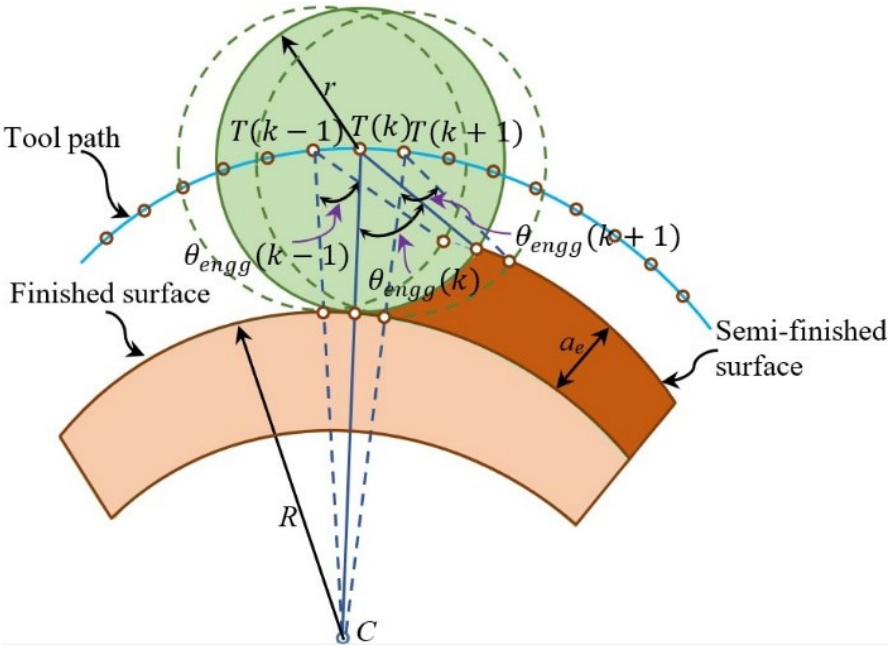


Fig. 5.3 Tool engagement for convex circular geometries

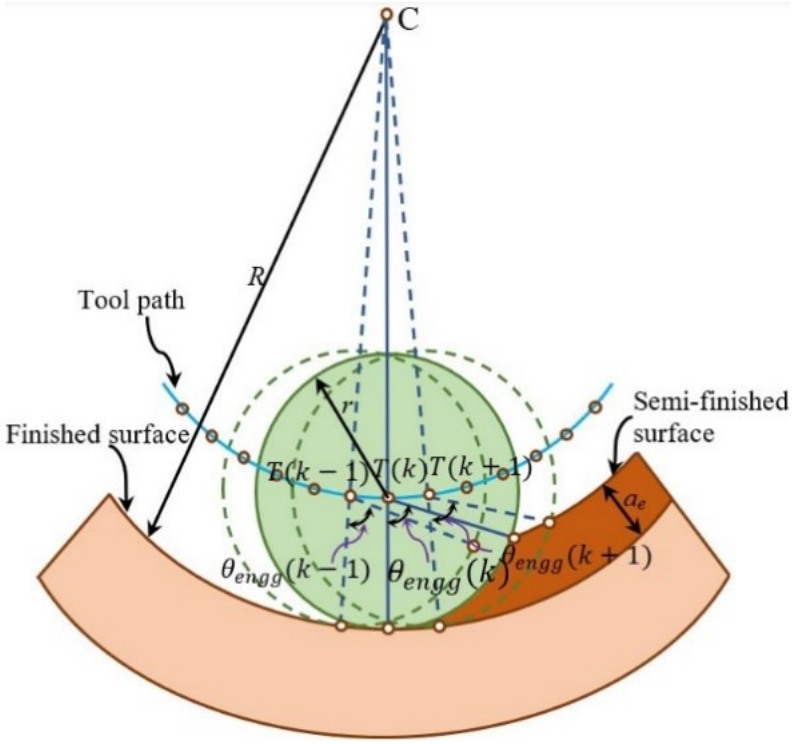


Fig. 5.4 Tool engagement for concave circular geometries

In case of variable curved component, the magnitudes of curvature vary at each and every point along the curve profile. Therefore, the radius of curvature does not remain constant at each point along the peripheral length of the curved geometry that makes calculation of engagement angle more challenging for milling operation. In order to simplify the problem, the total length of the curved geometry is segmented into a finite number of discrete sections with a specified arc length. Each arc segment is considered as a part of an osculating circle providing constant curvature value at each location. The radius of curvature and center point of each osculating circle are different along the peripheral length of cut unlike of circular geometry. The each and every arc segment having constant radius of curvature is composed of two nodal points. At each nodal point lying on the curve profile is defined by its normal vector ($\bar{V}_N$) and tangent vector ($\bar{V}_T$) in a specified location as shown in Fig. 5.5. This nodal point is also considered as exit point of cutter for peripheral milling and expressed as outward normal direction to the machined surface. For calculation of engagement angle, and other two points namely tool center point and entry point are also essential based on tool geometry and unmachined surface. Fig. 5.5 shows the schematic representation of tool engagement for variable curved geometry. In order to compute the magnitude of engagement angle for curved geometry, the following mathematical equation based on cosine rule is used.

$$\theta_{engg} = \text{acos}\left[\frac{r^2 + (R+r)^2 - C\text{B}^2}{2r(R+r)}\right] \tag{5.15}$$

where $r$ is radius of the tool, $R$ is radius of curvature of the local segment, $CB$ is the distance between the point $C$ and the point $B$. The point $B$ lies on the unmachined surface profile defining entry point of the tool. The point $C$ is the center of the osculating circle which varies according the curved machined surface profile unlike circular geometry.

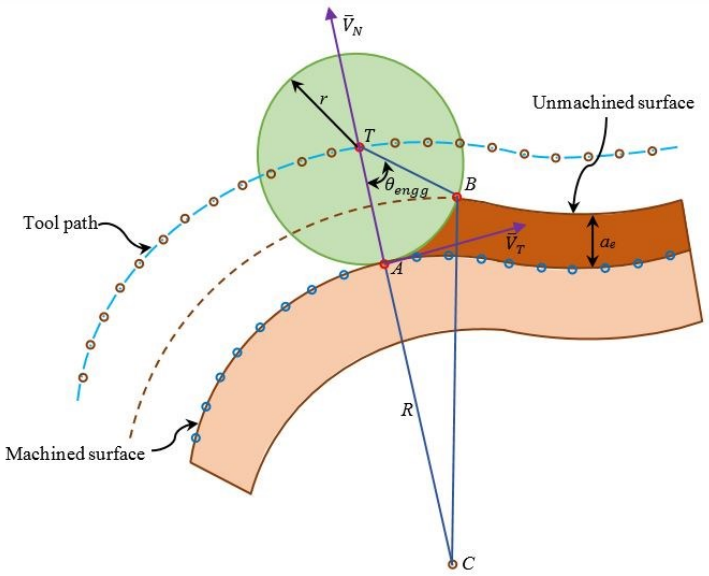


Fig. 5.5 Tool engagement for milling of variable curved geometry

### 5.3.3 Regulating constant tool engagement

The constant tool engagement method ensures the constant chip load resulting into more uniform force profile and stable machining process. The constant tool engagement is influenced by the positions of three points namely tool center, entry and exit points which are calculated based on machining conditions and workpiece geometry. In order to achieve the invariant property of tool engagement, the locations of these three points must be controlled and regulated in a given feed station. Later on, the same procedure must be followed in each and every feed station along the entire tool path to maintain constant chip load in machining. There are few approaches available in the literature regarding regulating constant chip load. Among them, the approach proposed by Stori and Wright [155] is more popular which deals with constant tool engagement for convex geometry by linear shifting of tool center along the outward normal direction to the workpiece to modify entry point of tool and regulate the constant engagement. As tool center shifts in the outward normal direction to the workpiece, the exit point also moves in the same direction due to circular

geometric shape of the tool. It results into reduction of entry angle influencing tool engagement angle. Depending upon the prescribed value of engagement angle, the linear shifting distance of tool center is decided. Initially, the curvature value of arc segment is calculated at each feed station. Then, depending upon the magnitude of constant engagement angle, the linear translation of cutter center is computed at every feed station. This process is iterated at each feed station to calculate the constant chip load along the entire cutter path. Although, the value of tool engagement remains constant in this approach, but the exit point also moves towards outward normal direction to the component. As the linear shifting of exit point from its desired position also takes place, it results into undercut situation (unwanted material remains on the workpiece) and overcut situation (more material will be removed from the workpiece). It leads to more surface errors (positive or negative) in the machined surface producing inaccurate parts.

### 5.3.4 Proposed algorithm

To overcome the limitation of the earlier approach, an alternative method is recommended by Uddin et al. [81,156] where the exit point of tool is kept in desired position without changing its location along with regulating constant tool engagement. This approach is applied for cutting force analysis of convex and concave circular geometries and gives satisfactory results. During machining of circular arc section, the position of center of the circle remains constant at each feed station for same radius of curvature although the location of the center will be inside or outside of the datum geometry based on concavity and convexity of the surface. In case of variable curved geometry, the position of center of osculating circle varies along with alteration of curvature value at each feed station. Secondly, the selection criteria for accomplishing constant tool engagement at desired level is missing from the earlier work. In the present work, a new algorithm is developed based on the earlier work done by Uddin et al. [81,156] and applied for variable curved geometry in order to develop energy efficient machining system. The present algorithm describes about computation of the cutter path trajectory corresponding to semi-finished workpiece maintaining tool engagement at a desired level along the contour parallel tool path. This is accomplished with the help of an initial planar curve that represents the contour of finished workpiece geometry. In order to regulate the tool engagement at constant level along the finishing path, it is required to determine a new curve profile that represents semi-finished workpiece geometry.

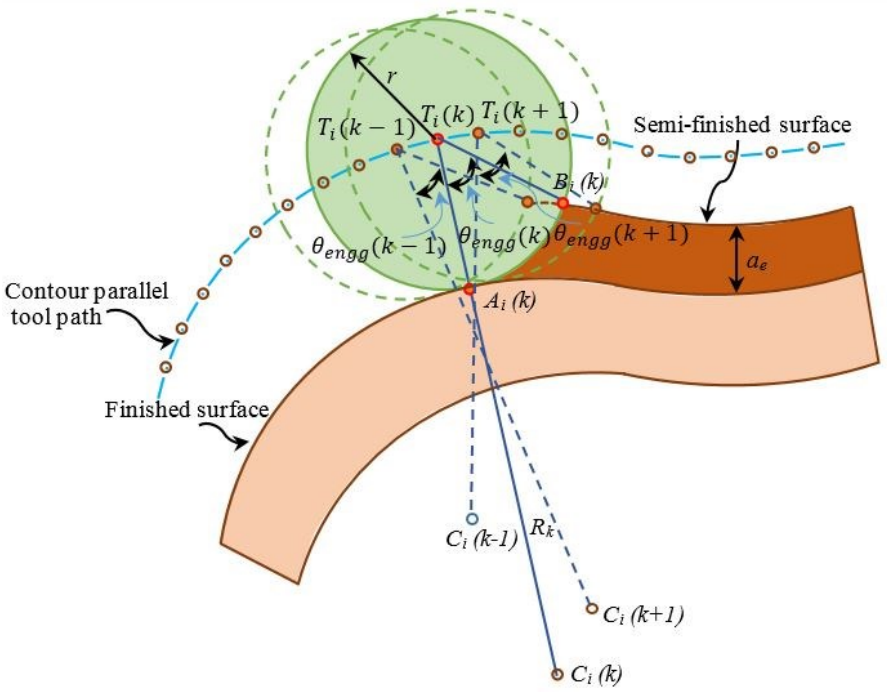


Fig. 5.6 Tool engagement at current, preceding and succeeding positions along the peripheral length

In order to illustrate the present algorithm comprehensively, three planar parametric curves, $(X_{sf}(u), Y_{sf}(u))$, $(X(u), Y(u))$, and $(X_t(u), Y_t(u))$ are shown in Fig. 5.6 to represent the trajectories of semi-finished surface, finished surface and tool path respectively. The contours of the semi-finished workpiece and the tool path are offset curves located away from the finished workpiece defined by Eq. (5.16) by a distance of radial depth of cut $(a_e)$ and cutter radius $(r)$ respectively. The both contours of the semi-finished workpiece and the tool path are determined using the Eqs. (5.17) and (5.18) with respect to finished workpiece which is used as a datum.

$$X = f(u), Y = g(u) \quad u1 < u < u2 \tag{5.16}$$

$$X_{sf}(u) = X(u) \pm a_e . \frac{Y'(u)}{\left[\left(X'(u)\right)^2 + \left(Y'(u)\right)^2\right]^{1/2}} \tag{5.17a}$$

$$Y_{sf}(u) = Y(u) \mp a_e . \frac{X'(u)}{\left[\left(X'(u)\right)^2 + \left(Y'(u)\right)^2\right]^{\frac{1}{2}}} \tag{5.17b}$$

$$X_t(u) = X(u) \pm r . \frac{Y'(u)}{\left[\left(X'(u)\right)^2 + \left(Y'(u)\right)^2\right]^{1/2}} \tag{5.18a}$$

$$Y_t(u) = Y(u) \mp r.\frac{X'(u)}{\left[\left(X'(u)\right)^2 + \left(Y'(u)\right)^2\right]^{\frac{1}{2}}} \quad (5.18b)$$

where $a_e$, and $r$ denote radial depth of cut and cutter radius respectively and $X'(u)$ and $Y'(u)$denote the differentiation of the parametric curve with respect to the curve parameter.

In order to determine the tool engagement at every feed position, the cutter contact path must be divided into a finite number of discrete segments with a length equal to the feed per tooth. The point $B_i(k)$ representing tool entry point corresponding to the position of the cutter centre $T_i(k)$ along the locus of tool path trajectory is the intersection of the milling cutter circumference and semi-finished workpiece profile. The coordinates of the point $B_i(k)$ is calculated using Eqs. (5.19) and (5.20) as given below. The subscript $i$ represents each machining pass and ranges from 1 to $i$ with the $i^{th}$ pass being referred to as the finishing pass and $k$ stands for each different point along the tool path and ranges from 1 to $N$.

$$X_{sf}(u_b) = X(u_b) \pm a_e.\frac{Y'(u_b)}{\left[\left(X'(u_b)\right)^2 + \left(Y'(u_b)\right)^2\right]^{1/2}} \quad (5.19a)$$

$$Y_{sf}(u_b) = Y(u_b) \mp a_e.\frac{X'(u_b)}{\left[\left(X'(u_b)\right)^2 + \left(Y'(u_b)\right)^2\right]^{\frac{1}{2}}} \quad (5.19b)$$

$$[X_t(u_t) - X_w(u_b)]^2 + [Y_t(u_t) - Y_w(u_b)]^2 = r^2 \quad (5.20)$$

The point $(C_i(k))$ is centre of local radius of curvature of geometry $(R_k)$ corresponding to the cutter exit point $A_i(k)$ located on the finished surface. The Eq. (5.21) is used to compute the engagement angle corresponding to the cutter center point $T_i(k)$.

$$\theta_{engg}(k) = \text{acos}\left[\frac{r^2 + (R_k + r)^2 - CB_i(k)^2}{2r.(R_k + r)}\right] \quad (5.21)$$

The tool engagement for different cutter center positions can be calculated in similar manner. The Eqs. (5.16) to (5.21) is used to determine the positions of the cutter center point and entry points corresponding to a contour parallel tool path which is an offset curve to the finish surface.

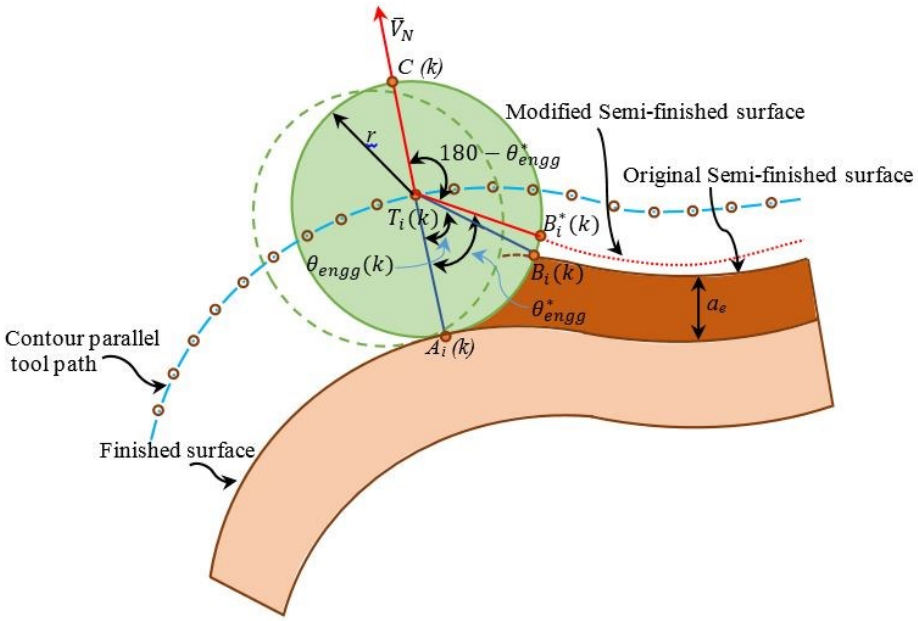


Fig. 5.7 Shifting of tool entry points

During computation of process geometry of variable curved workpiece, a data base is created to store the coordinates of each tool center point, entry point, exit point, and the values of engagement angle based on the finished surface without applying constant engagement method. The values of engagement angle at each feed station is different as the workpiece curvature varies along the finish surface. The purpose of the current algorithm is to determine the updated cutter entry point $B_i^*(k)$ corresponding to the kth tool center location along the cutter path according to the predefined engagement angle $\theta_{engg}^*(k)$. The value of the engagement angle is computed based on the machining conditions and permissible dimensional tolerance of the workpiece. Once, the data set of the new entry points are obtained, the trajectory of the modified semi-finished workpiece surface can be produced easily. Now, the generated modified semi-finished workpiece geometry is an offset planar curve to the contour of finished geometry as shown in Fig. 5.7. This modified geometry offers constant tool engagement along the entire cutter path while a finishing cut is to be carried out using a contour parallel tool path. In order to accomplish a semi-finished workpiece surface, the coordinates of modified points are transferred into the CAD/CAM/CAE commercial software (PTC CreO 9.0) and joined by a spline tool. It is also possible to produce the semi-finished tool path required for creating the semi-finished workpiece geometry by offsetting the best fitted curve by a distance equal to the cutter radius. The following steps are used to summarize the present algorithm for determining the modified semi-finished tool path.

Step 1: First, the entire cutter path is segmented into a finite number of discrete sections with a length equal to the feed per tooth. In every feed station, determine the center and radius of osculating circle, and cutter entry point using Eqs. (5.19) and (5.20). After that, the corresponding engagement angle is to be calculated using Eq. (5.21).

Step 2: Desired engagement angle is presumed based on the machining criteria.

Step 3: Calculate the tool center point $T_i(k)$ on the contour parallel tool path for a given tool exit point $A_i(k)$ by substituting the parameter $(u_a)$ in Eq. (5.18).

Step 4: Determine a modified entry point $(B_i^*(k))$ representing an intersecting point of the cutter circumference and the semi-finished workpiece trajectory for maintaining the modified cutting engagement angle $(\theta_{engg}^*(k))$ at the desired level. Firstly, the normal vector $(\bar{V}_N)$ at the tool center point is to be determined based on the slope equation (5.22) illustrated in Fig. 5.6. After that, compute the point $C(k)$ which is an intersecting point of the tool circumference and the normal vector with the help of matrix equation (5.23) for finding out coordinates at a distance $(r)$ from the tool center point $T_i(k)$ along the normal vector.

$$\tau = atan\left(\frac{Y'(u)}{X'(u)}\right) \tag{5.22}$$

$$\begin{bmatrix} x \\ y \end{bmatrix} = \begin{bmatrix} x_t \\ y_t \end{bmatrix} + r.\begin{bmatrix} \cos(\tau) \\ \sin(\tau) \end{bmatrix} \tag{5.23}$$

Where $(x_t, y_t)$ represents coordinates of tool center point $T_i(k)$ and $(x, y)$ represents coordinates of the point $C(k)$. The desired tool entry point $B_i^*(k)$ on semi-finished workpiece geometry can be obtained by rotating the line vector $T_i(k)C(k)$ about the point $T_i(k)$ by an amount of $\theta = (\pi - \theta_{engg}^*(k))$ using Eq. (5.24). The location of this new point will not be lying on the contour parallel semi-finished surface. It is located on circumference of tool for its given position along the tool path.

$$\begin{bmatrix} x^* \\ y^* \\ 1 \end{bmatrix} = \begin{bmatrix} 1 & 0 & -x_t \\ 0 & 1 & -y_t \\ 0 & 0 & 1 \end{bmatrix}\begin{bmatrix} \cos\theta & -\sin\theta & 0 \\ \sin\theta & \cos\theta & 0 \\ 0 & 0 & 1 \end{bmatrix}\begin{bmatrix} 1 & 0 & x_t \\ 0 & 1 & y_t \\ 0 & 0 & 1 \end{bmatrix}\begin{bmatrix} x \\ y \\ 1 \end{bmatrix} \tag{5.24}$$

Where $(x^*, y^*)$ represents coordinates of desired tool entry point $B_i^*(k)$

Step 5: Set parameter ($u_a = u_a + u$) and step index($k = k + 1$), then repeat steps 3 and 4 to get the coordinates of the modified entry point in the succeeding feed station. In order to determine the trajectory of the modified semi-finish surface, all these new entry points need to be calculated.

Step 6: The updated semi-finished surface is created by importing these points into the CAD/CAM/CAE software. However, the trajectory of modified semi-finished surface is not offset curve to finished surface.

Step 7: By offsetting the modified semi-finished curve created in Step 6 by an amount of tool radius($r$), the modified tool path is obtained for the modified semi-finished surface.

The schematic illustration of the modified semi-finished geometry achieved using the proposed approach and the contour parallel cutter path are presented in Fig. 5.7. The summary of the proposed algorithm is also shown in Fig. 5.8.

### 5.3.5 Criteria for selecting the desired value of constant engagement

The magnitude of the specified constant engagement angle at the desired level is determined by considering permissible cutting forces and dimensional tolerances of the component produced during the machining operation. The suitable cutting parameters and machining conditions will be selected for a given tool and workpiece pair. Any finite value of the engagement angle can be selected based on the actual engagement angle obtained during milling of variable curved component. This actual engagement angle is computed using Eq.5.21. As the workpiece curvature varies from beginning to end of cut, different values of engagement angle will be obtained and stored in the database. Therefore, the values of maximum and minimum engagement angle from the database is selected as a basis for the proposed approach. For instance, if the engagement angle increases beyond the desired value on a concave arc, the cutter path for semi-finish geometry will be modified to reduce the value of actual tool engagement. On the other side, if the engagement angle is lesser than the desired value on a convex arc, the cutter path for semi-finish geometry will be altered to increase the actual tool engagement. As a result, tool engagement is regulated at constant level along contour profile of workpiece. For a better understanding of tool path

modification, Fig. 5.9 depicts an example of a modified constant engagement tool path generated by the proposed technique. Both the semi-finishing path and the finishing path in Fig. 5.9(a) are contour parallel offset tool paths. Applying the proposed algorithm, the original semi-finishing tool path is changed into modified semi-finishing tool path so that the engagement angle along finishing path is maintained at a desired level as shown in Fig. 5.9(b).

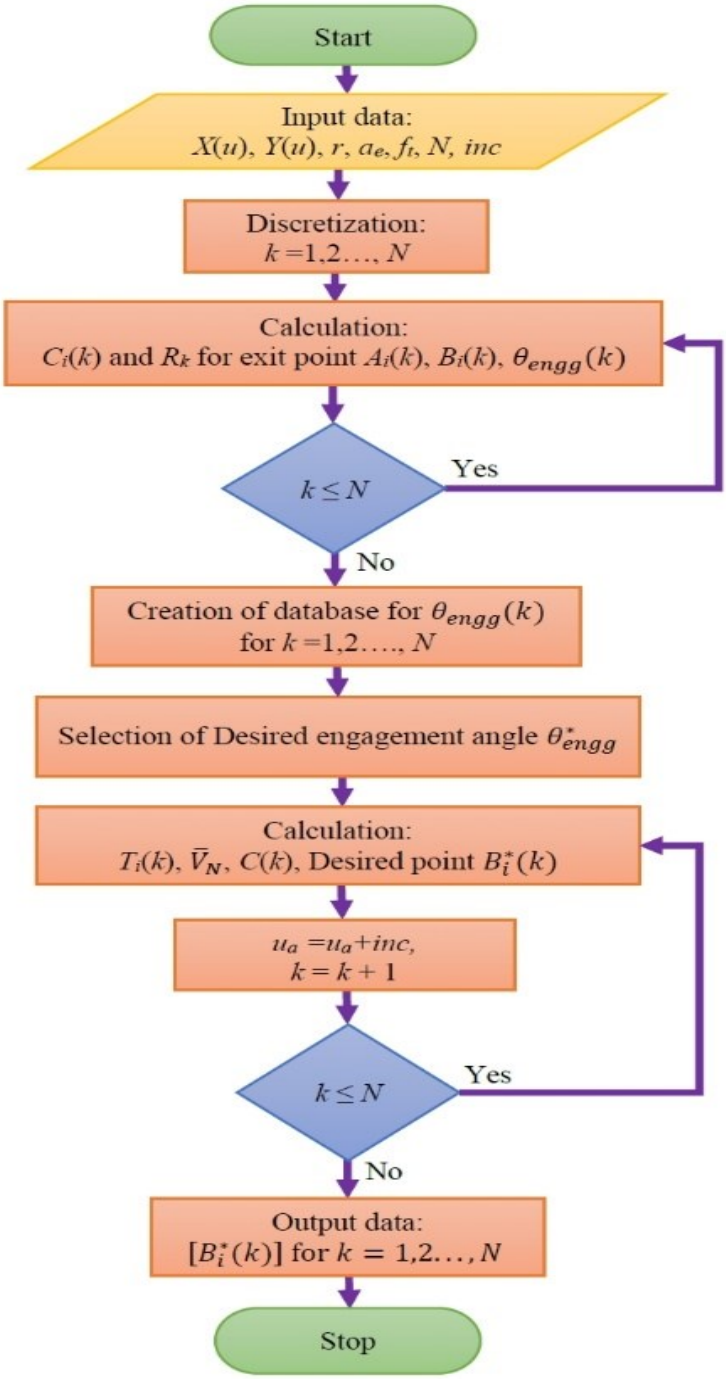


Fig. 5.8 Methodology for constant engagement algorithm

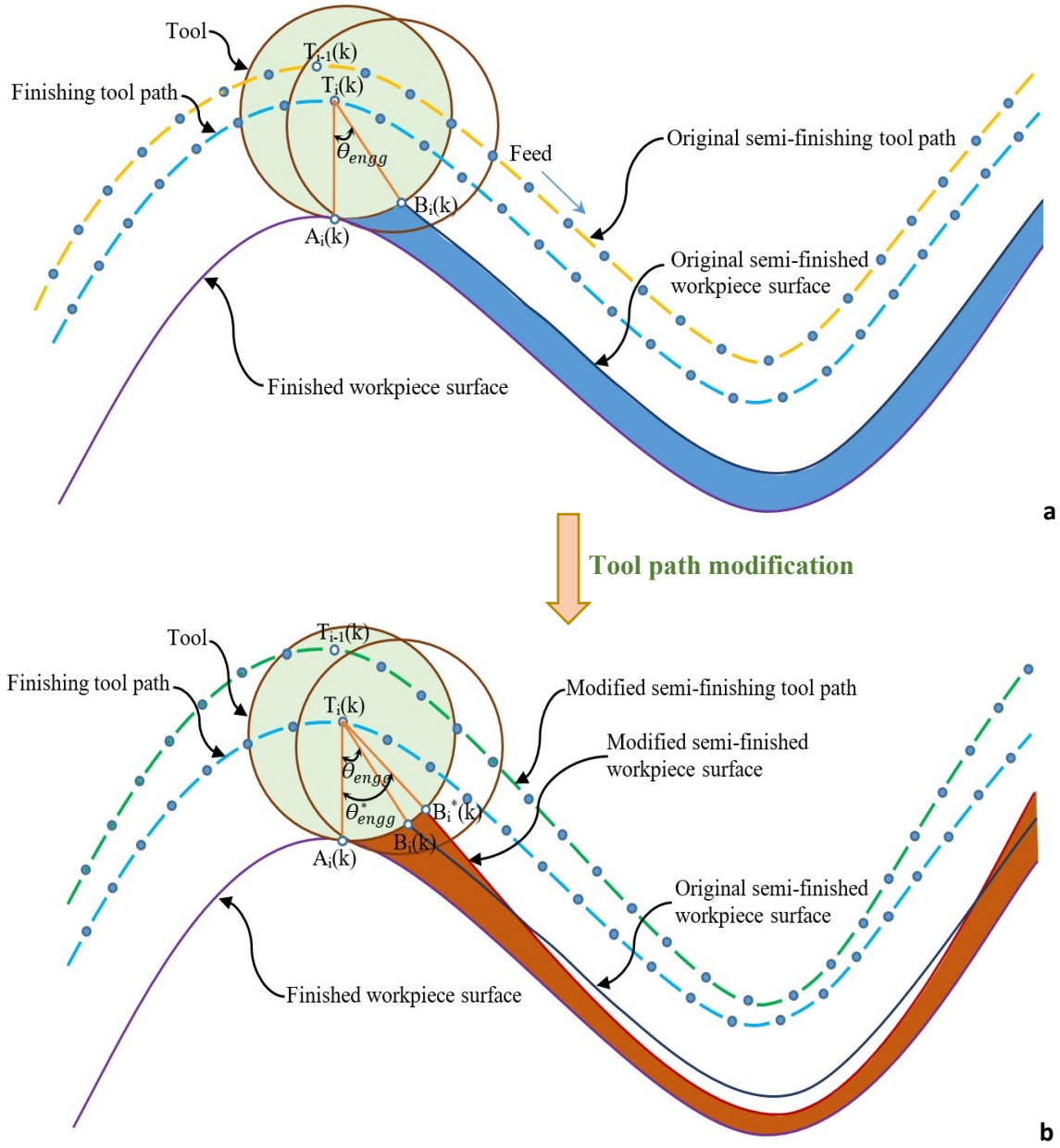


Fig. 5.9 Regulating cutter engagement by tool path modification

## 5.3.6 Computation of specific cutting energy

The specific energy consumption (SEC) for machining is expressed as the amount of energy required for removal of unit volume of material. It is directly associated with the effectiveness and efficiency of the machining process. Therefore, it is considered as an excellent indicator for performance evaluation of entire cutting process as well as machinability of workpiece material [157,158]. The high value of SEC causes large heat transfer rate and higher residual stresses developed in the workpiece resulting into poor surface integrity in the component, whereas lower value of SEC influences lesser damage

to the component [158]. The SEC is also a crucial parameter for measurement of the energy required for machining. The reduction in energy consumption during machining improves the process efficiency. It is expressed as:

$$SEC = \frac{E_{cutting}}{V_{material}} \tag{5.25}$$

$$SEC = \frac{P_{cutting}}{MRR} \tag{5.26}$$

## 5.4 Experimental Details

Three sets of milling experiments have been conducted for the calibration and validation of the proposed models. The first set of experiments has been performed to calibrate and determine the values of various coefficients used in the empirical power equations of the idle and auxiliary power models. The second set of experiments has been conducted for validation and assessment of performance of the proposed cutting power model. The third set of experiments has been performed to evaluate the effectiveness of the constant engagement algorithm for efficient milling discussed in the previous section. The experimental setup and machining conditions are discussed in the following subsections.

### 5.4.1 Experimental setup

All the experiments have been performed on three axis LMW JV-40 vertical machining center (VMC) fixed with a universal piezo-electric Kistler dynamometer (Type-9272) and a power logger (National Instrument). The detailed specifications of the VMC machine tool along with spindle and feed motors are given in Table 5.1. The vertical machining center is equipped with a FANUC controller of series Oi-MF CNC. The FANUC controller has linear and circular interpolation facilities that helps to perform machining of curved geometry.

Experimental setup for force measurement using a multi-channel piezo-electric dynamometer has been described in details in chapter 3. A dedicated power logger was used for measurement of total power consumption with the help of another DAQ system as shown in Fig. 5.10. The setup for power measurement is composed of various components such as voltage sensors (LEM LV25-P), current sensors (LEM LA55-P), NI-9215 data collecting cards, a compact DAQ card, LabVIEW software interface. The machine tool power

consumption for all machining experiments has been measured in-line at power supply port of electrical panel box of the CNC machine using voltage and current transducers.

Table 5.1 Technical specifications of the machine tool, spindle and feed motors

| **Machine tool specifications** | |
|---|---|
| Manufacturer | LMW JV- 40 |
| Power supply | 3 phase 415V 50HZ |
| Table travel (X × Y × Z) in mm | 500 × 400 × 450 |
| Spindle speed | 150-8000 RPM |
| ATC capacity | 20 |
| Maximum weight on table | 300 kg |
| Spindle motor power | 3/5.5 kW |
| Feed motor power (X) | 3 kW |
| Feed motor power (Y and Z) | 1.2 kW |
| **Spindle motor specifications** | |
| Speed | 800 rpm |
| Motor power | 5.5/7.5 kW |
| Maximum Torque | 32.3/58.7 Nm |
| **Feed motor specifications** | |
| Feed motor power (X and Y axis) | 1.2 kW |
| Feed motor power (Z axis) | 1.8 kW |
| Feed motor Torque (X & Y axes) | 7 Nm |
| Feed motor Torque (Z axis) | 11 Nm |

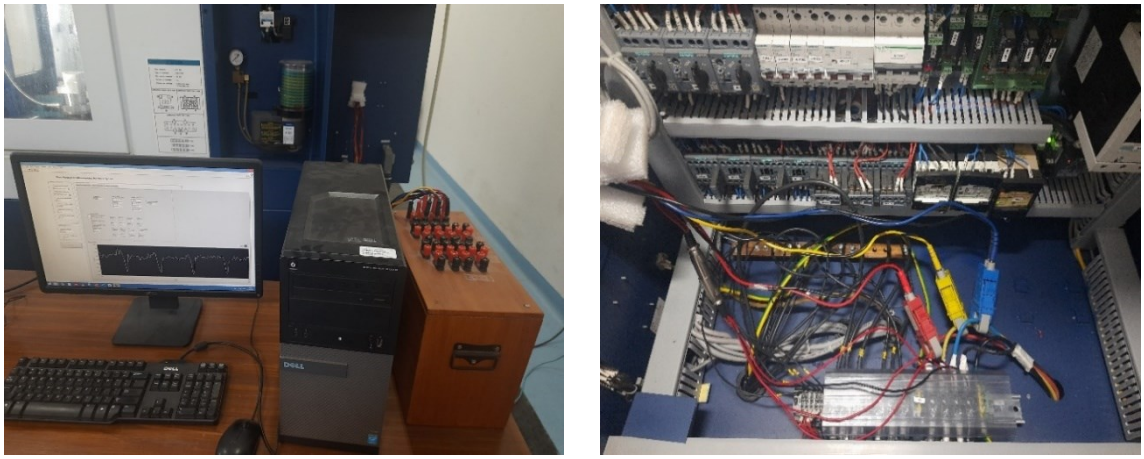

(a) (b)

Fig. 5.10 The experimental setup: (a) and (b) Installation of power mesurement setup

### 5.4.2 Machining conditions

The machining experiments have been carried out on rectangular, elliptical and sine wave curved workpieces of aluminium 6351-T6 for calibration and validation of the proposed model. The aluminium 6351-T6 alloy is extensively used in the aerospace industry. The rectangular workpiece is used mainly for the calibration and determination of various coefficients used in the various mathematical equations of power. A concave and convex type elliptical workpieces as shown in Chapter 3 are selected for validation and assessment of the effectiveness of the energy consumption models. A typical sine wave curved workpiece is used for validation and investigation of constant engagement algorithm. The machining parameters used for the first set of experiments are mentioned in Table 5.2. A total of 27 combinations are selected with varying axial immersion, spindle RPM and feed rate at three levels.

Table 5.2 Cutting conditions for auxiliary power

| $a_p$[mm] | $n$[rpm] | $f$[mm/min] |
|---|---|---|
| 2,3,4 | 2000 | 200,300,400 |
| 2,3,4 | 3000 | 200,300,400 |
| 2,3,4 | 4000 | 200,300,400 |

Table 5.3 Machining conditions for elliptical component

| **Workpiece geometry** | Elliptical concave<br>Elliptical convex |
|---|---|
| **Spindle speed** | 2000 rpm |
| **Nominal feed rate** | 400 mm/min |
| **Nominal feed per tooth** | 0.05 mm/tooth |
| **Axial depth of cut** | 3 mm |
| **Radial depth of cut** | 5 mm |
| **Length of machined surface** | 77 mm |
| **Tool diameter** | 16 mm |
| **Tool helix angle** | 30º |
| **Number of teeth of the cutter** | 4 |
| **Milling type** | Down milling with no coolant |

Table 5.3 describes the machining condition for performing the second set of experiments. The objective of these experiments is to validate and assess the effectiveness of the energy consumption model. For validation of constant engagement algorithm, experiments performed using machining conditions given in Table 5.4. During these experiments, the sampling data of cutting force and the respective power distribution are measured and recorded with respect to time. Later on, the force and power profiles are used for analysis and assessment of the performance of the proposed model.

Table 5.4 Experimental conditions used in experiments.

| **Machining conditions** | | | | | |
|---|---|---|---|---|---|
| **Workpiece** | | **Cutting Tool** | | **Cutting Parameters** | |
| Workpiece geometry | Sine wave curved | Cutting tool | HSS end mill | Radial depth of cut | 2.5 mm |
| Material of workpiece | Aluminum | Tool diameter | 16 mm | Axial depth of cut | 12 mm |
| Workpiece Dimensions | 100×100×75 mm | Tool overhang | 77 mm | Spindle speed | 2000 rpm |
| Base section | Square | Number of flutes | 4 | Feed rate | 400 mm/min |
| Base dimension | 100×100×25 mm | Helix angle | $30^0$ | Milling type | Down milling, no coolant |

## 5.4.3 Energy consumption model calibration

It is already mentioned that the idle power consumption depends on spindle rotation. The total power consumption ($P_{total}$) equals to idle power ($P_{idle}$) while the machine tool is in ON state without cutting and table movement. Therefore, the power consumed by the machine spindle in such a state is measured experimentally at various spindle RPMs. A statistical polynomial relationship is fitted between idle power and spindle RPM using standard linear least square (LLS) method. Table 5.5 shows the results for measured idle power for various spindle rotational speeds. The variation of idle power at different spindle RPMs can be seen from Fig. 5.11. A quadratic relationship is established between idle power and spindle RPM as expressed by Eq. (5.27).

$$P_{idle} = 0.00002.n^2 - 0.0144.n + 678.18 \quad (5.27)$$

Table 5.5 Data for measured idle power

| Sr. No. | Spindle rotation speed [rpm] | Idle power [W] |
|---|---|---|
| 1 | 500 | 670 |
| 2 | 1000 | 687 |
| 3 | 1500 | 723 |
| 4 | 2000 | 746 |
| 5 | 2500 | 780 |
| 6 | 3000 | 844 |
| 7 | 3500 | 932 |
| 8 | 4000 | 980 |
| 9 | 4500 | 1080 |
| 10 | 5000 | 1205 |

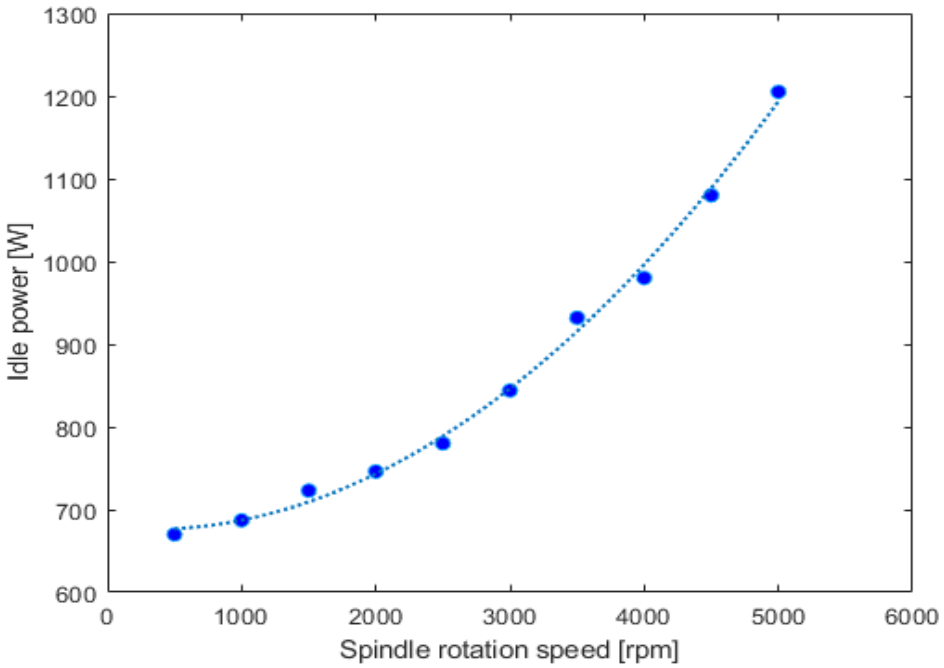


Fig. 5.11 Variation of idle power at different spindle rotational speeds

In order to determine the coefficients used in auxiliary power consumption, a separate set of experiments has been performed. Based on the machining experiments, experimental results are given in Table 5.6. The machine tool total power consumption is measured using power measurement setup, and the idle power and cutting power are calculated by using Eqs. (5.27) and (5.9) respectively. Based on these results, auxiliary power is calculated using Eq. (5.10). Later on, the variation of auxiliary power with respect

to cutting power has been studied using standard LLS method as shown in Fig. 5.12. It is observed that auxiliary power is gradually increasing with respect to cutting power. A quadratic relationship between the auxiliary and cutting power is formulated based on the measured results. Later on, the values of various coefficients are determined based on the quadratic relationship. After determining the values of coefficients, the auxiliary power can be expressed in terms of cutting power by Eq. (5.28).

$$P_{auxiliary} = 0.2632.\bar{P}_{cutting} + 0.0003.\bar{P}_{cutting}^{\ 2} \quad (5.28)$$

Table 5.6 Measured total power ($P_{total}$) and predicted cutting power ($\bar{P}_{cutting}$)

| Sr. No. | $a_p$ [mm] | $n$ [rpm] | $f$ [mm/min] | $P_{total}$ [w] | $\bar{P}_{cutting}$ [w] | Sr. No. | $a_p$ [mm] | $n$ [rpm] | $f$ [mm/min] | $P_{total}$ [w] | $\bar{P}_{cutting}$ [w] |
|---|---|---|---|---|---|---|---|---|---|---|---|
| 1 | 2 | 2000 | 200 | 1027 | 212.06 | 15 | 3 | 3000 | 400 | 1616 | 554.6 |
| 2 | 2 | 2000 | 300 | 1101 | 262.15 | 16 | 3 | 4000 | 200 | 1585 | 442.89 |
| 3 | 2 | 2000 | 400 | 1164 | 304.73 | 17 | 3 | 4000 | 300 | 1767 | 547.39 |
| 4 | 2 | 3000 | 200 | 1183 | 257.35 | 18 | 3 | 4000 | 400 | 1890 | 636.2 |
| 5 | 2 | 3000 | 300 | 1281 | 318.1 | 19 | 4 | 2000 | 200 | 1351 | 424.13 |
| 6 | 2 | 3000 | 400 | 1352 | 369.73 | 20 | 4 | 2000 | 300 | 1501 | 524.3 |
| 7 | 2 | 4000 | 200 | 1388 | 305.26 | 21 | 4 | 2000 | 400 | 1633 | 609.47 |
| 8 | 2 | 4000 | 300 | 1469 | 364.92 | 22 | 4 | 3000 | 200 | 1582 | 514.72 |
| 9 | 2 | 4000 | 400 | 1552 | 414.13 | 23 | 4 | 3000 | 300 | 1777 | 636.2 |
| 10 | 3 | 2000 | 200 | 1183 | 318.1 | 24 | 4 | 3000 | 400 | 1930 | 739.46 |
| 11 | 3 | 2000 | 300 | 1293 | 393.22 | 25 | 4 | 4000 | 200 | 1829 | 590.52 |
| 12 | 3 | 2000 | 400 | 1368 | 457.1 | 26 | 4 | 4000 | 300 | 2038 | 729.85 |
| 13 | 3 | 3000 | 200 | 1365 | 386.03 | 27 | 4 | 4000 | 400 | 2269 | 848.27 |
| 14 | 3 | 3000 | 300 | 1505 | 477.15 | | | | | | |

Finally, the mathematical relationship of total power consumption with the idle, cutting and auxiliary power is established. The total power consumption can also be described as function of idle and cutting power as per Eq. (5.29).

$$P_{total} = P_{idle} + 1.2632.\bar{P}_{cutting} + 0.0003.\bar{P}_{cutting}^{\ 2} \quad (5.29)$$

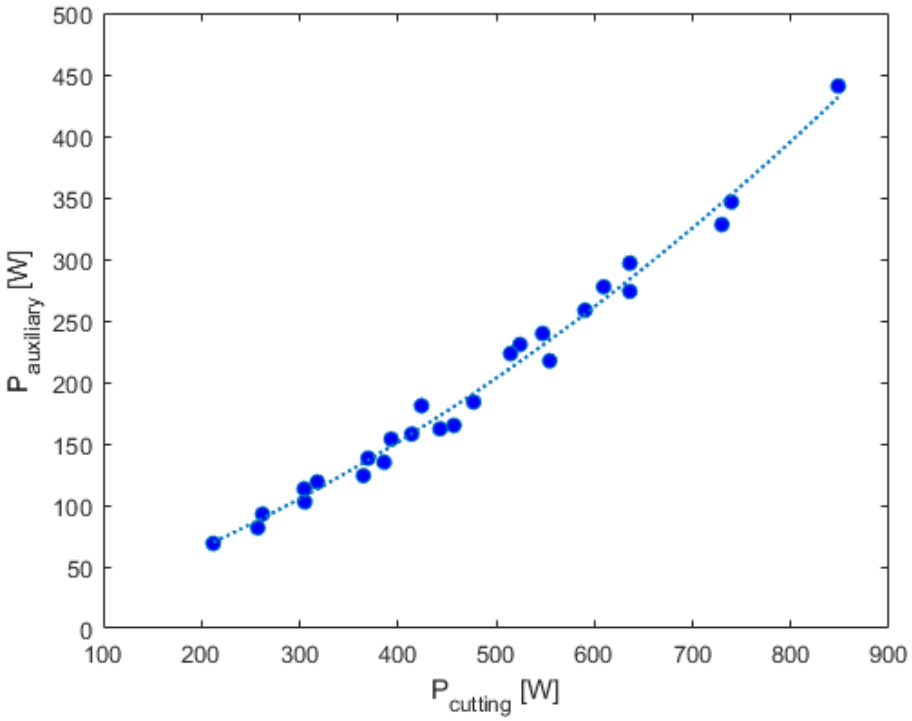


Fig. 5.12 Co-relationship between auxiliary and cutting power

## 5.5 Results and Discussions

For assessment of the effectiveness of the model, the energy consumption model is first validated using the data obtained from the third set of experiments. Subsequently, the predicted results are plotted and compared with their experimental counterparts. In addition, the influence of workpiece curvature on cutting forces and cutting power consumption in milling of curved workpieces are investigated. Later on, constant engagement strategy is compared with conventional cutting to order to confirm the acceptability of the present algorithm. Various milling strategies for variable curved geometry are also studied. The next section deals with validation and comparison of results achieved from experimental and computational investigations.

### 5.5.1 Validation of energy consumption model and comparison of results

This section deals with the model validation and comparison of computational results with their experimental counterpart results to assess performance of the model developed in MATLAB. In order to study the influence of workpiece curvature on power consumption, machining conditions for concave and convex elliptical geometries are kept identical. The parametric form of the elliptical geometry is written as

$$X(t) = a.\cos t \tag{5.30a}$$

$$Y(t) = b.\sin t \tag{5.30b}$$

where $a$ and $b$ are the radius on the X and Y axes respectively and $t$ is curve parameter which ranges from 0 to $2\pi$ for an elliptical geometry. The values of $a$ and $b$ are taken as 60 mm and 36.5 mm respectively during design of workpiece geometry. Figure 5.13 shows the details of elliptical workpiece geometry along with curvature variation from the start to the end of the profile.

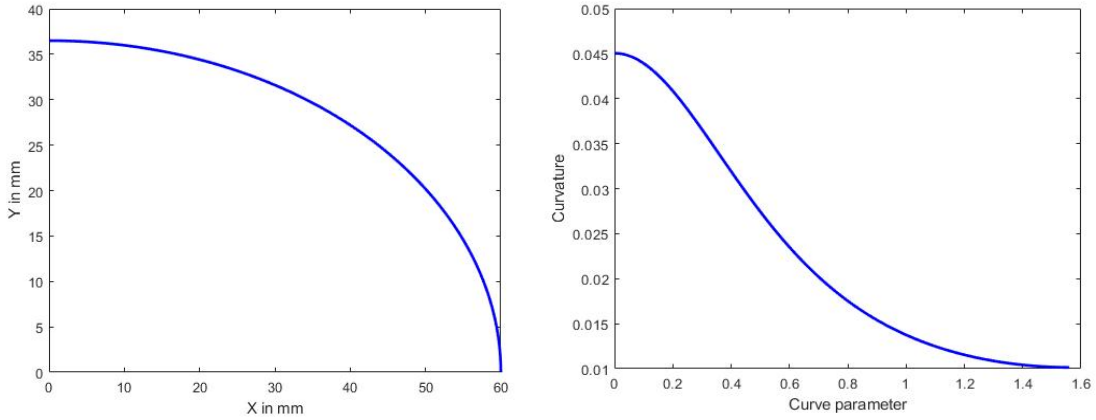


(a) Elliptical geometry in XY plane (b) Curvature variations for ellipse

Fig. 5.13 The details of elliptical workpiece geometry.

The second set of machining experiments given in Table 5.3 is performed to measure and collect experimental force and power consumption data. Later on, the predicted force and power consumption results which are achieved from the proposed model are compared with their measured counterpart. On the basis upon the predicted results, the proposed model is validated with a good agreement. Initially, the variations of cutting force and feed force components are studied with respect to curve parameters along the tool contact path for concave and convex elliptical workpieces. Next, the predicted results are plotted and compared with their measured counterpart results. The variation of power consumption is investigated with respect to curve parameters along the tool contact path for both types of geometries. A comparative study between concave and convex elliptical geometries has also been done on power profiles along the tool contact path.

Figure 5.14 shows the variation of cutting forces and feed forces with respect to curve parameter along the cutter contact path for concave and convex elliptical geometries.

As cutting force and feed force components are major controlling parameters for power consumption in milling of curved geometry, the understanding about variation of these force profiles is essential along the tool contact length. Down milling is performed for both these geometries where the uncut chip thickness varies from the maximum to the minimum value. The start and end of cut are the extreme right and top points of the curved geometry respectively as shown in Fig. 5.13. The cutting force component is gradually increasing for convex elliptical workpiece along the tool contact path from the beginning to end of cut which can be seen from Fig. 5.14a. But it is gradually decreasing for concave geometry. The variation of cutting force profiles for both these geometries is opposite to each other. As the curvature value is gradually decreasing for concave and convex elliptical geometries, the magnitude of uncut chip thickness gradually increases for convex and decreases for concave elliptical geometries. It results into variation in cutting force profiles for both these geometries. From Fig. 5.14b, it is noticed that feed force component is gradually decreasing for convex workpiece and gradually increasing for concave workpiece from the beginning to end of cut. In the presence of workpiece curvature, the feed per tooth along tool contact path and cutter engagement angle vary that lead to the change in the uncut chip thickness and corresponding force value. As there is a change in instantaneous feed per tooth along the tool contact path in the presence of curvature, the uncut chip thickness varies in the feed station. Therefore, the feed force profile varies along the peripheral length for both geometries.

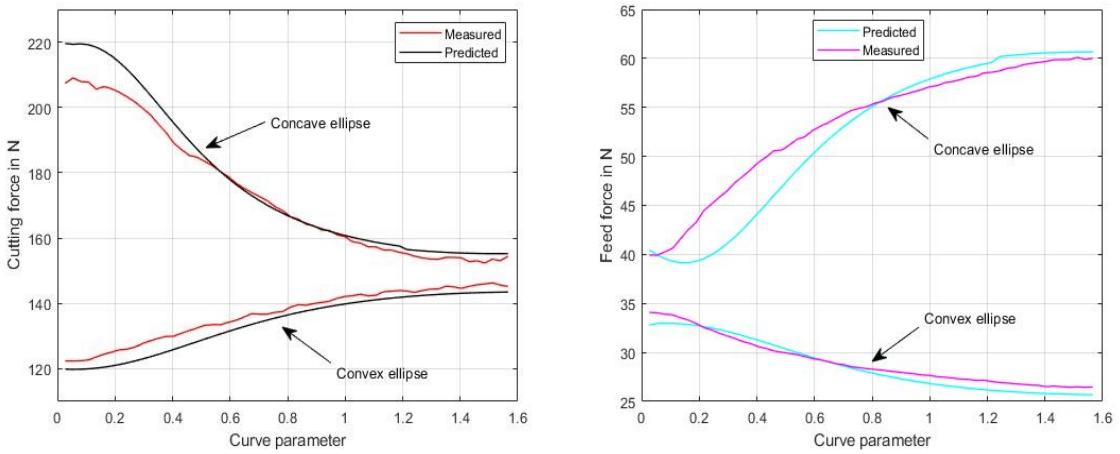


(a) Cutting force variation (b) Feed force variation

Fig. 5.14 Force variation with respect to curve parameter for concave and convex geometries

Figure 5.15 shows the variation of power consumption along the peripheral length for concave and convex elliptical workpieces. In case of concave elliptical geometry, the power profile is gradually decreasing from the start to end of cut as shown in Fig. 5.15a. It happens due to resultant effect of gradual declination of cutting force and inclination of feed force components. In case of convex elliptical geometry, the reverse trend of power profile is observed as shown in Fig. 5.15b. It happens due to the resultant effect of gradual increase of cutting forces and gradual diminishing of feed force components. In addition to that, it is also observed that machining of concave geometries deals with larger cutting forces due to greater tool-workpiece engagement and respective higher chip load. Hence, the higher cutting power consumption is observed due to greater cutting forces. Table 5.7 shows the predicted and measured power along with calculation of error for both concave and convex elliptical workpart. The average prediction error is 1.63% for concave elliptical geometry and 0.91% for convex elliptical geometry which indicates the accuracy and acceptability of the developed model.

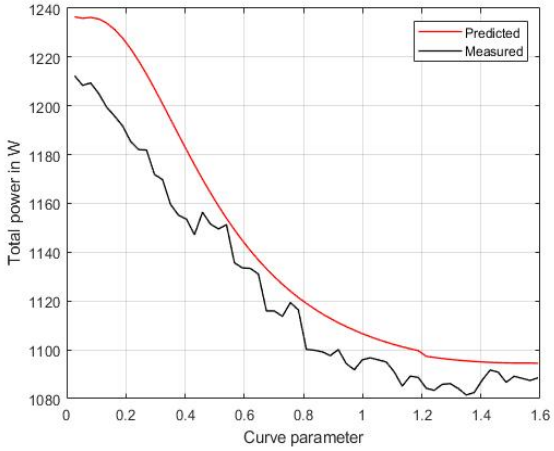


(a) Variation of power consumption for concave elliptical geometry

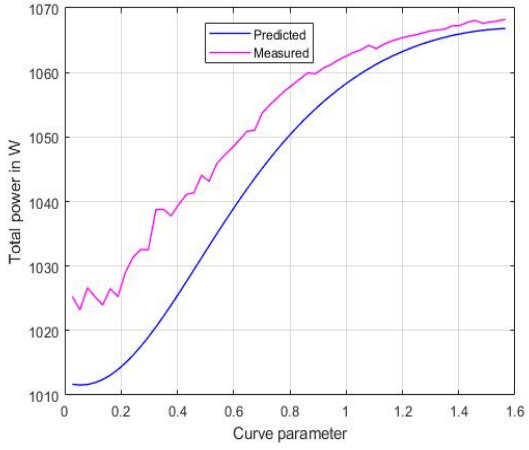


(b) Variation of power consumption for convex elliptical geometry

Fig. 5.15 Comparison of experimental and computational power variations for concave and convex elliptical geometry

Table 5.7 Comparison of the predicted power with measured power at different positions along tool path for concave and convex elliptical geometries

| Sr.No. | Concave elliptical geometry | | | Convex elliptical geometry | | |
|---|---|---|---|---|---|---|
| | Measured power (W) | Predicted power (W) | Prediction error (%) | Measured power (W) | Predicted power (W) | Prediction error (%) |
| 1 | 1235.9 | 1208.3 | 2.27 | 1011.6 | 1027.2 | 1.52 |
| 2 | 1181.9 | 1153.5 | 2.45 | 1025.7 | 1041.5 | 1.51 |
| 3 | 1119 | 1100.1 | 1.71 | 1050.8 | 1060.1 | 0.87 |
| 4 | 1097.3 | 1084.2 | 1.20 | 1063.5 | 1067.5 | 0.37 |
| 5 | 1094.5 | 1088.6 | 0.54 | 1066.8 | 1070.2 | 0.31 |
| | Average prediction error | | 1.63 | Average prediction error | | 0.91 |

### 5.5.2 Comparison of forces for straight, concave and convex circular geometry

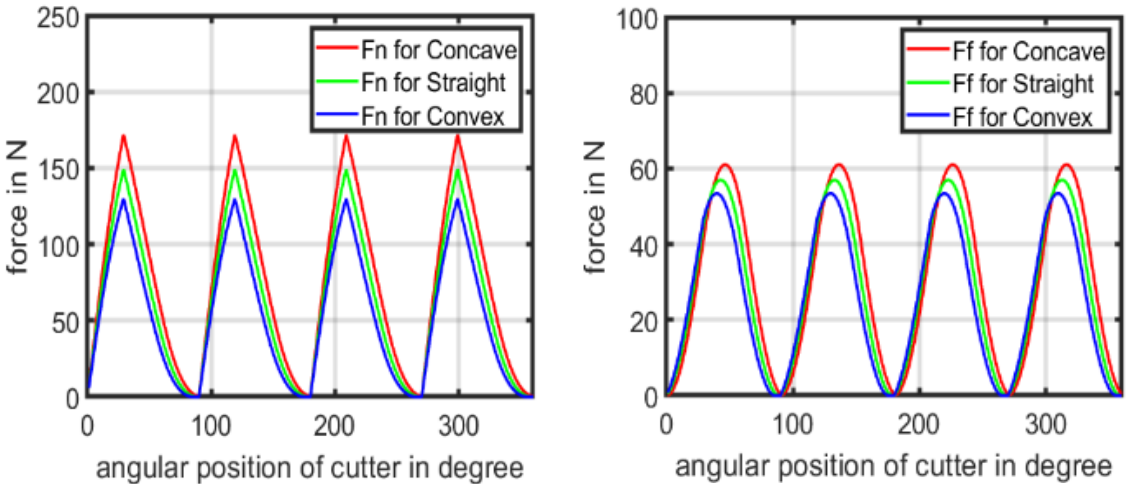


(a) Normal forces (b) Feed forces

Fig. 5.16 Comparison of estimated forces for concave, straight and convex geometry

A comparison between experimental and predicted results regarding forces for single revolution of cutting tool and power consumption are shown in Fig. 5.16 and 5.17. From the Fig. 5.16, it is observed that normal and feed force components are maximum for concave geometry as compared to straight and convex counterparts. This is due to higher chip loads for concave geometry as uncut chip thickness is more. The normal and feed force component are the lowest for convex geometry due to the least amount of chip load w.r.t straight and concave counterparts. Fig. 5.17 shows the estimated power trend for these three geometries along the peripheral length of cut. It is observed that total power consumption is maximum for concave geometry due to higher amount of cutting and feed forces. The total power consumption is the lowest for convex geometry due to the least amount of cutting

force and feed force components. The total power consumption for straight geometry lies between concave and convex geometries.

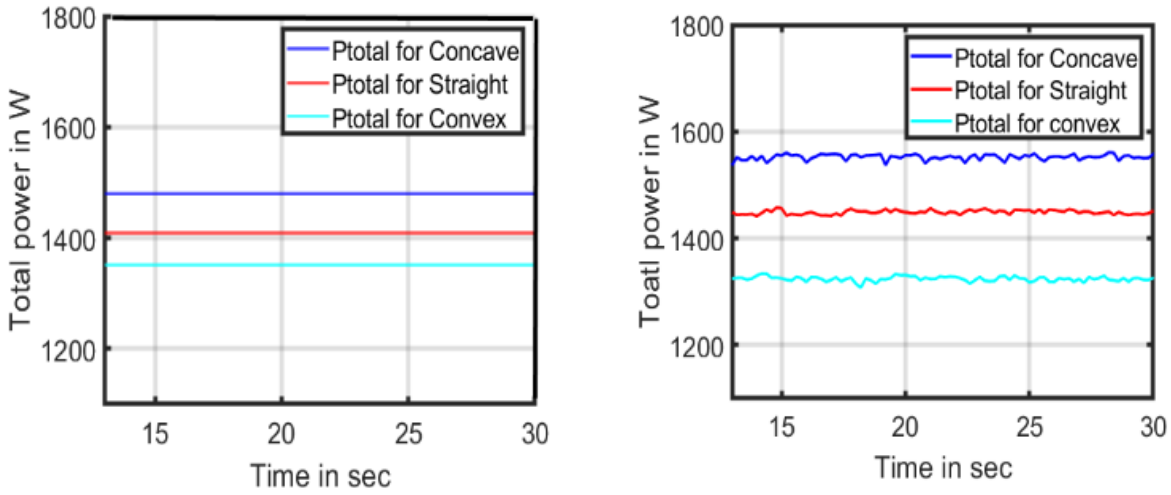


(a) Estimated results (b) Measured results

Fig. 5.17 Comparison of experimental and computational total power for concave, straight and convex geometry

### 5.5.3 Influence of workpiece curvature on cutting force and feed forces

This section deals with the influence of workpiece curvature on cutting force and feed force components for curved elliptical geometries. Figure 5.18 shows the variation of simulated cutting forces and feed forces with respect to workpiece curvature for concave and convex elliptical workpieces. It is seen from the Fig. 5.18a that in case of concave elliptical geometry, the cutting force increases gradually as the value of curvature increases. It takes place due to higher cutter engagement angle and concerned uncut chip thickness that results into higher cutting force component for concave geometry. But the reverse trend is noticed in case of feed force profile for concave geometry which can be seen from Fig. 5.18a. As the magnitude of feed per tooth along the tool contact path decreases gradually with increase of curvature value, the uncut chip thickness is affected that leads to gradual declination in the feed force profile. In case of convex elliptical geometry, the cutting force decreases gradually as the value of curvature increases along the tool contact path which can be seen from Fig. 5.18b. It happens due to reduction of cutter engagement angle and respective uncut chip thickness leading to decrease in cutting force component. But the feed force profile gradually increases as the magnitude of feed per tooth along tool contact path increases due to increase of curvature value.

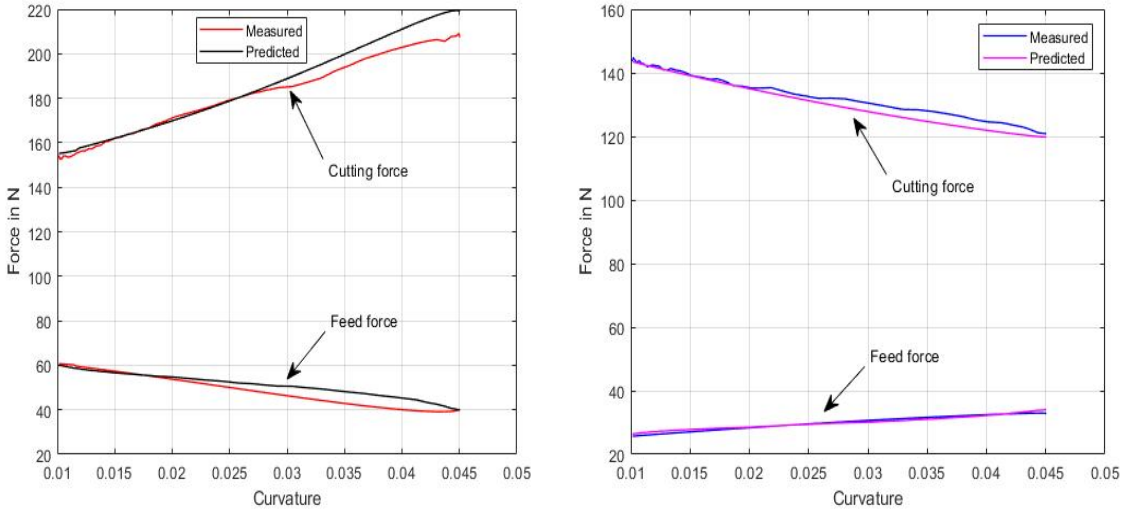


(a) Variation of cutting and feed forces for concave geometry

(b) Variation of cutting and feed forces for convex geometry

Fig. 5.18 Variation of cutting forces and feed forces with respect to curvature for concave and convex elliptical geometries

Figure 5.19 shows the variation of cutting force and feed forces for concave and convex elliptical geometries for performing comparative study between these geometries. From these graphs it is concluded that the workpiece curvature creates significant impacts on both the cutting force and feed force components during machining of variable curved geometry. Hence, the power consumption which is function of cutting force and feed force is influenced by workpiece curvature significantly which has been described in the following subsection.

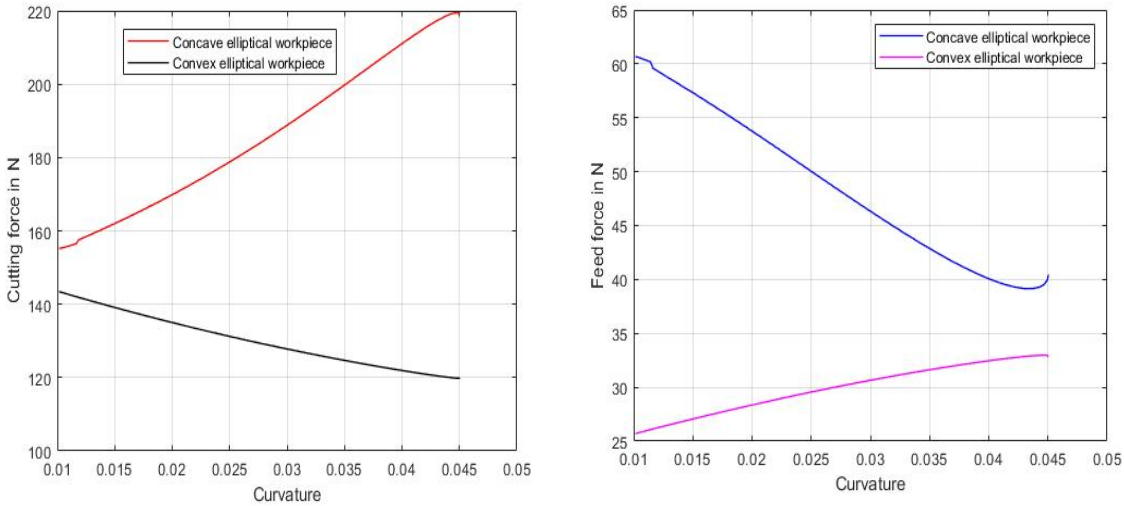


(a) Cutting forces for elliptical geometry

(b) Feed forces for elliptical geometry

Fig. 5.19 Comparison of cutting and feed forces for concave and convex elliptical geometry

### 5.5.4 Influence of workpiece curvature on power consumption

This section deals with the influence of workpiece curvature on power consumption for both concave and convex elliptical geometries. Figure 5.20 shows the variation of total power consumption along the tool contact path for concave and convex elliptical geometries. In case of concave elliptical geometry, the power profile increases gradually along the tool contact path from the start to end of cut which can be seen from Fig. 5.20a. Although for concave geometry, the feed force decreases but cutting force increases, their resultant effect decides the magnitude and nature of cutting power profile. Eventually, the power profile increases gradually along the peripheral length of workpiece for concave elliptical geometry. The reverse trend of cutting power profile is observed in case of convex elliptical geometry as shown in Fig. 5.20b. Although, the feed force increases and cutting force decreases for convex elliptical geometry with increase of curvature value, their combined effect decides the magnitude and nature of cutting power consumption for convex geometry. From the graph, it is concluded that cutting power consumption is a function of cutting and feed forces along with cutting speed of the tool. As cutting power depends on both cutting force and feed force components, the workpiece curvature influences the cutting power consumption significantly during machining of variable curved geometry.

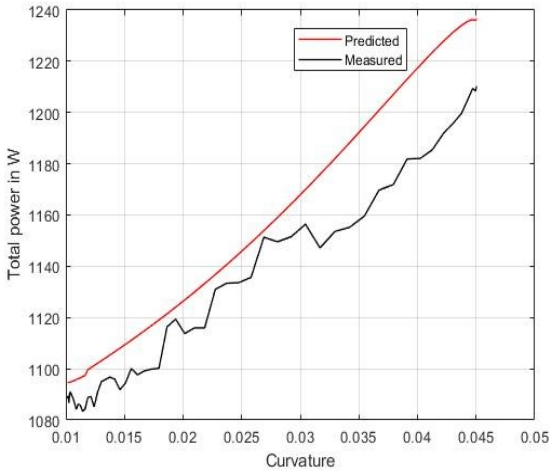


(a) Variation of cutting power for concave geometry

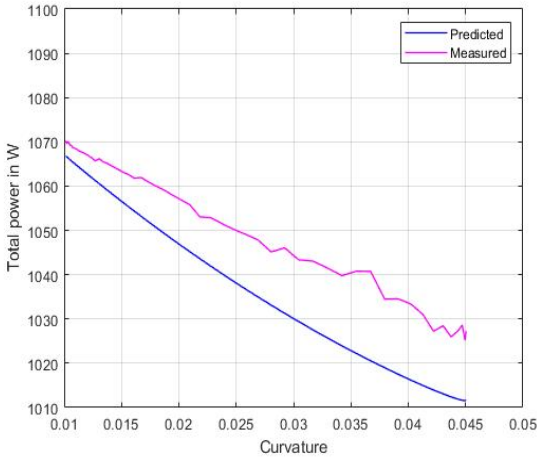


(b) Variation of cutting power for convex geometry

Fig. 5.20 Variation of cutting power consumption with respect to curvature for concave ellipse and convex ellipse geometries

### 5.5.5 Validation of the constant engagement algorithm

This subsection discusses about the experimental results of machining strategy to assess the performance of the proposed approach. The results obtained from the proposed algorithm developed in MATLAB are compared with their conventional counterparts. As a part of variable curved geometry, the sine wave curved workpiece composed of both concave and convex sections is used to implement the constant engagement tool path modification approach. The parametric equation of the sine wave curved geometry is expressed as:

$$X(u) = a.2\pi u, Y(u) = b.\sin(2\pi u) \quad 0 \leq u \leq 1$$

where the magnitudes of coefficients "$a$" and "$b$" are set as 12.1 and 12 respectively. The geometry of the sine wave curved workpiece is shown in Fig. 5.21a. The variation of curvature along the sine wave curve profile is also shown in Fig. 5.21b. The machining experiment is performed from right to left of the curved workpiece.

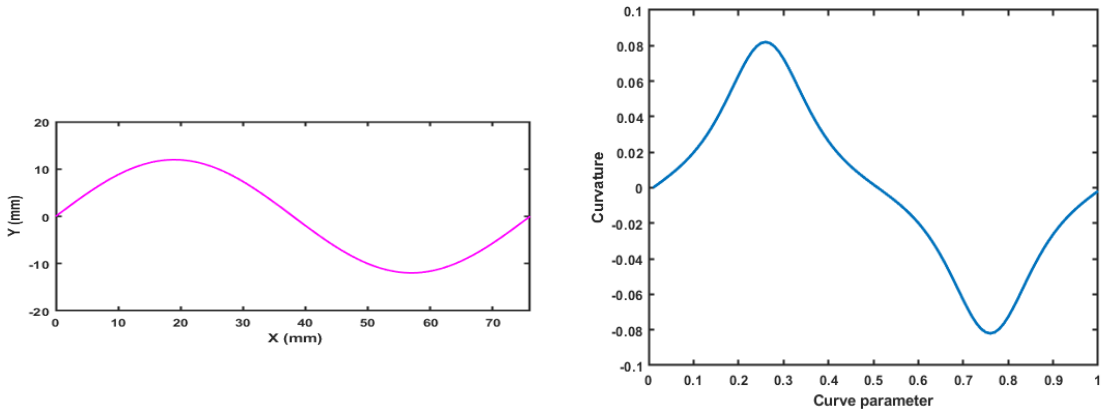


(a) Sine wave curved profile (b) Variation of workpiece curvature

Fig. 5.21 Workpiece geometry along with curvature variation

Based on the sine wave curved geometry, the various variables such as tool center point, entry point, exit point and respective cutter engagement angles are calculated for the aforementioned cutting conditions. In order to assess the efficacy of the proposed approach, the desired engagement angle for machining of variable curved geometry is assumed as same as the engagement angle of machining of straight geometry. The intended engagement angle is computed based on the radius of cutter (r) and the radial depth of cut ($a_e$). This criterion is selected because of maintaining constant tool engagement along the peripheral length of cut in machining of straight geometry where there is no effect of curvature on the process geometry of straight workpiece.

Fig. 5.22 shows the variation of experimental force components for machining of variable curved components using the conventional cutting where tool engagement varies according to workpiece curvature and the constant engagement tool path modification approach maintaining constant tool engagement along the curved profile. It is observed that the two force components ($Fx$ and $Fy$) vary according to workpiece curvature and tool engagement in conventional cutting. The average resultant force which is a vector summation of $Fx$ and $Fy$ components vary along the peripheral length of cut due to variation of tool engagement and concerned chip load in the conventional cutting. The magnitude of the resultant force is lower at convex section whereas, it is higher at concave section of workpiece geometry due to more tool engagement and concerned chip. In case of the practice of the constant engagement tool path modification approach, the two force components ($Fx$ and $Fy$) also vary according to workpiece curvature but the resultant force remains almost constant due to constant tool engagement and concerned chip load.

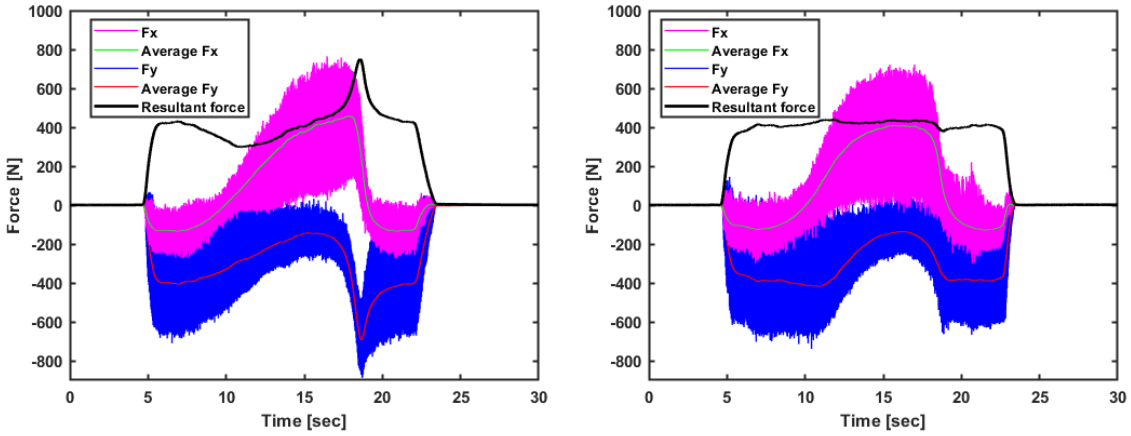


(a) Forces for conventional cutting (b) Forces for constant engagement method

Fig. 5.22 Variation of cutting forces in X and Y direction in conventional cutting and constant engagement method

Fig. 5.23 illustrates the variation of the power consumption during the milling of variable curved components using both methods. It is observed that the power consumption profile remains almost constant over the tool path during the practice of the proposed approach. Although, power profile will fluctuate in concave and convex sections more due to fluctuation of resultant forces which is clearly seen from the Figure 5.22a during the conventional cutting. The power consumption reduces with workpiece curvature in convex curved section whereas, it increases in the concave curved section due to the effect of more tool engagement and workpiece curvature.

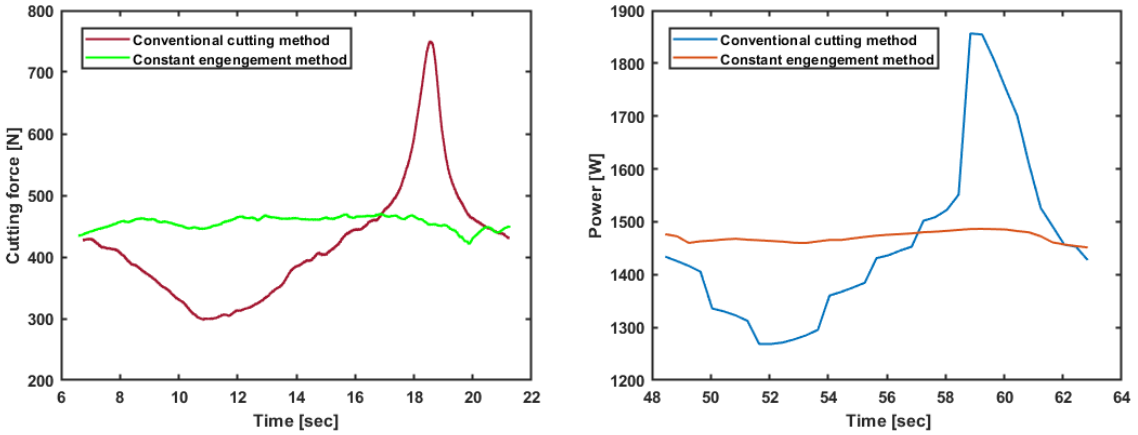


(a) Variation of resultant force (b) Variation of power consumption

Fig. 5.23 Variation of resultant forces and power consumption in conventional cutting and constant engagement method

### 5.5.6 Milling strategies for variable curved geometry

In order to explore towards an energy efficient milling for sustainable machining, a suitable milling strategy needs to be developed along with comparative studies of existing approaches. Therefore, four machining strategies are considered in the present research work for developing energy efficient milling of variable curved geometries under same machining conditions. The strategy-1 describes about conventional cutting in which entire machining process is performed based on contour parallel tool path. Generally, the radial depth of cut is assumed to be constant during finishing cut in this case. The strategy-2 illustrates about the constant engagement tool path modification approach for milling of variable curved geometry where magnitude of engagement angle is calculated based on the specified machining conditions by assuming machining of straight geometry. The determined value of tool engagement is used as a datum/reference in this case. The strategy-3 describes about the constant engagement tool path modification approach where the value of constant engagement angle is chosen based on the minimum engagement angle computed during the practice of strategy-1. Strategy-4 illustrates about the constant engagement tool path modification approach where the magnitude of constant engagement angle is selected based on the maximum engagement angle calculated during the use of strategy-1. The semifinished surface geometries will be different during practicing of abovementioned all these four strategies although, the finished surface geometry remains same. The summary about these four machining strategies are mentioned in the Table 5.8.

Table 5.8 Machining strategies

| Sr. No. | Strategy | Descriptions | Engagement angle |
|---|---|---|---|
| 1 | Strategy-1 | Conventional cutting | Variable |
| 2 | Strategy-2 | Constant Engagement (CE) method with prescribed engagement angle for machining of straight geometry. | Constant |
| 3 | Strategy-3 | Constant Engagement (CE) method with minimum engagement angle. | Constant |
| 4 | Strategy-4 | Constant Engagement (CE) method with maximum engagement angle. | Constant |

Fig. 5.24 shows a typical representation of the modified semi-finished workpiece geometry with respect to original semi-finish workpiece for various strategies. The modified semi-finished workpiece geometry varies during practice of various strategies namely strategy-2, strategy-3 and strategy-4 although, the finish workpiece geometry remains same. Fig. 5.24(a) illustrates the semi-finish workpiece geometry created during the practice of stategy-1 which is an offset planar curve to the finishing geometry offering variation in tool engagement along the milling cutter path. In strategy-2, the semi-finished geometry is modified according to the desired constant engagement value assuming machining along straight geometry. Therefore, the modified semi-finish geometry will be different than the original semi-finish geometry along the cutter path. The modified semi-finished geometry moves towards finished geometry in concave section indicating less cutter engagement. On the contrary, it moves away from the finished geometry in convex section, which indicates more tool engagement during finishing pass as shown in Fig. 5.24(b). The strategy-3 represents the machining situation where proposed algorithm is applied with minimum desired engagement angle. It is noticed from Fig. 5.24(c) that the modified semi-finished workpiece geometry shifts towards finished geometry in concave section representing lesser tool engagement in finishing pass. On other hand, the modified semi-finished workpiece geometry does not shift much as engagement angle is minimum in convex section. The strategy-4 represents the machining situation where the semi-finished geometry is modified with maximum desired engagement angle. It is noticed from Fig. 5.24(d) that, the modified semi-finished geometry does not shift much, as the engagement angle is maximum in

concave section. But, it moves away from the finished geometry in convex section indicating larger cutter engagement during finishing pass. The effective modification in the semi-finished geometry results into maintaining constant tool engagement at the desired level in machining of finishing pass during practicing of strategies-2 to 4.

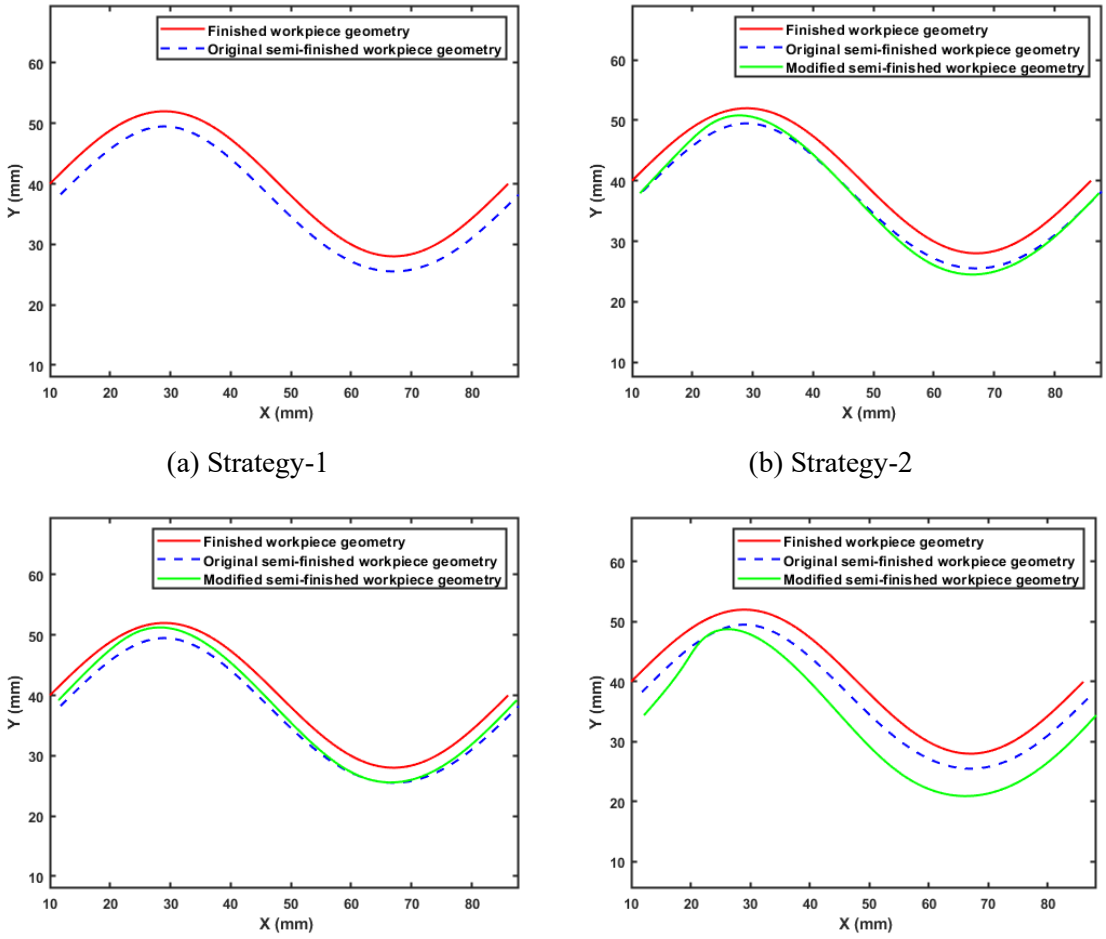


(a) Strategy-1 (b) Strategy-2

(c) Strategy-3 (d) Strategy-4

Fig. 5.24 Typical representation of modified semi-finished workpiece geometry for various strategies

In milling of variable curved component, the determination of uncut chip thickness is essential as it is directly affected by the tool engagement. As the chip load is governed by uncut chip thickness, the respective cutting force and power consumption will also alter with the variation of uncut chip thickness. Fig. 5.25 displays the variation of tool engagement and uncut chip thickness for various machining strategies and their relative comparisons among them. As strategy-1 deals with convention cutting of variable curved geometry, actual variation in tool engagement is observed along the peripheral length of cut which is clearly noticed from Fig. 5.25 (a). It is also noted that the magnitude of engagement angle

is more in concave section as compared to its convex counterparts. Once the proposed constant engagement algorithm is applied to sine wave curved geometry, it is noticed that engagement angle for various strategies 2-4 remained constant throughout the finishing path. The results indicate that the proposed algorithm eliminates the variation in engagement angle caused by workpiece curvature during milling of curved geometries. Although, the nature of the engagement angle remained at constant level along the cutter path, their magnitudes will be different as it is decided based on the different strategies. In similar way, the variations of the maximum uncut chip thickness for various strategies are seen from Fig. 5.25 (b). Although, the nature of the uncut chip thickness remains constant level along the tool path for strategies 2-4, their values will be different due to different magnitudes of engagement angles.

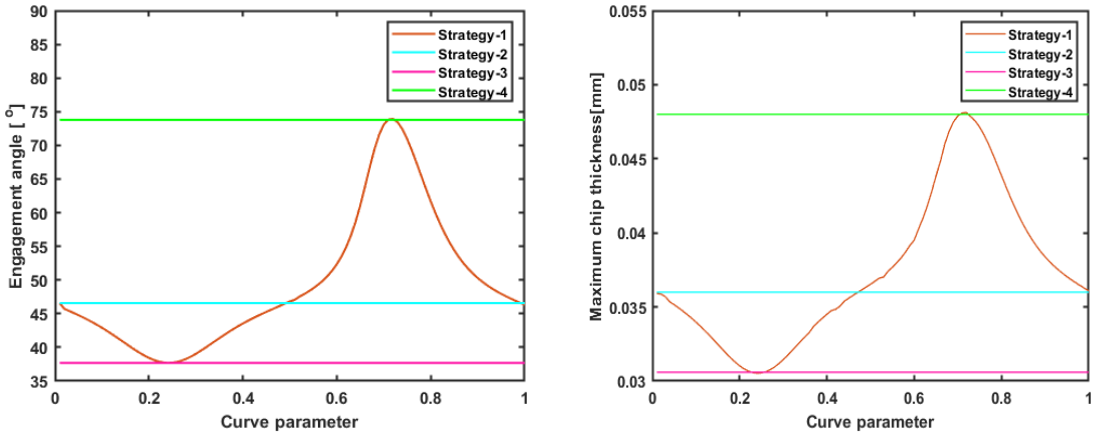


(a) Tool engagement (b) Uncut chip thickness

Fig. 5.25 Comparison of tool engagement and uncut chip thickness for various strategies

Fig. 5.26 illustrates the variation of resultant force profile along the cutter path for various machining strategies and their comparison among each other. It is observed that the average resultant force varies along the peripheral length of cut due to variation of tool engagement and concerned chip thickness for strategy-1. The average resultant force profile fluctuates more in concave segment as compared to convex section in the presence of curvature and tool engagement. When the proposed algorithm (Strategy 2-4) is applied for machining of variable curved geometries, it is evident that the resultant cutting force remains almost constant along the entire cutter path. While strategy-2 is applied, the magnitude of resultant cutting force at peak point is reduced up to 40% in the concave section and increased by almost 50% in convex section as compared with strategy-1. In similar way,

while strategy-3 is used, the magnitude of resultant cutting force at peak point is reduced up to 60% in the concave section and remains almost same in convex section as compared with strategy-1. While strategy-4 is applied, the magnitude of resultant cutting force at valley point is increased up to 150% in the convex section and remains almost same in concave section as compared with strategy-1. With applications of the suggested algorithm, the fluctuations of resultant cutting force get reduced up to large extent but the magnitude of the force may increase or decrease depending upon the selection criteria of the constant value of the engagement angle.

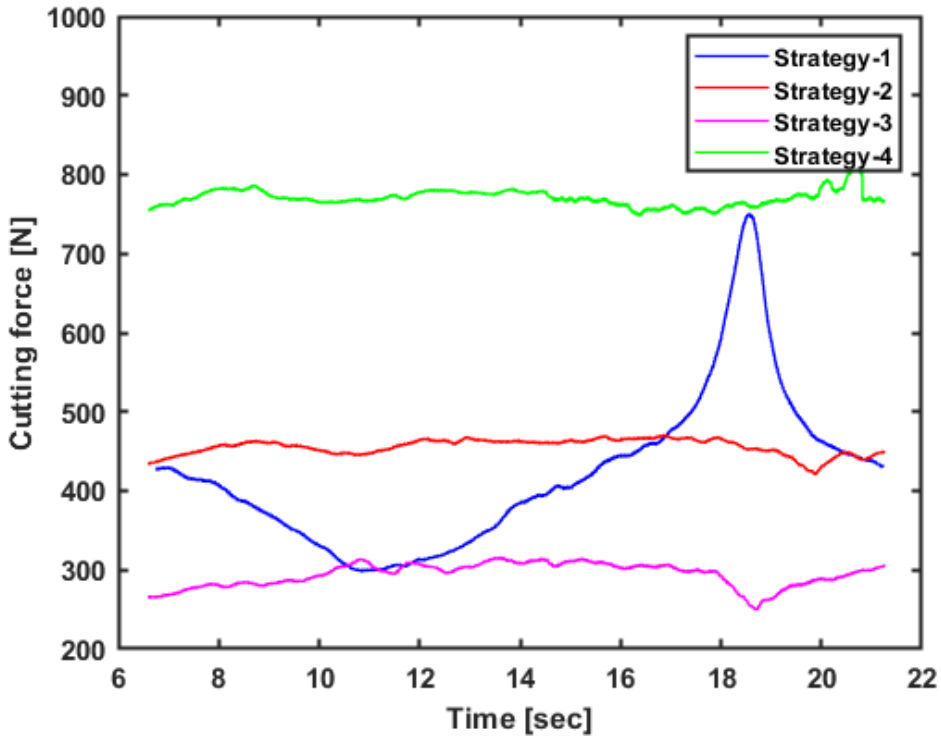


Fig. 5.26 Comparison of cutting force variations for various strategies

Fig. 5.27 depicts the variation of power profile along the cutter path for various machining strategies and their comparison among each other. It is observed that the fluctuations in total power consumption are reduced up to large extend while applying the proposed machining strategies 2-4. In case of strategy 2, the fluctuation of power consumption is reduced by around 22% at concave section and increased by almost 16% at convex section as compared to the strategy-1. In case of strategy-3, the fluctuation of power consumption is reduced by around 33% at concave segment and remains almost constant at convex section as compared to the strategy-1. The fluctuations of power consumption

profile during machining with strategy 4 is reduced by as much as 48% at convex section and remains same at concave section in comparison to strategy 1.

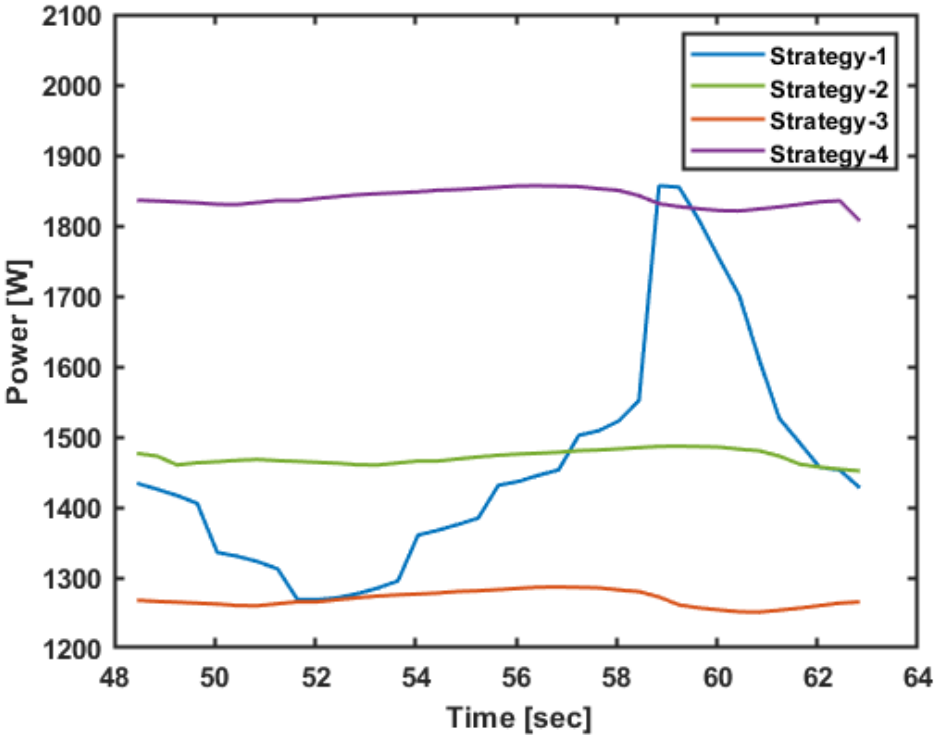


Fig. 5.27 Comparison of power profile variation for various strategies

### 5.5.7 Realization of energy efficiencies in machining

For comprehending the energy efficient machining, the material removal rate (MRR) and specific energy consumption (SEC) are used as the predominant output measures in peripheral milling. The material removal rate (MRR) in peripheral milling is influenced by axial depth of cut (ADOC), radial depth of cut (RDOC) and feed rate. In the present work, ADOC and feed rate remain constant throughout the milling operation. Therefore, the MRR majorly depends on RDOC which is influenced by uncut chip thickness. Fig. 5.28 depicts the variation of MRR along the cutter path for various strategies and their comparison among each other. As MRR is directly proportional to tool engagement, the actual variation in MRR is observed along peripheral length for strategy-1. The value of MRR is more in concave section as compared to its convex counterparts due to more tool engagement in this specific section. While, the proposed constant engagement algorithm is applied to sine wave curved geometry, it is noticed that the MRR for various strategies 2-4 remained constant in finishing path.

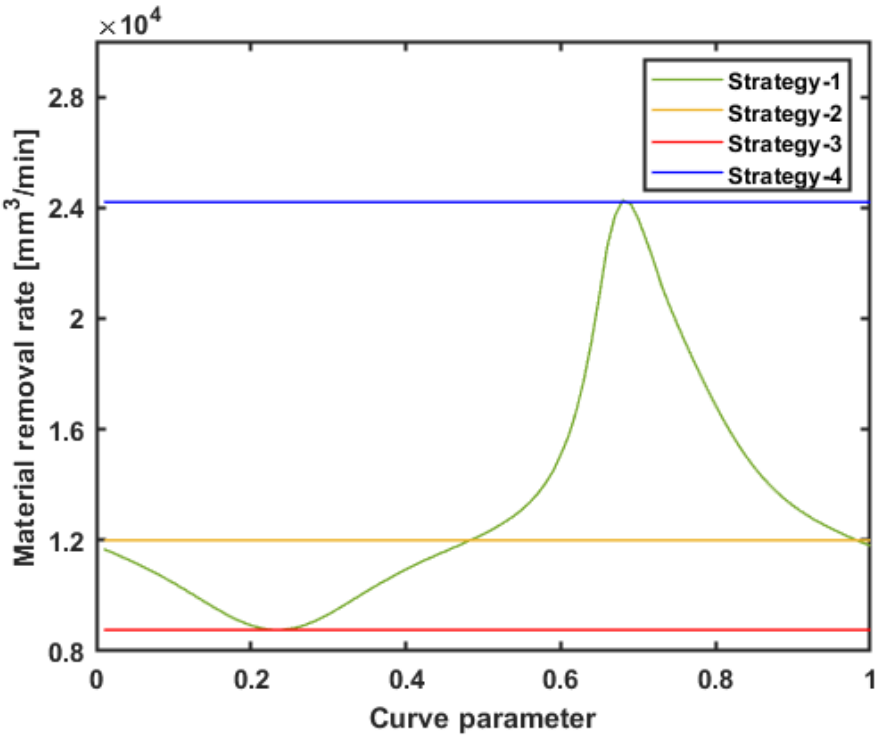


Fig. 5.28 Comparison of MRR variation for various machining strategies

Fig. 5.29 shows the energy consumption and specific cutting energy consumption for various strategies. The magnitudes of energy consumption and specific energy consumption is compared easily among various machining strategies. It is observed that energy consumption as well as specific energy consumption are minimum for strategy-3 and maximum for strategy-4 as compared to startegy-1. The energy consumption and specific cutting energy under strategy-2 remains almost same as strategy-1. Therefore, the strategy-3 is recommended for energy efficient milling process as the energy consumption is reduced almost 22 % with respect to the conventional cutting method.

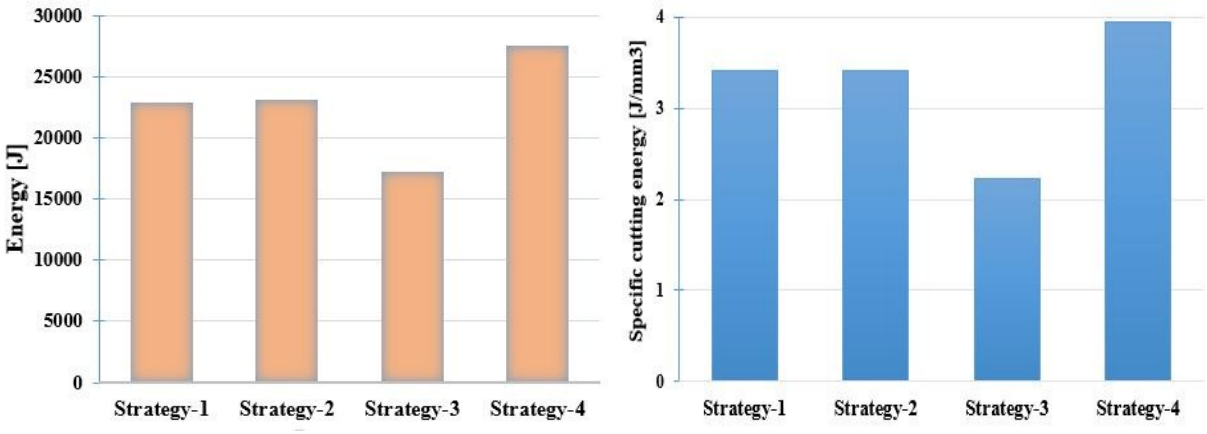


(a) Energy consumption (b) Specific energy consumption

Fig. 5.29 Comparison of energy and specific energy consumption for various machining strategies

## 5.6 Concluding Remarks

The current chapter represents a hybrid model of cutting power and a machining strategy based on constant engagement cutter path modification for milling of variable curved geometry towards developing an energy efficient machining. The analytical model for prediction of cutting forces and power is developed in MATLAB and validated using experimental work. It is found that the proposed model estimates the cutting forces and power within ± 2% in comparison with the experimental results. The model predicted and the experimental results are found to follow the similar trend for curved concave and convex geometries. The model also concentrates on the influence of workpiece curvature on cutting power consumption during milling of variable curved geometry. The proposed constant engagement algorithm is able to produce a modified semi-finish toolpath by offsetting the trajectory of modified semi-finished surface obtained by controlling constant engagement at the desired level at each feed station during the finishing pass. As tool engagement is constant, the uncut chip thickness and corresponding force and energy consumption remain constant. Therefore, the cutting power fluctuation that takes place due to variation of workpiece curvature is reduced up to certain extent. These models are validated by the milling experimental results.

# Chapter 6

# Error Compensation in Milling of Curved Geometries

## 6.1 Introduction

Inaccuracies in machined components caused by tool and workpiece deflections in peripheral milling are major obstacles in producing precise and quality parts. The physics and surface error generation mechanism in the presence of tool and workpiece deflections in peripheral milling were investigated in details in chapter 4. This chapter describes about error compensation approaches to eliminate the errors up to a large extent. It examines a hybrid error compensation methodology consisting of constant tool engagement and tool path modification approaches to overcome deflection induced surface errors. Both concave and convex surfaces have been used to examine the efficacy of the proposed hybrid error compensation scheme. The proposed hybrid error compensation scheme is validated using machining experiments. According to the proposed error compensation scheme, the CNC part programming for the modified tool path is made in off-line mode and implemented in real time cutting without hampering the actual machining productivity. The following subsection discusses the hybrid error compensation methodology adopted in the present work.

## 6.2 Hybrid Error Compensation Methodology

It is already mentioned in earlier chapter that in case of curved geometry, the workpiece curvature impacts the milling process geometry and respective cutting forces significantly, making the machining of curved geometries more complex and challenging. As the magnitude of workpiece curvature is different at each point along the periphery of workpiece, it is necessary to develop an error compensation technique which will take care of the concerned chip load at every feed station in the presence of tool and workpiece deflections. In order to take care of the concerned chip load, the feed rate regulation technique is proposed by various researchers. By varying the value of feed per tooth along the cutter contact path at every feed station, the concerned chip load can be computed and adjusted according to workpiece curvature during actual cutting. The feed rate regulation technique can be applicable for machining up to a certain extent to control the chip load during machining. The application of feed rate regulation technique makes a large technical challenge for CNC controller which should have capability to regulate feed rate based on

the initial workpiece geometry. The hardware modification of controller and other technical barriers are the biggest issues for implementing the feed rate regulation techniques. The machining time is also influenced depending upon actual feed rate during machining. Therefore, in most of the situations, the feed rate regulation technique is not adopted by machining practitioner universally.

Another alternative approach is the use of multi-pass cutting strategy which is more about conservative practice of process planning to regulate the concerned chip load and control the cutting forces. If the cutting force is regulated properly, deflection induced error can be controlled and reduced up to large extent. During practicing of multi-pass cutting, the cutting conditions such as RDOC, ADOC, feed rate and tool diameter need to be chosen carefully so that cutting forces will be minimal resulting into minimum surface errors on the machined component. Although, this method reduces the magnitude of surface errors but it greatly diminishes the machining productivity by increasing machining cycle time. Therefore, the multi-pass cutting technique creates a big obstacle to machining practitioner for adopting and practicing it in real scenario.

In order to take care of the limitations of feed rate regulation and multi-pass cutting techniques, off-line tool path modification scheme can be used as a suitable technique for reduction of surface error during machining of curved geometries. The proposed method deals with modification of the tool path based on estimated the tool and workpiece deflections and associated surface errors along the entire peripheral length of workpiece. The computed points generating the respective tool path will be made in off-line mode without hamper the machining productivity and machining efficiency. Therefore, the proposed methodology can be used as an alternative and prospective approach for machining of curved geometry.

The tool path modification approach significantly improves dimensional accuracy due to reduction of RDOC and respective chip load. As the ADOC remains same in this case, geometric error also remains invariant due to linear shifting of surface error profile towards the datum line. As the surface error profile remains identical after adopting this approach, significant reduction in geometric error is not observed. Keeping this limitation in mind, a new hybrid method is proposed to compensate the surface error magnitude as well as reduce the variation of surface errors along the axial length of cut. The proposed methodology illustrates the milling of curved surface in two stages. Firstly, it creates the

modified semi-finishing geometry with the help of developed constant engagement algorithm. Secondly, it generates the desired finished geometry with a modified tool path by the application mirror image method. The following subsections discusses about the constant engagement algorithm and tool path modification based on mirror image method.

### 6.2.1 Constant engagement (CE) method

It is already mentioned in chapter 5 that during machining of curved geometries, change in engagement angle happen continuously along tool path in presence of workpiece curvature. Fluctuations in force profile take place due to alteration in tool engagement and concerned uncut chip thickness in the presence of workpiece curvature. The continuous, non-uniform fluctuations in force profile create an obstacle in stable machining and also causes variation in surface error profile along tool path due to tool-workpiece deflection. Process planners struggle to increase machining productivity and accuracy because of the variation of the surface error profile with workpiece curvature. Regulation of engagement along the tool path turns into a useful tool in this circumstance for generating uniform tolerances on the manufactured components. A machining strategy which deals with constant engagement of tool along the peripheral length of cut helps to maintain consistent uncut chip thickness and concerned chip load and surface error profile. This constant engagement method is already discussed in details in chapter 5. This strategy helps to reduce the cutting power fluctuation occurred due to variation of workpiece curvature by regulating tool-workpiece engagement. This strategy also minimizes surface error variation along tool path during machining of curved geometries. The strategy proposes the machining of the curved parts into two steps. In first step, the modified semi-finished workpiece geometry is produced with the help of constant engagement algorithm that is discussed in chapter 5. In second step, the desired finish workpiece geometry is created by using the parallel tool path generation method. The tool path modification is done in first stage of the proposed hybrid error compensation methodology for maintaining constant chip load during finishing path. Although the constant engagement method reduces the chip load and maintains uniform surface error due to decreasing in force fluctuations but, certain amount of uniform surface error is present on the machined surface. Therefore, the mirror image method is applied to achieve the desired accuracy by reducing surface errors.

### 6.2.2 Mirror image (MI) method

During machining of straight and circular geometries, cutting force is maintained constant by keeping constant engagement angle, radial depth of cut, and maximum uncut chip thickness. As a result, the surface error profile remains invariant along the tool path. In order to reduce surface errors, the error compensation strategy based on tool path modification approach is applied. In this strategy, compensation can be accomplished by linear shifting of tool position along the normal direction of the machined surface by an amount of deflection value. The deflection value can be obtained from tool and workpiece deflection model developed in Chapter-3. As the machined surface is straight, the locus of tool center will also become straight maintaining a constant offset value which is equal to the deflection value as shown in Fig.6.1. For straight and circular geometries, the calculation procedure is little easy as offset distance calculation in one feed station is sufficient. There is no need to calculate the offset distance in every feed station as it remains constant along the tool path.

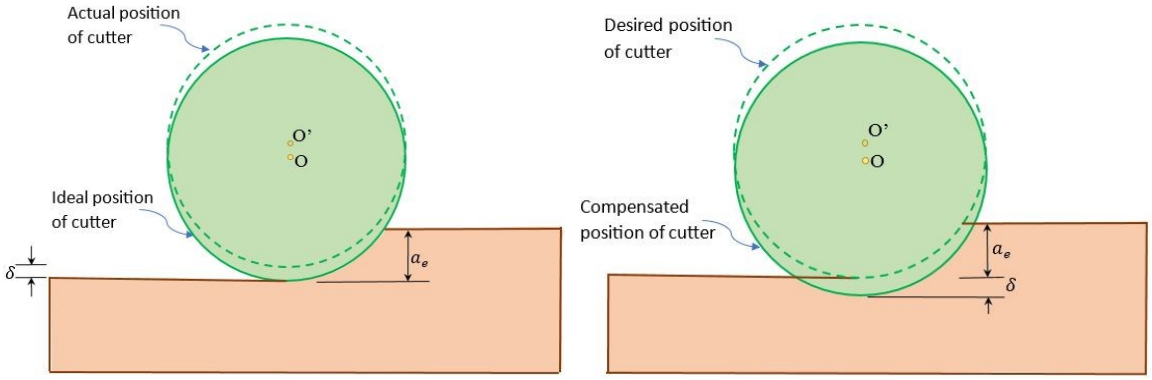


(a) Before compensation (b) After compensation

Fig. 6.1 Error compensation in straight geometry

In case of machining curved geometries, deflection induced surface error varies continuously along the tool path. Therefore, it is essential to compute deflection value at each and every feed station along the tool path making the compensation procedure more complicated. A schematic representation of a tool path with and without compensation scheme is shown in Fig. 6.2. A certain amount of material will be left on the machined surface as an undercut value as depicted in Fig. 6.2. The actual machined profile that is produced in this instance will differ from the desired machined profile and this surface error is caused by a variety of variables, including the cutting conditions, tool material, workpiece material the tool overhang, etc. For reduction of error between actual and desired machined profile, tool can be shifted towards machined surface by an amount that is dependent on

local value of surface error at feed station. In other terms, a compensated tool path is a variable offset curve of an ideal tool path. The offset value or compensation must be calculated for entire tool path. One method for calculating the compensation path is to shift the ideal path locally by an amount that is precisely equal to the estimated surface error at that location but in the other direction. This straightforward technique of mirroring will not work. The modified location modifies the radial depth of cut when compensations are performed by mirroring based on local surface error values, which changes the cutting forces and, consequently, the deflections. An iterative method must be used to compensate and generate a machined surface that is within the desired tolerances of the surface.

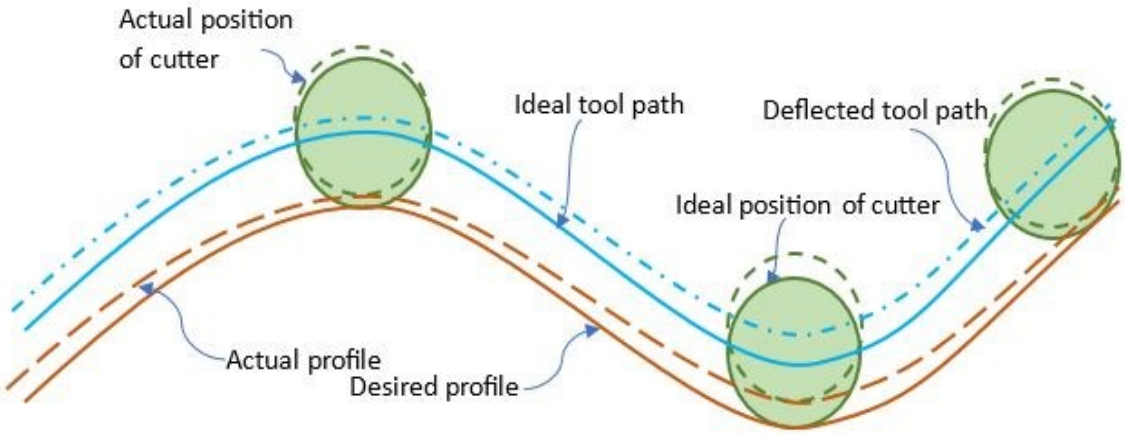


(a) Without error compensation

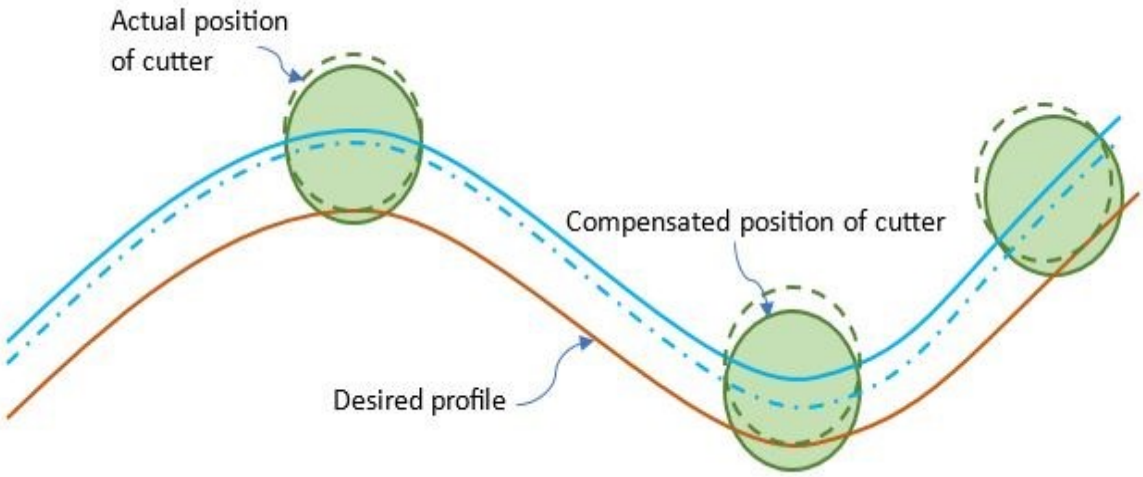


(b) With error compensation

Fig. 6.2 Error compensation in machining of curved geometries

Fig. 6.3 illustrates the iterative tool path compensation method at a single feed station. The ideal tool position is one that is programmed without taking deflection value

into account, whereas the actual tool position is one that considers the tool-workpiece deflection value. The tool position is shifted in the following iteration by the same amount as the surface error, but in the opposite direction, as depicted in the Fig. 6.3. Process geometry, cutting forces and surface error value are recalculated for this new tool position. The procedure is repeated until the surface error computed lies within the prescribed tolerance zone. This iterative compensation strategy is performed at every feed station throughout the whole tool path.

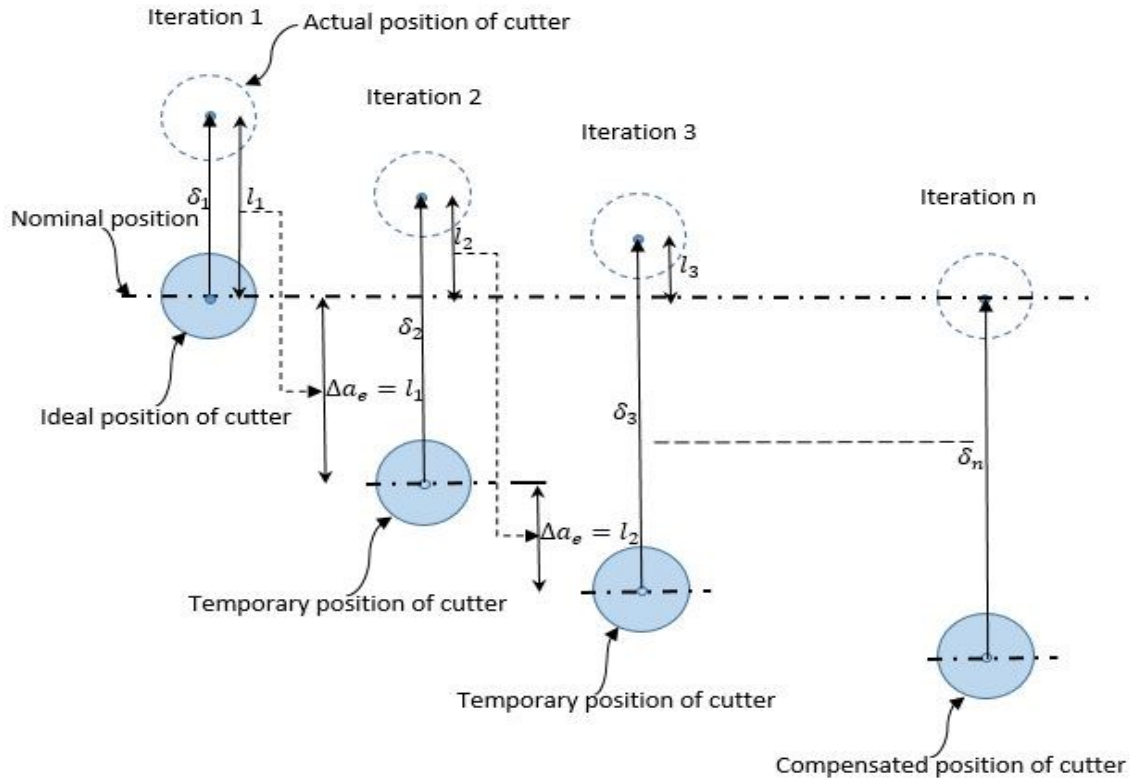


Fig. 6.3 Compensation methodology

The steps of the compensation technique can be expressed as follows:

Step 1: The tool and workpiece deflection are calculated at each feed station.

Step2: The current deflection value is added to the radial depth of cut to obtain the new modified radial depth of cut. Process geometry variables, cutting forces and associated deflections are recalculated using new modified radial depth of cut to determine new deflection value.

Step 3: The aforementioned procedure (Step 1-Step 2) is performed again until convergence is obtained.

Because of the complex nature of the tool and the workpiece engagement, the surface error profile along the axial depth of the cut is very non-uniform. To apply offset compensation method, it is important to select the appropriate reference for compensation. There are various options for choosing a reference plane for compensation since the fluctuation of surface error along the axial direction is significantly non-uniform.

#### 6.2.2.1 Application of MI method for thick-walled geometries

In case of machining of thick-walled curved geometries, this method allows for tool path modification without sacrificing machining productivity based on the estimated tool deflections and the associated surface error. This necessitates surface error prediction or measurement by a suitable means before compensation. A deflection model using analytical or numerical method can forecast the surface error. Here, a cantilever beam deflection model is used as discussed in Chapter 3. The Fig. 6.4 shows a flow chart for the tool deflection induced error compensation.

#### 6.2.2.2 Application of MI method for thin-walled geometries

As discussed in chapter 4, the machining of thin-walled geometries differs from that of thick-walled geometries in a number of ways. Workpiece deflections and resulting surface error are impacted by end effects and the effect of workpiece thinning during machining in both a qualitative and quantitative manner. This makes compensation technique complex for thin-walled geometries. The Fig. 6.5 shows a flow chart for the workpiece deflection induced error compensation.

### 6.2.3 Tool path modification (TPM) using hybrid method (HM)

The constant engagement method reduces axial variation in deflection induced surface errors during machining of variable curved geometries. An offset compensation method improves dimensional accuracy but geometrical tolerance remains same. In order to improve both dimensional and geometrical accuracy, a hybrid error compensation method is proposed based on constant engagement and offset compensation method. The method proposes the compensation of milling of curved surface in two stages: first, creating the modified semi-finishing geometry with the proposed constant engagement algorithm,

and then creating the desired finished geometry with a tool path modification by mirror image method.

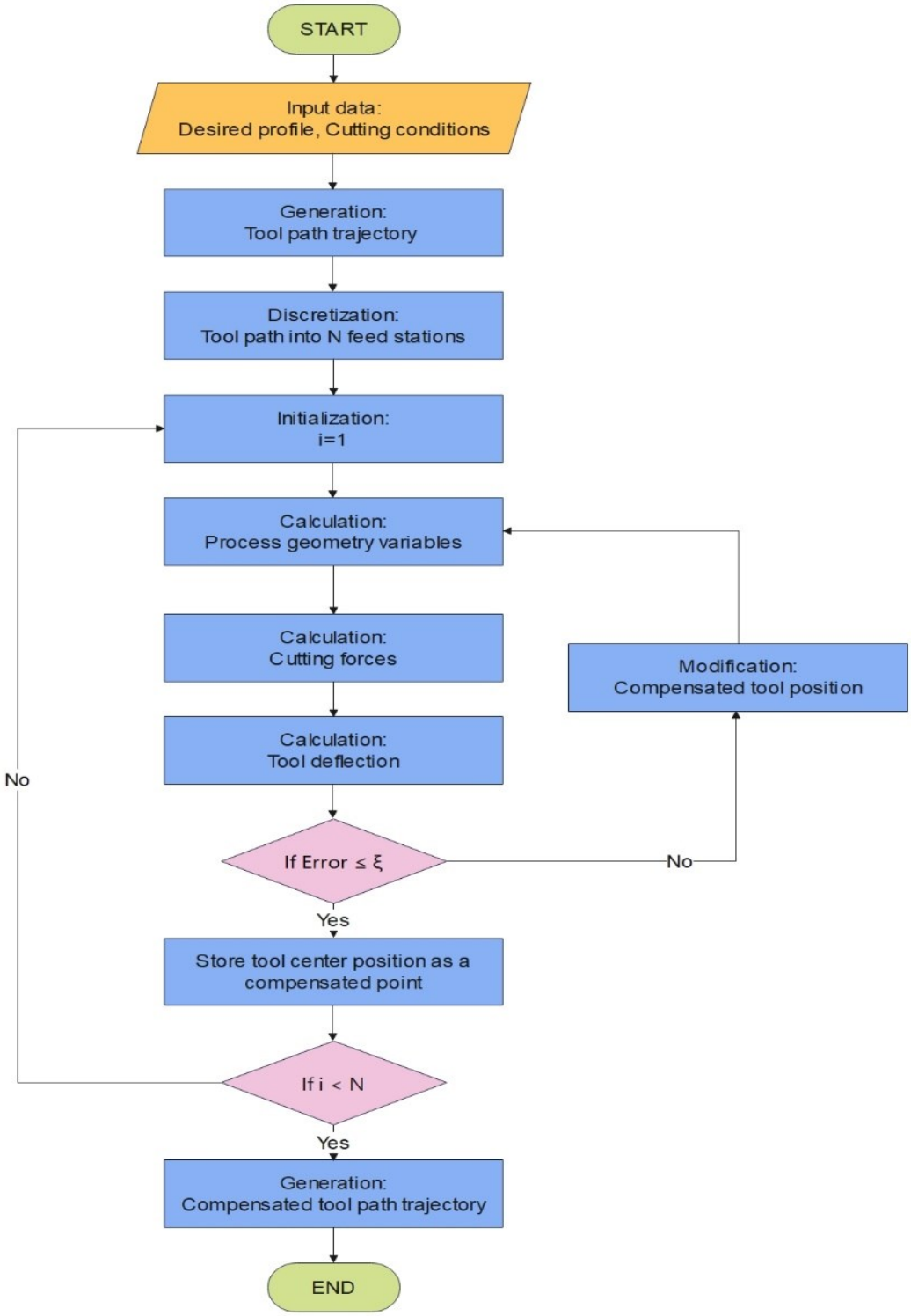


Fig. 6.4 Tool deflection induced error compensation

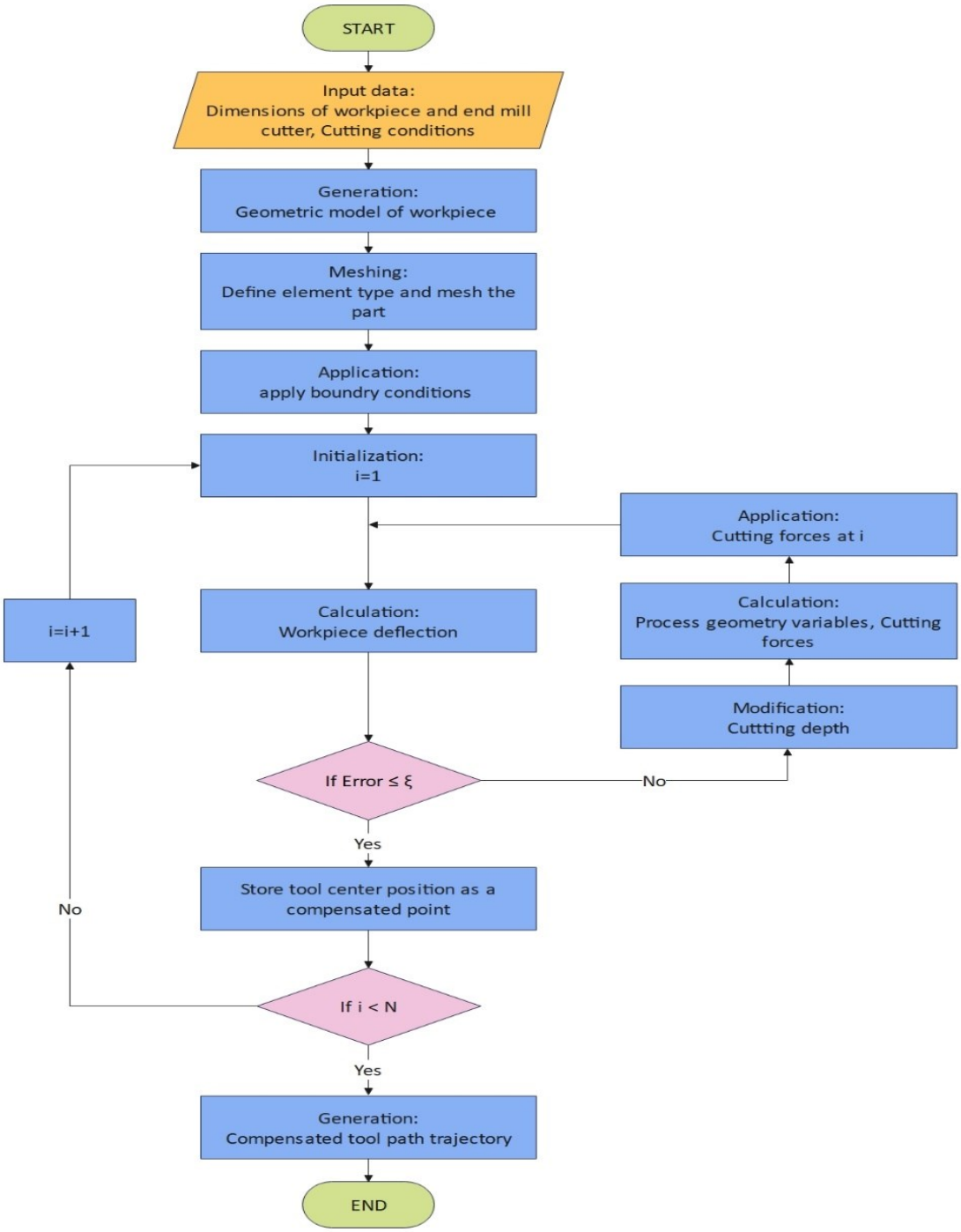


Fig. 6.5 Workpiece deflection induced error compensation

## 6.3 Machining Experiments

To evaluate the effectiveness of the proposed compensation technique and determine the potential of accuracy improvements for machined parts, machining experiments are performed on thick-walled and thin-walled curved geometries. The convex and concave geometries are two different kinds of curved geometries used for these experiments. The dimensional details of both types of curved geometries are given in

Chapter-3. The workpiece material for the machining experiments is Aluminium 6351-T6, and the tool is a high speed steel (HSS) end mill cutter with a 16 mm diameter. Table 6.2 provides a list of the various cutting conditions used for the machining experiments.

On the basis of the various computational models covered in Chapter 3, the cutter deflections and surface inaccuracy are calculated. Later on, machining experiments are conducted using a computer program that implements error compensation based on the algorithm covered in previous section. Three sets of machining experiments are performed on curved geometry. First, workpiece is machined without error compensation. After machining, surface error is measured along both peripheral and axial directions of machined components. Second set of machining experiments is carried out with offset compensation method (Mirror method). Based on hybrid method discussed earlier, third set of machining experiments are conducted with tool path compensation. In hybrid method, the lowest value along contour parallel tool path is used as desired constant engagement angle for modification of tool path in the proposed algorithm and it is maintained constant along entire tool path.

Table 6.1 Machining conditions for elliptical component

| **Workpiece geometry** / **Cutting parameters** | **Elliptical thick-walled geometries** | **Elliptical thin-walled geometries** |
|---|---|---|
| Axial depth of cut | 1 mm | 2 mm |
| Radial depth of cut | 25 mm | 15 mm |
| Length of overhang | 77 mm | 44 mm |
| Spindle speed | 2000 rpm | |
| Nominal feed rate | 400 mm/min | |
| Nominal feed per tooth | 0.05 mm/tooth | |
| Tool diameter | 16 mm | |
| Tool helix angle | 30º | |
| Number of teeth of the cutter | 4 | |
| Milling type | Down milling with no coolant | |

In each case, the middle plane of the estimated surface error profile is chosen as the reference, and the estimated surface error values in this plane are used as inputs for the compensation scheme to produce a modified tool path trajectory. In contrast, in a different

circumstance, a different compensation reference would be more appropriate. Surface errors after compensation using hybrid method (HM) are measured at same locations and compared with compensated results using offline compensation method (Mirror method (MM)), uncompensated measured results and estimated deflection results. The following subsections give a detailed analysis of compensated, uncompensated, and estimated results.

## 6.4 Results and Discussion

The thick-walled and thin-walled geometries are used to validate the proposed compensation approach (Hybrid method). Later on, offset compensation method (i.e. mirror method) used for comparison studies to further show the effectiveness of the proposed compensation method. In hybrid method, the lowest value along contour parallel tool path is used as desired constant engagement angle for modification of tool path by proposed algorithm and it is maintained constant along entire tool path. Experimental results are compared at four sections for both concave and convex elliptical geometries as shown in Fig.6.6. The section 1-3 represents start, mid and end section of workpiece along axial direction and section-4 represents section at particular height along peripheral direction of geometry. The section-1 lies in minimum curvature region whereas section-3 lies in maximum curvature region of workpiece.

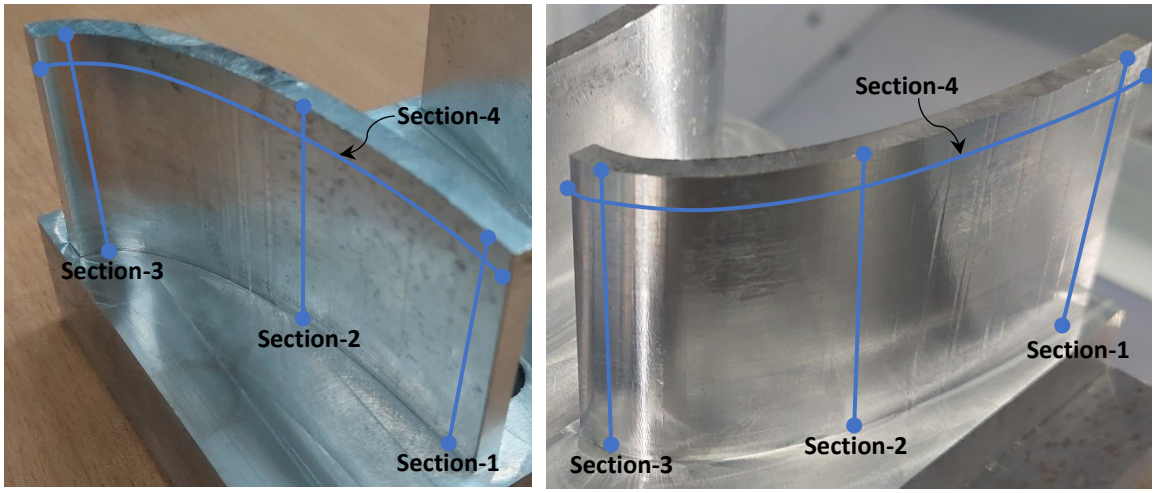


(a) Concave surface (b) Convex surface

Fig. 6.6 Illustration of four selected sections of elliptical geometry

### 6.4.1 Comparison of results with and without compensation scheme for thick-walled geometry

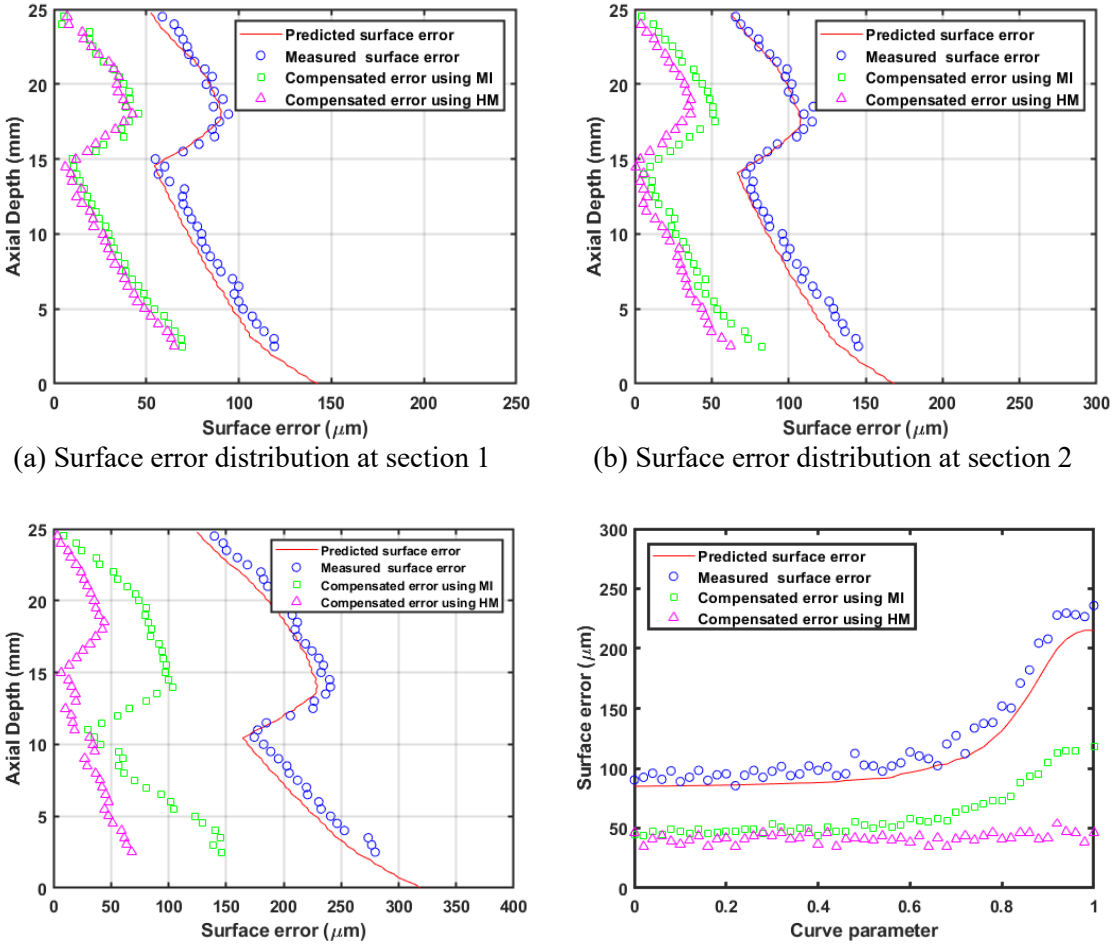


(a) Surface error distribution at section 1

(b) Surface error distribution at section 2

(c) Surface error distribution at section 3

(d) Surface error distribution at section 4

Fig. 6.7 Predicted and measured surface errors before and after compensation at four sections of the concave thick-walled geometry

The predicted and measured surface errors at four selected sections of the concave thick-walled geometry before and after compensation are shown in Fig. 6.7. The outcomes demonstrate that the proposed compensation approach significantly increases machined surface accuracy. It is important to note that, the surface error profile in terms of range and position of kinks does not remain constant after application of the proposed error compensation scheme. As the desired engagement angle is selected at section-1, surface error profile remains same after application of proposed method. But it changes after some time which can be observed at section-2 due to effect of constant engagement method. Significant amount of variation in surface error profile after implication of proposed compensation scheme is seen at section-3. But, surface error profile remains unchanged at

all sections 1-3 after application of mirror method. This proves that when the mirror method is used, the surface error profile is translated linearly from the uncompensated location to the nominal position. It can be concluded that the mirror method significantly improves the dimensional accuracy of elliptical workpiece but not the geometric error. Due to the unchanged surface error profile following the use of the mirror method, the improvements in geometric errors are negligible. Fig.6.7 (d) demonstrates that surface error along peripheral direction of workpiece improves significantly using hybrid method as compared to mirror image method. Surface error remains almost same at section-4 after implication of hybrid method but it varies continuously in case of mirror method. The variation of axial and peripheral surface errors at various sections of workpiece are provided in Table 6.2 and Table 6.3.

Table 6.2 Variation of range of axial surface errors at various sections

| **Section No.** | **Predicted results without compensation [$\mu m$]** | **Measured results without compensation [$\mu m$]** | **Compensated results using Mirror method [$\mu m$]** | **Compensated results using Hybrid method [$\mu m$]** |
|---|---|---|---|---|
| Section-1 | 71 | 73 | 70 | 66 |
| Section-2 | 77 | 80 | 83 | 62 |
| Section-3 | 123 | 129 | 122 | 64 |

Table 6.3 Variation of surface error along peripheral direction of workpiece at section-4

| **Section No.** | **Predicted results without compensation [$\mu m$]** | **Measured results of without compensation [$\mu m$]** | **Compensated results using Mirror method [$\mu m$]** | **Compensated results using Hybrid method [$\mu m$]** |
|---|---|---|---|---|
| Section-1 | 83 | 90 | 49 | 46 |
| Section-2 | 96 | 101 | 55 | 49 |
| Section-3 | 203 | 217 | 109 | 47 |

Fig. 6.8 illustrates the predicted and measured surface errors at four selected sections of the convex thick-walled geometry before and after compensation. It can be seen that surface accuracy improves remarkably after application of proposed error compensation methodology. Unlike concave geometries, desired engagement angle for milling of convex elliptical geometries is selected at section-3 results into unchanged surface error profile after

compensation using hybrid method at this section. Changes in surface error profile up to certain extent is observed at section-2. Among all sections, section-3 observed large amount of change in surface error profile in terms of range of surface error values and position of kinks due to large difference between engagement angle and desired engagement angle. Profile of surface error is maintained constant along peripheral length of workpiece using hybrid method. Surface error along peripheral direction of workpiece is reduced remarkably after implication of hybrid method compared to mirror method which can be seen at section-4 as illustrated in Fig. 6.8(d). The variation of axial and peripheral surface errors at various sections of workpiece are provided in Table 6.4 and Table 6.5.

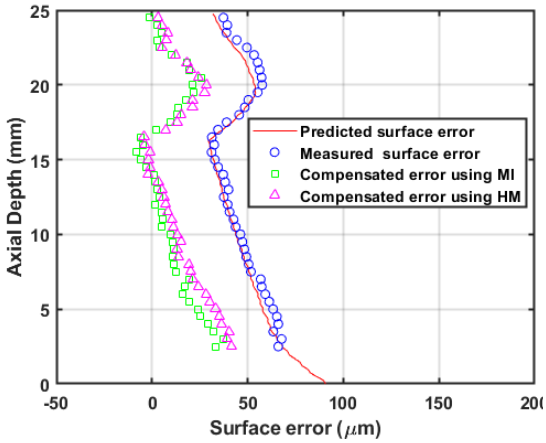


(a) Surface error distribution at section 1

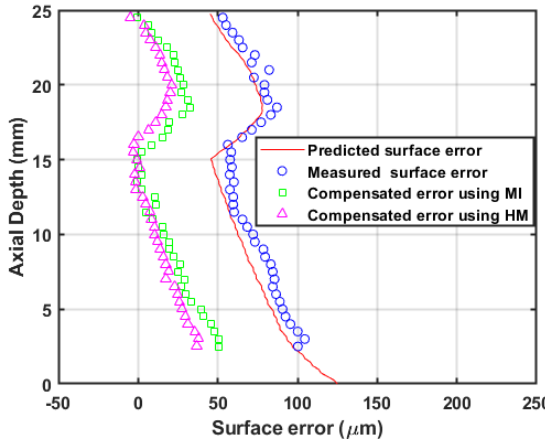


(b) Surface error distribution at section 2

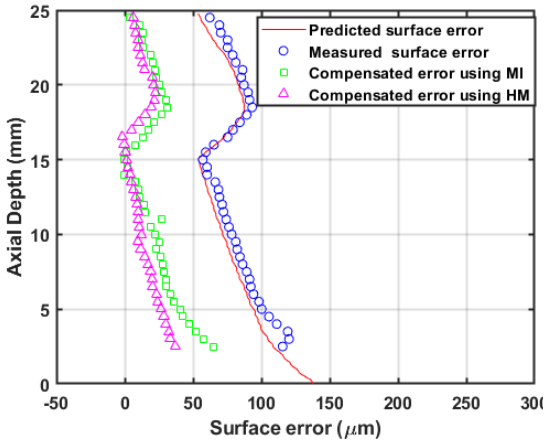


(c) Surface error distribution at section 3

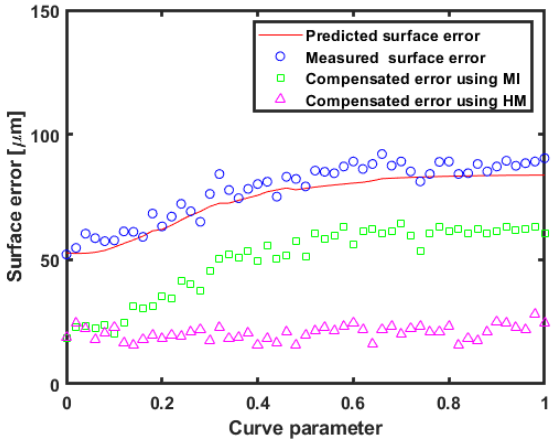


(d) Surface error distribution at section 4

Fig. 6.8 Predicted and measured surface errors before and after compensation at four sections of the convex thick-walled geometry

Table 6.4 Variation of range of surface error at various sections

| Section No. | Predicted results without compensation [$\mu m$] | Measured results without compensation [$\mu m$] | Compensated results using Mirror method [$\mu m$] | Compensated results using Hybrid method [$\mu m$] |
|---|---|---|---|---|
| Section-1 | 79 | 83 | 79 | 43 |
| Section-2 | 59 | 61 | 59 | 47 |
| Section-3 | 54 | 53 | 48 | 51 |

Table 6.5 Variation of surface error along peripheral direction of workpiece at section-4

| Section No. | Predicted results without compensation [$\mu m$] | Measured results without compensation [$\mu m$] | Compensated results using Mirror method [$\mu m$] | Compensated results using Hybrid method [$\mu m$] |
|---|---|---|---|---|
| Section-1 | 98 | 91 | 60 | 29 |
| Section-2 | 78 | 74 | 51 | 25 |
| Section-3 | 62 | 57 | 23 | 27 |

### 6.4.2 Comparison of results with and without compensation scheme for thin-walled geometry

The predicted and measured surface errors at four chosen sections of the concave thin-walled geometry before and after compensation are shown in Fig. 6.9. The changes in process geometry variables, cutting forces, surface errors with workpiece curvature, thinning effect, end effects and variation on rigidity of workpiece with workpiece curvature have taken into account for error compensation of thin-walled curved geometries. The results demonstrate the effectiveness of the proposed compensation methodology in reducing surface error in machining of thin-walled curved geometries. It is evident that the implementation of a proposed compensating approach has significantly decreased surface error on machined components. It's important to note that, after the introduction of a proposed compensation scheme, the profile of surface error changes in terms of range of error values and position of kinks as compared to mirror method. Also, surface error profile is maintained almost constant along peripheral direction of workpiece. The variation of axial and peripheral surface errors at various sections of workpiece are provided in Table 6.6 and Table 6.7.

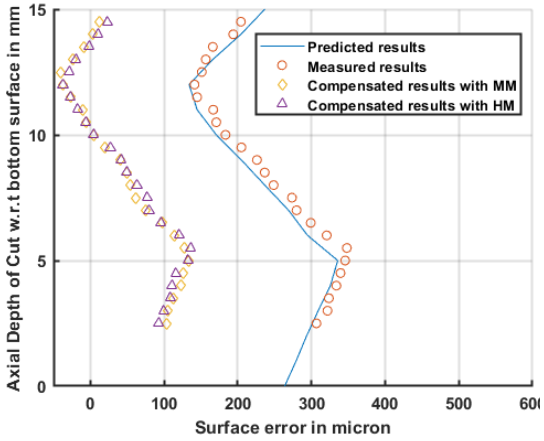


(a) Surface error distribution at section 1

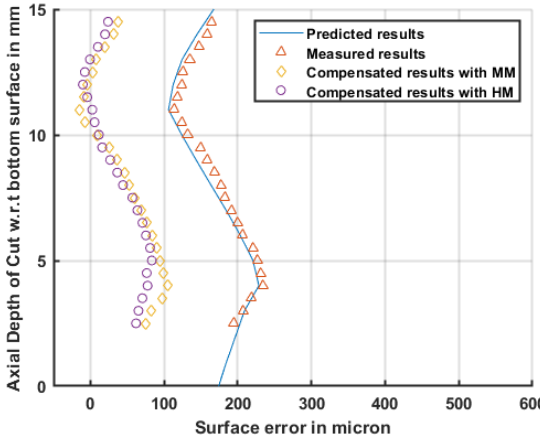


(b) Surface error distribution at section 2

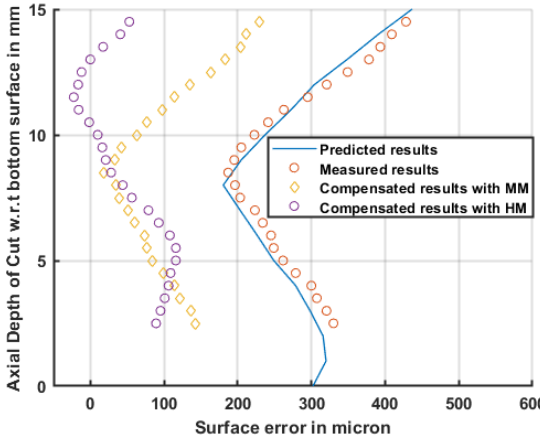


(c) Surface error distribution at section 3

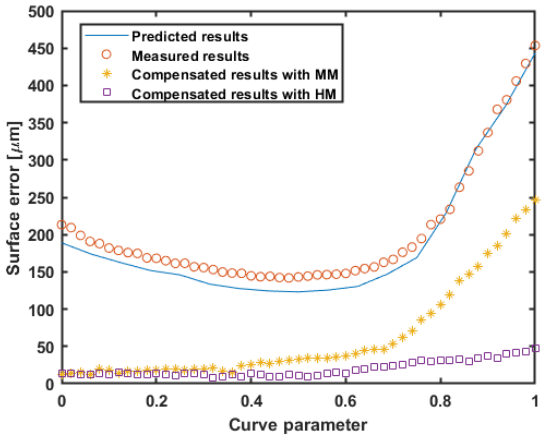


(d) Surface error distribution at section 4

Fig. 6.9 Predicted and measured surface errors before and after compensation at four sections of the concave thin-walled geometry

Table 6.6 Variation of range of surface error at various sections

| **Section No.** | **Predicted results without compensation [$\mu m$]** | **Measured results without compensation [$\mu m$]** | **Compensated results using Mirror method [$\mu m$]** | **Compensated results using Hybrid method [$\mu m$]** |
|---|---|---|---|---|
| Section-1 | 192 | 203 | 189 | 193 |
| Section-2 | 121 | 125 | 123 | 101 |
| Section-3 | 264 | 241 | 234 | 129 |

Table 6.7 Variation of surface error along peripheral direction of workpiece at section-4

| Section No. | Predicted results without compensation [$\mu m$] | Measured results without compensation [$\mu m$] | Compensated results using Mirror method [$\mu m$] | Compensated results using Hybrid method [$\mu m$] |
|---|---|---|---|---|
| Section-1 | 192 | 205 | 14 | 17 |
| Section-2 | 141 | 164 | 43 | 14 |
| Section-3 | 427 | 432 | 231 | 47 |

Fig. 6.10 illustrates the predicted and measured surface errors at four selected sections of the convex thin-walled geometry before and after compensation. Similar to concave geometries, surface error reduces remarkably after application of proposed compensation scheme. As profile of surface error changes, the proposed scheme significantly improves not only dimensional accuracy but also geometric tolerances. The variation of axial and peripheral surface errors at various sections of workpiece are provided in Table 6.8 and Table 6.9.

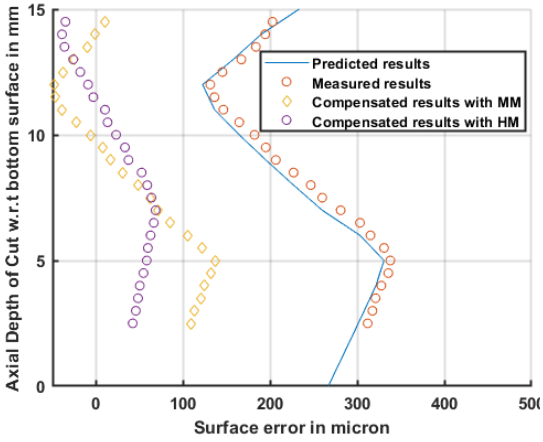


(a) Surface error distribution at section 1

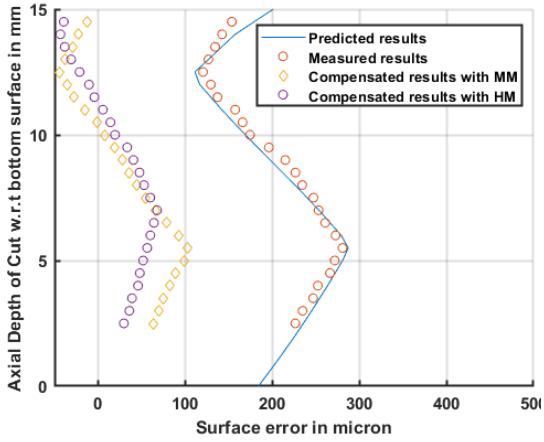


(b) Surface error distribution at section 2

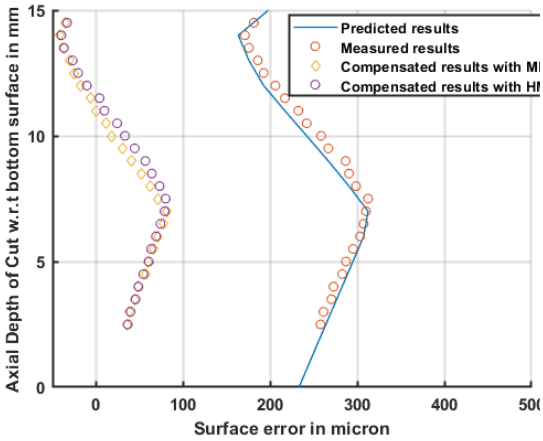


(c) Surface error distribution at section 3

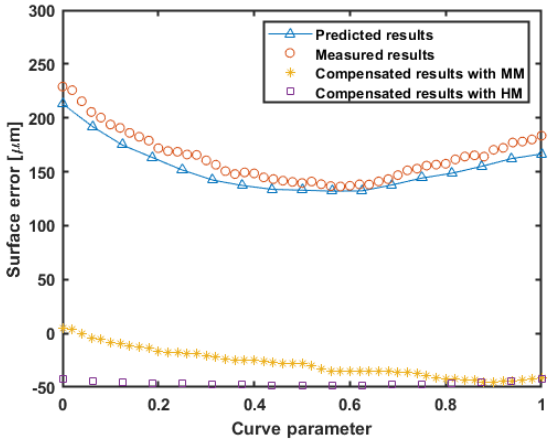


(d) Surface error distribution at section 4

Fig. 6.10 Predicted and measured surface errors before and after compensation at four sections of the convex thin-walled geometry

Table 6.8 Variation of range of surface error at various sections

| Section No. | Predicted results without compensation [$\mu m$] | Measured results without compensation [$\mu m$] | Compensated results using Mirror method [$\mu m$] | Compensated results using Hybrid method [$\mu m$] |
|---|---|---|---|---|
| Section-1 | 221 | 227 | 191 | 108 |
| Section-2 | 175 | 179 | 153 | 115 |
| Section-3 | 142 | 146 | 137 | 134 |

Table 6.9 Variation of surface error along peripheral direction of workpiece at section-4

| Section No. | Predicted results without compensation [$\mu m$] | Measured results without compensation [$\mu m$] | Compensated results using Mirror method [$\mu m$] | Compensated results using Hybrid method [$\mu m$] |
|---|---|---|---|---|
| Section-1 | 199 | 225 | 2 | -45 |
| Section-2 | 148 | 152 | -26 | -49 |
| Section-3 | 165 | 184 | -41 | -43 |

Based on the analysis of experimental and computational results, surface accuracy can be improved by 80% to 90% by using the proposed error compensation methodology. As a generic technique, this methodology can be applied to any type of production process, including job production, mass production, and batch production, without increasing machining time and utilizing full potential of the machine capabilities.

## 6.5 Concluding Remarks

In this chapter, a hybrid method for surface error compensation in the machining of curved geometries is presented. In this case, the fluctuation in process geometry, cutting forces, and surface error with workpiece curvature are taken into account for error compensation. Machining experiments have been conducted to evaluate the efficacy of the proposed compensation scheme. According to the results reported here, surface errors caused by deflections can be decreased up to large extent for curved geometries. The proposed approach will be a helpful tool for process planners and product designers for selection of process parameters and accomplishment of part tolerances.

# Chapter 7

# Conclusions

## 7.1 Summary

This thesis investigates the surface errors caused by tool and workpiece deflections and energy consumption in the machining of curved geometries. This is accomplished through the implementation of computer simulations and numerous machining experiments. According to the study, static tool and workpiece deformations during the machining are a significant problem since they not only affect dimensional accuracy but also geometric accuracy. Also, energy efficiency has become an integral part of metal cutting processes to improve economic and environmental performance, and increase competitiveness. Therefore, the main goal of the current research study is accurate prediction of tool and workpiece deflection induced surface errors and energy consumption in machining of curved geometries and minimize them to produce high-quality parts.

Surface errors and energy consumption are forecasted and analyzed using computational simulations of a milling process. It involves computing a number of different components, such as process geometry, cutting forces, cutting power, tool and workpiece deflections, and surface errors. The individual components used to simulate the milling process are presented with thorough explanation. These computational models are required in order to accurately forecast surface errors caused by tool or workpiece deflections and energy consumption in milling process. All these computational models are verified through machining experiments and estimated results are compared with their measured results to assess the efficacy of the proposed models.

Additionally, the present work incorporates many aspects related to the milling of curved geometries which include

a) Variation of surface error with RDOC and ADOC
b) Machining of concave and convex curved geometries
c) Effects of workpiece curvature on surface errors
d) Effects of workpiece curvature on cutting forces and cutting power
e) Study of milling strategies for curved geometries for constant tool engagement
f) Study of energy efficient machining
g) Study of error compensation in milling of curved geometries

## 7.2 Major Conclusions

The following significant conclusions are drawn from the work done and results discussed in the previous chapters:

- The proposed cutting types (Type I to Type VI) will give a comprehensive knowledge base about characterization of the machined surface for any machining conditions of milling.
- Surface error profiles in the machining of thin-walled straight, concave and convex geometries differ from their thick-walled counterparts both quantitatively and qualitatively. Although, the error profiles observed in few types of cutting in thick-wall machining and thin-wall machining are similar, the surface generation mechanism is completely different for them. A better comprehension about surface error generation described in the present thesis will help process planners in determining the best machining conditions and in implementing error compensation techniques.
- The ADOC and RDOC used as cutting conditions for milling can be converted easily into three important angular parameters namely engagement angle, sweep angle and tooth spacing angle based on mechanics of milling. These three parameters are more convenient to estimate surface error profiles and location of kinks in a machined surface.
- The predicted machined surface is capable to provide the three-dimensional visualization of actual machined surface with magnitudes of dimensional and geometric errors without conducting actual machining experiments and part measurements. As a result, it will be helpful to shorten the manufacturing lead time for new product development.
- In machining of thick-walled curved geometries, only alteration in cutting forces due to workpiece curvature is main factor in variation in surface errors. But, in machining of thin-walled curved geometries, the variation in cutting forces and workpiece rigidity due to workpiece curvature, variation in workpiece rigidity due to thinning effects, and end effects are major factors that cause the variation in surface errors in the machined component.

- Convex and concave sections on a machined surface should be taken into consideration while planning the process for peripheral milling of curved geometries. Process geometry variables, cutting forces, and surface error differ significantly between these two cases for given cutting parameters such as speed, feed, and depth of cut.
- For accurate estimation of power consumption, the role of workpiece curvature is significant, and it needs to be incorporated in the model. Otherwise, erroneous results are expected in the predicted force components and power consumption.
- Energy efficient machining strategy reduces energy consumption during machining of curved geometries by almost 22%. It also provides stable machining and reduces cutting force fluctuations, which increases the tool life due to reduction in tool wear.
- The proposed off-line hybrid error compensation method significantly improves dimensional and geometric accuracies by reducing surface errors caused due to tool or workpiece deflections. A reduction of 80% to 90% in tool and workpiece deflection errors is achieved for machining of curved geometries without sacrificing machining productivity.

From the present study covering computational models and machining experiments, it is observed that workpiece curvature has a significant impact on process geometry, cutting forces, cutting power, and surface errors during machining of curved geometries. This necessitates that machining of curved geometries should be treated differently from machining of straight geometries in terms of process planning. Additionally, different approaches should be taken when machining convex and concave geometries. A generic classification scheme of various types of cutting offers a fundamental framework for process planners and machining practitioners to fully understand and characterize dimensional and geometric errors under various machining conditions. A proposed machining strategy based on constant engagement cutter path modification for milling of variable curved geometries helps in developing energy efficient machining. An offline compensation method presented here for curved geometries will be helpful in industrial conditions to produce high-quality components without compromising machining productivity.

## 7.3 Scope of Future Work

The proposed study has numerous potential extensions. The following are some potential topics that could be addressed in relation to peripheral milling of curved geometries:

- Application of proposed classification scheme to the combined tool and workpiece deflection induced error.
- Effect of energy efficient machining strategy on workpiece surface quality and tool life.
- Study of the dynamics of machining of curved components along with the reduction of surface roughness.

# References


[1] Sol I Del, Rivero A, Norberto L, Gamez AJ. Thin-Wall Machining of Light Alloys : A Review of Models and Industrial Approaches. MDPI Mater 2019;19:1–28.

[2] International Energy Agency (IEA) (2016) World energy outlook special report 2016: energy and air pollution.

[3] Sihag N, Sangwan KS. An improved micro analysis-based energy consumption and carbon emissions modeling approach for a milling center. Int J Adv Manuf Technol 2019;104:705–21.

[4] Sihag N, Sangwan KS. A systematic literature review on machine tool energy consumption. J Clean Prod 2020;275:123125.

[5] Zhang L, Zheng L, Zhang ZH. An investigation of cutting forces in horizontal-mode peripheral milling of curved surfaces. Proc Inst Mech Eng Part B J Eng Manuf 2003;217:961–76.

[6] Budak E. Analytical models for high performance milling. Part I: Cutting forces, structural deformations and tolerance integrity. Int J Mach Tools Manuf 2006;46:1478–88.

[7] Tsai CL. Analysis and prediction of cutting forces in end milling by means of a geometrical model. Int J Adv Manuf Technol 2007;31:888–96.

[8] Rao S, Shunmugam MS. Analytical modeling of micro end-milling forces with edge radius and material strengthening effects. Mach Sci Technol 2012;16:205–27.

[9] Zhou L, Peng FY, Yan R, Yao PF, Yang CC, Li B. Analytical modeling and experimental validation of micro end-milling cutting forces considering edge radius and material strengthening effects. Int J Mach Tools Manuf 2015;97:29–41.

[10] Luo ZW, Zhao WX, Jiao L, Wang T, Yan P, Wang X Bin. Cutting force prediction in end milling of curved surfaces based on oblique cutting model. Int J Adv Manuf Technol 2017;89:1025–38.

[11] Moufki A, Le Coz G, Dudzinski D. End-milling of Inconel 718 Superalloy-An Analytical Modelling. Procedia CIRP 2017;58:358–63.

[12] Masmali M, Mathew P. An Analytical Approach for Machining Thin-walled Workpieces. Procedia CIRP 2017;58:187–92.

[13] Lin B, Wang L, Guo Y, Yao J. Modeling of cutting forces in end milling based on oblique cutting analysis. Int J Adv Manuf Technol 2016;84:727–36.

[14] Arsecularatne JA, Zhang LC, Montross C, Mathew P. On machining of hardened AISI D2 steel with PCBN tools. J Mater Process Technol 2006;171:244–52.

[15] Abou-El-Hossein KA, Kadirgama K, Hamdi M, Benyounis KY. Prediction of cutting force in end-milling operation of modified AISI P20 tool steel. J Mater Process Technol 2007;182:241–7.

[16] Ding T, Zhang S, Wang Y, Zhu X. Empirical models and optimal cutting parameters for cutting forces and surface roughness in hard milling of AISI H13 steel. Int J Adv Manuf Technol 2010;51:45–55.

[17] Zhang X, Zhang J, Zhou H, Ren Y, Xu M. A novel milling force model based on the influence of tool geometric parameters in end milling. Adv Mech Eng 2018;10:1–9.

[18] Bolar G, Das A, Joshi SN. Measurement and analysis of cutting force and product surface quality during end-milling of thin-wall components. Meas J Int Meas Confed 2018;121:190–204.

[19] Li B, Tian X, Zhang M. Modeling and multi-objective optimization of cutting parameters in the high-speed milling using RSM and improved TLBO algorithm. Int J Adv Manuf Technol 2020;111:2323–35.

[20] Kline WA, DeVor RE, Lindberg JR. The prediction of cutting forces in end milling with application to cornering cuts. Int J Mach Tool Des Res 1982;22:7–22.

[21] Ratchev S, Liu S, Huang W, Becker AA. A flexible force model for end milling of low-rigidity parts. J Mater Process Technol 2004;153–154:134–8.

[22] Wan M, Zhang WH. Calculations of chip thickness and cutting forces in flexible end milling. Int J Adv Manuf Technol 2006;29:637–47.

[23] Wan M, Zhang WH, Dang JW, Yang Y. A novel cutting force modelling method for cylindrical end mill. Appl Math Model 2010;34:823–36.

[24] Wei ZC, Wang MJ, Han XG. Cutting forces prediction in generalized pocket machining. Int J Adv Manuf Technol 2010;50:449–58.

[25] Wan M, Lu MS, Zhang WH, Yang Y. A new ternary-mechanism model for the prediction of cutting forces in flat end milling. Int J Mach Tools Manuf 2012;57:34–45.

[26] Perez H, Diez E, Marquez JJ, Vizan A. An enhanced method for cutting force estimation in peripheral milling. Int J Adv Manuf Technol 2013;69:1731–41.

[27] Wu B, Yan X, Luo M, Gao G. Cutting force prediction for circular end milling process. Chinese J Aeronaut 2013;26:1057–63.

[28] Aydin M, Uçar M, Cengiz A, Kurt M, Bakir B. A methodology for cutting force prediction in side milling. Mater Manuf Process 2014;29:1429–35.

[29] Hao H, Wang B, Tang W. Prediction of instantaneous milling force taking runout into account in peripheral milling of curved surface. Int J Adv Manuf Technol 2015;79:49–56.

[30] Han X, Tang L. Precise prediction of forces in milling circular corners. Int J Mach Tools Manuf 2015;88:184–93.

[31] Zhang X, Zhang J, Zhao WH. A new method for cutting force prediction in peripheral milling of complex curved surface. Int J Adv Manuf Technol 2016;86:117–28.

[32] Zhang Z, Li H, Meng G, Ren S, Zhou J. A new procedure for the prediction of the cutting forces in peripheral milling. Int J Adv Manuf Technol 2017;89:1709–15.

[33] Moges TM, Desai KA, Rao PVM. On modeling of cutting forces in micro-end milling operation. Mach Sci Technol 2017;21:562–81.

[34] Wimmer S, Ellinger J, Zaeh MF. A cutting force model for finishing processes using helical end mills with significant runout. Prod Eng 2018;12:703–14.

[35] Devor RE, Shareef IA. The Prediction of Surface Accuracy in End Milling. ASME, Journal of Engineering for Industry 1982; 10: 272-278.

[36] Budak E, Altintas Y. Peripheral milling conditions for improved dimensional accuracy. Int J Mach Tools Manuf 1994;34:907–18.

[37] Yun WS, Ko JH, Cho DW, Ehmann KF. Development of a virtual machining system, Part 2: Prediction and analysis of a machined surface error. Int J Mach Tools Manuf 2002;42:1607–15.

[38] Wang MY, Chang HY. A simulation shape error for end milling AL6061-T6. Int J Adv Manuf Technol 2003;22:689–96.

[39] Ryu SH, Lee HS, Chu CN. The form error prediction in side wall machining considering tool deflection. Int J Mach Tools Manuf 2003;43:1405–11.

[40] Dépincé P, Hascoët JY. Active integration of tool deflection effects in end milling. Part 1. Prediction of milled surfaces. Int J Mach Tools Manuf 2006;46:937–44.

[41] Aydın M, Uçar M, Cengiz A, Kurt M. Identification of static surface form errors from cutting force distribution in flat-end milling processes. J Brazilian Soc Mech Sci Eng 2015;37:1001–13.

[42] Soori M, Arezoo B, Habibi M. Tool deflection error of three-axis computer numerical control milling machines, monitoring and minimizing by a virtual machining system. J Manuf Sci Eng Trans ASME 2016;138:1–11.

[43] Nghiep TN, Sarhan AAD, Aoyama H. Analysis of tool deflection errors in precision CNC end milling of aerospace Aluminum 6061-T6 alloy. Meas J Int Meas Confed 2018;125:476–95.

[44] Ratchev S, Huang W, Liu S, Becker AA. Modelling and simulation environment for machining of low-rigidity components. J Mater Process Technol 2004;153–154:67–73.

[45] Wan M, Zhang WH. Efficient algorithms for calculations of static form errors in peripheral milling. J Mater Process Technol 2006;171:156–65.

[46] Aijun T, Zhanqiang L. Deformations of thin-walled plate due to static end milling force. J Mater Process Technol 2008;206:345–51.

[47] Gang L. Study on deformation of titanium thin-walled part in milling process. J Mater Process Technol 2009;209:2788–93.

[48] Izamshah R, Mo JPT, Ding S. Hybrid deflection prediction on machining thin-wall monolithic aerospace components. Proc Inst Mech Eng Part B J Eng Manuf 2012;226:592–605.

[49] Wu Q, Li DP, Ren L, Mo S. Detecting milling deformation in 7075 aluminum alloy thin-walled plates using finite difference method. Int J Adv Manuf Technol 2016;85:1291–302.

[50] Bolar G, Joshi SN. Three-dimensional numerical modeling, simulation and experimental validation of milling of a thin-wall component. Proc Inst Mech Eng Part B J Eng Manuf 2017;231:792–804.

[51] Li ZL, Tuysuz O, Zhu LM, Altintas Y. Surface form error prediction in five-axis flank milling of thin-walled parts. Int J Mach Tools Manuf 2018;128:21–32.

[52] Zhang J, Lin B, Fei J, Huang T, Xiao J, Zhang X, et al. Modeling and experimental validation for surface error caused by axial cutting force in end-milling process. Int J Adv Manuf Technol 2018;99:327–35.

[53] Yue C, Chen Z, Liang SY, Gao H, Liu X. Modeling machining errors for thin-walled parts according to chip thickness. Int J Adv Manuf Technol 2019;103:91–100.

[54] Agarwal A, Desai KA. Effect of workpiece curvature on axial surface error profile in flat end-milling of thin-walled components. Procedia Manuf 2020;48:498–507.

[55] Chiang HN, Junz Wang JJ. Generating mechanism and formation criteria of kinked surface in peripheral end milling. Int J Mach Tools Manuf 2011;51:816–30.

[56] Chiang HN, Junz Wang JJ. Generating mechanism and formation criteria of kinked surface in peripheral end milling. Int J Mach Tools Manuf 2011;51:816–30.

[57] Desai KA, Rao PVM. On cutter deflection surface errors in peripheral milling. J Mater Process Technol 2012;212:2443–54.

[58] Morelli L, Grossi N, Scippa A, Campatelli G. Surface error shape identification for 3-axis milling operations. Procedia CIRP 2020;101:126–9.

[59] Morelli L, Grossi N, Scippa A, Campatelli G. Extended classification of surface errors shapes in peripheral end-milling operations. J Manuf Process 2021;71:604–24.

[60] Yazar Z, Koch KF, Merrick T, Altan T. Feed rate optimization based on cutting force calculations in 3-axis milling of dies and molds with sculptured surfaces. Int J Mach Tools Manuf 1994;34:365–77.

[61] Law KMY, Geddam A, Ostafiev VA. Process-design approach to error compensation in the end milling of pockets. J Mater Process Technol 1999;89–90:238–44.

[62] Erdim H, Lazoglu I, Ozturk B. Feedrate scheduling strategies for free-form surfaces. Int J Mach Tools Manuf 2006;46:747–57.

[63] Smith S, Wilhelm R, Dutterer B, Cherukuri H, Goel G. Sacrificial structure preforms for thin part machining. CIRP Ann - Manuf Technol 2012;61:379–82.

[64] Wang J, Ibaraki S, Matsubara A. A cutting sequence optimization algorithm to reduce the workpiece deformation in thin-wall machining. Precis Eng 2017;50:506–14.

[65] Rober SJ, Shin YC, Nwokah ODI. A digital robust controller for cutting force control in the end milling process. J Dyn Syst Meas Control Trans ASME 1997;119:146–52.

[66] Yang MY, Choi JG. A tool deflection compensation system for end milling accuracy improvement. J Manuf Sci Eng Trans ASME 1998;120:222–9.

[67] Diez E, Perez H, Marquez J, Vizan A. Feasibility study of in-process compensation of deformations in flexible milling. Int J Mach Tools Manuf 2015;94:1–14.

[68] Yoshioka H, Shinno H, Sawano H, Tanigawa R. Monitoring of distance between diamond tool edge and workpiece surface in ultraprecision cutting using evanescent light. CIRP Ann - Manuf Technol 2014;63:341–4.

[69] Wang X, Bi Q, Zhu L, Ding H. Improved forecasting compensatory control to guarantee the remaining wall thickness for pocket milling of a large thin-walled part. Int J Adv Manuf Technol 2018;94:1677–88.

[70] Liu C, Li Y, Shen W. A real time machining error compensation method based on dynamic features for cutting force induced elastic deformation in flank milling. Mach Sci Technol 2018;22:766–86.

[71] Denkena B, Boujnah H. Feeling machines for online detection and compensation of tool deflection in milling. CIRP Ann 2018;67:423–6.

[72] Lo CC, Hsiao CY. A method of tool path compensation for repeated machining process. Int J Mach Tools Manuf 1998;38:205–13.

[73] Cho MW, Seo T Il, Kwon HD. Integrated error compensation method using OMM system for profile milling operation. J Mater Process Technol 2003;136:88–99.

[74] Chen Y, Gao J, Deng H, Zheng D, Chen X, Kelly R. Spatial statistical analysis and compensation of machining errors for complex surfaces. Precis Eng 2013;37:203–12.

[75] Huang N, Bi Q, Wang Y, Sun C. 5-Axis adaptive flank milling of flexible thin-walled parts based on the on-machine measurement. Int J Mach Tools Manuf 2014;84:1–8.

[76] Ge G, Du Z, Feng X, Yang J. An integrated error compensation method based on on-machine measurement for thin web parts machining. Precis Eng 2020;63:206–13.

[77] Raksiri C, Parnichkun M. Geometric and force errors compensation in a 3-axis CNC milling machine. Int J Mach Tools Manuf 2004;44:1283–91.

[78] Ratchev S, Liu S, Huang W, Becker AA. An advanced FEA based force induced error compensation strategy in milling. Int J Mach Tools Manuf 2006;46:542–51.

[79] Dépincé P, Hascoët JY. Active integration of tool deflection effects in end milling. Part 2. Compensation of tool deflection. Int J Mach Tools Manuf 2006;46:945–56.

[80] Rao VS, Rao PVM. Tool deflection compensation in peripheral milling of curved geometries. Int J Mach Tools Manuf 2006;46:2036–43.

[81] Uddin MS, Ibaraki S, Matsubara A, Nishida S, Kakino Y. A tool path modification approach to cutting engagement regulation for the improvement of machining accuracy in 2D milling with a straight end mill. J Manuf Sci Eng Trans ASME 2007;129:1069–79.

[82] Chen W, Xue J, Tang D, Chen H, Qu S. Deformation prediction and error compensation in multilayer milling processes for thin-walled parts. Int J Mach Tools Manuf 2009;49:859–64.

[83] Vahebi Nojedeh M, Habibi M, Arezoo B. Tool path accuracy enhancement through geometrical error compensation. Int J Mach Tools Manuf 2011;51:471–82.

[84] Zeroudi N, Fontaine M. Prediction of tool deflection and tool path compensation in ball-end milling. J Intell Manuf 2015;26:425–45.

[85] Ma W, He G, Zhu L, Guo L. Tool deflection error compensation in five-axis ball-end milling of sculptured surface. Int J Adv Manuf Technol 2016;84:1421–30.

[86] Gao Y yuan, Ma J wei, Jia Z yuan, Wang F ji, Si L kun, Song D ning. Tool path planning and machining deformation compensation in high-speed milling for difficult-to-machine material thin-walled parts with curved surface. Int J Adv Manuf Technol 2016;84:1757–67.

[87] Du Z, Zhang D, Hou H, Liang SY. Peripheral milling force induced error compensation using analytical force model and APDL deformation calculation. Int J Adv Manuf Technol 2017;88:3405–17.

[88] Zuo X, Zhang C, Li H, Wu X, Zhou X. Error analysis and compensation in machining thin-walled workpieces based on the inverse reconstruction model. Int J Adv Manuf Technol 2018;95:2369–77.

[89] Yue C, Liu X, Ding Y, Liang SY. Off-line error compensation in corner milling process. Proc Inst Mech Eng Part B J Eng Manuf 2018;232:1172–81.

[90] Hou Y, Zhang D, Mei J, Zhang Y, Luo M. Geometric modelling of thin-walled blade based on compensation method of machining error and design intent. J Manuf Process 2019;44:327–36.

[91] Huang WW, Zhang Y, Zhang XQ, Zhu LM. Wall thickness error prediction and compensation in end milling of thin-plate parts. Precis Eng 2020;66:550–63.

[92] Dietmair A, Verl A. A generic energy consumption model for decision making and energy efficiency optimisation in manufacturing. Int J Sustain Eng 2009;2:123–33.

[93] Avram OI, Xirouchakis P. Evaluating the use phase energy requirements of a machine tool system. J Clean Prod 2011;19:699–711.

[94] Mori M, Fujishima M, Inamasu Y, Oda Y. A study on energy efficiency improvement for machine tools. CIRP Ann - Manuf Technol 2011;60:145–8.

[95] He Y, Liu F, Wu T, Zhong FP, Peng B. Analysis and estimation of energy consumption for numerical control machining. Proc Inst Mech Eng Part B J Eng Manuf 2012;226:255–66.

[96] Balogun VA, Mativenga PT. Modelling of direct energy requirements in mechanical machining processes. J Clean Prod 2013;41:179–86.

[97] Moradnazhad M, Unver HO. Energy consumption characteristics of turn-mill machining. Int J Adv Manuf Technol 2017;91:1991–2016.

[98] Altıntaş RS, Kahya M, Ünver HÖ. Modelling and optimization of energy consumption for feature based milling. Int J Adv Manuf Technol 2016;86:3345–63.

[99] Edem IF, Mativenga PT. Modelling of energy demand from computer numerical control (CNC) toolpaths. J Clean Prod 2017;157:310–21.

[100] Gu W, Li Z, Chen Z, Li Y. An energy-consumption model for establishing an integrated energy-consumption process in a machining system. Math Comput Model Dyn Syst 2020;26:534–61.

[101] Yu S, Zhao G, Li C, Xu S, Zheng Z. Prediction models for energy consumption and surface quality in stainless steel milling. Int J Adv Manuf Technol 2021;117:3777–92.

[102] Gutowski T, Dahmus J, Thiriez A. Electrical energy requirements for manufacturing processes. Proc 13th CIRP Int Conf Life Cycle Eng LCE 2006 2006:623–8.

[103] Li W, Kara S. An empirical model for predicting energy consumption of manufacturing processes: A case of turning process. Proc Inst Mech Eng Part B J Eng Manuf 2011;225:1636–46.

[104] Aramcharoen A, Mativenga PT. Critical factors in energy demand modelling for CNC milling and impact of toolpath strategy. J Clean Prod 2014;78:63–74.

[105] Zhou L, Li J, Li F, Xu X, Wang L, Wang G, et al. An improved cutting power model of machine tools in milling process. Int J Adv Manuf Technol 2017;91:2383–400.

[106] Nguyen TT. Prediction and optimization of machining energy, surface roughness, and production rate in SKD61 milling. Meas J Int Meas Confed 2019;136:525–44.

[107] Yuan J, Shao H, Cai Y, Shi X. Energy efficiency state identification of milling processing based on EEMD-PCA-ICA. Meas J Int Meas Confed 2021;174:109014.

[108] Yoon HS, Lee JY, Kim MS, Ahn SH. Empirical power-consumption model for material removal in three-axis milling. J Clean Prod 2014;78:54–62.

[109] Sealy MP, Liu ZY, Zhang D, Guo YB, Liu ZQ. Energy consumption and modeling in precision hard milling. J Clean Prod 2016;135:1591–601.

[110] Xie J, Liu F, Huang J, Qiu H. Mapping acquisition of loading loss coefficient of main driving system of machine tools. Proc Inst Mech Eng Part B J Eng Manuf 2016;230:1264–71.

[111] Lv J, Tang R, Jia S, Liu Y. Experimental study on energy consumption of computer numerical control machine tools. J Clean Prod 2016;112:3864–74.

[112] Zhang C, Zhou Z, Tian G, Xie Y, Lin W, Huang Z. Energy consumption modeling and prediction of the milling process: A multistage perspective. Proc Inst Mech Eng Part B J Eng Manuf 2018;232:1973–85.

[113] Wang SM, Lee CY, Gunawan H, Yeh CC. An accuracy-efficiency-power consumption hybrid optimization method for CNC milling process. Appl Sci 2019;9.

[114] Wang Y, Li L, Lingling L, Cai W. Exploring the effect of un-deformed chip parameters on energy consumption for energy efficiency improvement in the milling. Procedia CIRP 2018;72:1380–5.

[115] Zhao G, Guo YB, Zhu P, Zhao Y. Energy Consumption Characteristics and Influence on Surface Quality in Milling. Procedia CIRP 2018;71:111–5.

[116] Tlhabadira I, Daniyan IA, Masu L, Mpofu K. Development of a model for the optimization of energy consumption during the milling operation of titanium alloy (Ti6Al4V). Mater Today Proc 2021;38:614–20.

[117] Liu N, Zhang YF, Lu WF. A hybrid approach to energy consumption modelling based on cutting power: A milling case. J Clean Prod 2015;104:264–72.

[118] Xie J, Liu F, Qiu H. An integrated model for predicting the specific energy consumption of manufacturing processes. Int J Adv Manuf Technol 2016;85:1339–46.

[119] Shi KN, Zhang DH, Liu N, Wang SB, Ren JX, Wang SL. A novel energy consumption model for milling process considering tool wear progression. J Clean Prod 2018;184:152–9..

[120] Shi KN, Ren JX, Wang SB, Liu N, Liu ZM, Zhang DH, et al. An improved cutting power-based model for evaluating total energy consumption in general end milling process. J Clean Prod 2019;231:1330–41.

[121] Yang D, Liu Y, Xie F, Xiao X. Analytical investigation of workpiece internal energy generation in peripheral milling of titanium alloy Ti–6Al–4V. Int J Mech Sci 2019;161–162.

[122] Wang Q, Zhang D, Tang K, Zhang Y. Energy consumption model for milling processes considering auxiliary load loss and its applications. Int J Adv Manuf Technol 2019;105:4309–23.

[123] Wang Q, Zhang D, Chen B, Zhang Y, Wu B. Energy consumption model for drilling processes based on cutting force. Appl Sci 2019;9.

[124] Venkata Rao K. Power consumption optimization strategy in micro ball-end milling of D2 steel via TLBO coupled with 3D FEM simulation. Meas J Int Meas Confed 2019;132:68–78.

[125] Zhang X, Yu T, Dai Y, Qu S, Zhao J. Energy consumption considering tool wear and optimization of cutting parameters in micro milling process. Int J Mech Sci 2020;178:105628.

[126] Yingjie Z. Energy efficiency techniques in machining process: A review. Int J Adv Manuf Technol 2014;71:1123–32.

[127] Peng T, Xu X. Energy-efficient machining systems: A critical review. Int J Adv Manuf Technol 2014;72:1389–406.

[128] Yusuf LA, Popoola K, Musa H. A review of energy consumption and minimisation strategies of machine tools in manufacturing process. Int J Sustain Eng 2021;14:1826–42.

[129] Yoon HS, Kim ES, Kim MS, Lee JY, Lee GB, Ahn SH. Towards greener machine tools - A review on energy saving strategies and technologies. Renew Sustain Energy Rev 2015;48:870–91.

[130] Abele E, Sielaff T, Schiffler A, Rothenbücher S. Analyzing energy consumption of machine tool spindle units and identification of potential for improvements of efficiency. Glocalized Solut. Sustain. Manuf. - Proc. 18th CIRP Int. Conf. Life Cycle Eng., Springer Science and Business Media, LLC; 2011, p. 280–5.

[131] Chen JL, Shen I, Huang H. Energy saving innovative design of green machine tools by case-based reasoning. In: GCSM 11th Glob Conf Sustain Manuf; 2013. p. 419–24.

[132] Fujishima M, Shimanoe H, Mori M. Reducing the energy consumption of machine tools. Int J Autom Technol 2017;11:601–7.

[133] Denkena B, Abele E, Brecher C, Dittrich MA, Kara S, Mori M. Energy efficient machine tools. CIRP Ann 2020;69:646–67.

[134] Ma F, Zhang H, Cao H, Hon KKB. An energy consumption optimization strategy for CNC milling. Int J Adv Manuf Technol 2017;90:1715–26.

[135] Shin SJ, Woo J, Rachuri S. Energy efficiency of milling machining: Component modeling and online optimization of cutting parameters. J Clean Prod 2017;161:12–29.

[136] Wang H, Zhong RY, Liu G, Mu WL, Tian X, Leng D. An optimization model for energy-efficient machining for sustainable production. J Clean Prod 2019;232:1121–33.

[137] Moreira LC, Li WD, Lu X, Fitzpatrick ME. Energy-Efficient machining process analysis and optimisation based on BS EN24T alloy steel as case studies. Robot Comput Integr Manuf 2019;58:1–12.

[138] Wirtz A, Biermann D, Wiederkehr P. Design and optimization of energy-efficient milling processes using a geometric physically-based process simulation system. Procedia CIRP, vol. 88, Elsevier B.V.; 2020, p. 270–5.

[139] Jacso A, Matyasi G, Szalay T. The fast constant engagement offsetting method for generating milling tool paths. Int J Adv Manuf Technol 2019;103:4293–305.

[140] Jacso A, Szalay T, Hu B. Optimizing the numerical algorithm in Fast Constant Engagement Offsetting Method for generating 2.5D milling tool paths. Int J Adv Manuf Technol 2020;108:2285–300.

[141] Lv J, Tang R, Tang W, Jia S, Liu Y, Cao Y. An investigation into methods for predicting material removal energy consumption in turning. J Clean Prod 2018;193:128–39.

[142] Martellotti ME An Analysis of the Milling Process. Trans ASME 1941; 83:677–695.

[143] Rao VS, Rao PVM. Effect of workpiece curvature on cutting forces and surface error in peripheral milling. Proc Inst Mech Eng Part B J Eng Manuf 2006;220:1399–407.

[144] Altintas Y. Manufacturing Automation: Metal Cutting Mechanics, Machine Tool Vibrations, and CNC Design. ASME. Appl. Mech. Rev. 2001; 54(5)

[145] Huang Y, Hoshi T. Improvement of flatness error in milling plate-shaped workpiece by application of side-clamping force. Precis Eng 2000; 24:364-370.

[146] Samuel G, Shunmugam M. Evaluation of straightness and flatness error using computational geometric techniques. Computer-Aided Design 1999;31:829-843.

[147] Pimenov DY, Guzeev VI, Krolczyk G, Mia M, Wojciechowski S. Modeling flatness deviation in face milling considering angular movement of the machine tool system components and tool flank wear. Precis Eng 2018;54:327–37.

[148] Wen XL, Zhu XC, Zhao YB, Wang DX, Wang FL. Flatness error evaluation and

verification based on new generation geometrical product specification (GPS). Precis Eng 2012;36:70–6.

[149] Eberhart R, Sixth JK. A new optimizer using particle swarm theory. Proc IEEE Symp Micro Mach Hum Sci Nagoys, Japan 1997:39–43.

[150] Pedrycz W, Sillitti A, Succi G. Computational intelligence: An introduction. Stud Comput Intell 2016;617:13–31.

[151] Rezaee Jordehi A, Jasni J. Parameter selection in particle swarm optimisation: a survey. J Exp Theor Artif Intell 2013;25:527–42.

[152] Yang L, DeVor RE, Kapoor SG. Analysis of force shape characteristics and detection of depth-of-cut variations in end milling. J Manuf Sci Eng 2005;127:454–62.

[153] Li L, Yan J, Xing Z. Energy requirements evaluation of milling machines based on thermal equilibrium and empirical modelling. J Clean Prod 2013;52:113–21.

[154] Hu S, Liu F, He Y, Peng B. Characteristics of additional load losses of spindle system of machine tools. J Adv Mech Des Syst Manuf 2010;4:1221–33.

[155] Stori JA, Wright PK. Constant engagement tool-path generation for convex geometries. J Manuf Syst 2002;21:468.

[156] Uddin MS, Ibaraki S, Matsubara A, Nishida S, Kakino Y. Constant engagement tool path generation to enhance machining accuracy in end milling. JSME Int Journal, Ser C Mech Syst Mach Elem Manuf 2006;49:43–9.

[157] Liu ZY, Sealy MP, Li W, Zhang D, Fang XY, Guo YB, et al. Energy consumption characteristics in finish hard milling. J Manuf Process 2018;35:500–7.

[158] Ma J, Ge X, Chang SI, Lei S. Assessment of cutting energy consumption and energy efficiency in machining of 4140 steel. Int J Adv Manuf Technol 2014;74:1701–8.

# List of publications

## 1. Papers in International Journals and Conference

a. **S.S.Pawar**, T.C. Bera, K.S. Sangwan, Modelling of Energy Consumption for Milling of Circular Geometry. Procedia CIRP 2021; 98:470–475.

b. **S.S. Pawar**, T.C. Bera, K.S. Sangwan, Energy consumption modelling in milling of variable curved geometry, International Journal of Advanced Manufacturing Technology 2022;120:1967-1987.

c. **S.S. Pawar**, T.C. Bera, K.S. Sangwan, Developing Energy Efficient Milling Strategy for Variable Curved Geometry Using Constant Engagement Method. Procedia CIRP 2023;116:402-407.

d. **S.S. Pawar**, T.C. Bera, K.S. Sangwan, Towards Energy Efficient Milling of Variable Curved Geometries. Journal of Manufacturing Processes 2023;94:497-511

## 2. Papers under Review

a. **S.S. Pawar**, T.C. Bera, K.S. Sangwan, Identification of a classification scheme of surface errors in peripheral milling.

# Brief Biography of Candidate

**Pawar Shrikant Shankarrao** is a PhD candidate in the department of Mechanical Engineering at Birla Institute of Technology and Science Pilani, Pilani Campus, India. He is a graduate in the discipline of Mechanical Engineering from College of Engineering Pune (COEP) and post graduate in Design Engineering from Birla Institute of Technology and Science Pilani, Pilani Campus, India. He has published research articles based upon his PhD work in international journals and conferences. His research interests are primarily in the field of machining processes, energy efficiency, CAD/CAM and CNC machining.

# Brief Biography of Supervisor and Co-Supervisor

## About the supervisor

**Prof. Tufan Chandra Bera** is an Associate Professor of Mechanical Engineering at Birla Institute of Technology and Science Pilani, Pilani Campus. He joined the BITS Pilani in 2010 as a faculty member of Mechanical Engineering Department. He has received PhD in Mechanical Engineering from Indian Institute of Technology Delhi, New Delhi in 2011. He spent almost two months at Purdue University, West Lafayette, Indiana, USA, 2017 as a postdoc visiting scholar. His area of interest in teaching is manufacturing science and engineering along with CAD/CAM and CNC Technology. His research interest includes Conventional and Unconventional Machining, CAD/CAM/CAE, Advanced Manufacturing Processes, Product Design and Development. He was professor-in-charge of Manufacturing Engineering Association (MNA), BITS Pilani, Pilani Campus for six years. He is also a Fellow of The Institution of Engineers (India) and Senior Member of The Indian Institution of Industrial Engineering.

## About Co-supervisor

**Prof. Kuldip Singh Sangwan** is a Senior Professor of Mechanical Engineering and the Chief of Worksop Unit at Birla Institute of Technology and Science Pilani, Pilani Campus. He is an active researcher in the field of sustainable manufacturing, green supply chain management, cyber physical production systems, energy efficient machining, industry 4,0, reverse logistics, lean manufacturing, life cycle engineering, and application of artificial intelligence in manufacturing system design. He has guided 12 PhDs and 9 PhDs are in progress. He has published more than 100 papers in international journals and conferences. He has an active collaboration with TU Braunschweig, Germany since last 10 years. He has established Joint Indo-German Experience Lab and Sustainable Manufacturing & Life Cycle Engineering Lab at BITS Pilani, Pilani Campus. Prof. Sangwan is a fellow of the Institution of Engineers (India) and at present is Chairman of its Pilani Centre.